

Discrete Ordinates Methods for Transport Problems with Curved Spatial Grids

by

Changyuan Liu

A dissertation submitted in partial fulfillment
of the requirements for the degree of
Doctor of Philosophy
(Nuclear Engineering and Radiological Sciences)
in The University of Michigan
2015

Doctoral Committee:

Professor Edward W. Larsen, Chair
Professor Michael R. Combi
Professor Thomas J. Downar
Professor William R. Martin

越调 小桃红

十月月下秋雨落，庭前鹿儿过，不知商周愁叹多。

至今朝 (zhao一声)，乾坤改易金殿没 (mo四声)。

锦绣重织，山河壮丽，同学英姿烁。

(作者：刘畅源)

This is my poem in the form of the verse from the Chinese Yuan Dynasty (1271-1368). It is written when I see the deers crossing north campus of University of Michigan. The deers are relaxed and innocent about Chinese last 175 struggling years. But the young graduates will now start a brighter future of China and the world.

© Changyuan Liu 2015

All Rights Reserved

For the future

ACKNOWLEDGEMENTS

I would like to first thank professor Edward Larsen for his endurance and patience for my research during the past 5 years, despite our thinking in different ways, speaking with different mother languages, and living across different generations.

Next, I would send my great gratitudes to Dr. Alex Bielajew for his introducing me to the nuclear sciences and long lasting cares during the way. Also, the retired undergraduate advisor Pam Derry took great care of my junior and senior years like a grandmother. Moreover, Prof. William Martin and Thomas Downar played important roles on my learning of the knowledge related to our field. Addiontially, Profs. Lumin Wang, Annalisa Manera and Michael Combi also accompanied me for feeling their kindness. Also the graduate coordinator Peggy Grammar showed me great kindness. I thank all of them.

During the past several years, several of my graduate classmates Ang Zhu, Yuxuan Liu, Jipu Wang, Tian Wei, Kendra Keady, Timothy Burke, Ben Yee, Ben Collins, Travis Trahan, Eric Baker and many of them accompanied me. Thank for the enjoyable time.

Han Gyu Joo from SNU, Nam Zhi Cho from KAIST, Kan Wang from Tsinghua Univ., Yun An Chao from Shanghai Jiaotong Univ., Akio Yamamoto from Nagoya Univ., Peter Miller from Univ. of Michigan, John Lee from Univ. of Michigan, Yanhua Yang, Yixue Chen, Hui Yu from SNPSDC, Shaohong Zhang from Nustar, Deokjung Lee from UNIST, Hongchun Wu from Xi'an Jiaotong Univ., Jiyu Zheng from Liaoning Herbepax Co., Zhongqin Lin from Shanghai Jiaotong Univ., and Zhaohua Liu from

CNNC-Jiangsu have given me many encouragements, which I really appreciate.

Also, I would like to send my special gratitudes to Xiaoruo Gai, Xirui Cao, Yimeng Xie, Yiwen Wu, Siyuan Tao, Ning Ding, Dongyun Xu, Yiduo Mei, Shiyu Xie, Lily Wu, Sitao Chen, Yifan Zhao, Tianhao Shao in the non-profit organization Dream Corps International. Ms. Shuyi Li from King-tech China also influenced me to be more responsibale for the society. Because of all of you, I realize what one individual can do for the children and the future of my beloved country, China and the world.

At the end, I would like to thank my parants: Mr. Zhicheng Wang and Ms. Yingjie Guan for your endless and countless love.

TABLE OF CONTENTS

DEDICATION	ii
ACKNOWLEDGEMENTS	iii
LIST OF FIGURES	viii
LIST OF TABLES	xix
ABSTRACT	xxii
CHAPTER	
I. Introduction	1
1.1 Background for Reactor Simulations	1
1.2 Historical Review of Numerical Methods	4
1.2.1 Monte Carlo Method	4
1.2.2 Deterministic Methods	6
1.3 Comparison of SN and MOC Methods	11
1.4 Thesis Outline	12
II. One-Dimensional Problems	16
2.1 The Scope of the Geometry	16
2.2 One-Dimensional Multigroup Discrete Ordinates Neutron Trans- port Equation	17
2.3 Auxiliary Equations	25
2.3.1 The Step Method (STEP)	27
2.3.2 The Step Characteristic Method (SC)	27
2.3.3 The Multiple Balance Method (MB)	30
2.4 Sweep	33
2.5 Numerical Results	34
2.5.1 Pin-cell Problem	35
2.5.2 Mini-assembly Problem	40

2.6	Road-map to Two-dimensional Geometry	44
III. Two-Dimensional Problems with Cartesian Spatial Grids . .		45
3.1	The Scope of Geometry	45
3.2	Two-Dimensional Multigroup Discrete Ordinates Neutron Trans- port Equation	47
3.3	Categorization of Boundaries	58
3.4	Auxiliary Equations	60
3.4.1	The Step Method (STEP)	61
3.4.2	The Simplified Step Characteristic Method (SSC) .	63
3.4.3	The Multiple Balance Method (MB)	68
3.5	Sweep	75
IV. Numerical Results for Two-Dimensional Problems with Carte- sian Spatial Grids		79
4.1	BWR Assembly Problem	80
4.2	LWR Assembly Problem with Burnable Absorber	86
V. Two-Dimensional Problems with Curved Spatial Grids . . .		92
5.1	The Scope of Geometry	92
5.1.1	Topology	95
5.1.2	Parametrization	96
5.1.3	Cell and Boundary Integrals	98
5.2	The Multigroup Discrete Ordinates Neutron Transport Equation	100
5.3	Re-entrant Boundaries	106
5.4	Categorization of Boundaries	109
5.5	Auxiliary Equations	113
5.5.1	The Step Method (STEP)	114
5.5.2	The Simplified Step Characteristic Method (SSC) .	114
5.5.3	The Multiple Balance Method (MB)	119
5.6	Sweep	125
VI. Numerical Results for Two-Dimensional One-group Problems with Curved Spatial Grids		132
6.1	One-group Cross Sections	133
6.2	Single Pin-cell Problems	134
6.2.1	Non-IFBA Pin-cell Problem	134
6.2.2	IFBA Pin-cell Problem	140
6.3	Mini-assembly Problem	146

VII. Numerical Results for Two-Dimensional Multigroup Problems with Curved Spatial Grids	153
7.1 WIMS-D Cross Section	153
7.2 Material Compositions	156
7.3 Geometry of Pin-cells	157
7.4 VERA Benchmark Problems	158
7.4.1 Problem 1A: Fuel Pin-cell without IFBA	158
7.4.2 VERA Benchmark Problem 1E: Fuel Pin-cell with IFBA	162
7.4.3 VERA Benchmark Problem 2A: Zero Power Fuel Assembly	165
7.5 Problems with a Large Flux Gradient	172
7.5.1 Mini-assembly Problem	172
7.5.2 VERA Benchmark Problem 2A with Vacuum Boundaries	173
7.6 Summary	181
VIII. Conclusions & Future Work	182
8.1 Conclusions	182
8.2 Future Work	185
BIBLIOGRAPHY	187

LIST OF FIGURES

Figure

1.1	An illustration of neutron interaction with a nucleus.	2
1.2	An example PWR reactor layout.	4
1.3	Reactor simulations scheme. Adapted from Figure 1.1 from <i>Hebert</i> (2009). The focus of this thesis is lattice calculations.	5
1.4	The state machine of Monte Carlo neutrons.	6
1.5	An illustration of the approximations of curved boundaries by piecewise-continuous linear segments in previous SN methods. In this thesis, we develop new methods to treat curved boundaries analytically. . .	9
1.6	An illustration of the MOC method.	10
1.7	The scope of problems for MOC and SN methods.	12
2.1	The one-dimensional spatial grid divides the space into I “ segments ”. The boundaries for the segment i are $x = x_{i-1}$ and $x = x_i$. i is an integer ranging from 1 to I	16
2.2	The angular variable μ is the cosine of the angle between the direction flight $\hat{\Omega}$ and the positive x -axis, which has a unit vector of \hat{i}	17
2.3	The illustration of the averaged angular flux of segment i and its end points	23
2.4	Categorization of the endpoints of a segment to be “incoming” or “outgoing”, based on whether the angular cosine μ_n is positive or negative.	26

2.5	The definitions of two linear weight functions $f_i^+(x)$ and $f_i^-(x)$, which are 1 at one end point, and 0 at the other end point.	30
2.6	The sweep order of the one-dimensional spatial grid. For $\mu_n > 0$, the segments are visited in the increasing order from segment 1 to segment I . For $\mu_n < 0$, the segments are visited in the decreasing order from segment I to segment 1.	34
2.7	A one-dimensional pin-cell geometry. The boundary conditions on both ends are reflecting . The coarse grid contains 4 segments, and the fine grid contains 8 segments.	36
2.8	The error comparisons for the one-dimensional pin-cell problem. The SN solutions are simulated with a variety of angular quadrature sets: S2, S4, S8, S16, S32. The dashed line is the Monte Carlo uncertainties within two standard deviations.	39
2.9	A one-dimensional mini-assembly problem. The boundary is reflecting on the left, and is vacuum on the right. The mini-assembly consists of 3 fuel pin-cells and one water pin-cell. The pin-cell pitch is 1.26 cm. For the coarse grid, each fuel pin-cell contains 8 segments. For the fine grid, each fuel pin-cell contains 16 segments. For the both coarse and fine grids, the water pin-cell contains 4 segments.	40
2.10	The error comparisons for the one-dimensional mini-assembly problem. The SN solutions are simulated with a variety of angular quadrature sets: S2, S4, S8, S16, S32. The dashed line is the Monte Carlo uncertainties within two standard deviations.	43
2.11	The origins of the two-dimensional deterministic methods.	44
3.1	The Cartesian grid, which is composed of $I \times J$ rectangles. There are $I + 1$ boundaries in the x direction, and $J + 1$ boundaries in the y direction.	46
3.2	The rectangle (i, j) is bounded with four lines with equations $x = x_{i-1}$, $x = x_i$, $y = y_{j-1}$ and $y = y_j$	46
3.3	An illustration of a unit vector $\hat{\Omega}$ and definitions of its components. φ is the azimuthal angle, which is defined as the angle counting from x -axis counterclockwise to the projection of $\hat{\Omega}$ onto the $x - y$ plane. θ is the polar angle, which is the angle needed to rotate z -axis to $\hat{\Omega}$. The range of θ is $0 \leq \theta \leq \pi$, and the range of φ is $0 \leq \varphi \leq 2\pi$	49

3.4	The illustration of the angles of the “ level symmetric ” $S2$ and $S4$ quadrature sets in the first octant. These angles preserve some symmetry conditions, the first of which is that the angles are symmetric for all 8 octants, the second of which is that the angles are symmetric for x -axis, y -axis and z -axis.	52
3.5	The averaged neutron fluxes of the rectangle (i, j) and its four boundaries.	55
3.6	For direction $\hat{\Omega}_n$, the averaged boundary flux is incoming if the neutron enters the rectangle through the boundary. It is outgoing if the neutron exits the rectangle through the boundary. The categorization of a boundary as incoming or outgoing depends on the sign of the x and y components of $\hat{\Omega}_n$. The incoming boundaries are marked as “ in ”, and the outgoing boundaries are marked as “ out ”.	59
3.7	Visualization of the auxiliary equations for the step method. The direction of flight is assumed with positive x and y components. Quantities that are equal are marked with the same colors. Quantities that are different are marked with the different colors.	62
3.8	In the simplified step characteristic method, the two-dimensional transport is approximated by a one-dimensional transport process along the t axis from $t = 0$ to $t = s$. s and d are the length and the width of the box marked in green. One side of the box is parallel to the direction of flight. The width d is the shallow of the rectangle (i, j) projected to a line perpendicular to the direction of flight. The green box and the rectangle (i, j) have the same area. These requirements determine the width and length of the green box.	65
3.9	Visualization of the auxiliary equations for the simplified step characteristic method. The direction of flight is assumed with positive x and y components.	67
3.10	The weight functions of the four boundaries of the rectangle (i, j) . The weight function of a boundary is 1 on the boundary.	68
3.11	Visualization of the balance equation and auxiliary equations for the multiple balance method. The direction of flight is assumed with positive x and y components. Quantities that are the same are marked with the same colors. Quantities that are different are marked with the different colors.	74

3.12	The sweep order of the Cartesian spatial grid for the direction with positive x and y components. The order begins with the rectangle with coordinate $(1, 1)$, and then sweeps row by row to the rectangle with coordinate (I, J)	76
3.13	The sweep order of the Cartesian spatial grid for the direction with negative x component and positive y component . The order begins with the rectangle with coordinate $(I, 1)$, and then sweeps row by row to the rectangle with coordinate $(1, J)$	77
3.14	The sweep order of the Cartesian spatial grid for the direction with negative x component and negative y component . The order begins with the rectangle with coordinate (I, J) , and then sweeps row by row to the rectangle with coordinate $(1, 1)$	77
3.15	The sweep order of the Cartesian spatial grid for the direction with positive x component and negative y component . The order begins with the rectangle with coordinate $(1, J)$, and then sweeps row by row to the rectangle with coordinate $(I, 1)$	78
4.1	The geometry of the BWR cell problem.	80
4.2	The grids of BWR assembly problem. The coarse grid has 6x6 rectangular cells, and the fine grid has 21x21 rectangular cells.	81
4.3	The pin-cell power of the Monte Carlo reference for the BWR assembly problem.	82
4.4	The error in k and max-min pin power ratio for the BWR assembly problem on the coarse grid. The MOC solutions are simulated with a variety of angular quadrature sets: A4P2, A4P4, and A8P4. The SN solutions are simulated with a variety of angular quadrature sets: S4, S8, S12, S16, and S20. The dashed line is the Monte Carlo reference.	84
4.5	The error in k and max-min pin power ratio for the BWR assembly problem on the fine grid. The MOC solutions are simulated with a variety of angular quadrature sets: A4P2, A4P4, and A8P4. The SN solutions are simulated with a variety of angular quadrature sets: S4, S8, S12, S16, and S20. The dashed line is the Monte Carlo reference.	85
4.6	The geometry of the LWR assembly problem with burnable absorber.	86
4.7	The grids of LWR assembly problem. The coarse grid has 6x6 rectangular cells, and the fine grid has 21x21 rectangular cells.	87

4.8	The pin-cell power of the Monte Carlo reference for the LWR assembly problem.	88
4.9	The error in k and the max-min pin power ratio for the LWR cell problem with burnable absorber on the coarse grid. The MOC solutions are simulated with a variety of angular quadrature sets: A4P2, A4P4, and A8P4. The SN solutions are simulated with a variety of angular quadrature sets: S4, S8, S12, S16, and S20. The dashed line is the Monte Carlo reference.	90
4.10	The error in k and max-min pin power ratio for the LWR cell problem with burnable absorber on the fine grid. The MOC solutions are simulated with a variety of angular quadrature sets: A4P2, A4P4, and A8P4. The SN solutions are simulated with a variety of angular quadrature sets: S4, S8, S12, S16, and S20. The dashed line is the Monte Carlo reference.	91
5.1	Example of planar geometry formed by lines and circular arcs. There are 13 spatial cells, and the spatial cell numbered “0” is green. The black lines are the boundaries inside, and the red lines are the boundaries of the outline.	93
5.2	A simplified PWR assembly, which is composed of a grid of squares. Each square may contain concentric circles, which is called a “ pin-cell ”. One example is marked in green, which is a guide tube. Most problems considered in this thesis are of this type. There is a “coarse” grid of square pin-cells, and each coarse cell has “fine” spatial cells bounded by lines and circular arcs.	94
5.3	Two cells and their boundaries. Two boundaries c_1 and c_2 have opposite directions when belonging two neighboring cells f_1 and f_2 . .	95
5.4	Normal vector $\hat{n}(t)$ of boundary c pointing to the “right”.	96
5.5	The parametrization of a linear boundary. The location \vec{O} is a point on the line and \hat{d} is a unit vector in the direction of the line. The points with parameter of $t = a$ and $t = b$ are the end points of the linear boundary.	97
5.6	The parametrization of a circular arc boundary. The location \vec{O} is the center of the circle, and r is the radius of the circle. The points with parameter of $t = a$ and $t = b$ are the end points of the circular arc boundary.	98

5.7	An example of a cell f and its boundaries $C(f)$. This example has four boundaries c_1, c_2, c_3 and c_4	102
5.8	An illustration of the averaged angular fluxes in direction $\hat{\Omega}_n$ and group g of cell f and its four boundaries c_1, c_2, c_3 and c_4	105
5.9	An illustration of four rays ①,②,③,④ in the direction $\hat{\Omega}_n$. Ray ① enters boundary c_2 and exits c_2 ; ray ② enters boundary c_2 and exits c_3 ; ray ③ enters boundary c_1 and exits c_3 ; ray ④ enters boundary c_1 and exits c_4 . c_2 is a “ re-entrant boundary ” of the direction $\hat{\Omega}_n$	107
5.10	Example of the applying of the “ rule of a fixed ”. The re-entrant boundary is c_2 . There are four rays ①,②,③,④ in the direction $\hat{\Omega}_n$. The cell is then split with a line which is perpendicular to $\hat{\Omega}_n$, and which passes \hat{O} , which is the center of the boundary c_2 . After, ray ① enters boundary c_2 and exits c_5 ; ray ② enters boundary c_2 and exits c_5 ; ray ③ enters boundary c_1 and exits c_5 ; Ray ④ enters boundary c_1 and exits c_5 . A re-entrant boundary no longer exists. The line added is marked as dashed to indicate the “split” is temporary only for the angle $\hat{\Omega}_n$	108
5.11	The cells numbered “[0]”, “[4]”, “[9]” and “[10]” of the left figure has re-entrant boundaries for the direction of $\hat{\Omega}$. The cells after split with a line passing through the center of the circle, which is perpendicular to $\hat{\Omega}$. It results cells numbered “[0]”, “[1]”, “[3]”, “[4]”, “[6]”, “[17]”, “[10]” and “[11]” in the right figure. There are no re-entrant boundaries after. The line added is marked as dashed to indicate the “split” is temporary only for the angle $\hat{\Omega}$	109
5.12	The categorization of boundaries as “ incoming ”, “ outgoing ” and “ parallel ”. A parallel boundary does not appear in this example.	110
5.13	An analytic criteria, which is based on the sign of the dot product between the A_1 vector and the direction of traveling $\hat{\Omega}_n$, for categorization of a boundary as “ incoming ”, “ outgoing ” and “ parallel ”.	112
5.14	Examples of curved spatial cells that one usually encounter in a pin-cell geometry. The cell-averaged and boundary averaged fluxes are labeled. For the direction of flight $\hat{\Omega}$, all boundaries are categorized as “incoming”, which is marked as “in”, or is categorized as “outgoing”, which is marked as “out”.	113
5.15	The STEP auxiliary equations for two example spatial cells that one usually encounters in a pin-cell geometry.	115

5.16	In the simplified step characteristic method, the two-dimensional transport is approximated by a one-dimensional transport process along the t axis from $t = 0$ to $t = s$. s and d are the length and the width of the box marked in green. One side of the box is parallel to the direction of flight. The width d is the shallow of the cell projected to a line perpendicular to the direction of flight. The green box has the same area as the that of the cell. These requirements determine the width and length of the green box. Two example spatial cells that one usually encounters in a pin-cell geometry are depicted in the figure.	116
5.17	The SSC auxiliary equations for two example spatial cells that one usually encounters in a pin-cell geometry.	119
5.18	The MB auxiliary equations for two example spatial cells that one usually encounters in a pin-cell geometry. The definitions of the terms $\vec{\alpha}_{c,d}$ and β_c are defined in equation (5.84). In these examples, only the boundary c_2 is outgoing, so only one auxiliary equation is needed.	126
5.19	The sweep process of four triangles for the direction of the $\hat{\Omega}$. The order is cell 0, 3, 2 and 1. The solving of each cell uses the fluxes of incoming boundaries obtained either from boundary conditions or from the fluxes of outgoing boundaries of cells solved earlier.	127
5.20	Boundary c is the an outgoing boundary of cell f_1 , and is an incoming boundary of cell f_2 . Then two nodes f_1 and f_2 and a directed edge from f_1 to f_2 are drawn in a graph.	128
5.21	A graph showing the sweep orders between two neighboring cells for the four-triangle geometry. In a sweeping, the cell at the starting node of a directed edge needs to be visited before the cell at the end node of a directed edge.	129
5.22	A graph showing the sweep orders between two neighboring cells for the pin-cell geometry. In a sweeping, the cell at the starting node of a directed edge needs to be visited before the cell at the end node of a directed edge.	130
5.23	A valid sweeping order of a pin-cell at direction $\hat{\Omega}$ is 13, 18, 14, 15, 12, 11, 4, 2, 6, 17, 16, 10, 9, 0, 1, 5, 3, 7, 8. The order is visualized in the graph.	131

5.24	A valid sweeping order of a coarse Cartesian grid of pin-cells at direction $\hat{\Omega}$ is determined in two stages. First, we sweep over the coarse grid with a procedure discussed in section 3.5, and second, we sweep each pin-cell fine grid based on the procedure discussed in this section.	131
6.1	Material types in a fuel pin-cell of a pressurized water reactor. Dimensions are exaggerated to show the clad, gap and IFBA, which are much thinner than depicted here.	134
6.2	The coarse grid and fine grid of the pin-cell without the IFBA coating outside the fuel cylinder. There are 32 spatial cells in the coarse grid and 304 spatial cells in the fine grid.	135
6.3	The error comparisons for the pin-cell problem without the IFBA layer on the coarse grid. The MOC solutions data points are simulated with a variety of angular quadrature sets: A4P2, A4P4, A8P4. The SN solutions data points are simulated with a variety of angular quadrature sets: S4, S8, S12, S16, S20. The dashed line is the Monte Carlo uncertainties within two standard deviations.	138
6.4	The error comparisons for the pin-cell problem without the IFBA layer on the fine grid. The MOC solutions data points are simulated with a variety of angular quadrature sets: A4P2, A4P4, A8P4. The SN solutions data points are simulated with a variety of angular quadrature sets: S4, S8, S12, S16, S20. The dashed line is the Monte Carlo uncertainties within two standard deviations.	139
6.5	The fine grid of spatial cells of a pin-cell with IFBA coating outside the fuel cylinder. There are 464 spatial cells. A zoom-in subplot is shown for the very fine spatial cells inside and near the IFBA layer.	140
6.6	The error comparisons for the pin-cell problem with a thin IFBA layer on the fine grid. The MOC solutions data points are simulated with a variety of angular quadrature sets: A4P2, A4P4, A8P4. The SN solutions data points are simulated with a variety of angular quadrature sets: S4, S8, S12, S16, S20. The dashed line is the Monte Carlo uncertainties within two standard deviations.	143
6.7	Detailed scalar flux inside and near the IFBA region. A dip in flux is observed because of large absorption cross section. MOC with wide ray spacing may result an unphysical low flux. See Figure 6.8 for an explanation.	144
6.8	A simplified depiction of MOC rays passing through a cell. When ray spacing is wide, there may be no tracks in the cell.	145

6.9	An illustration of the mini-assembly pin-cell layout. Four fuel pin-cells are in the center with reflected boundaries, which is surrounded by five moderator pin-cells with vacuum boundaries.	146
6.10	The coarse grid and fine grid. For each fuel pin-cell, there are 48 spatial cells in the coarse grid, and 96 spatial cells in the fine grid. For both cases, the moderator pin-cells have 16 spatial cells.	147
6.11	The pin-cell averaged fluxes, which are normalized to 1.0 for the pin-cell at coordinate (0,0). The percentage in red marks the relative error from the Monte Carlo reference, calculated with the formula defined in equation (2.68).	148
6.12	The comparisons of k and max-min pin power ratio for the mini-assembly problem on the coarse grid. The MOC solutions data points are simulated with a variety of angular quadrature sets: A4P2, A4P4, A8P4. The SN solutions data points are simulated with a variety of angular quadrature sets: S4, S8, S12, S16, S20. The dashed line is the Monte Carlo reference.	151
6.13	The comparisons of k and max-min pin power ratio for the mini-assembly problem on the fine grid. The MOC solutions data points are simulated with a variety of angular quadrature sets: A4P2, A4P4, A8P4. The SN solutions data points are simulated with a variety of angular quadrature sets: S4, S8, S12, S16, S20. The dashed line is the Monte Carlo reference.	152
6.14	MOC rays passing through a cell will divide it into one or more fine cells.	152
7.1	The fission spectrum in WIMS-D cross section library.	154
7.2	The geometry of pin-cells. Different materials are marked in different colors. The IFBA layer may not be present in a fuel pin-cell. The “instruction tubes” are “guide tube” pin-cells inserted in the middle of an LWR assembly. (<i>Godfrey, 2014</i>)	157
7.3	The spatial grid for Problem 1A: the fuel pin-cell without IFBA. All outer boundaries are reflecting.	159

7.4	Error comparisons for problem 1A. The MOC solution data points are simulated with a variety of angular quadrature sets: A4P2, A4P4, A8P4. The SN solution data points are also simulated with a variety of angular quadrature sets: S4, S8, S12, S16, S20. The dashed lines are the Monte Carlo uncertainties within two standard deviations. The uncertainties in the Monte Carlo results are so small that the dashed lines cannot be distinguished from each other.	161
7.5	The spatial grid for Problem 1E: the fuel pin-cell with an IFBA layer. All outer boundaries are reflecting.	162
7.6	Error comparisons for problem 1E. The MOC solution data points are simulated with a variety of angular quadrature sets: A4P2, A4P4, A8P4. The SN solution data points are also simulated with a variety of angular quadrature sets: S4, S8, S12, S16, S20. The dashed lines are the Monte Carlo uncertainties within two standard deviations. The uncertainties in the Monte Carlo results are so small that the dashed lines cannot be distinguished from each other.	164
7.7	The geometry of VERA benchmark problem 2A, which is a fuel assembly. There are 25 empty guide tubes and one centered instruction tube . All outer boundaries are reflecting.	165
7.8	The spatial grid for Problem 2A. All outer boundaries are reflecting.	166
7.9	Error comparisons for the problem 2A. The MOC solution data points are simulated with two angular quadrature sets: A4P2, A4P4. The SN solution data points are also simulated with two angular quadrature sets: S4, S8. The dashed line shows the Monte Carlo uncertainties within two standard deviations. The uncertainties in the Monte Carlo k -eigenvalues are so small that the dashed lines cannot be distinguished from each other.	168
7.10	Comparison of pin-cell power distributions for Problem 2A.	169
7.11	Comparison of pin-cell power error distributions for Problem 2A.	170
7.12	Validation of WIMS-D cross sections for problem 2A pin-cell power	171
7.13	The spatial grid for the mini-assembly problem, which consists of a 3x3 grid of pin-cells. The top and right boundaries next to the moderator pin-cells are vacuum, and the bottom and left boundaries next to the fuel pin-cells are reflecting.	173

7.14	Error comparisons for the mini-assembly problem. The MOC solution data points are simulated with a variety of angular quadrature sets: A4P2, A4P4, A8P4. The SN solution data points are also simulated with a variety of angular quadrature sets: S4, S8, S12, S16, S20. The dashed lines are the Monte Carlo uncertainties within two standard deviations. The uncertainties in the Monte Carlo k -eigenvalues are so small that the dashed lines cannot be distinguished from each other.	175
7.15	Pin-power distribution from the MC, MOC, STEP, SSC and MB method. The uncertainty in the pin-power and the error between other methods othan than MC and the MC method is provided as well.	176
7.16	Error comparisons for the problem 2A with vacuum boundaries. The MOC solution data points are simulated with two angular quadrature sets: A4P2, A4P4. The SN solution data points are also simulated with two angular quadrature sets: S4, S8. The dashed line shows the Monte Carlo uncertainties within two standard deviations. The uncertainties in the Monte Carlo k -eigenvalues are so small that the dashed lines cannot be distinguished from each other.	178
7.17	Comparison of pin-cell power distributions for Problem 2A with vacuum boundaries.	179
7.18	Comparison of pin-cell power error distributions for Problem 2A with vacuum boundaries.	180

LIST OF TABLES

Table

1.1	Comparison between SN and MOC methods	13
2.1	List of definitions of terms in the one-dimensional neutron transport equation	18
2.2	List of selected 1-D quadrature sets, with $\mu_n > 0$	20
2.3	List of definitions of terms in the one-dimensional discrete ordinates equation	21
2.4	List of definitions of terms in the one-dimensional neutron balance equation	24
2.5	List of numerical methods' abbreviations and their definitions . . .	35
2.6	List of one-group cross section	35
2.7	List of k -effective and time cost of the pin-cell problem	37
2.8	List of solutions of the pin-cell problem	38
2.9	List of k -effective and time cost of the mini-assembly problem . . .	41
2.10	List of solutions of the mini-assembly problem	42
3.1	List of definitions of terms in the two-dimensional neutron transport equation	48
3.2	List of selected first few quadrature sets, within in the first octant .	51
3.3	List of definitions of terms in the two-dimensional neutron transport equation	53

3.4	List of definitions of terms in the two-dimensional Cartesian neutron balance equation	56
3.5	List of the categorization of the boundaries of the rectangle (i, j) . .	60
4.1	List of numerical methods' abbreviations and their definitions . . .	79
4.2	List of two-group cross sections for the BWR assembly problem . .	81
4.3	List of k -effectives, time costs, and max-min pin power ratios of the BWR assembly problem	83
4.4	List of two-group cross sections for the LWR assembly problem with burnable absorber	87
4.5	List of k -effectives, time costs and max-min pin power ratios of the LWR cell problem	89
5.1	List of topology terms	96
5.2	List of definitions of terms in neutron transport equation	101
5.3	List of definitions of additional terms in discrete ordinate equation .	102
5.4	List of definitions of additional terms in cell-integrated discrete ordinate equation	103
5.5	List of definitions of source terms in neutron balance equation . . .	106
5.6	The criteria for categorization of the boundaries of a cell at a specific direction	111
6.1	List of number of angles in selected quadrature sets	133
6.2	List of one-group cross section	133
6.3	Pin-cell Dimension Information	135
6.4	List of k -effective, time & storage cost of non-IFBA pin-cell problem	136
6.5	List of solution of non-IFBA pin-cell problem	137
6.6	List of k -effective, time & storage cost of IFBA pin-cell problem . .	141

6.7	List of solution of IFBA pin-cell problem	142
6.8	List of k-effective, time & storage cost of the mini-assembly problem	149
6.9	List of pin-cell power of the mini-assembly problem	150
7.1	List of material compositions (<i>Godfrey, 2014</i>)	156
7.2	Pin-cell Dimension Information (<i>Godfrey, 2014</i>)	158
7.3	List of k -effective versus time cost for Problem 1A	160
7.4	List of collision rates (CR) for Problem 1A	160
7.5	Validation of WIMS-D cross section for problem 1A	161
7.6	List of k -effective versus time cost for Problem 1E	163
7.7	List of collision rates (CR) for Problem 1E	163
7.8	Validation of WIMS-D cross section for problem 1E	165
7.9	List of k -effective versus time & pin-cell power for Problem 2A . . .	167
7.10	Validation of WIMS-D cross section for problem 2A k -eigenvalue . .	171
7.11	List of k -effective versus time cost for mini-assembly problem	174
7.12	List of pin-cell power of the mini-assembly problem	174
7.13	List of k -effective versus time & pin-cell power for Problem 2A Vaccum	177

ABSTRACT

Discrete Ordinates Methods for Transport Problems with Curved Spatial Grids

by

Changyuan Liu

Chair: Edward Larsen

The method of characteristics (MOC) has been favored for many recent whole core transport codes; some current research codes are: the nTRACER code (*Hyun et al.*, 2014) from Seoul National University, the MPACT code (*MPACT Team*, 2013) from the University of Michigan, and the Dragon code (*Marleau et al.*, 2013) from École Polytechnique de Montréal. However, it is well-known that whole core transport with MOC is both computationally expensive and requires significant storage. On the other hand, discrete ordinates (SN) methods have been successfully applied to large systems, as has been demonstrated by the computer code Attila (*Lucas*, 2005).

However, all previous discrete-ordinates methods implemented in available production computer codes were formulated only for problems containing spatial cells with planar boundaries. This creates geometric approximations and inefficiencies for modeling any physical system with curved boundaries – the curved boundaries must be approximated using a greatly many very fine spatial cells, each fine cell having a planar boundary.

In this thesis, we derive, implement, and test 2-D discrete ordinates methods, which are applicable for systems having curved interfaces between material regions,

and which treat these curved surfaces analytically. The key benefits of “these” discrete ordinates methods on curved spatial grids over the MOC method include: (i) the ability to use standard highly-optimized quadrature sets, (ii) a single user-specified spatial grid, (iii) a simple extension to 3-D transport, and (iv) a small memory footprint for the computer.

CHAPTER I

Introduction

Discrete ordinates methods are widely used for nuclear reactor simulations. This chapter introduces the background of the discrete-ordinates problems considered in this thesis and reviews the historical developments of relevant numerical methods. The end of the chapter provides an overview of the remaining chapters of the thesis.

1.1 Background for Reactor Simulations

Neutron physics is a discipline of the study of interactions between neutrons and atoms. When interacting with nuclei, neutrons can scatter, be captured, or cause the nuclei to fission, producing several fast neutrons. (See Figure 1.1 for a depiction of these possibilities.) Such interactions are described with mathematical equations, in which the neutron distribution is expressed as a function of space, angle and energy. We define the neutron density as $N(\vec{x}, \hat{\Omega}, E)$, where $N(\vec{x}, \hat{\Omega}, E)d\vec{x}d\hat{\Omega}dE$ is the number of neutrons at location \vec{x} within $d\vec{x}$, traveling in the direction $\hat{\Omega}$ within $d\hat{\Omega}$, with energy E within dE . Nuclear engineers traditionally define another quantity for the description of the neutron distribution. It is the “angular flux”, defined as:

$$\psi(\vec{x}, \hat{\Omega}, E) = vN(\vec{x}, \hat{\Omega}, E), \quad (1.1)$$

where v is the neutron speed. Since for reactor simulations, the kinetic energy of neutrons is low enough that relativistic kinetics is not necessary, the relationship between velocity and energy follows from Newtonian kinetics:

$$E = \frac{1}{2}m_n v^2, \quad (1.2)$$

where m_n is the neutron mass.

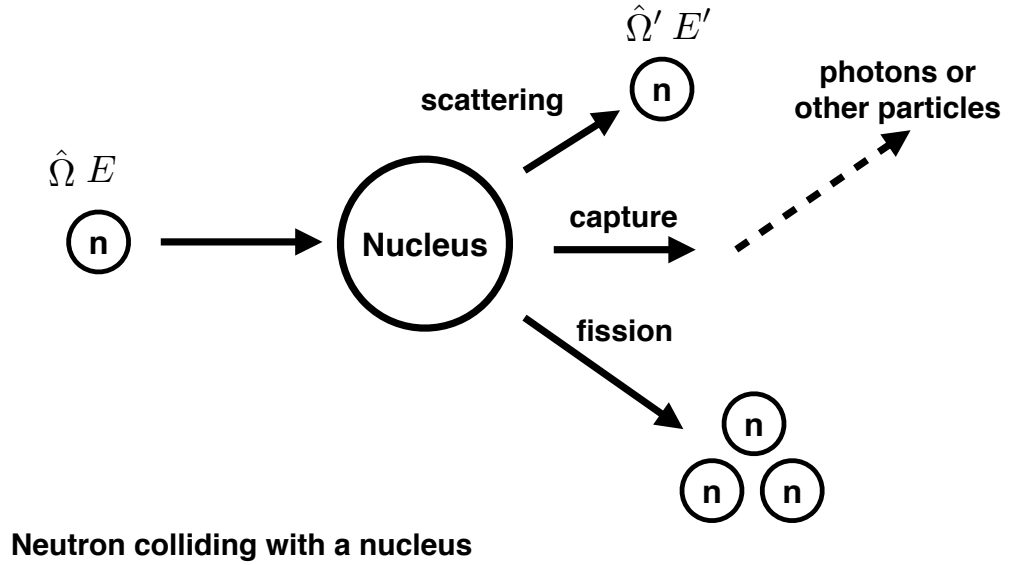


Figure 1.1: An illustration of neutron interaction with a nucleus.

In reactor physics, the neutron angular flux $\psi(\vec{x}, \hat{\Omega}, E)$ (at location \vec{x} in direction $\hat{\Omega}$ for energy E) is obtained by solving the neutron transport equation:

$$\begin{aligned} & \hat{\Omega} \cdot \vec{\nabla} \psi(\vec{x}, \hat{\Omega}, E) + \Sigma_t(\vec{x}, E) \psi(\vec{x}, \hat{\Omega}, E) \\ &= \int_0^{E_{max}} \int_{4\pi} \Sigma_s(\vec{x}, \hat{\Omega} \cdot \hat{\Omega}', E' \rightarrow E) \psi(\vec{x}, \hat{\Omega}', E') d\hat{\Omega}' dE' + \frac{\chi(\vec{x}, E)}{4\pi k} \int_0^{E_{max}} \nu \Sigma_f(\vec{x}, E') \phi(\vec{x}, E') dE', \end{aligned}$$

$$\vec{x} \in \mathcal{R}^3, \quad |\hat{\Omega}| = 1, \quad 0 \leq E \leq E_{max},$$

where $\phi(\vec{x}, E)$ is the scalar flux at location \vec{x} for energy E . $\Sigma_t(\vec{x}, E)$ is the macroscopic

total cross section at location \vec{x} for energy E ; $\Sigma_s(\vec{x}, \hat{\Omega} \cdot \hat{\Omega}', E' \rightarrow E)$ is the macroscopic differential scattering cross section at location \vec{x} for scattering from energy E' and angle $\hat{\Omega}'$ to energy E and angle $\hat{\Omega}$; $\chi(E)$ is the fission energy spectrum; $\nu\Sigma_f(\vec{x}, E)$ is the macroscopic fission yield cross section at location \vec{x} for energy E ; E_{max} is the maximum energy. The scalar flux and the angular flux are related by:

$$\phi(\vec{x}, E) = \int_{4\pi} \psi(\vec{x}, \hat{\Omega}, E) d\hat{\Omega}, \quad (1.3)$$

where the integral ($\int_{4\pi} \cdot d\hat{\Omega}$) is the surface integral over the unit sphere $|\hat{\Omega}| = 1$.

Solutions of the neutron transport equation are essential to nuclear reactor simulations. Nuclear engineers use the calculated power distributions and k -eigenvalues to help design and ensure the safety of nuclear reactors.

There are many types of nuclear reactors. In this thesis, example problems are taken from *light water reactors* (LWRs), which include *pressurized water reactors* (PWRs) and *boiling water reactors* (BWRs). Figure 1.2 depicts a horizontal cut through a typical PWR reactor core, which contains a collection of fuel assemblies. Each assembly contains a rectangular array of square pin-cells, and each pin-cell contains concentric circles in the center. Typically, a fuel pin-cell contains an inner ring of fuel, outside of which is a ring of clad. There is a gap between the fuel and clad regions. The clad is then surrounded by moderator, which is light water for LWRs.

Reactor simulations involve many mutually connected problems. The experimentalists prepare cross sections, which are then processed to data libraries for nuclear engineers to use. One of the widely-used cross section libraries is the ENDF library prepared by Brookhaven National Laboratory (*McLane, 2001*). With the cross sections defined, nuclear engineers perform reactor calculations for fuel management, reactor design, or operation simulations. “Lattice calculations” are at the center of reactor calculations. A “lattice” in a reactor is typically an assembly, as shown

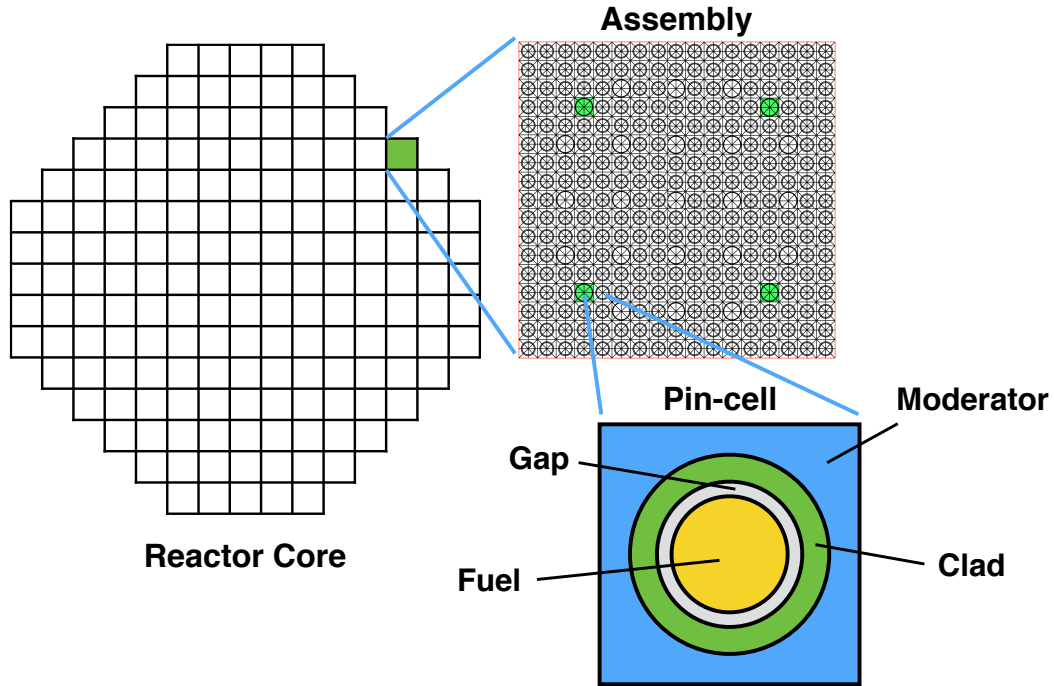


Figure 1.2: An example PWR reactor layout.

in Figure 1.2. The scope of problems for reactor simulations is depicted in Figure 1.3. Considering its geometry complexity, accurate lattice calculations are a serious challenge. In this thesis, we discuss new numerical methods for lattice calculations.

1.2 Historical Review of Numerical Methods

Historically, two distinct categories of computational methods were independently developed for lattice calculations: Monte Carlo and deterministic methods. Here we briefly introduce both methods.

1.2.1 Monte Carlo Method

Monte Carlo methods date back to the Manhattan Project in World War II (*Metropolis and Ulam, 1949*). The Monte Carlo solution process involves a simulation of neutron physics using a large number of “Monte Carlo neutrons”, each of

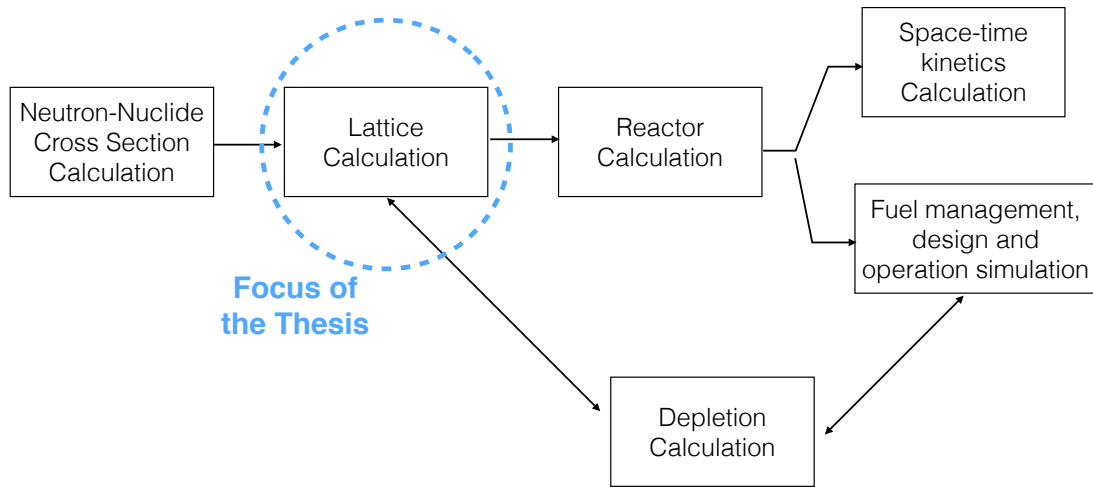


Figure 1.3: Reactor simulations scheme. Adapted from Figure 1.1 from *Hebert (2009)*. The focus of this thesis is lattice calculations.

which possesses a location \vec{x} , a direction $\hat{\Omega}$, and an energy E . While a neutron is traveling in space, it can reach an outer boundary and leak out, reach an inner boundary and continue traveling, or collide with a nucleus and trigger an event. When a collision event occurs, a neutron can scatter, be captured, or fission into one or more fast neutrons. Figure 1.4 illustrates the change of a neutron’s state. Because random numbers are used to probabilistically sample the occurrence of each event, this method was named the “Monte Carlo” method. The textbooks *Lewis and Miller Jr. (1984)*; *Spanier and Gelbard (1969)* and *Lux and Koblinger (1991)* discuss Monte Carlo methods in detail. One of the most well-known and widely-used Monte Carlo computer codes is MCNP, developed by Los Alamos National Library (*Briesmeister, 1997*).

The major advantage of the Monte Carlo method is that there are no approximations in energy, space, and traveling direction. The major disadvantage of the Monte Carlo method is its requirement of significant computational resources to minimize the statistical errors. This is because statistical errors are inversely proportional to

the square root of the number of neutrons simulated. Therefore to reduce the statistical errors by a factor of 10, it is necessary to use 100 times more neutrons, so the computational cost increases by a factor of 100. Because Monte Carlo is expensive in computational cost, a fundamentally different kind of method called “deterministic” has been developed.

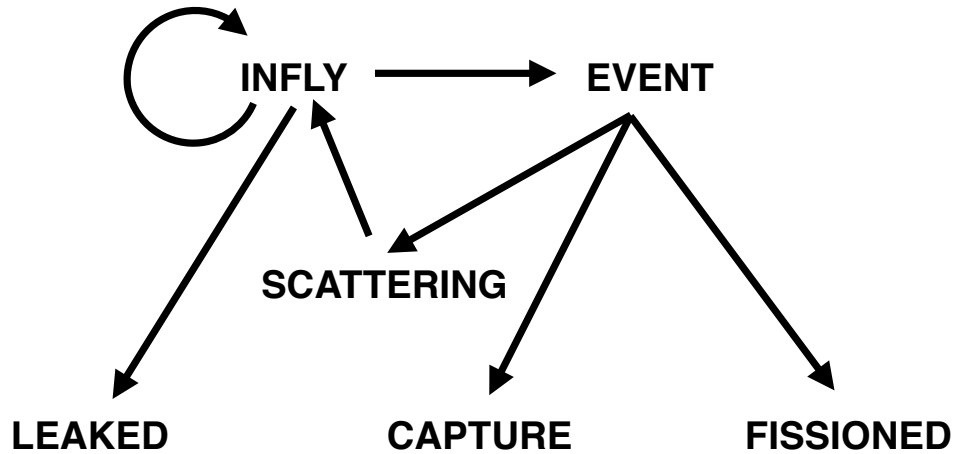


Figure 1.4: The state machine of Monte Carlo neutrons.

1.2.2 Deterministic Methods

Deterministic methods, unlike Monte Carlo methods, have no uncertainties due to statistical errors. However, they instead all have truncation errors. There are many deterministic methods, such as: diffusion, spherical harmonics (PN), discrete ordinates (SN), simplified PN (SPN), collision probability, and recent method of characteristics (MOC) methods. (*Hebert, 2009*) We provide a historical review of MOC and SN methods only, because of their accuracy and capabilities for a wide range of problems, while the other methods are either less accurate or applicable only for problems with limited type of geometries. Also, MOC and SN are the methods relevant to the work in this thesis.

In a deterministic method, the spatial, angular, and energy variables are all discretized. (For reactor kinetics problems, the time variable is discretized as well.) En-

ergy is divided into a grid of intervals, and each interval is called an energy “group”. We assume that there are G energy groups, and each group has the interval $[E_g, E_{g-1}]$. The multigroup neutron transport equation is obtained by integrating equation 1.3 over the group:

$$\begin{aligned} & \hat{\Omega} \cdot \vec{\nabla} \psi_g(\vec{x}, \hat{\Omega}) + \Sigma_{t,g}(\vec{x}) \psi_g(\vec{x}, \hat{\Omega}) \\ &= \sum_{g'=1}^G \int_{4\pi} \Sigma_{s,g' \rightarrow g}(\vec{x}, \hat{\Omega} \cdot \hat{\Omega}') \psi_{g'}(\vec{x}, \hat{\Omega}') d\hat{\Omega}' + \frac{\chi_g(\vec{x})}{4\pi k} \sum_{g=1}^G \nu \Sigma_{f,g'}(\vec{x}) \phi_g(\vec{x}), \end{aligned}$$

$$\vec{x} \in \mathcal{R}^3, \quad |\hat{\Omega}| = 1, \quad 1 \leq g \leq G,$$

where the multigroup fluxes and cross sections are defined using:

$$\psi_g(\vec{x}, \hat{\Omega}) = \int_{E_g}^{E_{g-1}} \psi(\vec{x}, \hat{\Omega}, E) dE, \quad (1.4)$$

$$\phi_g(\vec{x}) = \int_{E_g}^{E_{g-1}} \phi(\vec{x}, E) dE, \quad (1.5)$$

$$\Sigma_{t,g}(\vec{x}) \approx \frac{\int_{E_g}^{E_{g-1}} \Sigma_t(\vec{x}, E) \psi(\vec{x}, \hat{\Omega}, E) dE}{\psi_g(\vec{x}, \hat{\Omega})}, \quad (1.6)$$

$$\Sigma_{s,g' \rightarrow g}(\vec{x}, \hat{\Omega} \cdot \hat{\Omega}') \approx \frac{\int_{E_g}^{E_{g-1}} \Sigma_s(\vec{x}, \hat{\Omega} \cdot \hat{\Omega}', E') \psi(\vec{x}, \hat{\Omega}', E') dE'}{\psi_g(\vec{x}, \hat{\Omega})}, \quad (1.7)$$

$$\chi_g(\vec{x}) = \int_{E_g}^{E_{g-1}} \chi(\vec{x}, E) dE, \quad (1.8)$$

$$\nu \Sigma_{f,g}(\vec{x}) \approx \frac{\int_{E_g}^{E_{g-1}} \nu \Sigma_f(\vec{x}, E) \phi(\vec{x}, E) dE}{\phi_g(\vec{x})}. \quad (1.9)$$

A detailed discussion of the multigroup approximation can be found in textbooks such as *Hebert* (2009).

1.2.2.1 Discrete Ordinates (SN) Methods

One class of deterministic methods is the SN method, which was originally developed in the field of cosmic radiation. (*Chandrasekhar, 1960*) The adoption of SN methods for neutron transport was done by Carlson. (*Carlson and Bell, 1958*)

In SN methods, the angular variable $\hat{\Omega}$ in the multigroup transport equation (1.4) is discretized by a finite set of unit vectors $\hat{\Omega}_n$:

$$\begin{aligned} & \hat{\Omega}_n \cdot \vec{\nabla} \psi_{n,g}(\vec{x}) + \Sigma_{t,g}(\vec{x}) \psi_{n,g}(\vec{x}) \\ &= \sum_{g=1}^G \sum_{m=1}^N \omega_m \Sigma_{s,g' \rightarrow g}(\vec{x}, \hat{\Omega}_n \cdot \hat{\Omega}_m) \psi_{n,g'}(\vec{x}) + \frac{\chi_g(\vec{x})}{4\pi k} \sum_{g=1}^G \nu \Sigma_{f,g'}(\vec{x}) \phi_g(\vec{x}), \end{aligned}$$

$$\vec{x} \in \mathcal{R}^3, \quad 1 \leq n \leq N, \quad 1 \leq g \leq G,$$

where

$$\psi_{n,g}(\vec{x}) = \psi_g(\vec{x}, \hat{\Omega}_n). \quad (1.10)$$

Each angle $\hat{\Omega}_n$ is associated with a weight ω_n , so that the angular integral can be replaced by a weighted sum. If we have N angles, the relationship between the scalar and angular fluxes is:

$$\phi_g(\vec{x}) = \sum_{n=1}^N \omega_n \psi_{n,g}(\vec{x}). \quad (1.11)$$

The discrete ordinates equations are then integrated over spatial cells, and equations for the unknown average cell and edge fluxes are derived. Detailed discussions of the spatial differencing schemes in the discrete ordinates method can be found in Chapter II of this thesis for 1-D problems, and in Chapter III and V for 2-D problems.

A paper by K.D. Lathrop in 1969 discussed spatial differencing schemes for 2-D Cartesian geometries. (*Lathrop, 1969*) In 1973, W.H. Reed and T.R. Hill general-

ized SN methods to triangular meshes, to enable the treatment of problems more geometrically complex than Cartesian geometry. (*Reed and Hill, 1973*) Since then, many SN computer codes have been developed. TRIDENT, for example, is a triangular mesh SN code developed in 1978. (*Seed and Miller Jr., 1978*) More recently, in 2003, the Oak Ridge National Library released the NEWT computer code (*DeHart, 2003*), which is based on polygonal geometries. The geometry in all these discrete ordinates codes is based on spatial grids formed by cells with linear boundaries. For problems containing circular or curved spatial grids, approximations of a curve by piecewise-continuous linear segments are required, as illustrated in Figure 1.5. One of the reasons why SN codes in the past dealt only with linear boundaries is to avoid the “re-entrant” boundaries that occur in curved spatial grids. Chapter V in this thesis introduces our approach to handle these “re-entrant” boundaries.

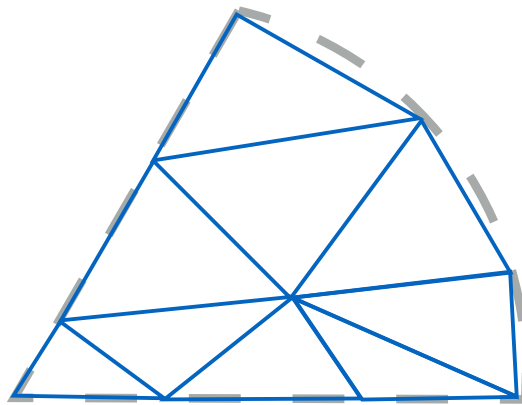


Figure 1.5: An illustration of the approximations of curved boundaries by piecewise-continuous linear segments in previous SN methods. In this thesis, we develop new methods to treat curved boundaries analytically.

1.2.2.2 Method of Characteristics (MOC)

Because previous SN methods approximated curved spatial grids with triangles or rectangles, the MOC method was developed by Askew in 1972 (*Askew, 1972*), in which the treatment of geometries is in done more accurately. Since it was first implemented in the WIMS-E code, the MOC method has been favored for many recent whole-core transport computer codes; some current research codes are: the *MPact* code from the University of Michigan, the *nTRACER* code from Seoul National University, and the *Dragon* code from École Polytechnique de Montréal.

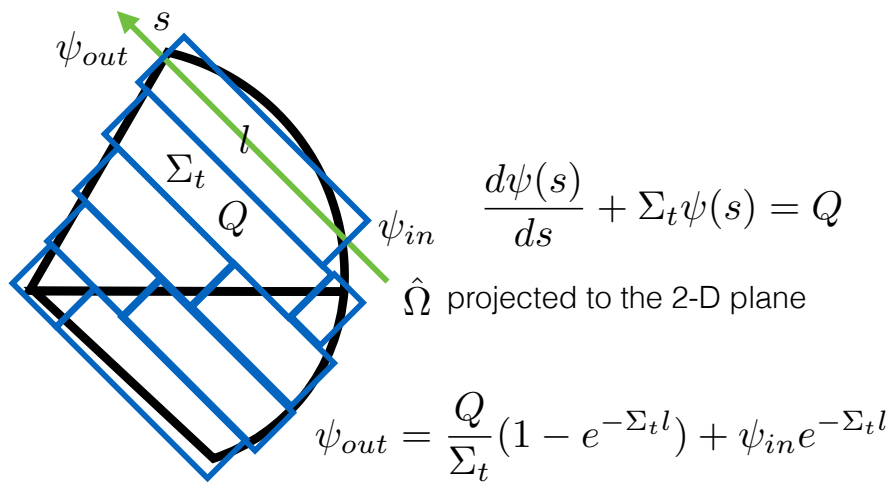


Figure 1.6: An illustration of the MOC method.

The MOC method assumes each spatial cell to have a constant source of neutrons Q and a constant total cross section Σ_t . The neutron transport inside this cell is calculated by solving 1-D transport equations on a bundle of equally-spaced rays that pass through the cell. For each ray, the incoming flux is known, and the outgoing flux is calculated. Detailed discussions of the MOC method can be found in *Hebert (2009)*.

Two key approximations of MOC are that:

- The source is “flat” (constant) inside a spatial cell;
- The spatial cells are approximated with “rasterized” fine rectangles surrounding the fine rays segments to accurately approximate curved boundaries.

See Figure 1.6 for an illustration of the MOC method. We note that, although both MOC and SN involve the discretization of the angular variable, MOC is *not* considered to be an SN method in this thesis because of its use of two fine spatial grids: the geometrical “flat source” regions on which the scattering and fission sources are represented as spatially constant, and the fine rectangles surrounding the “ray segments” (see Figure 1.6).

1.2.2.3 New in the Thesis

We consider two categories of deterministic methods: SN and MOC. SN methods have been applicable to geometries with spatial grids having linear boundaries, while the MOC method is applicable to spatial grids having curved boundaries. In this thesis, we generalize SN methods also to curved spatial grids. The new SN methods treat curved boundaries analytically, and the flat source approximation is not required in the “multiple balance” discrete-ordinates method. Detailed discussions of SN methods are introduced later in Chapter III and V of this thesis.

1.3 Comparison of SN and MOC Methods

The reason for generalizing SN methods to geometries with curved spatial grids, is not only to provide an alternative method to MOC, but also that SN methods have some advantages over MOC. Table 1.1 compares the SN and MOC methods.

The key benefits of discrete ordinates methods include: (i) the use of a standard, highly-optimized quadrature sets, (ii) a single user-specified spatial grid, (iii)

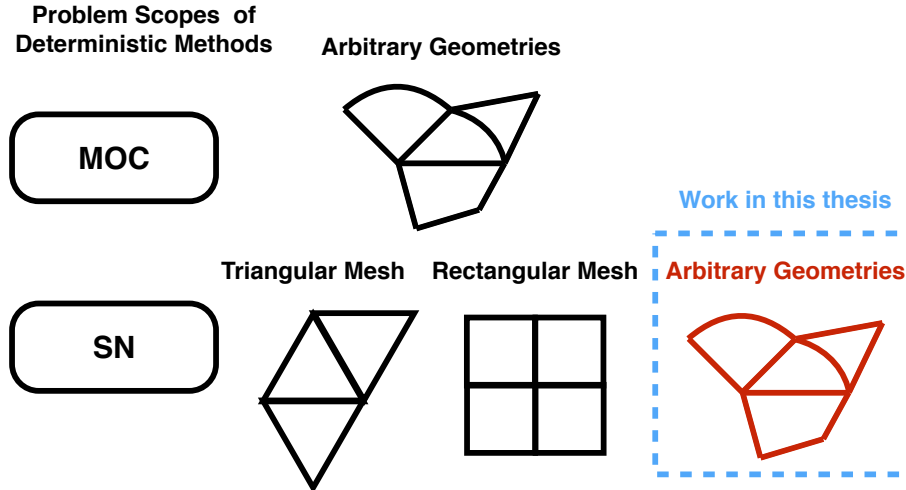


Figure 1.7: The scope of problems for MOC and SN methods.

a straightforward extension to 3-D transport, and (iv) a small memory footprint for the computer.

Disadvantages of the MOC method include: (i) the necessity of using non-standard, non-optimized “modular” quadrature sets, (ii) two fine spatial grids, (iii) a very costly extension to 3-D, and (iv) a large computer memory footprint.

A feature that makes the SN methods more complicated is the required special approach to handle “re-entrant” curved boundaries, which is discussed in detail in Chapter V in this thesis.

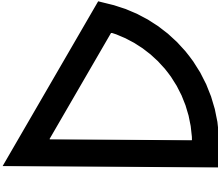


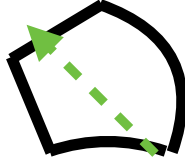
1.4 Thesis Outline

Here, we provide brief summaries of the remaining chapters in this thesis.

Chapter II

This chapter reviews three known discrete-ordinates methods for 1-D problems: the step method (STEP), the step characteristic method (SC), and the multiple balance method (MB). Among these, the multiple balance method is re-derived here in a new way, which enables the generalization of this method to 2-D

Table 1.1: Comparison between SN and MOC methods

Aspect of Comparison	SN Methods	MOC Method
Quadrature Sets	Standard quadrature sets.	Unoptimized “modular” quadrature sets.
Spatial Grids	 <p data-bbox="667 625 992 722">SN methods need only one “flat source” spatial grid.</p>	 <p data-bbox="992 625 1339 722">MOC method needs both a “flat source” grid and a fine spatial grid of spacing rays.</p>
Storage (Computer Memory Footprint)	Only cell dependent geometry information is stored, which does not depend on direction of flight.	Ray segment information for all directions of flight is stored.
3-D Transport	When extended from 2-D to 3-D, the computational cost increases only linearly proportional to the number of “layers” in z-direction. Extension to 3-D is straightforward.	When extended from 2-D to 3-D, the computational cost increases dramatically, which is not only linearly proportional to the number of “layers” in z-direction, but also inversely proportional to ray spacing. Extension to 3-D is difficult.
Curved Edges	 <p data-bbox="667 1423 992 1520">SN methods need to split “re-entrant” curved edges. (see Chapter V.)</p>	 <p data-bbox="992 1392 1339 1455">MOC methods need no split of the curved edges.</p>

problems. Numerical results for two simple problems are also discussed, for which the MB method is found to be more accurate than the step and SC methods.

Chapter III

This chapter discusses three discrete-ordinates methods for 2-D Cartesian grid problems: the step method (STEP), the simplified step characteristic method (SSC), and the multiple balance method (MB). The 2-D MB and SSC methods are new, and are introduced here for the first time. The implementations of the new MB and SSC methods are no more complicated than for existing discrete ordinates methods.

Chapter IV

This chapter studies numerical implementations of the methods described in Chapter III for two small LWR 2D Cartesian-grid problems. One problem contains a burnable absorber pin-cell. The SN methods described in Chapter III are found to be comparable in accuracy to the MOC method on a very coarse spatial grid. On a finer spatial grid, the SSC and MB methods are more accurate than the MOC method.

Chapter V

This chapter generalizes the three Cartesian-grid discrete-ordinates methods derived in Chapter III to 2-D spatial grids having curved boundaries. New terminology is introduced to describe linear and circular boundaries in an analytic form. A special “splitting” approach to deal with “re-entrant” boundaries is introduced. The problem of finding the “sweep order” is also solved.

Chapter VI

This chapter studies the performance of the discrete-ordinates methods derived in Chapter V for three problems with one-group cross sections: two pin-cell problems and one mini-assembly problem. The MB method is found to be competitive with the MOC method, and for problems with substantial spatial variations in the neutron flux, the MB method is seen to be significantly more accurate than MOC.

Chapter VII

This chapter studies the accuracy of discrete-ordinates methods derived in Chapter V with multigroup cross sections generated from the 172-group WIMS-D cross section library. The problems studied include the CASL VERA benchmark problem 1A, 1E, 2A, and a mini-assembly problem. The MB method is found to be comparable to MOC in both accuracy and computational cost. For difficult problems having large spatial flux gradients, the MB method is significantly more accurate. Our results suggest that MB can be an alternative method to MOC for reactor simulations.

Chapter VIII

This final chapter summarizes the accomplishments in this thesis, and discusses future work. The benefits of MB methods are summarized, including: the use of standard optimized quadrature sets, a single spatial grid, a small memory usage, and a straightforward extension to 3-D problems.

CHAPTER II

One-Dimensional Problems

The discrete ordinates method is a traditional method for solving the neutron transport equation. This chapter treats one-dimensional discrete ordinates problems, which the readers may be familiar with. So this chapter serves as a review. Another purpose of this chapter is to familiarize the reader with the notation used in this thesis.

2.1 The Scope of the Geometry

The one-dimensional space is divided into I “segments”, where the segment numbered i has the left end point $x = x_{i-1}$ and right end point $x = x_i$. The one-dimensional grid is visualized in Figure 2.1.

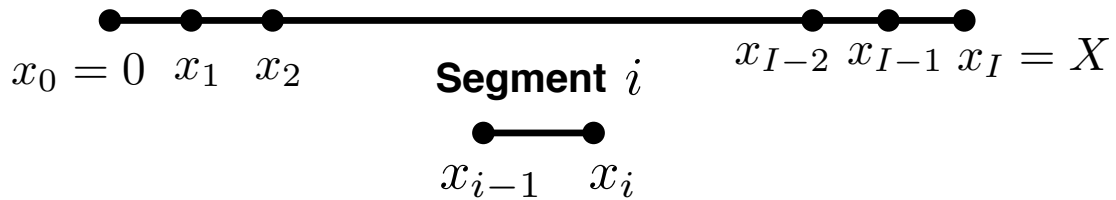


Figure 2.1: The one-dimensional spatial grid divides the space into I “**segments**”. The boundaries for the segment i are $x = x_{i-1}$ and $x = x_i$. i is an integer ranging from 1 to I .

2.2 One-Dimensional Multigroup Discrete Ordinates Neutron Transport Equation

For one-dimensional problems, the neutron angular flux depends on one location variable x , one angular variable μ , and the the energy group number g . The angular variable μ is the cosine of the angle between between the positive x -axis, the unit vector of which is \hat{i} , and the direction of flight is $\hat{\Omega}$. These are illustrated in Figure 2.2.

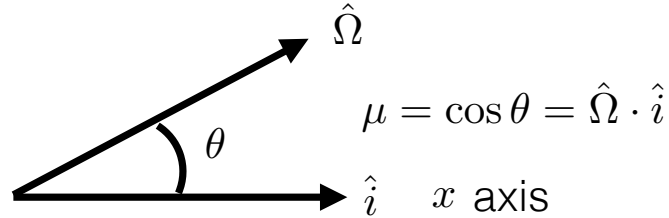


Figure 2.2: The angular variable μ is the cosine of the angle between the direction flight $\hat{\Omega}$ and the positive x -axis, which has a unit vector of \hat{i} .

The 1-D multigroup transport equation for an eigenvalue problem is:

$$\mu \frac{\partial \psi_g(x, \mu)}{\partial x} + \Sigma_{t,g}(x) \psi_g(x, \mu) = \frac{1}{2} \sum_{g'=1}^G \Sigma_{s,g' \rightarrow g}(x) \phi_{g'}(x) + \frac{\chi_g(x)}{2k} \sum_{g'=1}^G \nu \Sigma_{f,g'}(x) \phi_{g'}(x),$$

$$0 \leq x \leq X, \quad -1 \leq \mu \leq 1, \quad 1 \leq g \leq G. \quad (2.1)$$

The definitions of the quantities in the equation (2.1) are listed in Table 2.1.

The relationship between the scalar flux and the angular flux is:

$$\phi_g(x) = \int_{-1}^1 \psi_g(x, \mu) d\mu. \quad (2.2)$$

The angular cosine μ is continuous in the interval $[-1, 1]$, which can be discretized

Table 2.1: List of definitions of terms in the one-dimensional neutron transport equation

TERM	TYPE	EXPLANATION
x	scalar	the spatial variable
μ	scalar	the cosine of the angle between the direction of flight and the positive x -axis. See Figure 2.2.
G	integer	the total number of energy groups
g	integer	the energy group index, $1 \leq g \leq G$
$\psi_g(x, \mu)$	scalar	the angular flux of group g , at location x , traveling with angular cosine μ
$\phi_g(x)$	scalar	the scalar flux of group g , at location x
$\Sigma_{t,g}(x)$	scalar	the macroscopic total cross section of group g , at x
$\Sigma_{s,g' \rightarrow g}(x)$	scalar	the macroscopic isotropic scattering cross section from group g' to g , at location x
$\nu\Sigma_{f,g}(x)$	scalar	the macroscopic neutron yield fission cross section of group g , at location x
$\chi_g(x)$	scalar	the probability of neutron fissioned into energy group g , at location x (the fission spectrum)
k	scalar	the effective reactivity coefficient, the eigenvalue of the equation.

with a set of finite angles $\mu_n, 1 \leq n \leq M$. The angular cosine μ_n is associated with a weight ω_n . These weights are chosen to approximate the integral of any function $f(\mu)$ as a weighted sum:

$$\int_{-1}^1 f(\mu) d\mu \approx \sum_{n=1}^M f(\mu_n) \omega_n, \quad (2.3)$$

$$2 = \sum_{n=1}^M \omega_n. \quad (2.4)$$

The angular cosines μ_n and weights ω_n are defined so that the approximation in equation (2.3) is exact for low order polynomials:

$$\int_{-1}^1 p(\mu) d\mu = \sum_{n=1}^M p(\mu_n) \omega_n, \quad \text{for } p = \text{low order polynomial}, \quad (2.5)$$

where a polynomial of μ of order m has the form:

$$p_m(\mu) = \sum_{i=0}^m a_i \mu^i. \quad (2.6)$$

The set $\{(\mu_n, \omega_n)\}$ is called a “**quadrature set**”:

$$\text{“quadrature set”} = \{(\mu_n, \omega_n), 1 \leq n \leq M_N\}, \quad (2.7)$$

where N is an even integer indicating the level of quadrature set, and M_N is the total number of angular cosines. The larger N is, the more angles there are.

It is a work of art to find good quadrature sets, where many researches have been involved (*Hebert, 2009*). A basic requirement of these 1-D quadrature sets is symmetry in the sense that:

$$\text{If } (\mu_n, \omega_n) \in SN \text{ quadrature set} \quad : \quad (-\mu_n, \omega_n) \in SN \text{ quadrature set.} \quad (2.8)$$

The first few of the quadrature sets used in this thesis are listed in Table 2.2, which are standard Gaussian quadrature sets dated back to early researches in the field of cosmic radiation transfer (*Anderson and Hord, 1977*).

Next, we study the discrete ordinates equation for the angular cosine μ_n :

$$\mu_n \frac{\partial \psi_{n,g}(x)}{\partial x} + \Sigma_{t,g}(x) \psi_{n,g}(x) = \frac{1}{2} \sum_{g'=1}^G \Sigma_{s,g' \rightarrow g}(x) \phi_{g'}(x) + \frac{\chi_g(x)}{2k} \sum_{g'=1}^G \nu \Sigma_{f,g'}(x) \phi_{g'}(x),$$

$$0 \leq x \leq X, 1 \leq n \leq M, 1 \leq g \leq G. \quad (2.9)$$

The definitions of additional terms can be found in Table 2.3. The angular flux and

Table 2.2: List of selected 1-D quadrature sets, with $\mu_n > 0$

N	M_N	DIRECTION μ_n	WEIGHT ω_n
1	2	1.0	.577350269189626
2	4	.861136311594053	.347854845137454
		.339981043584856	.652145154862546
4	8	.960289856497536	.101228536290376
		.796666477413627	.222381034453374
		.525532409916329	.313706645877887
		.183434642495650	.362683783378363
8	16	.989400934991650	.027152459411754
		.944575023073233	.062253523938648
		.865631202387832	.095158511682493
		.755404408355003	.124628971255534
		.617876244402644	.149595988816577
		.458016777657227	.169156519395003
		.281603550779259	.182603415044924
		.095012509837637	.189450610455067
16	32	.997263861849482	.007018610009470
		.985611511545268	.016274394730906
		.964762255587506	.025392065309262
		.934906075937740	.034273862913021
		.896321155766052	.042835898022227
		.849367613732570	.050998059262376
		.794483795967942	.058684093478536
		.732182118740290	.065822222776362
		.663044266930215	.072345794108849
		.587715757240762	.078193895787070
		.506899908932229	.083311924226947
		.421351276130635	.087652093004404
		.331868602282128	.091173878695764
		.239287362252137	.093844399080805
		.144471961582796	.095638720079275
		.048307665687738	.096540088514726

the scalar flux now have the relationship:

$$\phi_g(x) = \sum_{n=1}^M \omega_n \psi_{n,g}(x), \quad (2.10)$$

$$\psi_{n,g}(x) = \psi_g(x, \mu_n). \quad (2.11)$$

Next, we integrate the discrete ordinates equation (2.9) over the segment i bounded

Table 2.3: List of definitions of terms in the one-dimensional discrete ordinates equation

TERM	TYPE	EXPLANATION
μ_n	scalar	the angular cosine at index n . See Figure 2.2.
ω_n	scalar	the weight of μ_n
$\psi_{n,g}(x)$	scalar	the angular flux of group g , at location x , traveling with angular cosine μ_n

by the interval $[x_{i-1}, x_i]$. (See Figure 2.1.) We obtain:

$$\begin{aligned}
\text{Leakage:} & \int_{x_{i-1}}^{x_i} \mu_n \frac{\partial \psi_{n,g}(x)}{\partial x} dx \\
\text{Collision:} & + \int_{x_{i-1}}^{x_i} \Sigma_{t,g}(x) \psi_{n,g}(x) dx \\
\text{Scattering:} & = \frac{1}{2} \sum_{g'=1}^G \int_{x_{i-1}}^{x_i} \Sigma_{s,g' \rightarrow g}(x) \phi_{g'}(x) dx \\
\text{Fission:} & + \frac{1}{2k} \sum_{g'=1}^G \int_{x_{i-1}}^{x_i} \chi_g(x) \nu \Sigma_{f,g'}(x) \phi_{g'}(x) dx, \\
& 1 \leq i \leq I, 1 \leq n \leq M, 1 \leq g \leq G. \tag{2.12}
\end{aligned}$$

We assume that the material is homogeneous inside a segment i , and that the cross sections are:

$$\Sigma_{t,g}(x) = \Sigma_{t,g,i}, \tag{2.13}$$

$$\Sigma_{s,g' \rightarrow g}(x) = \Sigma_{s,g' \rightarrow g,i}, \tag{2.14}$$

$$\nu \Sigma_{f,g}(x) = \nu \Sigma_{f,g,i}, \tag{2.15}$$

$$\chi_g(x) = \chi_{g,i}, \tag{2.16}$$

for $x_{i-1} \leq x \leq x_i$, $1 \leq i \leq I$.

The integral of the “leakage” term in equation (2.12) is:

$$\int_{x_{i-1}}^{x_i} \mu_n \frac{\partial \psi_{n,g}(x)}{\partial x} dx = \mu_n (\psi_{n,g}(x_i) - \psi_{n,g}(x_{i-1})). \quad (2.17)$$

To simplify equation (2.12), some averaged quantities are defined:

$$\psi_{n,g,i} = \psi_{n,g}(x_i), \quad (2.18)$$

$$\bar{\psi}_{n,g,i} = \frac{1}{h_i} \int_{x_{i-1}}^{x_i} \psi_{n,g}(x) dx, \quad (2.19)$$

$$\bar{\phi}_{g,i} = \frac{1}{h_i} \int_{x_{i-1}}^{x_i} \phi_g(x) dx, \quad (2.20)$$

$$\phi_{g,i} = \phi_g(x_i), \quad (2.21)$$

$$1 \leq i \leq I, \quad 1 \leq n \leq M, \quad 1 \leq g \leq G,$$

where the length of the segment h_i is:

$$h_i = x_i - x_{i-1}, \quad (2.22)$$

and the relationship between the averaged scalar flux and the angular fluxes now becomes:

$$\bar{\phi}_{g,i} = \sum_{n=1}^M \bar{\psi}_{n,g,i} \omega_n, \quad (2.23)$$

$$\phi_{g,i} = \sum_{n=1}^M \psi_{n,g,i} \omega_n. \quad (2.24)$$

An illustration of the averaged angular flux of segment i and its end points is shown in Figure 2.3.

Table 2.4: List of definitions of terms in the one-dimensional neutron balance equation

TERM	TYPE	EXPLANATION
h_i	scalar	the length of segment i , i.e. $x_i - x_{i-1}$
$\Sigma_{t,g,i}$	scalar	the macroscopic total cross section at segment i , for neutrons with group g
$\Sigma_{s,g' \rightarrow g,i}$	scalar	the isotropic macroscopic scattering cross section at segment i , scattering from group g' to group g
$\chi_{g,i}$	scalar	the neutron fission probability into group g for segment i (the “ fission spectrum ”)
$\nu\Sigma_{f,g,i}$	scalar	the macroscopic neutron yield cross section for segment i , for energy group g
$\psi_{n,g,i}$	scalar	the angular flux at $x = x_i$, for neutrons traveling with angular cosine μ_n , for group g
$\bar{\psi}_{n,g,i}$	scalar	the averaged angular flux for segment i , for neutrons traveling with angular cosine μ_n , for group g
$\bar{\phi}_{g,i}$	scalar	the averaged scalar flux for segment i , for group g
$\phi_{g,i}$	scalar	the scalar flux at $x = x_i$, for group g
$\bar{Q}_{s,g,i}$	scalar	the averaged scattering source in group g , for segment i , see equation (2.27)
$\bar{Q}_{f,g,i}$	scalar	the averaged fission source in group g , for segment i , see equation (2.28)
$Q_{f,g,i}^-$	scalar	the averaged fission source in group g , at $x = x_i$, for the segment i , see equation (2.31)
$Q_{f,g,i}^+$	scalar	the averaged fission source in group g , at $x = x_i$, for the segment $i + 1$, see equation (2.32)
$Q_{s,g,i}^-$	scalar	the averaged scattering source in group g , at $x = x_i$, for the segment i , see equation (2.29)
$Q_{s,g,i}^+$	scalar	the averaged scattering source in group g , at $x = x_i$, for the segment $i + 1$, see equation (2.30)

and the following endpoint source terms:

$$Q_{s,g,i}^- = \frac{1}{2} \sum_{g'=1}^G \Sigma_{s,g' \rightarrow g,i} \phi_{g',i}, \quad (2.29)$$

$$Q_{s,g,i}^+ = \frac{1}{2} \sum_{g'=1}^G \Sigma_{s,g' \rightarrow g,i+1} \phi_{g',i}, \quad (2.30)$$

$$Q_{f,g,i}^- = \frac{\chi_{g,i}}{2} \sum_{g'=1}^G \Sigma_{f,g',i} \phi_{g',i}, \quad (2.31)$$

$$Q_{f,g,i}^+ = \frac{\chi_{g,i}}{2} \sum_{g'=1}^G \Sigma_{f,g',i+1} \phi_{g',i}, \quad (2.32)$$

$$(2.33)$$

with which the neutron balance equation (2.26) is simplified as:

$$\mu_n \frac{\psi_{n,g,i} - \psi_{n,g,i-1}}{h_i} + \Sigma_{t,g,i} \bar{\psi}_{n,g,i} = \bar{Q}_{s,g,i} + \frac{1}{k} \bar{Q}_{f,g,i},$$

$$1 \leq i \leq I, \quad 1 \leq n \leq M, \quad 1 \leq g \leq G. \quad (2.34)$$

2.3 Auxiliary Equations

For segment i , there are 3 unknowns for neutrons traveling in angular cosine μ_n , for group g :

$$\bar{\psi}_{n,g,i}, \psi_{n,g,i-1}, \psi_{n,g,i}. \quad (2.35)$$

(See Figure 2.3.) Based on the sign of the angular cosine μ_n , the endpoint flux is either “**incoming**” or “**outgoing**”. Figure 2.4 visualizes the two cases that $\mu_n > 0$ and $\mu_n < 0$. The flux at the incoming end point is called the incoming flux, and the flux at the outgoing end point is called the outgoing flux.

With a process called “**sweeping**” discussed later, the incoming fluxes can be considered as known quantities. So the unknowns are $\bar{\psi}_{n,g,i}$ and the outgoing flux.

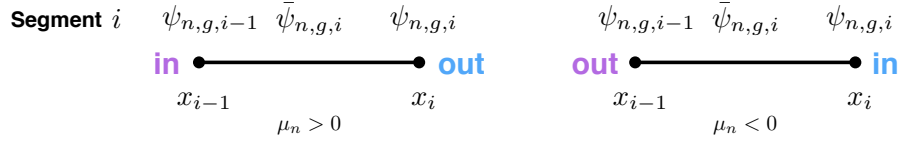


Figure 2.4: Categorization of the endpoints of a segment to be “incoming” or “outgoing”, based on whether the angular cosine μ_n is positive or negative.

Hence, for segment i , the knowns and unknowns are:

$$\mu_n > 0 :$$

$$\mathbf{Knowns} : \psi_{n,g,i-1}, \quad (2.36)$$

$$\mathbf{Unknowns} : \bar{\psi}_{n,g,i}, \psi_{n,g,i}, \quad (2.37)$$

$$\mu_n < 0 :$$

$$\mathbf{Knowns} : \psi_{n,g,i}, \quad (2.38)$$

$$\mathbf{Unknowns} : \bar{\psi}_{n,g,i}, \psi_{n,g,i-1}. \quad (2.39)$$

For segment i , because we have two unknowns in total, two equations are required. The neutron balance equation (2.34) provides one equation, so one more equation is required. The additional equations are called “**auxiliary equations**”, which have the form:

$$\mu_n > 0 :$$

$$g(\bar{\psi}_{n,g,i}, \psi_{n,g,i}) = 0,$$

$$\mu_n < 0 :$$

$$g(\bar{\psi}_{n,g,i}, \psi_{n,g,i-1}) = 0. \quad (2.40)$$

In the following subsections, three different methods are introduced, each having a

different auxiliary equation. The first method is the “**step method**”, which is a traditional discrete ordinates method to solve one-dimensional problems. The second method is the “**step characteristic method**”, which can be generalized to solve two-dimensional problems as a method called the “**simplified step characteristic method**”. The third method is the “**multiple balance method**”, which was first invented for 1-D problems by Morel & Larsen in 1990 (*Morel and Larsen, 1990*).

2.3.1 The Step Method (STEP)

The “**step method**” is the simplest traditional discrete ordinates method. In this method, the auxiliary equation assumes that the outgoing flux equals the segment-averaged flux. So the auxiliary equation in the form of equation (2.40) is:

$$\begin{aligned}
 \mu_n > 0 & : \\
 \bar{\psi}_{n,g,i} & = \psi_{n,g,i}, \\
 \mu_n < 0 & : \\
 \bar{\psi}_{n,g,i} & = \psi_{n,g,i-1}.
 \end{aligned} \tag{2.41}$$

2.3.2 The Step Characteristic Method (SC)

We assume the scattering and fission source terms in the discrete ordinates equation (2.9) to be constant:

$$\frac{1}{2} \sum_{g'=1}^G \Sigma_{s,g' \rightarrow g}(x) \phi_{g'}(x) \approx \bar{Q}_{s,g,i}, \tag{2.42}$$

$$\frac{\chi_g(x)}{2} \sum_{g'=1}^G \nu \Sigma_{f,g'}(x) \phi_{g'}(x) \approx \bar{Q}_{f,g,i}. \tag{2.43}$$

The material in segment i is also assumed to be homogeneous. We obtain the first-order differential equation:

$$\mu_n \frac{\partial \psi_{n,g}^{sc}(x)}{\partial x} + \Sigma_{t,g,i} \psi_{n,g}^{sc}(x) = \bar{Q}_{s,g,i} + \frac{1}{k} \bar{Q}_{f,g,i},$$

$$x_{i-1} \leq x \leq x_i, \quad 1 \leq n \leq M, \quad 1 \leq g \leq G, \quad (2.44)$$

which is solved for $\psi_{n,g}^{sc}(x)$. The quantities are defined in Table 2.4. The solution to equation (2.44) is:

$$\begin{aligned} \psi_{n,g}^{sc}(x) &= \psi_{n,g}^{sc}(x_{i-1}) \exp(-\Sigma_{t,g,i}(x - x_{i-1})/\mu_n) \\ &+ \frac{\bar{Q}_{s,g,i} + \frac{1}{k} \bar{Q}_{f,g,i}}{\Sigma_{t,g,i}} (1 - \exp(-\Sigma_{t,g,i}(x - x_{i-1})/\mu_n)). \end{aligned} \quad (2.45)$$

The angular flux at x_i is:

$$\begin{aligned} \psi_{n,g}^{sc}(x_i) &= \psi_{n,g}^{sc}(x_{i-1}) \exp(-\Sigma_{t,g,i}h_i/\mu_n) \\ &+ \frac{\bar{Q}_{s,g,i} + \frac{1}{k} \bar{Q}_{f,g,i}}{\Sigma_{t,g,i}} (1 - \exp(-\Sigma_{t,g,i}h_i/\mu_n)). \end{aligned} \quad (2.46)$$

Moreover, the averaged flux is:

$$\begin{aligned} \bar{\psi}_{n,g,i}^{sc} &= \frac{1}{h_i} \int_{x_{i-1}}^{x_i} \psi_{n,g}(x) dx \\ &= \frac{\bar{Q}_{s,g,i} + \frac{1}{k} \bar{Q}_{f,g,i}}{\Sigma_{t,g,i}} \left(1 - \frac{1 - \exp(-\Sigma_{t,g,i}h_i/\mu_n)}{\Sigma_{t,g,i}h_i/\mu_n} \right) \end{aligned} \quad (2.47)$$

$$+ \psi_{n,g}^{sc}(x_{i-1}) \frac{1 - \exp(-\Sigma_{t,g,i}h_i/\mu_n)}{\Sigma_{t,g,i}h_i/\mu_n}. \quad (2.48)$$

Eliminating $\psi_{n,g}^{sc}(x_{i-1})$ in equations (2.46) and (2.47), we get:

$$\begin{aligned}\psi_{n,g}^{sc}(x_i) &= \frac{\bar{Q}_{s,g,i} + \frac{1}{k}\bar{Q}_{f,g,i}}{\Sigma_{t,g,i}} \left(1 - \frac{(\Sigma_{t,g,i}h_i/\mu_n) \exp(-\Sigma_{t,g,i}h_i/\mu_n)}{1 - \exp(-\Sigma_{t,g,i}h_i/\mu_n)} \right) \\ &+ \bar{\psi}_{n,g,i}^{sc} \frac{(\Sigma_{t,g,i}h_i/\mu_n) \exp(-\Sigma_{t,g,i}h_i/\mu_n)}{1 - \exp(-\Sigma_{t,g,i}h_i/\mu_n)}.\end{aligned}\quad (2.49)$$

The auxiliary equations are obtained by setting the angular fluxes ψ to the solution ψ^{sc} :

$$\psi_{n,g,i-1} = \psi_{n,g}^{sc}(x_{i-1}), \quad (2.50)$$

$$\psi_{n,g,i} = \psi_{n,g}^{sc}(x_i), \quad (2.51)$$

$$\bar{\psi}_{n,g,i} = \bar{\psi}_{n,g,i}^{sc}. \quad (2.52)$$

with which the method is called the “**step characteristic method**”. We introduce equations (2.50), (2.51), (2.52) into equation (2.49) to get the step characteristic auxiliary equation for the case $\mu_n > 0$:

$$\begin{aligned}\mu_n > 0 & : \\ \psi_{n,g,i} &= \frac{\bar{Q}_{s,g,i} + \frac{1}{k}\bar{Q}_{f,g,i}}{\Sigma_{t,g,i}} \left(1 - \frac{(\Sigma_{t,g,i}h_i/\mu_n) \exp(-\Sigma_{t,g,i}h_i/\mu_n)}{1 - \exp(-\Sigma_{t,g,i}h_i/\mu_n)} \right) \\ &+ \bar{\psi}_{n,g,i} \frac{(\Sigma_{t,g,i}h_i/\mu_n) \exp(-\Sigma_{t,g,i}h_i/\mu_n)}{1 - \exp(-\Sigma_{t,g,i}h_i/\mu_n)}.\end{aligned}\quad (2.53)$$

Similarly, for the case $\mu_n < 0$, the auxiliary equation is:

$$\begin{aligned}\mu_n < 0 & : \\ \psi_{n,g,i-1} &= \frac{\bar{Q}_{s,g,i} + \frac{1}{k}\bar{Q}_{f,g,i}}{\Sigma_{t,g,i}} \left(1 - \frac{(-\Sigma_{t,g,i}h_i/\mu_n) \exp(\Sigma_{t,g,i}h_i/\mu_n)}{1 - \exp(\Sigma_{t,g,i}h_i/\mu_n)} \right) \\ &+ \bar{\psi}_{n,g,i} \frac{(-\Sigma_{t,g,i}h_i/\mu_n) \exp(\Sigma_{t,g,i}h_i/\mu_n)}{1 - \exp(\Sigma_{t,g,i}h_i/\mu_n)}.\end{aligned}\quad (2.54)$$

The equations (2.53) and (2.54) provide the “step characteristic” auxiliary equations.

2.3.3 The Multiple Balance Method (MB)

The auxiliary equations in the step method and the simplified characteristic method contain no neutron physics. So it is more favorable if the auxiliary equations have forms similar to the neutron balance equation. Morel and Larsen in 1990 (*Morel and Larsen, 1990*) invented such a method, called the “**multiple balance**” method, which is described in this section. Besides the MB method described here, *Yee and Larsen (2015)* recently proposed other 1-D MB methods, but they are not introduced here because of the difficulty to be generated to 2-D geometries.

For segment i , we define two linear weight functions for the two endpoints. The weight function evaluates to 1 at one end point, and 0 at the other end point. Figure 2.5 illustrates these weight functions:

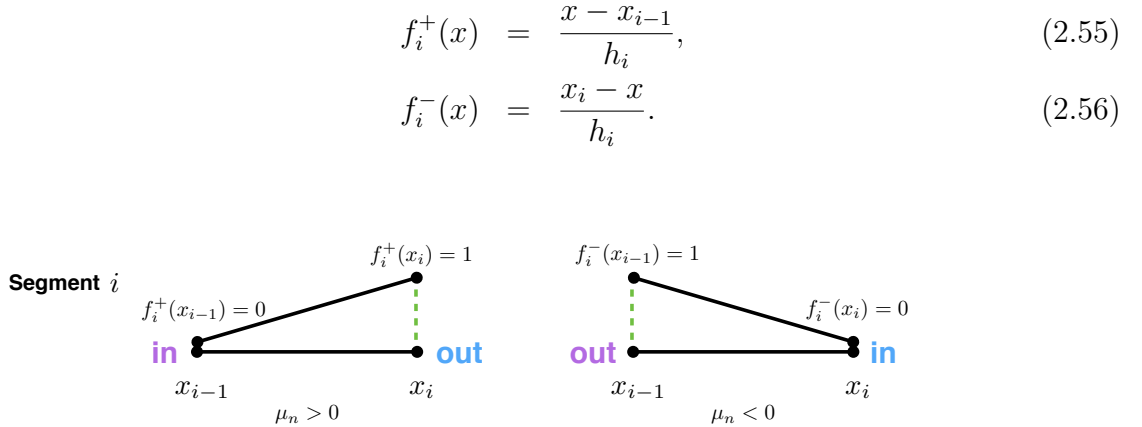


Figure 2.5: The definitions of two linear weight functions $f_i^+(x)$ and $f_i^-(x)$, which are 1 at one end point, and 0 at the other end point.

The weight function $f_i^+(x)$ is used with positive angular cosines $\mu_n > 0$, and the the weight function $f_i^-(x)$ is used with negative angular cosines $\mu_n < 0$. Without loss of generality, we assume $\mu_n > 0$. The auxiliary equations are obtained by integrating the discrete ordinates equation (2.9) with the weight function $f_i^+(x)$, as shown in

Figure 2.5. This integration resembles the finite element method. But in the multiple balance method, the flux is not assumed to have a predefined shape. After the integration, we get:

$$\begin{aligned}
\text{Leakage:} & \int_{x_{i-1}}^{x_i} f_i^+(x) \mu_n \frac{\partial \psi_{n,g}(x)}{\partial x} dx \\
\text{Collision:} & + \int_{x_{i-1}}^{x_i} f_i^+(x) \Sigma_{t,g}(x) \psi_{n,g}(x) dx \\
\text{Scattering:} & = \frac{1}{2} \sum_{g'=1}^G \int_{x_{i-1}}^{x_i} f_i^+(x) \Sigma_{s,g' \rightarrow g}(x) \phi_{g'}(x) dx \\
\text{Fission:} & + \frac{1}{2k} \sum_{g'=1}^G \int_{x_{i-1}}^{x_i} f_i^+(x) \chi_g(x) \nu \Sigma_{f,g'}(x) \phi_{g'}(x) dx \quad , \\
& 0 \leq x \leq X, \quad 1 \leq n \leq M, \quad 1 \leq g \leq G. \tag{2.57}
\end{aligned}$$

To get the auxiliary equation, all integrals in equation (2.57) are approximated by the averaged flux and endpoint flux. The approximation sets the fluxes in the “collision”, “scattering” and “fission” terms to be the outgoing flux:

$$\psi_{n,g}(x) \approx \psi_{n,g,i}, \quad x_{i-1} \leq x \leq x_i, \tag{2.58}$$

$$\phi_g(x) \approx \phi_{g,i}, \quad x_{i-1} \leq x \leq x_i. \tag{2.59}$$

The leakage term in equation (2.57) becomes exactly:

$$\begin{aligned}
\text{Leakage:} & \int_{x_{i-1}}^{x_i} f_i^+(x) \mu_n \frac{\partial \psi_{n,g}(x)}{\partial x} \\
& = \mu_n (f_i^+(x_i) \psi_{n,g,i} - f_i^+(x_{i-1}) \psi_{n,g,i-1}) - \mu_n \int_{x_{i-1}}^{x_i} \frac{1}{h_i} \psi_{n,g}(x) dx \\
& = \mu_n (\psi_{n,g,i} - \bar{\psi}_{n,g,i}). \tag{2.60}
\end{aligned}$$

For the collision term, we assume that the angular flux equals the angular flux at the

outgoing endpoint, as in equation (2.58). The collision term becomes:

$$\begin{aligned}
\text{Collision:} \quad & \int_{x_{i-1}}^{x_i} f_i^+(x) \Sigma_{tr,g}(x) \psi_{n,g}(x) dx \\
& \approx \int_{x_{i-1}}^{x_i} f_i^+(x) \Sigma_{tr,g,i} \psi_{n,g,i} dx \\
& = \frac{h_i}{2} \Sigma_{tr,g,i} \psi_{n,g,i}.
\end{aligned} \tag{2.61}$$

For the scattering & fission terms, we also assume that the flux equal the flux at the outgoing endpoint, as in equation (2.59). The scattering term becomes:

$$\begin{aligned}
\text{Scattering:} \quad & \frac{1}{2} \sum_{g'=1}^G \int_{x_{i-1}}^{x_i} f_i^+(x) \Sigma_{s,g' \rightarrow g}(x) \phi_{g'}(x) dx \\
& \approx \frac{1}{2} \sum_{g'=1}^G \int_{x_{i-1}}^{x_i} f_i^+(x) \Sigma_{s,g' \rightarrow g}(x) \phi_{g',i} dx \\
& = \frac{1}{2} \frac{h_i}{2} \sum_{g'=1}^G \Sigma_{s,g' \rightarrow g,i} \phi_{g',i} \\
& = \frac{h_i}{2} Q_{s,g,i}^-
\end{aligned} \tag{2.62}$$

and the fission term becomes:

$$\begin{aligned}
\text{Fission:} \quad & \frac{1}{2k} \sum_{g'=1}^G \int_{x_{i-1}}^{x_i} f_i^+(x) \chi_g(x) \nu \Sigma_{f,g'}(x) \phi_{g'}(x) dx \\
& \approx \frac{\chi_{g,i}}{2k} \sum_{g'=1}^G \int_{x_{i-1}}^{x_i} f_i^+(x) \nu \Sigma_{f,g'}(x) \phi_{g',i} dx \\
& = \frac{1}{2} \frac{h_i}{2} \frac{\chi_{g,i}}{2k} \sum_{g'=1}^G \nu \Sigma_{f,g',i} \phi_{g',i} \\
& = \frac{h_i}{2} Q_{f,g,i}^-
\end{aligned} \tag{2.63}$$

See Table 2.27 for definitions of the quantities. Introducing the four approximations

(2.60), (2.61), (2.62) and (2.63) into equation (2.57), we get:

$$\mu_n (\psi_{n,g,i} - \bar{\psi}_{n,g,i}) + \frac{h_i}{2} \Sigma_{tr,g,i} \psi_{n,g,i} = \frac{h_i}{2} Q_{s,g,i}^- + \frac{1}{k} \frac{h_i}{2} Q_{f,g,i}^- \quad (2.64)$$

We divide equation (2.64) by the term $\frac{1}{2}h_i$ to get the multiple balance auxiliary equation for $\mu_n > 0$:

$$\begin{aligned} \mu_n > 0 : \\ \mu_n \frac{\psi_{n,g,i} - \bar{\psi}_{n,g,i}}{h_i/2} + \Sigma_{tr,g,i} \psi_{n,g,i} = Q_{s,g,i}^- + \frac{1}{k} Q_{f,g,i}^- \end{aligned} \quad (2.65)$$

When the angular cosines are negative $\mu_n < 0$, the auxiliary equations are obtained by integrating equation (2.9) with the weight function $f_i^-(x)$. Following a similar process, we obtain the multiple balance auxiliary equation for $\mu_n < 0$:

$$\begin{aligned} \mu_n < 0 : \\ |\mu_n| \frac{\bar{\psi}_{n,g,i} - \psi_{n,g,i-1}}{h_i/2} + \Sigma_{tr,g,i} \psi_{n,g,i-1} = Q_{s,g,i-1}^+ + \frac{1}{k} Q_{f,g,i-1}^+ \end{aligned} \quad (2.66)$$

The auxiliary equations (2.65) and (2.66) can be viewed as the neutron balance equation centered at the outgoing endpoint. So the method is named as the “**multiple balance method**”. Now for each cell and direction of flight, the number of unknowns (which is 3) equals the number of available equations (balance equation plus 2 auxiliary equations).

2.4 Sweep

The previous sections introduce how to solve for the unknown segment-averaged and endpoint fluxes. Recall Figure 2.1 that the geometry is a one-dimensional spatial grid of segments. Each segment is visited once, where segment-averaged and endpoint

fluxes are updated. The process of visiting all segments exactly once is called a “sweep”. And the order of visit is called a “sweeping order”. The sweep order must satisfy the condition that the incoming flux of a segment is calculated before the segment is visited.

When the angular cosine is positive $\mu_n > 0$, the segments are visited in the increasing order from segment 1 to segment I . When the angular cosine is negative $\mu_n < 0$, the segments are visited in the decreasing order from segment I to segment 1. The sweep orders are illustrated in Figure 2.6.

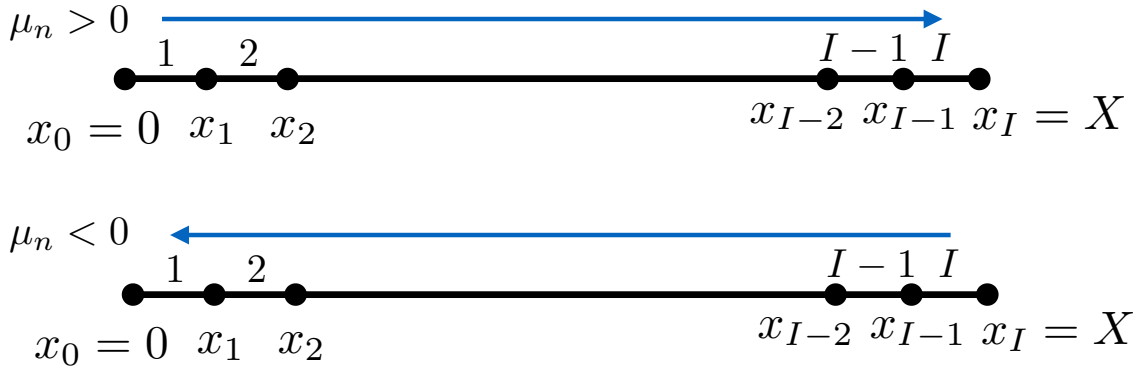


Figure 2.6: The sweep order of the one-dimensional spatial grid. For $\mu_n > 0$, the segments are visited in the increasing order from segment 1 to segment I . For $\mu_n < 0$, the segments are visited in the decreasing order from segment I to segment 1.

2.5 Numerical Results

The one-dimensional methods are compared for simple problems, to give the reader a brief idea about how these methods behave. For simplicity, the names of the methods are abbreviated in Table 2.5. Since the MC solutions have no truncation errors in space and angle, it serves as the reference to measure how accurate SN methods are. We use a very large number of particles to minimize the statistical

errors.

Table 2.5: List of numerical methods' abbreviations and their definitions

METHOD	DESCRIPTION
“ MC ”	Monte Carlo
“ <i>string</i> Sn ”	SN method with the level of angles equals n , with method <i>string</i> . “ STEP ” stands for the step method. “ SC ” stands for the step characteristic method. “ MB ” stands for the multiple balance method.

2.5.1 Pin-cell Problem

The first problem is designed to simulate a nuclear reactor fuel pin-cell (Figure 1.2) with a pitch of 1.26 cm. The radius of the fuel region is 0.4096 cm, the outer radius of the gap is 0.418 cm, and the outer radius of the clad is 0.475 cm. The geometry is shown in Figure 2.7. The boundary conditions on both ends are **reflecting**. Two types of grids are defined: one is the coarse grid with 4 segments, and the other is the fine grid with 8 segments.

The fuel region is denoted as “**F**”, the gap is denoted as “**G**”, the clad is denoted as “**C**”, and the moderator region is denoted as “**M**”. For simplicity, a set of one-group cross sections are provided in Table 2.6, which is adapted from a 3.1wt% enriched UO_2 fuel pin-cell of the AP1000 reactor.

Table 2.6: List of one-group cross section

MATERIAL	ABSORPTION Σ_a (cm ⁻¹)	NUFISSION $\nu\Sigma_f$ (cm ⁻¹)	FISSION Σ_f (cm ⁻¹)	SCATTERING Σ_s (cm ⁻¹)
Fuel (F)	0.121437	0.19427	0.0788062	0.377744
Gap (G)	0	0	0	3.08906E-05
Clad (C)	0.00313575	0	0	0.280904
Moderator (M)	0.0116829	0	0	1.06112

Table 2.7 summarizes the k -eigenvalue comparison and the time cost, and Table 2.8 summarizes the solutions and the error analysis. For reference, 100 million

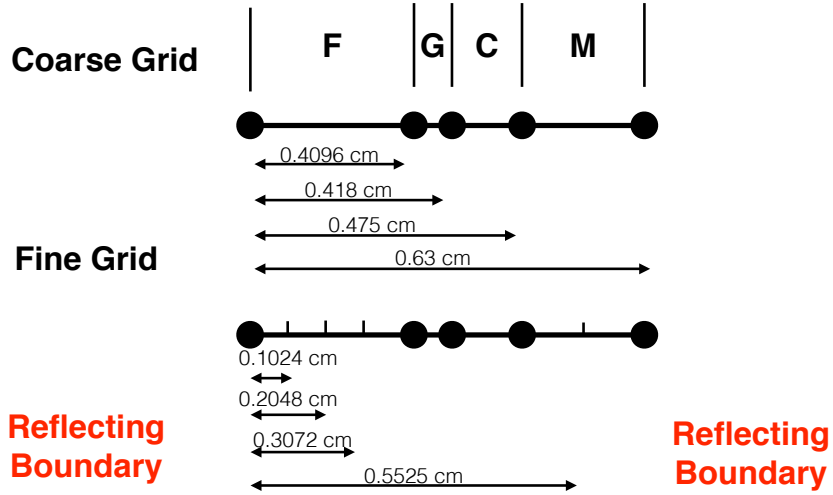


Figure 2.7: A one-dimensional pin-cell geometry. The boundary conditions on both ends are **reflecting**. The coarse grid contains 4 segments, and the fine grid contains 8 segments.

Monte Carlo particles were simulated, resulting in a reference k -eigenvalue with an uncertainty of 2 pcm, and a reference flux with an uncertainty of 0.005%.

In the error analysis, errors in the effective k -eigenvalue are measured by the difference from the Monte Carlo reference, which is measured in a unit called pcm, where:

$$1 \text{ pcm} = 10^{-5}. \quad (2.67)$$

Given a scalar flux solution $\bar{\phi}_i$ and a reference solution $\bar{\phi}_i^{ref}$, the difference between the two is measured with the relative 2-norm, defined as:

$$\left\| \frac{\bar{\phi} - \bar{\phi}^{ref}}{\bar{\phi}^{ref}} \right\|_2 = \sqrt{\frac{1}{N} \sum_{i=1}^N \left(\frac{\bar{\phi}_i - \bar{\phi}_i^{ref}}{\bar{\phi}_i^{ref}} \right)^2}. \quad (2.68)$$

Figure 2.8 plots the errors in k -eigenvalues and fluxes versus the time cost per iteration. Each curve contains data points generated by a variety of angular quadra-

Table 2.7: List of k -effective and time cost of the pin-cell problem

METHOD	KEFF	KEFF ERROR. (pcm)	TIME PER IT- ERATION (ms)
MC	1.538453	2.0	Reference
Coarse Grid			
STEP S2	1.538449	-0.4	0.024
STEP S4	1.538529	7.6	0.024
STEP S8	1.538600	14.7	0.032
STEP S16	1.538641	18.8	0.032
STEP S32	1.538656	20.3	0.035
SC S2	1.538277	-17.6	0.023
SC S4	1.538320	-13.3	0.025
SC S8	1.538385	-6.8	0.025
SC S16	1.538435	-1.8	0.030
SC S32	1.538448	-0.5	0.040
MB S2	1.538297	-15.6	0.023
MB S4	1.538358	-9.5	0.023
MB S8	1.538437	-1.6	0.025
MB S16	1.538488	3.5	0.031
MB S32	1.538501	4.8	0.037
Fine Grid			
STEP S2	1.538342	-11.1	0.025
STEP S4	1.538401	-5.2	0.030
STEP S8	1.538469	1.6	0.030
STEP S16	1.538515	6.2	0.035
STEP S32	1.538528	7.5	0.053
SC S2	1.538277	-17.6	0.026
SC S4	1.538321	-13.2	0.029
SC S8	1.538388	-6.5	0.033
SC S16	1.538439	-1.4	0.044
SC S32	1.538452	-0.1	0.056
MB S2	1.538280	-17.3	0.026
MB S4	1.538327	-12.6	0.029
MB S8	1.538396	-5.7	0.029
MB S16	1.538447	-0.6	0.039
MB S32	1.538459	0.6	0.056

ture sets: S2, S4, S8, S16, S32. Because the problem is so simple, the measured time contains a significant part other than the pure computation, which includes for example the memory accessing time. The values are rounded to 0.001 ms, so when two data points have time value differed less than 0.001 ms, they can be plotted with

Table 2.8: List of solutions of the pin-cell problem

METHOD	FUEL FLUX	GAP FLUX	CLAD FLUX	MOD- ERATOR FLUX	FLUX ERROR (%)
MC	1.00000	0.99807	0.99775	0.99611	0.005
Coarse Grid					
STEP S2	1.00000	0.99802	0.99782	0.99618	0.005
STEP S4	1.00000	0.99732	0.99702	0.99477	0.086
STEP S8	1.00000	0.99670	0.99630	0.99352	0.164
STEP S16	1.00000	0.99637	0.99585	0.99280	0.210
STEP S32	1.00000	0.99626	0.99565	0.99255	0.226
SC S2	1.00000	0.99960	0.99954	0.99920	0.195
SC S4	1.00000	0.99921	0.99912	0.99844	0.147
SC S8	1.00000	0.99863	0.99847	0.99729	0.075
SC S16	1.00000	0.99821	0.99797	0.99641	0.020
SC S32	1.00000	0.99813	0.99783	0.99620	0.007
MB S2	1.00000	0.99939	0.99934	0.99884	0.172
MB S4	1.00000	0.99883	0.99873	0.99778	0.104
MB S8	1.00000	0.99811	0.99794	0.99638	0.016
MB S16	1.00000	0.99766	0.99742	0.99549	0.041
MB S32	1.00000	0.99755	0.99725	0.99527	0.056
Fine Grid					
STEP S2	1.00000	0.99919	0.99898	0.99805	0.128
STEP S4	1.00000	0.99870	0.99841	0.99701	0.064
STEP S8	1.00000	0.99812	0.99771	0.99581	0.015
STEP S16	1.00000	0.99772	0.99720	0.99502	0.064
STEP S32	1.00000	0.99760	0.99701	0.99478	0.080
SC S2	1.00000	0.99959	0.99955	0.99920	0.195
SC S4	1.00000	0.99920	0.99910	0.99842	0.146
SC S8	1.00000	0.99860	0.99844	0.99725	0.072
SC S16	1.00000	0.99815	0.99791	0.99634	0.015
SC S32	1.00000	0.99806	0.99777	0.99613	0.001
MB S2	1.00000	0.99958	0.99953	0.99915	0.192
MB S4	1.00000	0.99917	0.99908	0.99833	0.141
MB S8	1.00000	0.99857	0.99840	0.99711	0.064
MB S16	1.00000	0.99813	0.99788	0.99621	0.009
MB S32	1.00000	0.99803	0.99773	0.99600	0.006

the same time value.

This problem has a quite flat flux, which means the change of flux in space is small. Despite the flat solution, we can still see that the fine grid has more accurate solutions. Moreover, the SC method and the MB method are more accurate than the

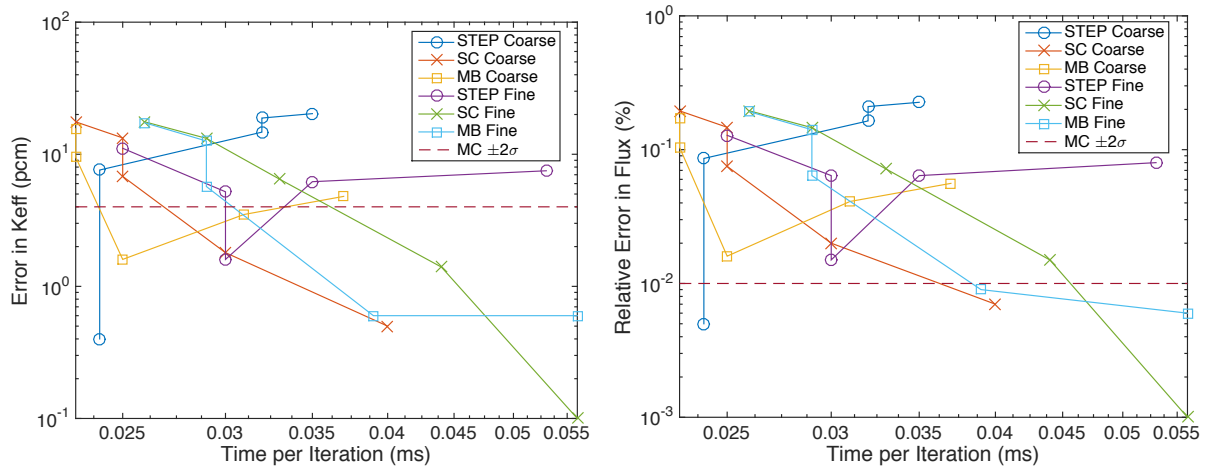


Figure 2.8: The error comparisons for the one-dimensional pin-cell problem. The SN solutions are simulated with a variety of angular quadrature sets: S2, S4, S8, S16, S32. The dashed line is the Monte Carlo uncertainties within two standard deviations.

STEP method.

In conclusion, the first problem suggests that the SC and the MB methods are more accurate. In the next subsection, we examine a larger problem with a less-flat flux.

2.5.2 Mini-assembly Problem

The next problem is a mini-assembly, which consists of 3 fuel pin-cells and 1 water pin-cell. The boundary condition on the side of the fuel pin-cell is reflecting, and on the side of the water pin-cell is vacuum. The pitch of the fuel pin-cell is 1.26 cm.

Figure 2.9 describes the geometry in detail. There are two types of spatial grids: the coarse grid and the fine grid. The cross sections can be found in Table 2.6.

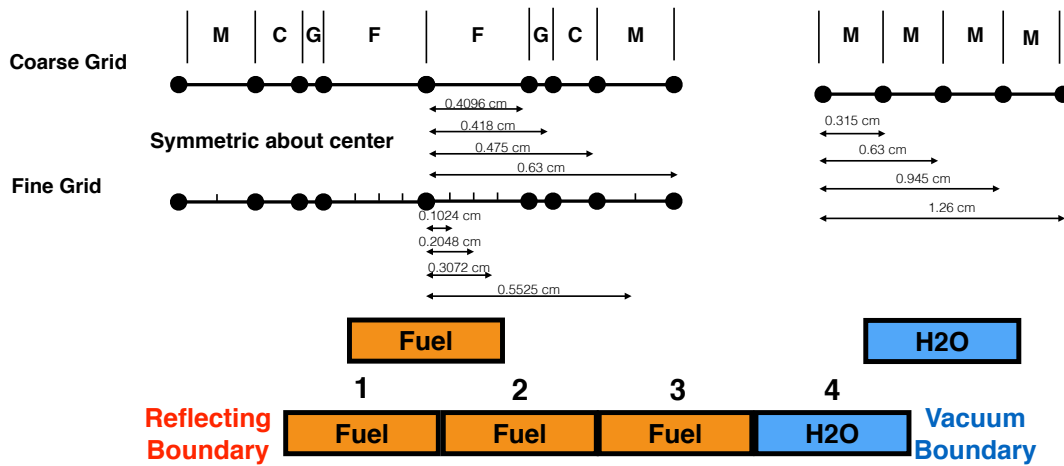


Figure 2.9: A one-dimensional mini-assembly problem. The boundary is **reflecting** on the left, and is **vacuum** on the right. The mini-assembly consists of 3 fuel pin-cells and one water pin-cell. The pin-cell pitch is 1.26 cm. For the coarse grid, each fuel pin-cell contains 8 segments. For the fine grid, each fuel pin-cell contains 16 segments. For the both coarse and fine grids, the water pin-cell contains 4 segments.

Table 2.9 summarizes the k -eigenvalue comparison and the time cost, and Table 2.10 summarizes the solutions and the error analysis. The fluxes are averaged over a pin-cell. For reference, 300 million Monte Carlo particles were simulated, resulting in a reference k -eigenvalue with an uncertainty of 7.3 pcm, and a reference flux has with uncertainty of 0.002%.

Figure 2.8 plots the errors in k -eigenvalues and fluxes versus the time cost per iteration. In comparison, the MB method is more accurate than the SC method,

Table 2.9: List of k -effective and time cost of the mini-assembly problem

METHOD	KEFF	KEFF ERROR. (pcm)	TIME PER IT- ERATION (ms)
MC	1.127767	7.3	Reference
Coarse Grid			
STEP S2	1.055969	-7179.8	0.028
STEP S4	1.085370	-4239.7	0.030
STEP S8	1.090129	-3763.8	0.034
STEP S16	1.091719	-3604.8	0.048
STEP S32	1.092194	-3557.3	0.070
SC S2	1.095436	-3233.1	0.025
SC S4	1.118654	-911.3	0.032
SC S8	1.121026	-674.1	0.044
SC S16	1.122197	-557.0	0.071
SC S32	1.122549	-521.8	0.104
MB S2	1.101207	-2656.0	0.028
MB S4	1.125118	-264.9	0.032
MB S8	1.127776	0.9	0.042
MB S16	1.128895	112.8	0.062
MB S32	1.129177	141.0	0.091
Fine Grid			
STEP S2	1.060484	-6728.3	0.034
STEP S4	1.088716	-3905.1	0.042
STEP S8	1.092952	-3481.5	0.055
STEP S16	1.094482	-3328.5	0.081
STEP S32	1.094900	-3286.7	0.123
SC S2	1.096241	-3152.6	0.039
SC S4	1.119509	-825.8	0.048
SC S8	1.121909	-585.8	0.075
SC S16	1.123100	-466.7	0.105
SC S32	1.123434	-433.3	0.157
MB S2	1.100357	-2741.0	0.039
MB S4	1.124082	-368.5	0.046
MB S8	1.126554	-121.3	0.061
MB S16	1.127654	-11.3	0.093
MB S32	1.127917	15.0	0.143

which is more accurate than the STEP method. The flux for this problem has a significant tilt - it is much less “flat” than in the first problem. (See Table 2.10.) A possible reason why the MB method is the most accurate is because the derivation of the MB method does not assume the flux is flat in a segment, while the other

Table 2.10: List of solutions of the mini-assembly problem

METHOD	PIN- CELL 1 FLUX	PIN- CELL 2 FLUX	PIN- CELL 3 FLUX	PIN- CELL 4 FLUX	FLUX ERROR (%)
MC	1.00000	0.90813	0.73070	0.38933	0.002
Coarse Grid					
STEP S2	1.00000	0.90338	0.71948	0.39666	1.243
STEP S4	1.00000	0.90483	0.72043	0.39003	0.732
STEP S8	1.00000	0.90599	0.72381	0.39211	0.604
STEP S16	1.00000	0.90611	0.72452	0.39267	0.613
STEP S32	1.00000	0.90615	0.72466	0.39282	0.619
SC S2	1.00000	0.90430	0.72206	0.39011	0.636
SC S4	1.00000	0.90634	0.72474	0.38577	0.620
SC S8	1.00000	0.90707	0.72728	0.38826	0.278
SC S16	1.00000	0.90715	0.72776	0.38875	0.221
SC S32	1.00000	0.90718	0.72788	0.38894	0.206
MB S2	1.00000	0.90486	0.72362	0.38892	0.519
MB S4	1.00000	0.90716	0.72738	0.38510	0.592
MB S8	1.00000	0.90788	0.73006	0.38785	0.195
MB S16	1.00000	0.90794	0.73042	0.38847	0.113
MB S32	1.00000	0.90797	0.73048	0.38866	0.087
Fine Grid					
STEP S2	1.00000	0.89741	0.70276	0.38528	2.067
STEP S4	1.00000	0.89930	0.70378	0.37898	2.323
STEP S8	1.00000	0.90072	0.70818	0.38192	1.857
STEP S16	1.00000	0.90086	0.70906	0.38269	1.755
STEP S32	1.00000	0.90091	0.70922	0.38291	1.731
SC S2	1.00000	0.90379	0.72063	0.38883	0.732
SC S4	1.00000	0.90577	0.72296	0.38421	0.854
SC S8	1.00000	0.90654	0.72557	0.38669	0.496
SC S16	1.00000	0.90662	0.72610	0.38719	0.426
SC S32	1.00000	0.90666	0.72624	0.38741	0.401
MB S2	1.00000	0.90491	0.72377	0.38960	0.507
MB S4	1.00000	0.90721	0.72744	0.38585	0.501
MB S8	1.00000	0.90793	0.73015	0.38869	0.091
MB S16	1.00000	0.90799	0.73051	0.38933	0.015
MB S32	1.00000	0.90801	0.73055	0.38954	0.030

methods, i.e. STEP and SC methods both assume the flux in a segment to be flat.

In conclusion, although the two one-dimensional problems are simple, the MB method is more advantageous than the STEP and SC methods. In later chapters, the MB method is generalized to two-dimensional problems, and we compare the

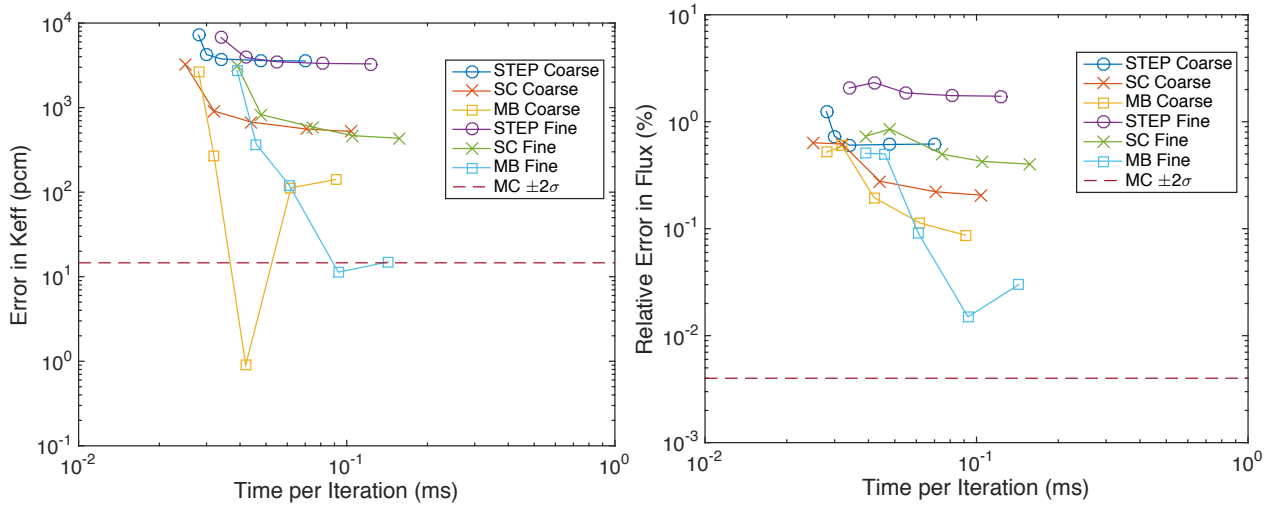


Figure 2.10: The error comparisons for the one-dimensional mini-assembly problem. The SN solutions are simulated with a variety of angular quadrature sets: S2, S4, S8, S16, S32. The dashed line is the Monte Carlo uncertainties within two standard deviations.

generalized MB method with other SN methods. Moreover, the widely used MOC method can be viewed as a generalization of the SC method in two-dimensional space. So comparisons between the MB and the MOC methods are also studied.

2.6 Road-map to Two-dimensional Geometry

In this chapter, several deterministic methods are studied: the STEP method, the SC method, and the MB method. In two-dimension space, these methods have been generalized to the 2-D method of characteristic (MOC), the 2-D step method (STEP), the 2-D simplified step characteristic method (SSC), and the 2-D multiple balance method (MB). The origins of the 2-D methods are shown in Figure 2.11. Among all these, the MOC is widely used, which originates from the SC method. In this thesis, we categorize the 2-D STEP, SSC, MB methods as SN methods, but we do not categorize MOC as an SN method.

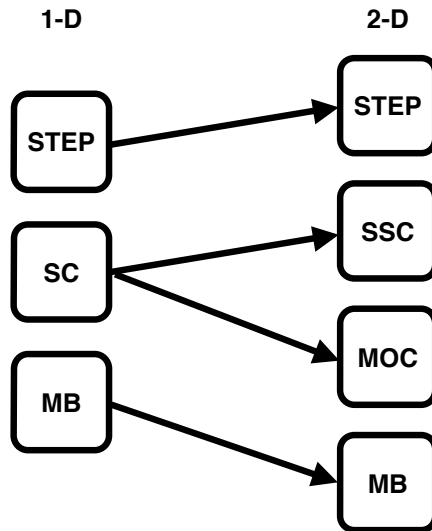


Figure 2.11: The origins of the two-dimensional deterministic methods.

CHAPTER III

Two-Dimensional Problems with Cartesian Spatial Grids

After a review of the discrete ordinates method in one-dimensional problems, two-dimensional problems are now introduced. In this chapter, we consider problems with Cartesian grids, where all spatial cells are rectangular. In later chapters, more general two-dimensional problems with curved spatial grids are studied.

3.1 The Scope of Geometry

The Cartesian grid consists of rectangular spatial cells. We assume that the system is divided into $I \times J$ rectangles. See Figure 3.1. The rectangle at the coordinate (i, j) has four boundaries $x = x_{i-1}$, $x = x_i$, $y = y_{j-1}$ and $y = y_j$. This rectangle and its boundaries are illustrated in Figure 3.2.

$$\text{Rectangle } (i, j) : 1 \leq i \leq I, 1 \leq j \leq J, \quad (3.1)$$

$$\text{Left boundary } x_{i-1} : 1 \leq i \leq I, \quad (3.2)$$

$$\text{Right boundary } x_i : 1 \leq i \leq I, \quad (3.3)$$

$$\text{Bottom boundary } y_{j-1} : 1 \leq j \leq J, \quad (3.4)$$

$$\text{Top boundary } y_j : 1 \leq j \leq J. \quad (3.5)$$

The rectangle (i, j) is named as $S(i, j)$:

$$S(i, j) = \{(x, y) | x_{i-1} \leq x \leq x_i, y_{j-1} \leq y \leq y_j\}. \quad (3.6)$$

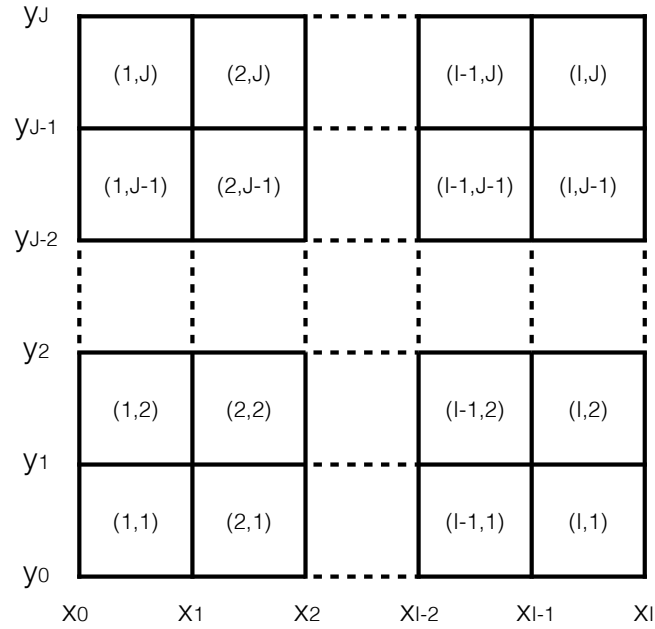


Figure 3.1: The Cartesian grid, which is composed of $I \times J$ rectangles. There are $I + 1$ boundaries in the x direction, and $J + 1$ boundaries in the y direction.

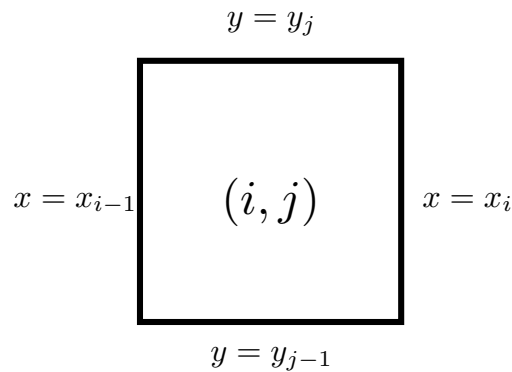


Figure 3.2: The rectangle (i, j) is bounded with four lines with equations $x = x_{i-1}$, $x = x_i$, $y = y_{j-1}$ and $y = y_j$.

3.2 Two-Dimensional Multigroup Discrete Ordinates Neutron Transport Equation

In two-dimensional space, the neutron angular flux depends on two location variables x, y , two angular variables η, ξ , and the energy group number g . These variables are defined in Table 3.1. The multigroup transport equation for an eigenvalue problem is:

$$\begin{aligned} & \eta \frac{\partial \psi_g(x, y, \eta, \xi)}{\partial x} + \xi \frac{\partial \psi_g(x, y, \eta, \xi)}{\partial y} + \Sigma_{t,g}(x, y) \psi_g(x, y, \eta, \xi) \\ &= \frac{1}{4\pi} \sum_{g'=1}^G \Sigma_{s,g' \rightarrow g}(x, y) \phi_{g'}(x, y) + \frac{\chi_g(x, y)}{4\pi k} \sum_{g'=1}^G \nu \Sigma_{f,g'}(x, y) \phi_{g'}(x, y), \end{aligned}$$

$$x_0 \leq x \leq x_I, \quad y_0 \leq y \leq y_J, \quad 0 \leq \eta^2 + \xi^2 \leq 1, \quad 1 \leq g \leq G.$$

(See Figure 3.1.) The definitions of the quantities appearing in equation (3.7) are also listed in Table 3.1. The direction of flight is $\hat{\Omega} = (\eta, \xi, \mu)$. An illustration of the angular variables are explained in Figure 3.3, with the following definitions:

$$\xi(\theta, \varphi) = \sin \theta \cos \varphi = \sqrt{1 - \mu^2} \cos \varphi, \quad (3.7)$$

$$\eta(\theta, \varphi) = \sin \theta \sin \varphi = \sqrt{1 - \mu^2} \sin \varphi, \quad (3.8)$$

$$\mu(\theta, \varphi) = \cos \theta, \quad (3.9)$$

$$\xi^2 + \eta^2 + \mu^2 = 1. \quad (3.10)$$

The relationship between the scalar flux and the angular flux is:

$$\phi_g(x, y) = \int_{-1}^1 \int_0^{2\pi} \psi_g(x, y, \xi, \eta) d\varphi d\mu. \quad (3.11)$$

Table 3.1: List of definitions of terms in the two-dimensional neutron transport equation

TERM	TYPE	EXPLANATION
x	scalar	the x -coordinate
y	scalar	the y -coordinate
η	scalar	the x -component of the unit direction of flight vector
ξ	scalar	the y -component of the unit direction of flight vector
μ	scalar	the z -component of the unit direction of flight vector
g	integer	the energy group
G	integer	the total number of energy groups
$\psi_g(x, y, \eta, \xi)$	scalar	the angular flux for group g , at location (x, y) , in direction (η, ξ, μ) , where $\mu = \sqrt{1 - \eta^2 - \xi^2}$.
$\phi_g(x, y)$	scalar	the scalar flux for group g , at location (x, y) . See equation (3.11) for definition.
$\Sigma_{t,g}(x, y)$	scalar	the macroscopic total cross section at location (x, y) , energy group g
k	scalar	the effective reactivity coefficient, the eigenvalue of the equation
$\Sigma_{s,g' \rightarrow g}(x, y)$	scalar	the isotropic macroscopic scattering cross section at location (x, y) , for scattering from energy group g' to energy group g
$\chi_g(x, y)$	scalar	the neutron fission probability into group g at location (x, y) (the “ fission spectrum ”)
$\nu\Sigma_{f,g}(x, y)$	scalar	the macroscopic neutron yield cross section at location (x, y) , for energy group g

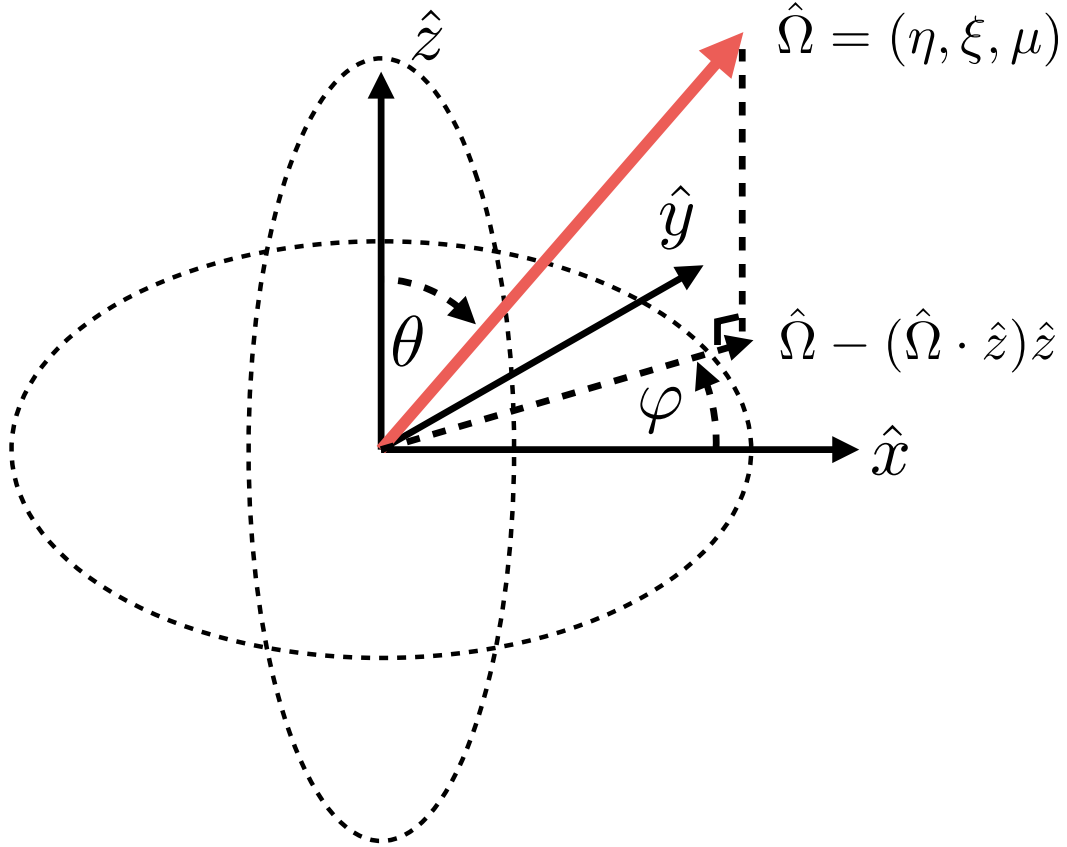


Figure 3.3: An illustration of a unit vector $\hat{\Omega}$ and definitions of its components. φ is the azimuthal angle, which is defined as the angle counting from x -axis counterclockwise to the projection of $\hat{\Omega}$ onto the $x - y$ plane. θ is the polar angle, which is the angle needed to rotate z -axis to $\hat{\Omega}$. The range of θ is $0 \leq \theta \leq \pi$, and the range of φ is $0 \leq \varphi \leq 2\pi$.

The angular variable $\hat{\Omega}$ is continuous on the surface of the unit sphere:

$$\hat{\Omega} \in "4\pi" = \{\hat{v} \in \mathcal{R}^3 : |\hat{v}| = 1\}, \quad (3.12)$$

which can be discretized with a set of finite angles $\hat{\Omega}_n$, $1 \leq n \leq M$. The angle $\hat{\Omega}_n$ is associated with a weight ω_n . These weights are chosen so as to approximate the

integral of any function $f(\hat{\Omega})$ with a weighted sum:

$$\int_{4\pi} f(\hat{\Omega}) d\hat{\Omega} \approx \sum_{n=1}^M f(\hat{\Omega}_n) \omega_n, \text{ for } f = \text{any function}, \quad (3.13)$$

$$4\pi = \sum_{n=1}^M \omega_n. \quad (3.14)$$

$\hat{\Omega}_n$ and ω_n are defined so that the approximation (3.13) is exact for low order polynomials:

$$\int_{4\pi} p(\hat{\Omega}) d\hat{\Omega} = \sum_{n=1}^M p(\hat{\Omega}_n) \omega_n, \text{ for } p = \text{low order polynomial} \quad (3.15)$$

where a polynomial of $\hat{\Omega}$ of order m has the form:

$$p_m(\hat{\Omega}) = \sum_{i+j+k=m, i \geq 0, j \geq 0, k \geq 0} a_{i,j,k} \eta^i \xi^j \mu^k. \quad (3.16)$$

The set $\{(\hat{\Omega}_n, \omega_n)\}$ is called a “**quadrature set**”:

$$\text{“quadrature set”} = \{(\hat{\Omega}_n, \omega_n), 1 \leq n \leq M_N\}, \quad (3.17)$$

where N is an even integer, indicating the *level* of quadrature set, and M_N is the total number of angles in the quadrature set. The larger N is, the more angles there are.

These angles preserve some symmetry conditions, the first of which is that the angles and weights are symmetric for all 8 octants, the second of which is that the angles and weights are symmetric across the x -axis, y -axis and z -axis. Mathematically, these

conditions can be expressed as:

$$\text{If } (\eta, \xi, \mu) \in SN \text{ quadrature set} : (\pm\eta, \pm\xi, \pm\mu) \in SN \text{ quadrature set, (3.18)}$$

$$: (\eta, \mu, \xi) \in SN \text{ quadrature set, (3.19)}$$

$$: (\xi, \eta, \mu) \in SN \text{ quadrature set, (3.20)}$$

$$: (\xi, \mu, \eta) \in SN \text{ quadrature set, (3.21)}$$

$$: (\mu, \xi, \eta) \in SN \text{ quadrature set, (3.22)}$$

$$: (\mu, \eta, \xi) \in SN \text{ quadrature set. (3.23)}$$

If the conditions in equations (3.18), (3.19), (3.20), (3.21), (3.22), (3.23) are satisfied, the quadrature set is said to be “**level symmetric**”. The level symmetric quadrature sets up to S_{20} are used in this thesis (Hebert, 2009). The low order quadratures sets are listed in Table 3.2.

Table 3.2: List of selected first few quadrature sets, within in the first octant

N	M_N	DIRECTION $\hat{\Omega}_n$	WEIGHT $\omega_n/4\pi$
2	8	{5.773503e-01, 5.773503e-01, 5.773503e-01}	1/8
4	24	{3.500212e-01, 3.500212e-01, 8.688903e-01}	1/24
		{3.500212e-01, 8.688903e-01, 3.500212e-01}	1/24
		{8.688903e-01, 3.500212e-01, 3.500212e-01}	1/24
6	48	{2.666354e-01, 2.666354e-01, 9.261809e-01}	2.201577e-02
		{6.815077e-01, 2.666354e-01, 6.815077e-01}	1.965089e-02
		{2.666354e-01, 6.815077e-01, 6.815077e-01}	1.965089e-02
		{9.261809e-01, 2.666354e-01, 2.666354e-01}	2.201577e-02
		{6.815077e-01, 6.815077e-01, 2.666354e-01}	1.965089e-02
		{2.666354e-01, 9.261809e-01, 2.666354e-01}	2.201577e-02
8	80	{2.182178e-01, 2.182178e-01, 9.511898e-01}	1.512345e-02
		{5.773503e-01, 2.182178e-01, 7.867958e-01}	1.134260e-02
		{2.182178e-01, 5.773503e-01, 7.867958e-01}	1.134260e-02
		{7.867958e-01, 2.182178e-01, 5.773503e-01}	1.134260e-02
		{5.773503e-01, 5.773503e-01, 5.773503e-01}	1.157406e-02
		{2.182178e-01, 7.867958e-01, 5.773503e-01}	1.134260e-02
		{9.511898e-01, 2.182178e-01, 2.182178e-01}	1.512345e-02
		{7.867958e-01, 5.773503e-01, 2.182178e-01}	1.134260e-02
		{5.773503e-01, 7.867958e-01, 2.182178e-01}	1.134260e-02
		{2.182178e-01, 9.511898e-01, 2.182178e-01}	1.512345e-02

The level symmetric $S2$ and $S4$ quadrature sets in the first octant are illustrated in Figure 3.4.

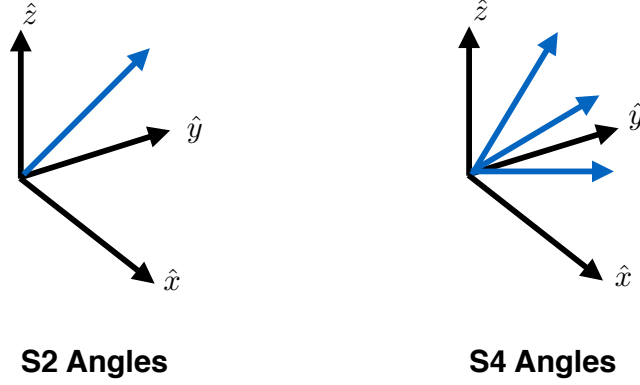


Figure 3.4: The illustration of the angles of the “level symmetric” $S2$ and $S4$ quadrature sets in the first octant. These angles preserve some symmetry conditions, the first of which is that the angles are symmetric for all 8 octants, the second of which is that the angles are symmetric for x -axis, y -axis and z -axis.

Then, the discrete ordinates equation for angle $\hat{\Omega}_n$ is:

$$\begin{aligned} & \eta_n \frac{\partial \psi_{n,g}(x, y)}{\partial x} + \xi_n \frac{\partial \psi_{n,g}(x, y)}{\partial y} + \Sigma_{t,g}(x, y) \psi_{n,g}(x, y) \\ &= \frac{1}{4\pi} \sum_{g'=1}^G \Sigma_{s,g' \rightarrow g}(x, y) \phi_{g'}(x, y) + \frac{\chi_g(x, y)}{4\pi k} \sum_{g'=1}^G \nu \Sigma_{f,g'}(x, y) \phi_{g'}(x, y), \end{aligned}$$

$$x_0 \leq x \leq x_I, \quad y_0 \leq y \leq y_J, \quad 1 \leq n \leq M, \quad 1 \leq g \leq G.$$

The definitions of additional terms can be found in Table 3.3. The angular flux and the scalar flux have the relationship:

$$\phi_g(x, y) = \sum_{n=1}^M \omega_n \psi_{n,g}(x, y), \quad (3.24)$$

$$\psi_{n,g}(x, y) = \psi_g(x, y, \eta_n, \xi_n). \quad (3.25)$$

Table 3.3: List of definitions of terms in the two-dimensional neutron transport equation

TERM	TYPE	EXPLANATION
$\hat{\Omega}_n$	unit vector	the direction of flight, $\hat{\Omega}_n = (\eta_n, \xi_n, \mu_n)$
η_n	scalar	the x -component of $\hat{\Omega}_n$
ξ_n	scalar	the y -component of $\hat{\Omega}_n$
μ_n	scalar	the z -component of $\hat{\Omega}_n$
ω_n	scalar	the weight of the angle at index n , i.e. $\hat{\Omega}_n$
$\psi_{n,g}(x, y)$	scalar	the angular flux of group g , at location (x, y) , in direction $\hat{\Omega}_n$

Next, we integrate the discrete ordinates equation (3.24) over the rectangle $S(i, j)$ (see equation (3.6)), which is the rectangle (i, j) , bounded by lines $x = x_{i-1}$, $x = x_i$, $y = y_{j-1}$ and $y = y_j$. We obtain:

$$\begin{aligned}
& \int_{x_{i-1}}^{x_i} \int_{y_{j-1}}^{y_j} \left(\eta_n \frac{\partial \psi_{n,g}(x, y)}{\partial x} + \xi_n \frac{\partial \psi_{n,g}(x, y)}{\partial y} \right) dy dx \\
& + \int_{x_{i-1}}^{x_i} \int_{y_{j-1}}^{y_j} \Sigma_{t,g}(x, y) \psi_{n,g}(x, y) dy dx \\
& = \frac{1}{4\pi} \sum_{g'=1}^G \int_{x_{i-1}}^{x_i} \int_{y_{j-1}}^{y_j} \Sigma_{s,g' \rightarrow g}(x, y) \phi_{g'}(x, y) dy dx \\
& + \frac{\chi_g(x, y)}{4\pi k} \sum_{g'=1}^G \int_{x_{i-1}}^{x_i} \int_{y_{j-1}}^{y_j} \nu \Sigma_{f,g'}(x, y) \phi_{g'}(x, y) dy dx,
\end{aligned}$$

$$1 \leq i \leq I, 1 \leq j \leq J, 1 \leq n \leq M, 1 \leq g \leq G.$$

The integrals of the differential terms are:

$$\begin{aligned}
& \int_{x_{i-1}}^{x_i} \int_{y_{j-1}}^{y_j} \left(\eta_n \frac{\partial \psi_{n,g}(x, y)}{\partial x} + \xi_n \frac{\partial \psi_{n,g}(x, y)}{\partial y} \right) dy dx \\
& = \int_{y_{j-1}}^{y_j} \eta_n (\psi_{n,g}(x_i, y) - \psi_{n,g}(x_{i-1}, y)) dy \\
& + \int_{x_{i-1}}^{x_i} \xi_n (\psi_{n,g}(x, y_j) - \psi_{n,g}(x, y_{j-1})) dx.
\end{aligned}$$

To simplify equation (3.26), some averaged quantities are defined:

$$\psi_{n,g,i,j}^x = \frac{1}{h_j} \int_{y_{j-1}}^{y_j} \psi_{n,g}(x_i, y) dy, \quad (3.26)$$

$$\psi_{n,g,i,j}^y = \frac{1}{w_i} \int_{x_{i-1}}^{x_i} \psi_{n,g}(x, y_j) dx, \quad (3.27)$$

$$\bar{\psi}_{n,g,i,j} = \frac{1}{A_{i,j}} \int_{x_{i-1}}^{x_i} \int_{y_{j-1}}^{y_j} \psi_{n,g}(x, y) dx dy, \quad (3.28)$$

$$\bar{\phi}_{g,i,j} = \frac{1}{A_{i,j}} \int_{x_{i-1}}^{x_i} \int_{y_{j-1}}^{y_j} \phi_g(x, y) dx dy, \quad (3.29)$$

$$\phi_{g,i,j}^x = \frac{1}{h_j} \int_{y_{j-1}}^{y_j} \phi_g(x_i, y) dy, \quad (3.30)$$

$$\phi_{g,i,j}^y = \frac{1}{w_i} \int_{x_{i-1}}^{x_i} \phi_g(x, y_j) dx, \quad (3.31)$$

$$1 \leq i \leq I, 1 \leq j \leq J, 1 \leq n \leq M, 1 \leq g \leq G,$$

where w_i , h_j and $A_{i,j}$ are defined as:

$$w_i = x_i - x_{i-1}, \quad (3.32)$$

$$h_j = y_j - y_{j-1}, \quad (3.33)$$

$$A_{i,j} = w_i h_j, \quad (3.34)$$

and the relationships between the scalar flux and the angular fluxes are:

$$\bar{\phi}_{g,i,j} = \sum_{n=1}^M \bar{\psi}_{n,g,i,j} w_n, \quad (3.35)$$

$$\phi_{g,i,j}^x = \sum_{n=1}^M \psi_{n,g,i,j}^x w_n, \quad (3.36)$$

$$\phi_{g,i,j}^y = \sum_{n=1}^M \psi_{n,g,i,j}^y w_n. \quad (3.37)$$

An illustration of the averaged flux of the rectangle (i, j) and its boundaries is given in Figure 3.5.

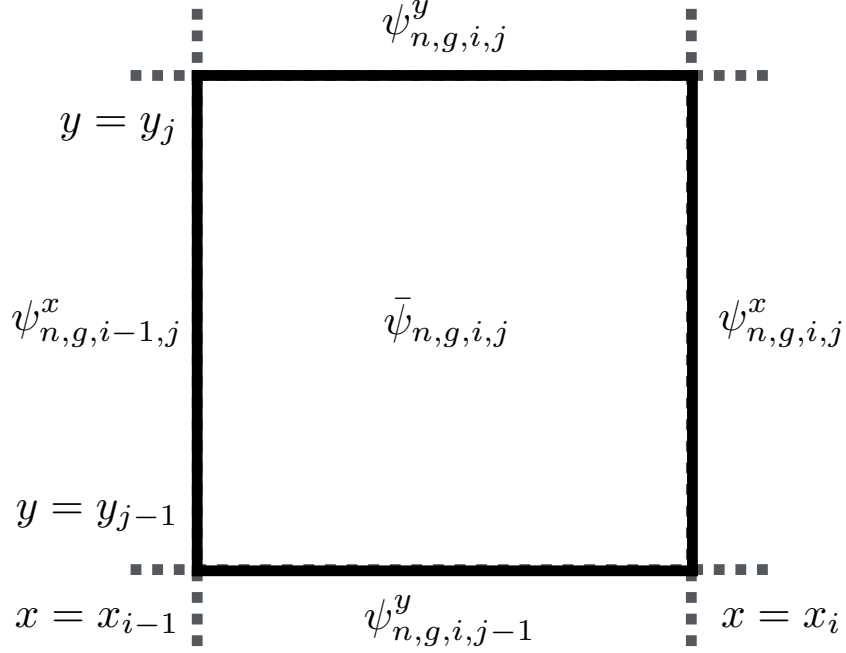


Figure 3.5: The averaged neutron fluxes of the rectangle (i, j) and its four boundaries.

Next, we assume the material inside the rectangle (i, j) to be homogeneous. The spatially-integrated discrete ordinates equation (3.26) then becomes:

$$\begin{aligned} & \eta_n h_j (\psi_{n,g,i,j}^x - \psi_{n,g,i-1,j}^x) + \xi_n w_i (\psi_{n,g,i,j}^y - \psi_{n,g,i,j-1}^y) + \Sigma_{t,g,i,j} A_{i,j} \bar{\psi}_{n,g,i,j} \\ &= \frac{1}{4\pi} \sum_{g'=1}^G \Sigma_{s,g' \rightarrow g,i,j} A_{i,j} \bar{\phi}_{g',i,j} + \frac{\chi_{g,i,j}}{4\pi k} \sum_{g'=1}^G \nu \Sigma_{f,g',i,j} A_{i,j} \bar{\phi}_{g',i,j}, \end{aligned}$$

$$1 \leq i \leq I, 1 \leq j \leq J, 1 \leq n \leq M, 1 \leq g \leq G,$$

where the definitions of additional terms are shown in Table 3.4.

To proceed, we divide equation (3.38) by the area $A_{i,j}$, and recall $A_{i,j} = w_i h_j$, to

Table 3.4: List of definitions of terms in the two-dimensional Cartesian neutron balance equation

TERM	TYPE	EXPLANATION
w_i	scalar	the width of the rectangle (i, j) , i.e. $x_i - x_{i-1}$
h_j	scalar	the height of the rectangle (i, j) , i.e. $y_j - y_{j-1}$
$A_{i,j}$	scalar	the area of the rectangle (i, j)
$\Sigma_{t,g,i,j}$	scalar	the macroscopic total cross section, of the rectangle (i, j) , for group g
$\Sigma_{s,g' \rightarrow g,i,j}$	scalar	the isotropic macroscopic scattering cross section, of the rectangle (i, j) , scattering from group g' to group g
$\chi_{g,i,j}$	scalar	the neutron fission probability into group g , for the rectangle (i, j) (the “ fission spectrum ”)
$\nu \Sigma_{f,g,i,j}$	scalar	the macroscopic neutron yield cross section of the rectangle (i, j) , for group g
$\psi_{n,g,i,j}^x$	scalar	the averaged angular flux for the boundary at $x = x_i$ with $y_{j-1} \leq y \leq y_j$, traveling in direction $\hat{\Omega}_n$, in group g
$\psi_{n,g,i,j}^y$	scalar	the averaged angular flux for the boundary at $y = y_j$ with $x_{i-1} \leq x \leq x_i$, traveling in direction $\hat{\Omega}_n$, in group g
$\bar{\psi}_{n,g,i,j}$	scalar	the averaged angular flux for the rectangle (i, j) , traveling in direction $\hat{\Omega}_n$, in group g
$\bar{\phi}_{g,i,j}$	scalar	the averaged scalar flux for the rectangle (i, j) , for group g
$\phi_{g,i,j}^x$	scalar	the averaged scalar flux for the boundary at $x = x_i$ with $y_{j-1} \leq y \leq y_j$, for group g
$\phi_{g,i,j}^y$	scalar	the averaged scalar flux for the boundary at $y = y_j$ with $x_{i-1} \leq x \leq x_i$, for group g
$\bar{Q}_{s,g,i,j}$	scalar	the averaged scattering source of group g in the rectangle (i, j) , see equation (3.38)
$\bar{Q}_{f,g,i,j}$	scalar	the averaged fission source of group g in the rectangle (i, j) , see equation (3.39)
$Q_{s,g,i,j}^{x,-}$	scalar	the averaged scattering source of group g for the boundary at $x = x_i$ with $y_{j-1} \leq y \leq y_j$, for the rectangle (i, j) , see equation (3.40)
$Q_{s,g,i,j}^{x,+}$	scalar	the averaged scattering source of group g for the boundary at $x = x_i$ with $y_{j-1} \leq y \leq y_j$, for the rectangle $(i + 1, j)$, see equation (3.41)
$Q_{s,g,i,j}^{y,-}$	scalar	the averaged scattering source of group g for the boundary at $y = y_j$ with $x_{i-1} \leq x \leq x_i$, for the rectangle (i, j) , see equation (3.42)
$Q_{s,g,i,j}^{y,+}$	scalar	the averaged scattering source of group g for the boundary at $y = y_j$ with $x_{i-1} \leq x \leq x_i$, for the rectangle $(i, j + 1)$, see equation (3.43)

TERM	TYPE	EXPLANATION
$Q_{f,g,i,j}^{x,-}$	scalar	the averaged fission source of group g for the boundary at $x = x_i$ with $y_{j-1} \leq y \leq y_j$, for the rectangle (i, j) , see equation (3.44)
$Q_{f,g,i,j}^{x,+}$	scalar	the averaged fission source of group g for the boundary at $x = x_i$ with $y_{j-1} \leq y \leq y_j$, for the rectangle $(i + 1, j)$, see equation (3.45)
$Q_{f,g,i,j}^{y,-}$	scalar	the averaged fission source of group g for the boundary at $y = y_j$ with $x_{i-1} \leq x \leq x_i$, for the rectangle (i, j) , see equation (3.46)
$Q_{f,g,i,j}^{y,+}$	scalar	the averaged fission source of group g for the boundary at $y = y_j$ with $x_{i-1} \leq x \leq x_i$, for the rectangle $(i, j + 1)$, see equation (3.47)

obtain:

$$\begin{aligned}
& \eta_n \frac{\psi_{n,g,i,j}^x - \psi_{n,g,i-1,j}^x}{w_i} + \xi_n \frac{\psi_{n,g,i,j}^y - \psi_{n,g,i,j-1}^y}{h_j} + \Sigma_{t,g,i,j} \bar{\psi}_{n,g,i,j} \\
& = \frac{1}{4\pi} \sum_{g'=1}^G \Sigma_{s,g' \rightarrow g,i,j} \bar{\phi}_{g',i,j} + \frac{\chi_{g,i,j}}{4\pi k} \sum_{g'=1}^G \nu \Sigma_{f,g',i,j} \bar{\phi}_{g',i,j},
\end{aligned}$$

$$1 \leq i \leq I, 1 \leq j \leq J, 1 \leq n \leq M, 1 \leq g \leq G.$$

Equation (3.38) describes the “balance” of neutrons inside the rectangle (i, j) , so it is called the “**neutron balance equation**”. Furthermore, we define the following cell-averaged source terms:

$$\bar{Q}_{s,g,i,j} = \frac{1}{4\pi} \sum_{g'=1}^G \Sigma_{s,g' \rightarrow g,i,j} \bar{\phi}_{g',i,j}, \quad (3.38)$$

$$\bar{Q}_{f,g,i,j} = \frac{\chi_{g,i,j}}{4\pi} \sum_{g'=1}^G \nu \Sigma_{f,g',i,j} \bar{\phi}_{g',i,j}, \quad (3.39)$$

and the following boundary-averaged source terms:

$$Q_{s,g,i,j}^{x,-} = \frac{1}{4\pi} \sum_{g'=1}^G \Sigma_{s,g' \rightarrow g,i,j} \phi_{g',i,j}^x, \quad (3.40)$$

$$Q_{s,g,i,j}^{x,+} = \frac{1}{4\pi} \sum_{g'=1}^G \Sigma_{s,g' \rightarrow g,i+1,j} \phi_{g',i,j}^x, \quad (3.41)$$

$$Q_{s,g,i,j}^{y,-} = \frac{1}{4\pi} \sum_{g'=1}^G \Sigma_{s,g' \rightarrow g,i,j} \phi_{g',i,j}^y, \quad (3.42)$$

$$Q_{s,g,i,j}^{y,+} = \frac{1}{4\pi} \sum_{g'=1}^G \Sigma_{s,g' \rightarrow g,i,j+1} \phi_{g',i,j}^y, \quad (3.43)$$

$$Q_{f,g,i,j}^{x,-} = \frac{\chi_{g,i,j}}{4\pi} \sum_{g'=1}^G \nu \Sigma_{f,g',i,j} \phi_{g',i,j}^x, \quad (3.44)$$

$$Q_{f,g,i,j}^{x,+} = \frac{\chi_{g,i,j}}{4\pi} \sum_{g'=1}^G \nu \Sigma_{f,g',i+1,j} \phi_{g',i,j}^x, \quad (3.45)$$

$$Q_{f,g,i,j}^{y,-} = \frac{\chi_{g,i,j}}{4\pi} \sum_{g'=1}^G \nu \Sigma_{f,g',i,j} \phi_{g',i,j}^y, \quad (3.46)$$

$$Q_{f,g,i,j}^{y,+} = \frac{\chi_{g,i,j}}{4\pi} \sum_{g'=1}^G \nu \Sigma_{f,g',i,j+1} \phi_{g',i,j}^y, \quad (3.47)$$

with which the neutron balance equation (3.38) is simplified as:

$$\eta_n \frac{\psi_{n,g,i,j}^x - \psi_{n,g,i-1,j}^x}{w_i} + \xi_n \frac{\psi_{n,g,i,j}^y - \psi_{n,g,i,j-1}^y}{h_j} + \Sigma_{t,g,i,j} \bar{\psi}_{n,g,i,j} = \bar{Q}_{s,g,i,j} + \frac{1}{k} \bar{Q}_{f,g,i,j}$$

$$1 \leq i \leq I, \quad 1 \leq j \leq J, \quad 1 \leq n \leq M, \quad 1 \leq g \leq G. \quad (3.48)$$

3.3 Categorization of Boundaries

Let us consider the rectangle (i, j) and the direction $\hat{\Omega}_n$. Figure 3.5 illustrates the rectangle and its boundaries. The four boundaries of the rectangle can be categorized as either “**incoming**” or “**outgoing**”. A boundary is incoming if the neutron traveling at $\hat{\Omega}_n$ enters the rectangle through the boundary. A boundary is outgoing if the neutron traveling at $\hat{\Omega}_n$ exits the rectangle through the boundary. For a boundary,

the outer normal vector points away from the rectangle. Then the categorization of a boundary depends on the sign of the vector product of its outer normal vector \hat{n} and the direction $\hat{\Omega}$:

$$\text{“Incoming”} : \hat{\Omega} \cdot \hat{n} < 0, \quad (3.49)$$

$$\text{“Outgoing”} : \hat{\Omega} \cdot \hat{n} > 0. \quad (3.50)$$

See Figure 3.6 for an illustration.

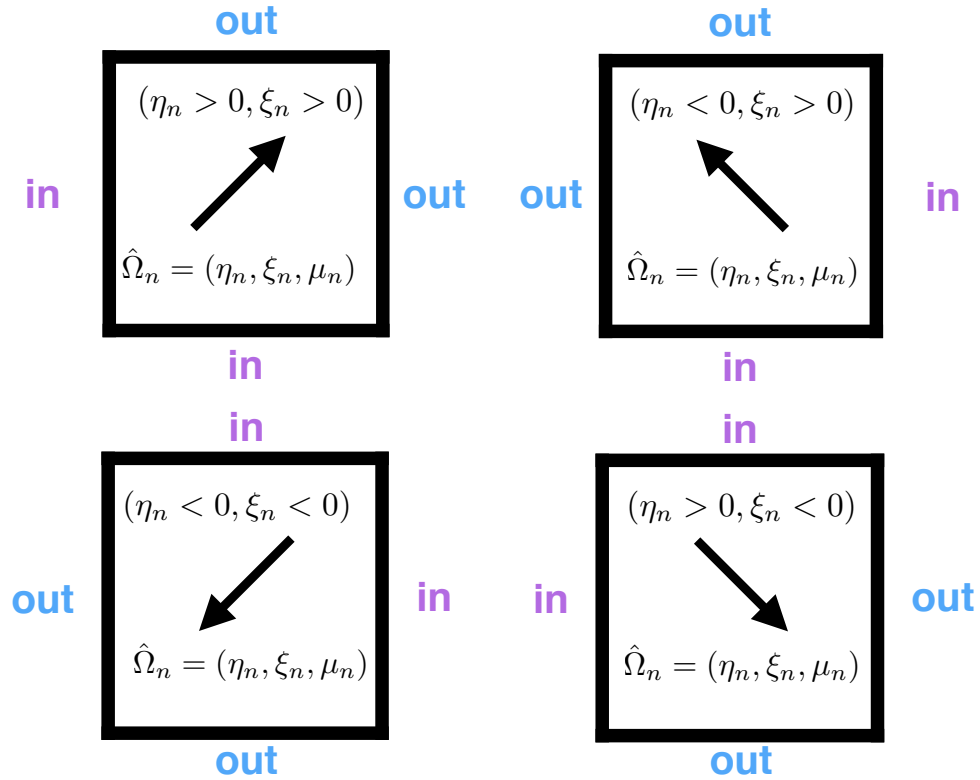


Figure 3.6: For direction $\hat{\Omega}_n$, the averaged boundary flux is incoming if the neutron enters the rectangle through the boundary. It is outgoing if the neutron exits the rectangle through the boundary. The categorization of a boundary as incoming or outgoing depends on the sign of the x and y components of $\hat{\Omega}_n$. The incoming boundaries are marked as “**in**”, and the outgoing boundaries are marked as “**out**”.

Table 3.5: List of the categorization of the boundaries of the rectangle (i, j)

SIGN of η_n	SIGN of ξ_n	CATE- GORY OF $\psi_{n,g,i-1,j}^x$	CATEGORY OF $\psi_{n,g,i,j}^x$	CATE- GORY OF $\psi_{n,g,i,j-1}^y$	CATEGORY OF $\psi_{n,g,i,j}^y$
positive(+)	positive(+)	incoming	outgoing	incoming	outgoing
negative(-)	positive(+)	outgoing	incoming	incoming	outgoing
negative(-)	negative(-)	outgoing	incoming	outgoing	incoming
positive(+)	negative(-)	incoming	outgoing	outgoing	incoming

See Figure 3.6 for an illustration.

From Figure 3.6, the categorization of the boundaries as incoming or outgoing depends on the direction $\hat{\Omega}_n$. There are four possibilities in which the projection of $\hat{\Omega}_n$ onto the $x - y$ plane is in either the first, the second, the third or the fourth quadrant. Detailed categorizations are shown in Table 3.5.

3.4 Auxiliary Equations

For the rectangle (i, j) , there are 5 unknowns in direction $\hat{\Omega}_n$ and group g :

$$\bar{\psi}_{n,g,i,j}, \psi_{n,g,i-1,j}^x, \psi_{n,g,i,j}^x, \psi_{n,g,i,j-1}^y, \psi_{n,g,i,j}^y. \quad (3.51)$$

(See Figure 3.5 for definitions.) From our discussion in the previous subsection 3.3, two of the boundaries in (3.51) are incoming, and the other two are outgoing. With a process called “**sweeping**” discussed later, the fluxes on the incoming boundaries can be considered as known. So the unknowns are $\bar{\psi}_{n,g,i,j}$ and the fluxes on the two outgoing boundaries. The neutron balance equation (3.48) provides one equation relating these unknowns. Because we have three unknowns in total, two more equations, one for each outgoing boundary, are required. These additional equations are called the “**auxiliary equations**”.

In the following subsections, three different methods are introduced, each having different auxiliary equations. The first one is the “**step method**”, which is a

traditional discrete ordinates method to solve the neutron transport equation with Cartesian spatial cells. The other two methods are the “**simplified step characteristic method**” and the “**multiple balance method**”, which are newly introduced in this thesis.

Without loss of generality, we assume that the direction of flight $\hat{\Omega} = (\eta, \xi, \mu)$ has positive x and y components:

$$\hat{\Omega}_n = (\eta_n, \xi_n, \mu_n), \quad \eta_n > 0, \quad \xi_n > 0, \quad (3.52)$$

with which and as given by Table 3.5, the fluxes on the outgoing boundaries are $\psi_{n,g,i,j}^x, \psi_{n,g,i,j}^y$. Therefore the unknowns are:

$$\mathbf{Unknowns} : \bar{\psi}_{n,g,i,j}, \psi_{n,g,i,j}^x, \psi_{n,g,i,j}^y, \quad (3.53)$$

and the knowns are:

$$\mathbf{Knowns} : \psi_{n,g,i-1,j}^x, \psi_{n,g,i,j-1}^y. \quad (3.54)$$

In addition to the balance equation (3.48), two more “**auxiliary equations**” in the form of:

$$g(\bar{\psi}_{n,g,i,j}, \psi_{n,g,i,j}^x, \psi_{n,g,i,j}^y) = 0 \quad (3.55)$$

are required.

3.4.1 The Step Method (STEP)

The “**step method**” is the probably simplest traditional discrete ordinates method (Lathrop, 1969). In this method, the auxiliary equations assume that the outgoing fluxes equal the area-averaged flux. So the two auxiliary equations in the form of

equation (3.55) are:

$$\eta_n > 0 \ \& \ \xi_n > 0 :$$

$$\psi_{n,g,i,j}^x = \bar{\psi}_{n,g,i,j}, \tag{3.56}$$

$$\psi_{n,g,i,j}^y = \bar{\psi}_{n,g,i,j}. \tag{3.57}$$

Figure 3.7 visualizes these equation.

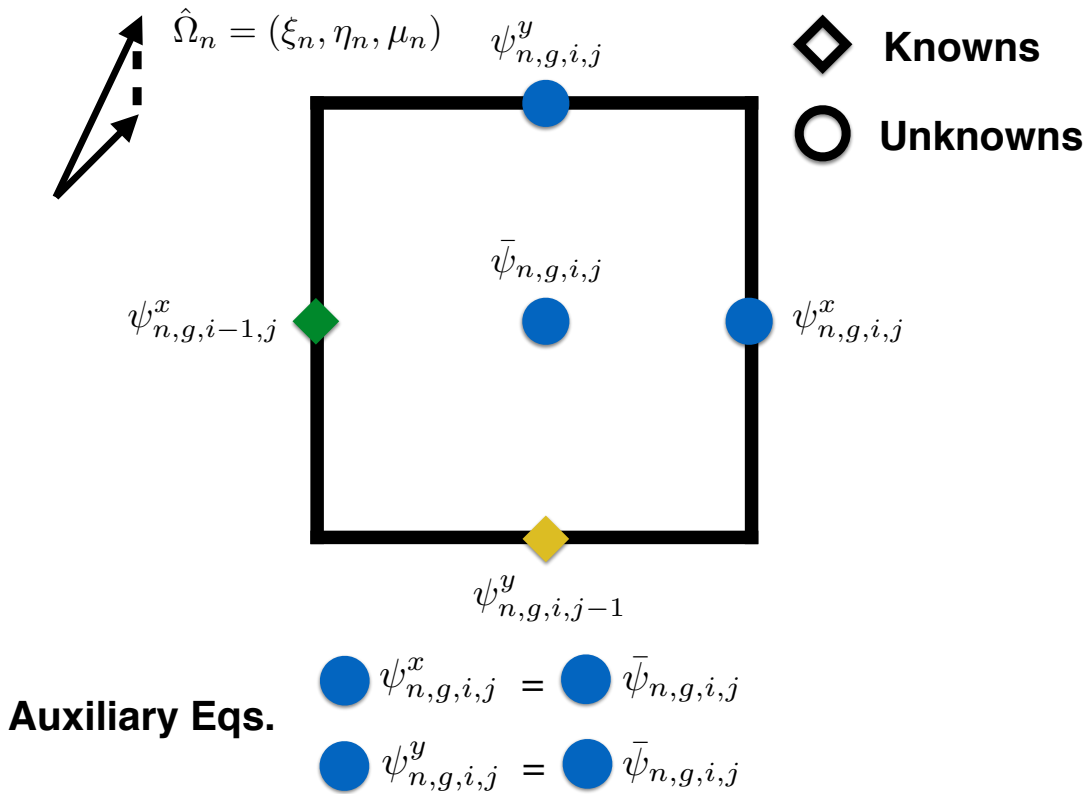


Figure 3.7: Visualization of the auxiliary equations for the step method. The direction of flight is assumed with positive x and y components. Quantities that are equal are marked with the same colors. Quantities that are different are marked with the different colors.

As is shown in the figure, the direction of flight assumes that $\hat{\Omega} = (\eta, \xi, \mu)$ has

positive x and y components. The auxiliary equation for other cases are:

$$\eta_n < 0 \ \& \ \xi_n > 0 :$$

$$\psi_{n,g,i-1,j}^x = \bar{\psi}_{n,g,i,j}, \quad (3.58)$$

$$\psi_{n,g,i,j}^y = \bar{\psi}_{n,g,i,j}, \quad (3.59)$$

and

$$\eta_n < 0 \ \& \ \xi_n < 0 :$$

$$\psi_{n,g,i-1,j}^x = \bar{\psi}_{n,g,i,j}, \quad (3.60)$$

$$\psi_{n,g,i,j-1}^y = \bar{\psi}_{n,g,i,j}, \quad (3.61)$$

and

$$\eta_n > 0 \ \& \ \xi_n < 0 :$$

$$\psi_{n,g,i,j}^x = \bar{\psi}_{n,g,i,j}, \quad (3.62)$$

$$\psi_{n,g,i,j-1}^y = \bar{\psi}_{n,g,i,j}. \quad (3.63)$$

3.4.2 The Simplified Step Characteristic Method (SSC)

Even though neutron transport is in two dimensions, it can be approximated as transporting on characteristic lines (projected in 2-D plane) along 1-D directions of flight. The length of the characteristic line can be approximated as s , which is defined as:

$$d = h_j |\eta_n| + w_i |\xi_n|, \quad (3.64)$$

$$s = \frac{w_i h_j}{d}, \quad (3.65)$$

where

$$w_i = x_i - x_{i-1}, \quad (3.66)$$

$$h_j = y_j - y_{j-1}. \quad (3.67)$$

In these formula, a box with length s and width d has been placed with the side of the length parallel to the direction of flight. See Figure 3.8 for an illustration of this box, as marked as the green area.

The height d as defined in equation (3.64) is the shadow of the rectangle (i, j) onto a line that is perpendicular to the direction of flight. The length s is chosen so that the area of the box, i.e. $s d$, equals the area of the rectangle (i, j) :

$$s d = w_i h_j. \quad (3.68)$$

The approximate one-dimensional transport equation is:

$$\mu_n \frac{d\psi_{1d}(t)}{dt} + \Sigma_t \psi_{1d}(t) = \bar{Q}, \quad 0 \leq t \leq s, \quad (3.69)$$

where the transport cross section and the source terms are defined as:

$$\Sigma_t = \Sigma_{t,g,i,j}, \quad (3.70)$$

$$\bar{Q} = \bar{Q}_{s,g,i,j} + \frac{1}{k} \bar{Q}_{f,g,i,j}. \quad (3.71)$$

The solution of this one-dimensional transport equation (3.69) is:

$$\psi_{1d}(t) = \frac{\bar{Q}}{\Sigma_t} (1 - e^{-\Sigma_t t / \mu_n}) + \psi_{1d}(0), \quad 0 \leq t \leq s, \quad (3.72)$$

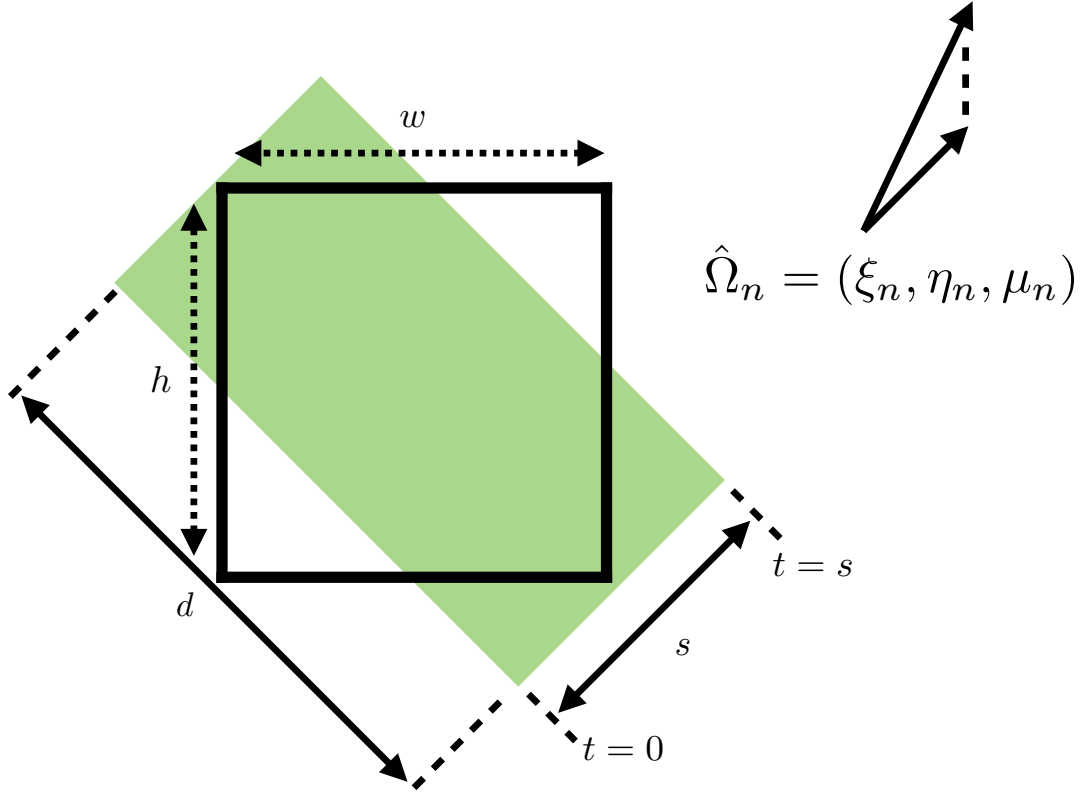


Figure 3.8: In the simplified step characteristic method, the two-dimensional transport is approximated by a one-dimensional transport process along the t axis from $t = 0$ to $t = s$. s and d are the length and the width of the box marked in green. One side of the box is parallel to the direction of flight. The width d is the shallow of the rectangle (i, j) projected to a line perpendicular to the direction of flight. The green box and the rectangle (i, j) have the same area. These requirements determine the width and length of the green box.

and the evaluation of the flux at the end $t = s$ is:

$$\psi_{1d}(s) = \frac{\bar{Q}}{\Sigma_t} (1 - e^{-\Sigma_t s / \mu_n}) + \psi_{1d}(0), \quad (3.73)$$

where $\psi_{1d}(0)$ is chosen to be an average of the incoming flux:

$$\psi_{1d}(0) = \frac{h_j |\eta_n| \psi_{n,g,i-1,j}^x + w_i |\xi_n| \psi_{n,g,i,j-1}^y}{h_j |\eta_n| + w_i |\xi_n|}, \quad (3.74)$$

which is defined even though it is not used in derivation of auxiliary equations. The averaged flux on this one-dimensional line is:

$$\bar{\psi}_{1d} = \frac{1}{s} \int_0^s \psi_{1d}(t) dt \quad (3.75)$$

$$= \frac{\bar{Q}}{\Sigma_t} \left(1 - \frac{1 - e^{-\Sigma_t s / \mu_n}}{\Sigma_t s / \mu_n} \right) + \psi_{1d}(0) \frac{1 - e^{-\Sigma_t s / \mu_n}}{\Sigma_t s / \mu_n}. \quad (3.76)$$

Eliminating $\psi_{1d}(0)$ in equations (3.73) and (3.76), we get:

$$\psi_{1d}(s) = \frac{\bar{Q}}{\Sigma_t} \left(1 - \frac{(\Sigma_t s / \mu_n) e^{-\Sigma_t s / \mu_n}}{1 - e^{-\Sigma_t s / \mu_n}} \right) + \bar{\psi}_{1d} \frac{(\Sigma_t s / \mu_n) e^{-\Sigma_t s / \mu_n}}{1 - e^{-\Sigma_t s / \mu_n}}. \quad (3.77)$$

We assume that the outgoing fluxes equal the one-dimensional flux at the end point, and that the area-averaged flux $\bar{\psi}_{n,g,i,j}$ equals the averaged flux of the one-dimensional transport:

$$\psi_{n,g,i,j}^x = \psi_{n,g,i,j}^y = \psi_{1d}(s), \quad (3.78)$$

$$\bar{\psi}_{n,g,i,j} = \bar{\psi}_{1d}. \quad (3.79)$$

Figure 3.9 illustrates the auxiliary equations derived from the one-dimensional transport. Next, we define the distance l to simplify the equations:

$$l = s / \mu_n. \quad (3.80)$$

We introduce equations (3.78) and (3.79) into equation (3.77) to get:

$$\psi_{n,g,i,j}^x = \psi_{n,g,i,j}^y = \frac{\bar{Q}}{\Sigma_t} \left(1 - \frac{(\Sigma_t l) e^{-\Sigma_t l}}{1 - e^{-\Sigma_t l}} \right) + \bar{\psi}_{n,g,i,j} \frac{(\Sigma_t l) e^{-\Sigma_t l}}{1 - e^{-\Sigma_t l}}. \quad (3.81)$$

The auxiliary equations (3.81) above apply for the case that the x and y components of the direction of flight $\hat{\Omega}_n$ are positive. The auxiliary equations for other

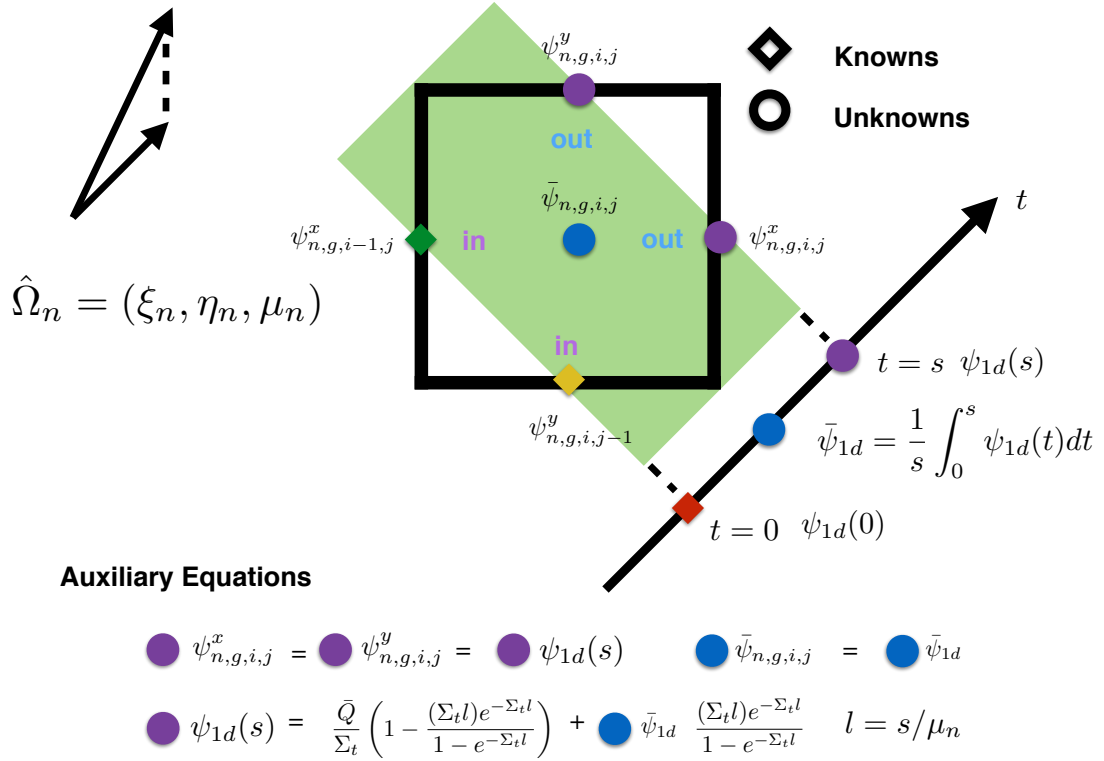


Figure 3.9: Visualization of the auxiliary equations for the simplified step characteristic method. The direction of flight is assumed with positive x and y components.

cases are:

$$\eta_n < 0 \ \& \ \xi_n > 0 :$$

$$\psi_{n,g,i-1,j}^x = \psi_{n,g,i,j}^y = \frac{\bar{Q}}{\Sigma_t} \left(1 - \frac{(\Sigma_t l) e^{-\Sigma_t l}}{1 - e^{-\Sigma_t l}} \right) + \bar{\psi}_{n,g,i,j} \frac{(\Sigma_t l) e^{-\Sigma_t l}}{1 - e^{-\Sigma_t l}}, \quad (3.82)$$

$$\eta_n < 0 \ \& \ \xi_n < 0 :$$

$$\psi_{n,g,i-1,j}^x = \psi_{n,g,i,j-1}^y = \frac{\bar{Q}}{\Sigma_t} \left(1 - \frac{(\Sigma_t l) e^{-\Sigma_t l}}{1 - e^{-\Sigma_t l}} \right) + \bar{\psi}_{n,g,i,j} \frac{(\Sigma_t l) e^{-\Sigma_t l}}{1 - e^{-\Sigma_t l}}, \quad (3.83)$$

$$\eta_n > 0 \ \& \ \xi_n < 0 :$$

$$\psi_{n,g,i,j}^x = \psi_{n,g,i,j-1}^y = \frac{\bar{Q}}{\Sigma_t} \left(1 - \frac{(\Sigma_t l) e^{-\Sigma_t l}}{1 - e^{-\Sigma_t l}} \right) + \bar{\psi}_{n,g,i,j} \frac{(\Sigma_t l) e^{-\Sigma_t l}}{1 - e^{-\Sigma_t l}}. \quad (3.84)$$

Our simulations show that the simplified step characteristic (SSC) method is more accurate than the step method. Moreover, the SSC method has the advantage that solutions from auxiliary equations are always positive.

3.4.3 The Multiple Balance Method (MB)

The auxiliary equations in the step, and the simplified characteristic methods contain no neutron physics. So it is more favorable if the auxiliary equations are similar to the neutron balance equation. Here we generalize the 1-D multiple balance method, introduced in section 2.3.3, to two-dimensional problems a Cartesian grid.

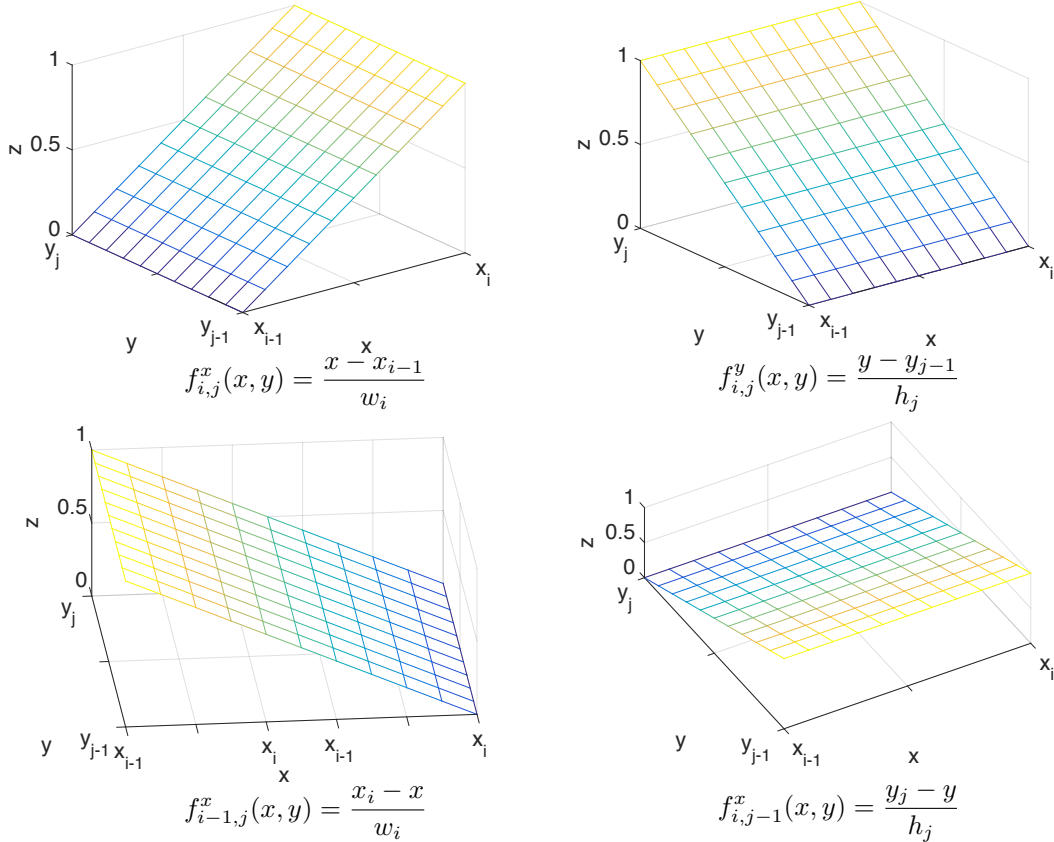


Figure 3.10: The weight functions of the four boundaries of the rectangle (i, j) . The weight function of a boundary is 1 on the boundary.

Consider the rectangle (i, j) . To derive the auxiliary equations, a weight function is defined for each boundary. The weight functions are linear and equal to 1 on a certain boundary and equal to 0 on the opposite boundary:

$$f_{i,j}^x(x, y) = \frac{x - x_{i-1}}{w_i}, \quad (3.85)$$

$$f_{i,j}^y(x, y) = \frac{y - y_{j-1}}{h_j}, \quad (3.86)$$

$$f_{i-1,j}^x(x, y) = \frac{x_i - x}{w_i}, \quad (3.87)$$

$$f_{i,j-1}^y(x, y) = \frac{y_j - y}{h_j}. \quad (3.88)$$

The auxiliary equations are obtained by integrating the discrete ordinates equation (3.24) with the weight function for the outgoing boundaries. (For any angle $\hat{\Omega}_n$, see Table 3.5 to see which boundary is outgoing.) This integration resembles the finite element method. But in the multiple balance method, the flux in each rectangular cell is not assumed to have a predefined shape.

The neutron balance equation can be thought of as: the leakage term plus the collision term equals the scattering source plus the fission source:

$$\begin{array}{ccccccc} \text{Leakage} & + & \text{Collision} & = & \text{Scattering} & + & \text{Fission} \\ \hat{\Omega} \cdot \int_f \vec{\nabla} \psi_g(\vec{x}) d\vec{x} + \int_f \Sigma_t \psi_g(\vec{x}) d\vec{x} & = & \frac{1}{4\pi} \sum_{g'} \int_f \Sigma_s \phi_{g'}(\vec{x}) d\vec{x} + \frac{\chi_g}{4\pi k} \sum_{g'} \int_f \nu \Sigma_f \phi_{g'}(\vec{x}) d\vec{x}. \end{array}$$

For the auxiliary equation of the multiple balance method, the discrete ordinates equation is multiplied by the weight function $f_d(\vec{x})$ for an outgoing boundary d , and integrating over the cell:

$$\begin{array}{ccccccc} \text{Leakage} & + & \text{Collision} & = & \text{Scattering} & + & \text{Fission} \\ \hat{\Omega} \cdot \int_f f_d(\vec{x}) \vec{\nabla} \psi_g(\vec{x}) d\vec{x} + \int_f f_d(\vec{x}) \Sigma_t \psi_g(\vec{x}) d\vec{x} & = & \frac{1}{4\pi} \sum_{g'} \int_f f_d(\vec{x}) \Sigma_s \phi_{g'}(\vec{x}) d\vec{x} + \frac{\chi_g}{4\pi k} \sum_{g'} \int_f f_d(\vec{x}) \nu \Sigma_f \phi_{g'}(\vec{x}) d\vec{x}. \end{array}$$

By the divergence theorem, we have exactly:

$$\int_f f_d(\vec{x}) \vec{\nabla} \psi_g(\vec{x}) d\vec{x} = \sum_{c \in \partial f} \oint_c f_d(\vec{x}) \psi(\vec{x}) \hat{n}(\vec{x}) ds - \int_f [\vec{\nabla} f_d(\vec{x})] \psi(\vec{x}) d\vec{x}, \quad (3.89)$$

where the flux in boundary integral terms are approximated by the boundary-averaged value, and the flux in the volume integral terms is approximated by the cell-averaged value:

$$\oint_c f_d(\vec{x}) \psi(\vec{x}) \hat{n}(\vec{x}) ds \approx \oint_c f_d(\vec{x}) \psi_c \hat{n}(\vec{x}) ds, \quad (3.90)$$

$$\int_f [\vec{\nabla} f_d(\vec{x})] \psi(\vec{x}) d\vec{x} \approx \int_f [\vec{\nabla} f_d(\vec{x})] \bar{\psi} d\vec{x}. \quad (3.91)$$

The multiple balance approximation sets the fluxes in the ‘‘collision’’, ‘‘scattering’’ and ‘‘fission’’ terms to be the outgoing flux:

Approximations for Auxiliary Equation for the Boundary d :

Leakage	Collision	Scattering	Fission
$\int_f f_d \vec{\nabla} \psi(\vec{x}) d\vec{x} \approx \sum_{c \in \partial f} \oint_c f_d \psi_c \hat{n} ds - \int_f [\vec{\nabla} f_d] \bar{\psi} d\vec{x}$	$\psi(\vec{x}) \approx \psi_d$	$\phi(\vec{x}) \approx \phi_d$	$\phi(\vec{x}) \approx \phi_d$

Without loss of generality, we derive the auxiliary equations for the case with positive η_n and positive ξ_n . The weight functions corresponding to the outgoing boundaries are $f_{i,j}^x(x, y)$ and $f_{i,j}^y(x, y)$. We multiply the differential discrete ordinates equation

(3.24) with $f_{i,j}^x(x, y)$, and integrate over the rectangular cell, obtaining:

$$\begin{aligned}
\text{Leakage:} & \int_{x_{i-1}}^{x_i} \int_{y_{j-1}}^{y_j} \frac{x - x_{i-1}}{w_i} \left(\eta_n \frac{\partial \psi_{n,g}(x, y)}{\partial x} + \xi_n \frac{\partial \psi_{n,g}(x, y)}{\partial y} \right) dy dx \\
\text{Collision:} & + \int_{x_{i-1}}^{x_i} \int_{y_{j-1}}^{y_j} \frac{x - x_{i-1}}{w_i} \Sigma_{t,g}(x, y) \psi_{n,g}(x, y) dy dx \\
\text{Scattering:} & = \frac{1}{4\pi} \sum_{g'=1}^G \int_{x_{i-1}}^{x_i} \int_{y_{j-1}}^{y_j} \frac{x - x_{i-1}}{w_i} \Sigma_{s,g' \rightarrow g}(x, y) \phi_{g'}(x, y) dy dx \\
\text{Fission:} & + \frac{\chi_g(x, y)}{4\pi k} \sum_{g'=1}^G \int_{x_{i-1}}^{x_i} \int_{y_{j-1}}^{y_j} \frac{x - x_{i-1}}{w_i} \nu \Sigma_{f,g'}(x, y) \phi_{g'}(x, y) dy dx, \\
& 1 \leq i \leq I, 1 \leq j \leq J, 1 \leq n \leq M, 1 \leq g \leq G. \tag{3.92}
\end{aligned}$$

To obtain an equation depending only on $\bar{\psi}_{n,g,i,j}$, $\psi_{n,g,i,j}^x$, $\psi_{n,g,i,j}^y$ (see equation (3.55) for the form of the auxiliary equations), careful approximations are applied to equation (3.92) according to the discussions above. The first approximation is applied to the leakage term, where the flux on each cell boundary is assumed to be constant:

$$\begin{aligned}
\text{Leakage:} & \int_{x_{i-1}}^{x_i} \int_{y_{j-1}}^{y_j} \frac{x - x_{i-1}}{w_i} \left(\eta_n \frac{\partial \psi_{n,g}(x, y)}{\partial x} + \xi_n \frac{\partial \psi_{n,g}(x, y)}{\partial y} \right) dy dx \\
& = \eta_n \int_{y_{j-1}}^{y_j} \psi_{n,g}(x_i, y) dy - \frac{1}{w_i} \eta_n \int_{x_{i-1}}^{x_i} \int_{y_{j-1}}^{y_j} \psi_{n,g}(x, y) dy dx \\
& + \xi_n \int_{x_{i-1}}^{x_i} \frac{x - x_{i-1}}{w_i} (\psi_{n,g}(x, y_j) - \psi_{n,g}(x, y_{j-1})) dx \\
& \approx \eta_n h_j \psi_{n,g,i,j}^x - \eta_n h_j \bar{\psi}_{n,g,i,j} + \xi_n \int_{x_{i-1}}^{x_i} \frac{x - x_{i-1}}{w_i} (\psi_{n,g,i,j}^y - \psi_{n,g,i,j-1}^y) dx \\
& = \eta_n h_j \psi_{n,g,i,j}^x - \eta_n h_j \bar{\psi}_{n,g,i,j} + \frac{1}{2} \xi_n w_i \psi_{n,g,i,j}^y - \frac{1}{2} \xi_n w_i \psi_{n,g,i,j-1}^y. \tag{3.93}
\end{aligned}$$

(see equation (3.29) for definitions of averaged scalar flux terms.) The second ap-

proximation is applied to the collision term, where the flux inside the cell is assumed to be a constant and equal to the outgoing flux:

$$\begin{aligned}
\text{Collision:} \quad & \int_{x_{i-1}}^{x_i} \int_{y_{j-1}}^{y_j} \frac{x - x_{i-1}}{w_i} \Sigma_{t,g}(x, y) \psi_{n,g}(x, y) dy dx \\
& \approx \int_{x_{i-1}}^{x_i} \int_{y_{j-1}}^{y_j} \frac{x - x_{i-1}}{w_i} \Sigma_{t,g,i,j} \psi_{n,g,i,j}^x dy dx \\
& = \frac{1}{2} w_i h_j \Sigma_{t,g,i,j} \psi_{n,g,i,j}^x.
\end{aligned} \tag{3.94}$$

The approximation in equation (3.94) might seem strange, since when integrating over a cell, it is more natural to assume the flux to be a constant and equal to the cell-averaged flux. However in the multiple balance equation, each term in the auxiliary equation is meant to resemble the balance equation, “centered” on the boundary of a cell. Therefore, the approximation in equation (3.94) assumes that the flux inside the cell is taken to be equal to the outgoing flux. This approximation is applied to the scattering and fission term as well.

$$\begin{aligned}
\text{Scattering:} \quad & \int_{x_{i-1}}^{x_i} \int_{y_{j-1}}^{y_j} \frac{x - x_{i-1}}{w_i} \Sigma_{s,g' \rightarrow g}(x, y) \phi_{g'}(x, y) dy dx \\
& \approx \int_{x_{i-1}}^{x_i} \int_{y_{j-1}}^{y_j} \frac{x - x_{i-1}}{w_i} \Sigma_{s,g' \rightarrow g,i,j} \phi_{g',i,j}^x dy dx \\
& = \frac{1}{2} w_i h_j \Sigma_{s,g' \rightarrow g,i,j} \phi_{g',i,j}^x,
\end{aligned} \tag{3.95}$$

$$\begin{aligned}
\text{Fission:} \quad & \int_{x_{i-1}}^{x_i} \int_{y_{j-1}}^{y_j} \frac{x - x_{i-1}}{w_i} \nu \Sigma_{f,g'}(x, y) \phi_{g'}(x, y) dy dx \\
& \approx \int_{x_{i-1}}^{x_i} \int_{y_{j-1}}^{y_j} \frac{x - x_{i-1}}{w_i} \nu \Sigma_{f,g',i,j} \phi_{g',i,j}^x dy dx \\
& = \frac{1}{2} w_i h_j \nu \Sigma_{f,g',i,j} \phi_{g',i,j}^x.
\end{aligned} \tag{3.96}$$

(see equation (3.29) for definitions of averaged scalar flux terms.) Introducing the four approximations (3.93), (3.94), (3.95) and (3.96) into equation (3.92), we get:

$$\begin{aligned} & \eta_n h_j \psi_{n,g,i,j}^x - \eta_n h_j \bar{\psi}_{n,g,i,j} + \frac{1}{2} \xi_n w_i \psi_{n,g,i,j}^y - \frac{1}{2} \xi_n w_i \psi_{n,g,i,j-1}^y + \frac{1}{2} w_i h_j \Sigma_{t,g,i,j} \psi_{n,g,i,j}^x \\ &= \frac{1}{4\pi} \sum_{g'=1}^G \frac{1}{2} w_i h_j \Sigma_{s,g' \rightarrow g,i,j} \phi_{g',i,j}^x + \frac{\chi_{g,i,j}}{4\pi k} \sum_{g'=1}^G \frac{1}{2} w_i h_j \nu \Sigma_{f,g',i,j} \phi_{g',i,j}^x. \end{aligned}$$

We recall the definition of the source terms from equations (3.40) and (3.39). The equation (3.97) then reduces to:

$$\begin{aligned} & \eta_n h_j \psi_{n,g,i,j}^x - \eta_n h_j \bar{\psi}_{n,g,i,j} + \frac{1}{2} \xi_n w_i \psi_{n,g,i,j}^y - \frac{1}{2} \xi_n w_i \psi_{n,g,i,j-1}^y + \frac{1}{2} w_i h_j \Sigma_{t,g,i,j} \psi_{n,g,i,j}^x \\ &= \frac{1}{2} w_i h_j Q_{s,g,i,j}^{x,-} + \frac{1}{2} w_i h_j Q_{f,g,i,j}^{x,-}. \end{aligned}$$

We divide equation (3.97) by the term $\frac{1}{2} w_i h_j$ to obtain the desired auxiliary equation for the right boundary $x = x_i$:

$$\eta_n \frac{\psi_{n,g,i,j}^x - \bar{\psi}_{n,g,i,j}}{w_i/2} + \xi_n \frac{\psi_{n,g,i,j}^y - \psi_{n,g,i,j-1}^y}{h_j} + \Sigma_{t,g,i,j} \psi_{n,g,i,j}^x = Q_{s,g,i,j}^{x,-} + \frac{1}{k} Q_{f,g,i,j}^{x,-}. \quad (3.97)$$

If we integrate the differential discrete ordinates equation (3.24) with $f_{i,j}^y(x, y)$, and follow the process as described above, the resultant equation is the desired auxiliary equation for the top boundary $y = y_j$:

$$\xi_n \frac{\psi_{n,g,i,j}^y - \bar{\psi}_{n,g,i,j}}{h_j/2} + \eta_n \frac{\psi_{n,g,i,j}^x - \psi_{n,g,i-1,j}^x}{w_i} + \Sigma_{t,g,i,j} \psi_{n,g,i,j}^y = Q_{s,g,i,j}^{y,-} + \frac{1}{k} Q_{f,g,i,j}^{y,-}, \quad (3.98)$$

where we refer to equation (3.42) and equation (3.39) for the definition of the source terms. We recall the neutron balance equation (3.48):

$$\eta_n \frac{\psi_{n,g,i,j}^x - \psi_{n,g,i-1,j}^x}{w_i} + \xi_n \frac{\psi_{n,g,i,j}^y - \psi_{n,g,i,j-1}^y}{h_j} + \Sigma_{t,g,i,j} \bar{\psi}_{n,g,i,j} = \bar{Q}_{s,g,i,j} + \frac{1}{k} \bar{Q}_{f,g,i,j},$$

which is similar to the auxiliary equations (3.97) and (3.98). So the method is named as the “**multiple balance method**”. These auxiliary equations are visualized in Figure 3.11. Now for each cell and direction of flight, the number of unknowns, which is 3, equals the number of available equations, which consists of the balance equation and 2 auxiliary equations.

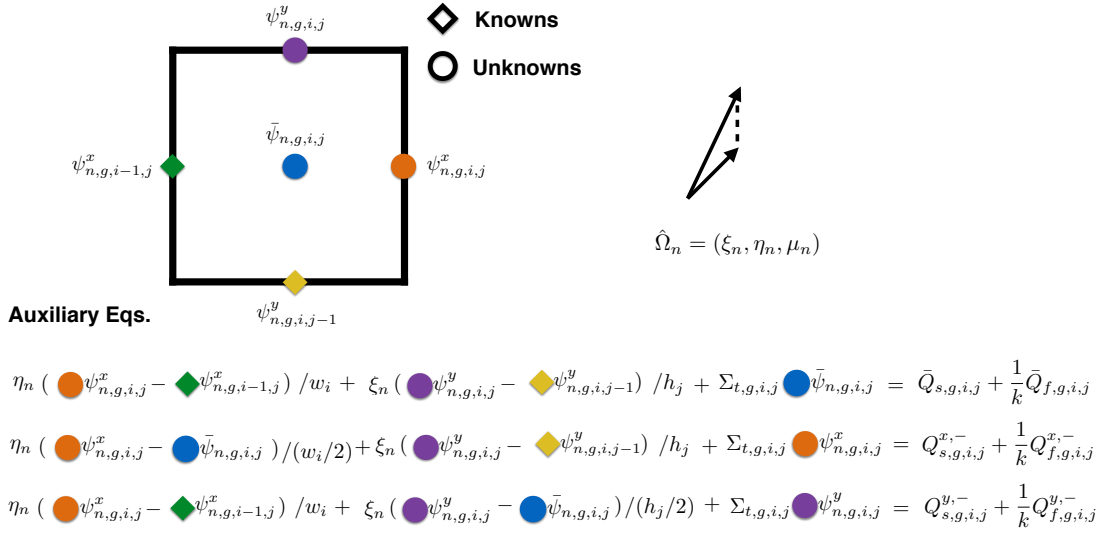


Figure 3.11: Visualization of the balance equation and auxiliary equations for the multiple balance method. The direction of flight is assumed with positive x and y components. Quantities that are the same are marked with the same colors. Quantities that are different are marked with the different colors.

The auxiliary equations (3.97) and (3.98) above are valid for the case that the x

and y components are positive. The auxiliary equations for other cases are:

$\eta_n < 0$ & $\xi_n > 0$:

$$\eta_n \frac{\psi_{n,g,i-1,j}^x - \bar{\psi}_{n,g,i,j}}{w_i/2} + \xi_n \frac{\psi_{n,g,i,j}^y - \psi_{n,g,i,j-1}^y}{h_j} + \Sigma_{t,g,i,j} \psi_{n,g,i-1,j}^x = Q_{s,g,i-1,j}^{x,+} + \frac{1}{k} Q_{f,g,i-1,j}^{x,+}, \quad (3.99)$$

$$\xi_n \frac{\psi_{n,g,i,j}^y - \bar{\psi}_{n,g,i,j}}{h_j/2} + \eta_n \frac{\psi_{n,g,i,j}^x - \psi_{n,g,i-1,j}^x}{w_i} + \Sigma_{t,g,i,j} \psi_{n,g,i,j}^y = Q_{s,g,i,j}^{y,-} + \frac{1}{k} Q_{f,g,i,j}^{y,-}, \quad (3.100)$$

and

$\eta_n < 0$ & $\xi_n < 0$:

$$\eta_n \frac{\psi_{n,g,i-1,j}^x - \bar{\psi}_{n,g,i,j}}{w_i/2} + \xi_n \frac{\psi_{n,g,i,j}^y - \psi_{n,g,i,j-1}^y}{h_j} + \Sigma_{t,g,i,j} \psi_{n,g,i-1,j}^x = Q_{s,g,i-1,j}^{x,+} + \frac{1}{k} Q_{f,g,i-1,j}^{x,+}, \quad (3.101)$$

$$\xi_n \frac{\psi_{n,g,i,j-1}^y - \bar{\psi}_{n,g,i,j}}{h_j/2} + \eta_n \frac{\psi_{n,g,i,j}^x - \psi_{n,g,i-1,j}^x}{w_i} + \Sigma_{t,g,i,j} \psi_{n,g,i,j-1}^y = Q_{s,g,i,j-1}^{y,+} + \frac{1}{k} Q_{f,g,i,j-1}^{y,+}, \quad (3.102)$$

and

$\eta_n > 0$ & $\xi_n < 0$:

$$\eta_n \frac{\psi_{n,g,i,j}^x - \bar{\psi}_{n,g,i,j}}{w_i/2} + \xi_n \frac{\psi_{n,g,i,j}^y - \psi_{n,g,i,j-1}^y}{h_j} + \Sigma_{t,g,i,j} \psi_{n,g,i,j}^x = Q_{s,g,i,j}^{x,-} + \frac{1}{k} Q_{f,g,i,j}^{x,-}, \quad (3.103)$$

$$\xi_n \frac{\psi_{n,g,i,j-1}^y - \bar{\psi}_{n,g,i,j}}{h_j/2} + \eta_n \frac{\psi_{n,g,i,j}^x - \psi_{n,g,i-1,j}^x}{w_i} + \Sigma_{t,g,i,j} \psi_{n,g,i,j-1}^y = Q_{s,g,i,j-1}^{y,+} + \frac{1}{k} Q_{f,g,i,j-1}^{y,+}. \quad (3.104)$$

3.5 Sweep

The previous sections introduce how to solve for the unknown cell-averaged and boundary fluxes for a single rectangle. We recall Figure 3.2 that the geometry is

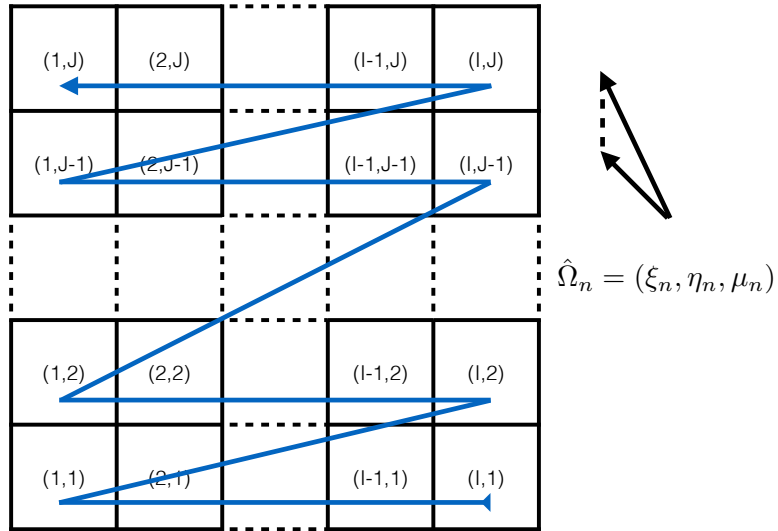


Figure 3.13: The sweep order of the Cartesian spatial grid for the direction with negative x component and positive y component . The order begins with the rectangle with coordinate $(I, 1)$, and then sweeps row by row to the rectangle with coordinate $(1, J)$.

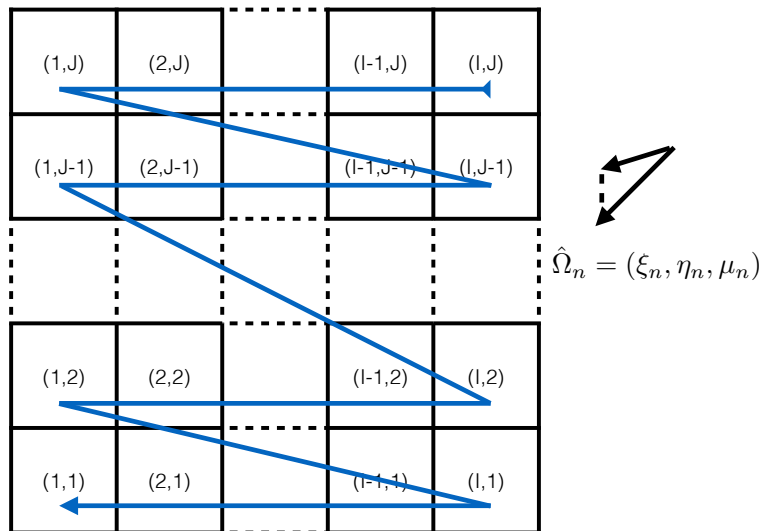


Figure 3.14: The sweep order of the Cartesian spatial grid for the direction with negative x component and negative y component . The order begins with the rectangle with coordinate (I, J) , and then sweeps row by row to the rectangle with coordinate $(1, 1)$.

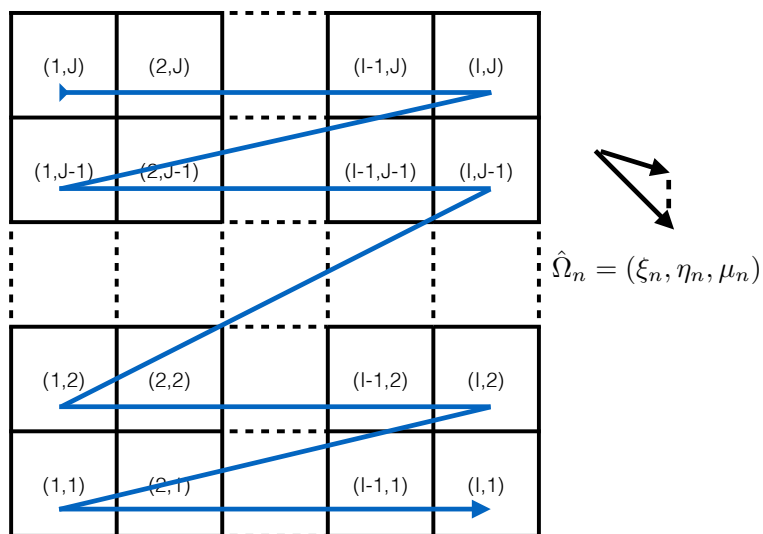


Figure 3.15: The sweep order of the Cartesian spatial grid for the direction with positive x component and negative y component . The order begins with the rectangle with coordinate $(1, J)$, and then sweeps row by row to the rectangle with coordinate $(I, 1)$.

CHAPTER IV

Numerical Results for Two-Dimensional Problems with Cartesian Spatial Grids

The performance of the discrete ordinates (SN) methods on 2-D Cartesian spatial grids are studied in this chapter. For simplicity, the names of methods are abbreviated in Table 4.1. Since MC solutions have no truncation errors in space and angle, these solutions serve as the reference. We simulate a very large number of particles to minimize the statistical errors. The two problems discussed were published in 1982. They were good benchmarks for 2-D Cartesian grid computer codes developed at that time (*Li et al.*, 2013).

Table 4.1: List of numerical methods' abbreviations and their definitions

METHOD	DESCRIPTION
“MC”	Monte Carlo
“MOC $A_m P_n D_d$ ”	Method of characteristics with m azimuthal angles in a quadrant, n polar angles in an octant, and a ray spacing of d cm.
“ <i>string</i> Sn”	SN method with the level of angles equals n , with method <i>string</i> . “STEP” stands for the step method. “SSC” stands for the simplified step characteristic method. “MB” stands for the multiple balance method.

4.1 BWR Assembly Problem

First we consider a boiling water reactor (BWR) assembly problem, which contains 4x4 fuel pins in the center, enclosed by light water. The materials have two energy groups, where the fission spectrum is 1.0 in the first group and 0.0 in the second group. The four outer boundaries are reflecting. Figure 4.1 illustrates the geometry. Table 4.2 lists the two-group cross sections.

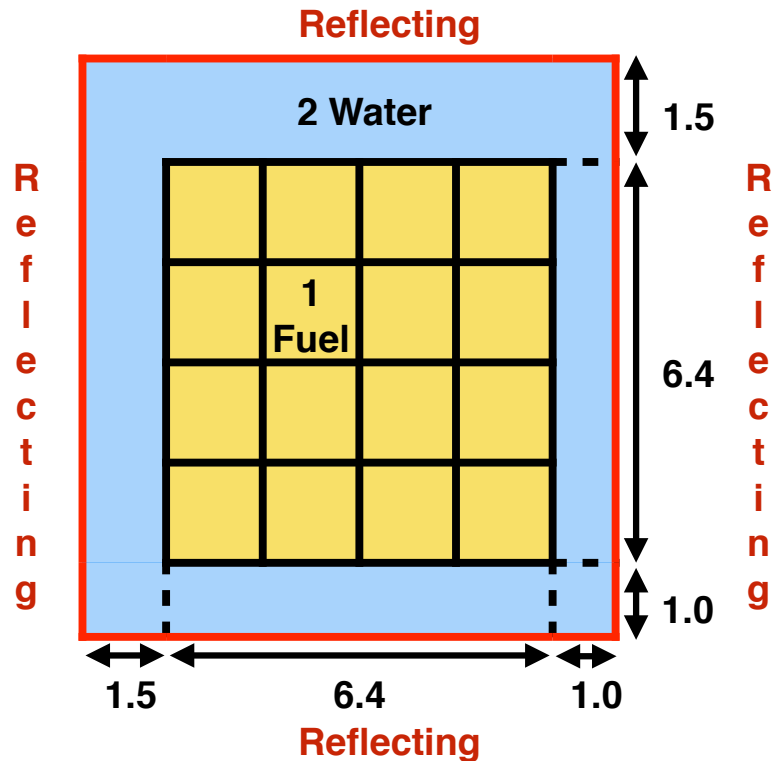


Figure 4.1: The geometry of the BWR cell problem.

To study the truncation errors in the deterministic methods, we investigate a coarse grid of 6x6 rectangular cells and a fine grid of 21x21 rectangular cells. Figure 4.2 illustrates the coarse grid and the fine grid.

Table 4.3 summarizes the k -eigenvalue comparison and the time cost, and the maximum to minimum(max-min) pin power ratio. For the reference Monte Carlo

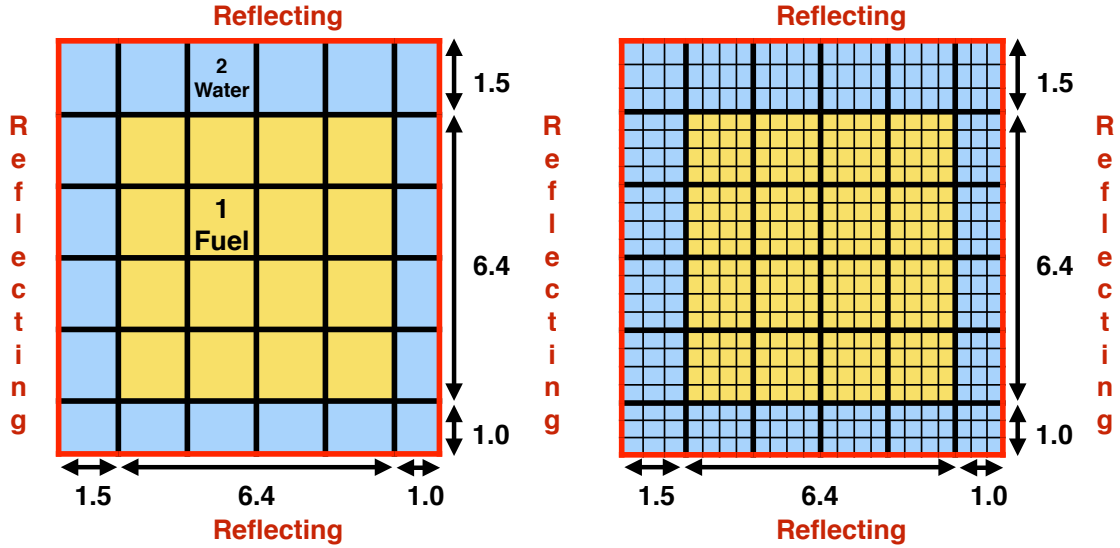


Figure 4.2: The grids of BWR assembly problem. The coarse grid has 6x6 rectangular cells, and the fine grid has 21x21 rectangular cells.

Table 4.2: List of two-group cross sections for the BWR assembly problem

MATERIAL	GROUP i	ABSORP- TION Σ_a (cm^{-1})	NUFISSION $\nu\Sigma_f$ (cm^{-1})	TRANS- PORT Σ_t (cm^{-1})	SCATTERING (cm^{-1}), GROUP j		$\Sigma_{s,i\rightarrow j}$
					1	2	
1	1	8.62700E-3	6.20300E-3	1.96647E-1	1.78000E-1	1.00200E-2	
	2	6.95700E-2	1.10100E-1	5.96159E-1	1.08900E-3	5.25500E-1	
2	1	6.84000E-4	0.	2.22064E-1	1.99500E-1	2.18800E-2	
	2	8.01600E-3	0.	8.87874E-1	1.55800E-3	8.78300E-1	

calculation, 50 million Monte Carlo particles were simulated, so that the reference k -eigenvalue has an uncertainty of 12.5 pcm, and the reference max-min pin power ratio has an uncertainty of 0.0005.

The Monte Carlo pin-cell power distribution is shown in Figure 4.3, in which the pin-cell power is normalized so that the maximum is 1.0. The problem is symmetric about the diagonal from top-left to bottom-right, as are the pin-cell powers. The Monte Carlo uncertainties are about 0.0005.

Next, we study the difference in k -eigenvalues and the maximum to minimum

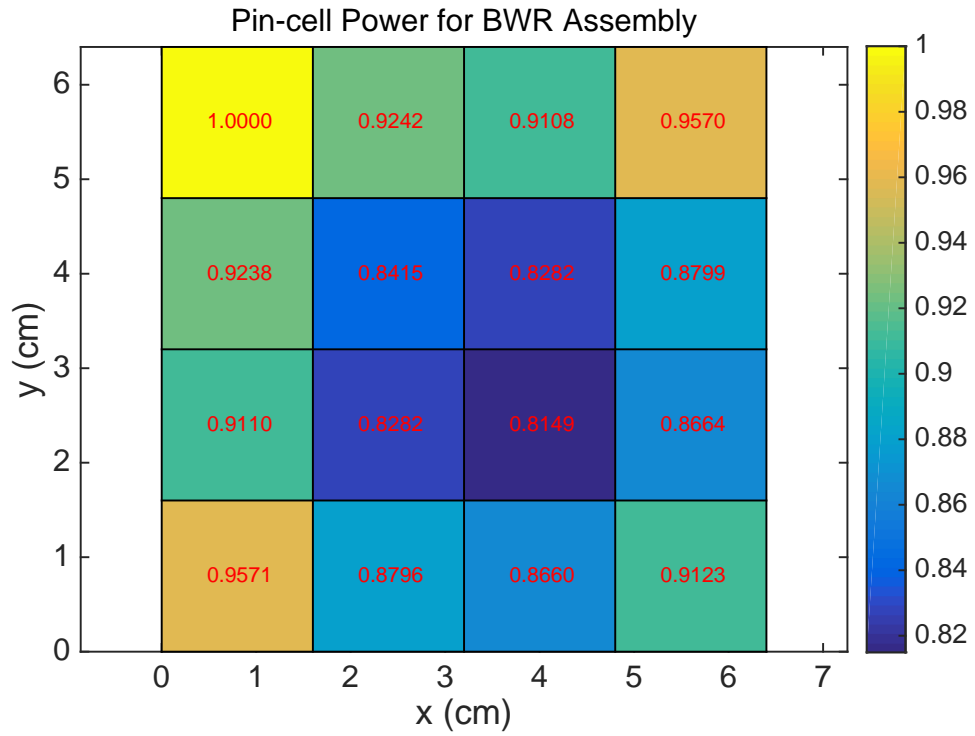


Figure 4.3: The pin-cell power of the Monte Carlo reference for the BWR assembly problem.

ratio of the pin-cell power.

Table 4.3: List of k -effectives, time costs, and max-min pin power ratios of the BWR assembly problem

METHOD	KEFF	KEFF ERROR. (pcm)	TIME PER IT- ERATION (ms)	Max-min Pin Power Ratio	
MC	1.212352	12.5	Reference	1.2271	\pm 0.0005
Coarse Grid					
MOC D0.5 A4P2	1.217459	510.8	0.421	1.1911	
MOC D0.5 A4P4	1.217392	504.1	0.569	1.1915	
MOC D0.5 A8P4	1.217124	477.3	0.911	1.1971	
MOC D0.2 A4P2	1.217778	542.7	0.768	1.1930	
MOC D0.2 A4P4	1.217710	535.9	1.122	1.1934	
MOC D0.2 A8P4	1.217072	472.0	2.122	1.1940	
MOC D0.1 A4P2	1.217471	511.9	1.392	1.1925	
MOC D0.1 A4P4	1.217402	505.1	2.102	1.1929	
MOC D0.1 A8P4	1.217130	477.9	4.275	1.1935	
STEP S4	1.215507	315.5	0.359	1.1304	
STEP S8	1.213787	143.5	0.989	1.1289	
STEP S16	1.213106	75.4	2.659	1.1280	
SSC S4	1.219611	725.9	0.398	1.168	
SSC S8	1.218131	578.0	1.195	1.168	
SSC S16	1.217545	519.4	3.052	1.168	
MB S4	1.206832	-552.0	0.978	1.215	
MB S8	1.205432	-691.9	2.406	1.207	
MB S16	1.204961	-739.1	9.537	1.206	
Fine Grid					
MOC D0.5 A4P2	1.130444	-8190.8	0.914	1.1965	
MOC D0.5 A4P4	1.130416	-8193.5	1.482	1.1968	
MOC D0.5 A8P4	0.826982	-38536.9	2.794	1.2337	
MOC D0.2 A4P2	1.213789	143.7	2.123	1.2258	
MOC D0.2 A4P4	1.213738	138.6	3.430	1.2262	
MOC D0.2 A8P4	1.213275	92.4	6.882	1.2254	
MOC D0.1 A4P2	1.213523	117.1	4.121	1.2249	
MOC D0.1 A4P4	1.213471	111.9	6.645	1.2253	
MOC D0.1 A8P4	1.213275	92.4	13.090	1.2254	
STEP S4	1.215466	311.4	3.583	1.1998	
STEP S8	1.214062	171.0	12.466	1.1944	
STEP S16	1.213551	120.0	63.514	1.1931	
SSC S4	1.215768	341.6	3.936	1.2181	
SSC S8	1.214500	214.8	14.928	1.2130	
SSC S16	1.214036	168.4	68.183	1.2122	
MB S4	1.213016	66.5	11.592	1.2336	
MB S8	1.211896	-45.5	40.161	1.2256	
MB S16	1.211502	-84.9	210.452	1.2246	

Figures 4.4 and 4.5 plot the k -eigenvalues errors and max-min pin power ratio as a function of computation time. Not surprisingly, the fine grid solutions are seen to be more accurate than the coarse grid solution.

BWR Cell Coarse Grid

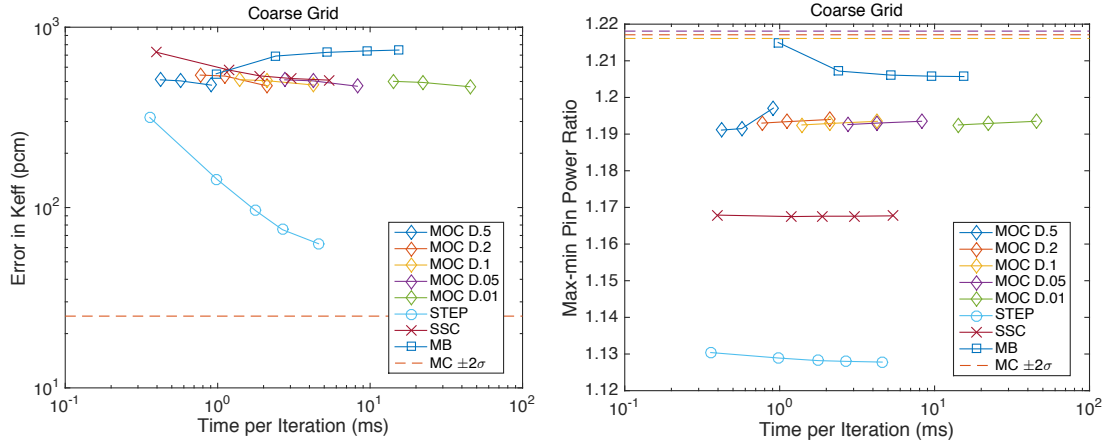


Figure 4.4: The error in k and max-min pin power ratio for the BWR assembly problem on the coarse grid. The MOC solutions are simulated with a variety of angular quadrature sets: A4P2, A4P4, and A8P4. The SN solutions are simulated with a variety of angular quadrature sets: S4, S8, S12, S16, and S20. The dashed line is the Monte Carlo reference.

On the coarse grid, the errors in k are similar, but the STEP method is surprisingly the best. For the max-min pin power ratio, the MB method is the most accurate, then is MOC, SSC, and STEP is order of decreasing accuracy.

BWR Cell Fine Grid

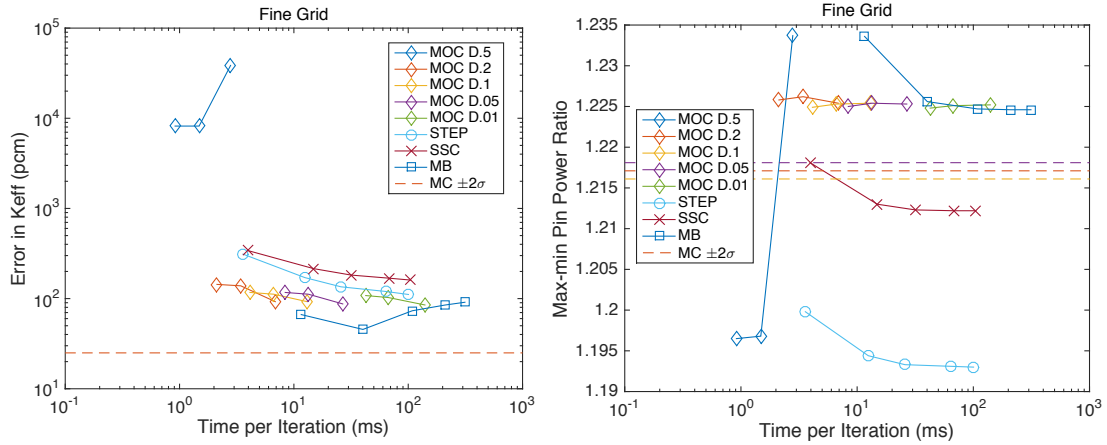


Figure 4.5: The error in k and max-min pin power ratio for the BWR assembly problem on the fine grid. The MOC solutions are simulated with a variety of angular quadrature sets: A4P2, A4P4, and A8P4. The SN solutions are simulated with a variety of angular quadrature sets: S4, S8, S12, S16, and S20. The dashed line is the Monte Carlo reference.

On the fine grid, the MB method has most accurate k . For the max-min pin power ratio, the MB and MOC methods are equally accurate. But SSC method is surprisingly the best. The MOC solution with 0.5 cm ray spacing is very inaccurate, because the ray spacing is wider than the size of the fine cells. In the next subsection, a problem with a strong absorber is studied.

4.2 LWR Assembly Problem with Burnable Absorber

The second problem is an light water reactor (LWR) assembly problem, which contains 4x4 pin-cells in the center, enclosed by light water. One of the pin-cells is filled with a burnable absorber, which has a strong absorption. The materials have two energy groups, where the fission spectrum is 1.0 in the first energy and 0.0 in the second energy group. The four outer boundaries are reflecting. Figure 4.6 illustrates the geometry. Table 4.4 lists the two-group cross sections.

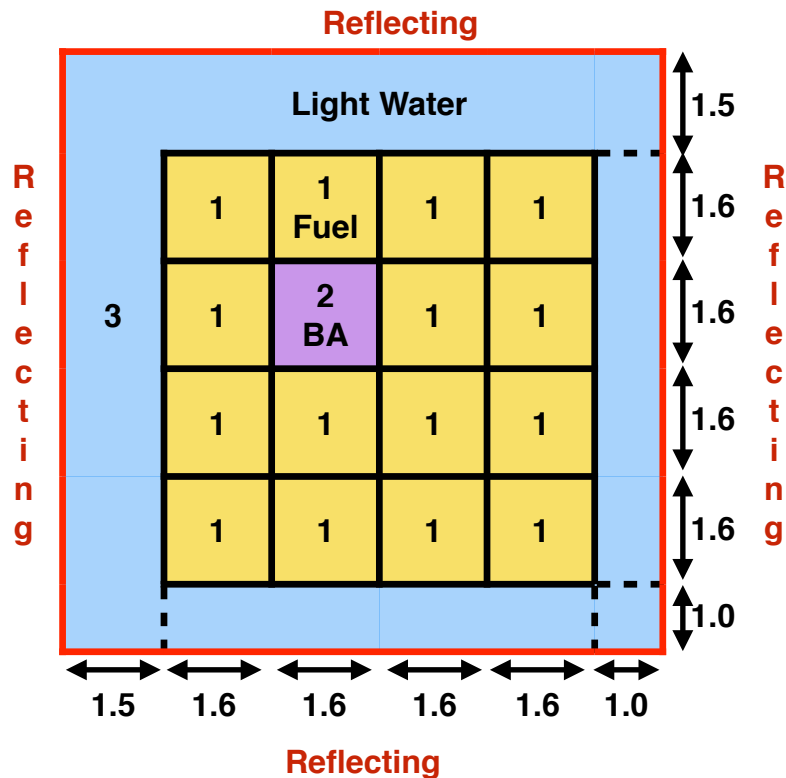


Figure 4.6: The geometry of the LWR assembly problem with burnable absorber.

Similar to the first problem, we investigate two grids. Figure 4.7 illustrates the coarse grid and fine grid.

Table 4.5 compares the k -eigenvalues, the time costs, and max-min pin power ratios. For the Monte Carlo reference calculation, 100 million Monte Carlo particles

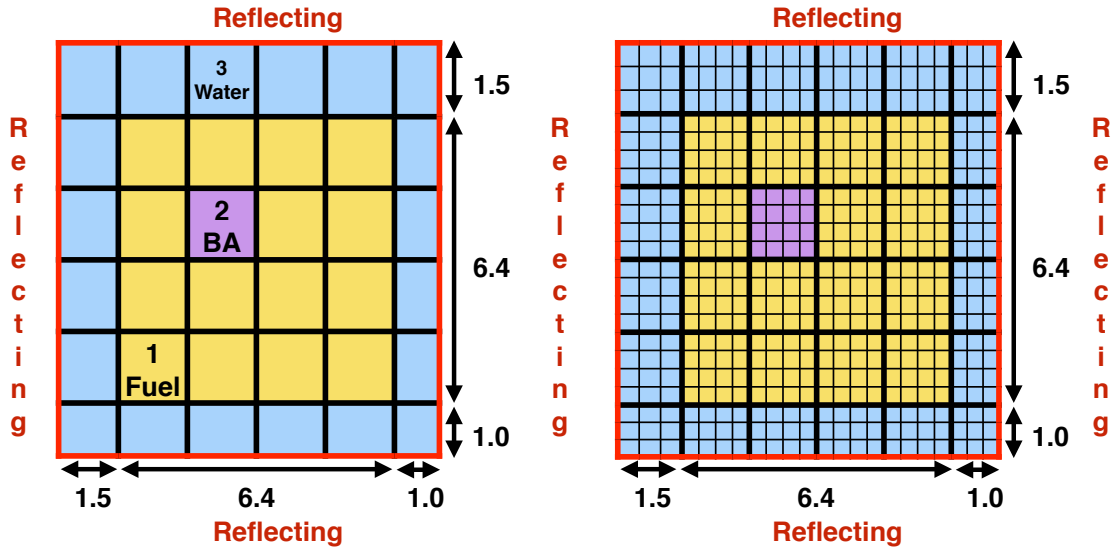


Figure 4.7: The grids of LWR assembly problem. The coarse grid has 6x6 rectangular cells, and the fine grid has 21x21 rectangular cells.

Table 4.4: List of two-group cross sections for the LWR assembly problem with burnable absorber

MATERIAL	GROUP i	ABSORPTION Σ_a (cm^{-1})	NUFISSION $\nu\Sigma_f$ (cm^{-1})	TOTALE Σ_t (cm^{-1})	SCATTERING (cm^{-1}), GROUP j	
					1	2
1	1	9.00000E-3	6.20000E-3	1.99000E-1	1.80000E-1	1.00000E-2
	2	7.00000E-2	1.10000E-1	6.01000E-1	1.00000E-3	5.30000E-1
2	1	9.00000E-3	6.20000E-3	1.99000E-1	1.80000E-1	1.00000E-2
	2	3.00000E+0	1.10000E-1	3.53100E+0	1.00000E-3	5.30000E-1
3	1	7.00000E-4	0.	2.22700E-1	2.00000E-1	2.20000E-2
	2	8.00000E-3	0.	8.90000E-1	2.00000E-3	8.80000E-1

were simulated, so that the reference k -eigenvalue has an uncertainty of 1.8 pcm, and the max-min pin power ratio has an uncertainty of 0.0010%.

The Monte Carlo pin-cell power is shown in Figure 4.8, in which the pin-cell power is normalized so that the maximum is 1.0. The problem is symmetric about the diagonal from top-left to bottom-right, so as the pin-cell powers. The Monte Carlo uncertainties in the value are about 0.0010.

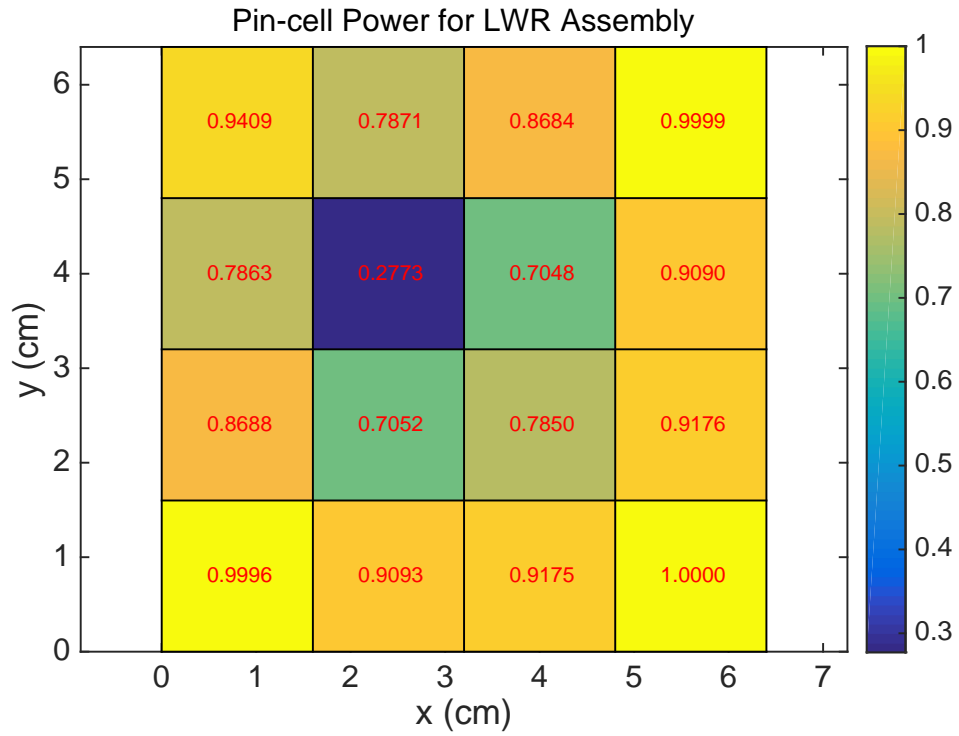


Figure 4.8: The pin-cell power of the Monte Carlo reference for the LWR assembly problem.

Next, we study the difference in k -eigenvalues and the maximum to minimum ratio of the pin-cell power.

Table 4.5: List of k -effectives, time costs and max-min pin power ratios of the LWR cell problem

METHOD	KEFF	KEFF ERROR. (pcm)	TIME PER IT- ERATION (ms)	Max-min Pin Power Ratio	
MC	1.212352	12.5	Reference	3.6063	\pm 0.0010
Coarse Grid					
MOC D0.5 A4P2	0.856899	-2391.4	0.428	3.3343	
MOC D0.5 A4P4	0.857103	-2371.0	0.561	3.3376	
MOC D0.5 A8P4	0.857085	-2372.8	0.922	3.3315	
MOC D0.2 A4P2	0.863002	-1781.1	0.787	3.3663	
MOC D0.2 A4P4	0.863210	-1760.2	1.123	3.3697	
MOC D0.2 A8P4	0.865128	-1568.5	2.123	3.3875	
MOC D0.1 A4P2	0.863676	-1713.7	1.400	3.3721	
MOC D0.1 A4P4	0.863883	-1692.9	2.142	3.3755	
MOC D0.1 A8P4	0.864604	-1620.8	4.253	3.3857	
STEP S4	0.865328	-1548.5	0.373	3.3353	
STEP S8	0.869974	-1083.8	0.995	3.3774	
STEP S16	0.871599	-921.4	2.761	3.3912	
SSC S4	0.846108	-3470.5	0.392	3.2439	
SSC S8	0.851100	-2971.2	1.202	3.2812	
SSC S16	0.852849	-2796.4	3.089	3.2954	
MB S4	0.898525	1771.3	1.000	3.8393	
MB S8	0.900787	1997.4	2.388	3.8431	
MB S16	0.901629	2081.6	10.560	3.8482	
Fine Grid					
MOC D0.5 A4P2	0.819722	-6109.0	0.893	3.5392	
MOC D0.5 A4P4	0.819860	-6095.3	1.421	3.5421	
MOC D0.5 A8P4	0.622445	-25836.8	2.742	3.1689	
MOC D0.2 A4P2	0.876254	-455.8	2.098	3.5556	
MOC D0.2 A4P4	0.876399	-441.4	3.434	3.5586	
MOC D0.2 A8P4	0.877735	-307.8	6.704	3.5709	
MOC D0.1 A4P2	0.876638	-417.4	4.062	3.5597	
MOC D0.1 A4P4	0.876783	-402.9	6.840	3.5628	
MOC D0.1 A8P4	0.877283	-352.9	13.933	3.5706	
STEP S4	0.865271	-1554.2	3.876	3.4382	
STEP S8	0.868390	-1242.3	13.231	3.4534	
STEP S16	0.869472	-1134.1	61.240	3.4593	
SSC S4	0.862534	-1827.8	4.297	3.4531	
SSC S8	0.866061	-1475.1	15.796	3.4684	
SSC S16	0.867315	-1349.7	68.754	3.4765	
MB S4	0.880738	-7.4	12.459	3.6344	
MB S8	0.882675	186.3	41.535	3.6222	
MB S16	0.883457	264.5	224.036	3.6272	

Figures 4.9 and 4.10 plot the errors in the k -eigenvalues and fluxes as a function of computation time. Again, the fine grid solutions are more accurate than the coarse grid solution.

LWR Cell Coarse Grid

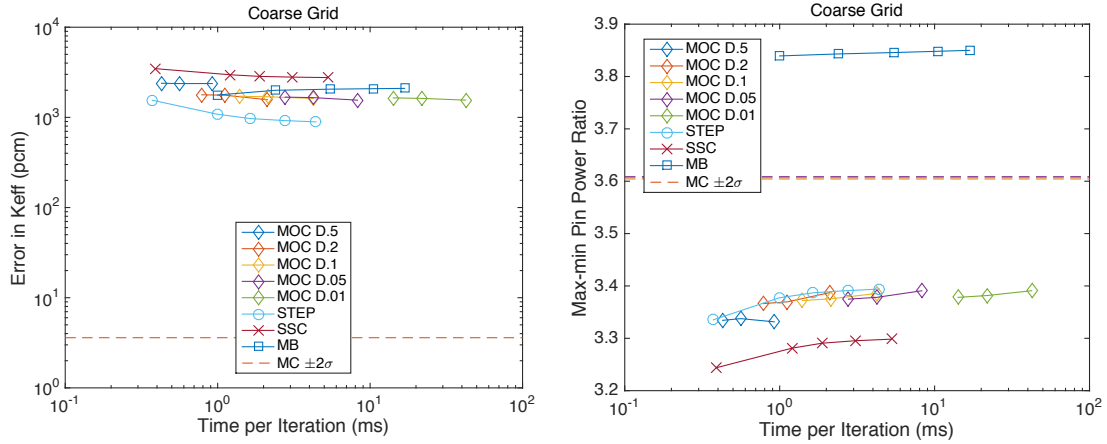


Figure 4.9: The error in k and the max-min pin power ratio for the LWR cell problem with burnable absorber on the coarse grid. The MOC solutions are simulated with a variety of angular quadrature sets: A4P2, A4P4, and A8P4. The SN solutions are simulated with a variety of angular quadrature sets: S4, S8, S12, S16, and S20. The dashed line is the Monte Carlo reference.

The accuracies of different methods on the coarse grid are comparable. For the max-min pin power ratio, the MB method over-estimates the ratio, but other methods underestimate it.

LWR Cell Fine Grid

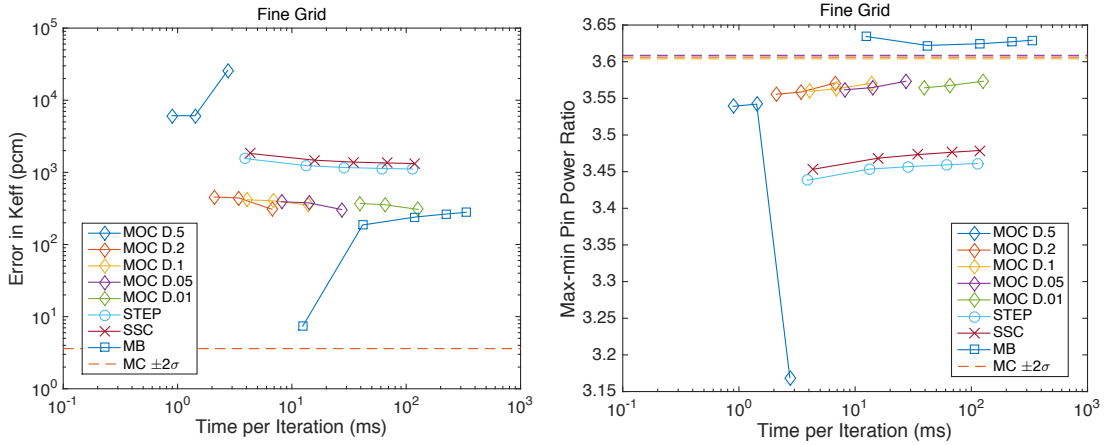


Figure 4.10: The error in k and max-min pin power ratio for the LWR cell problem with burnable absorber on the fine grid. The MOC solutions are simulated with a variety of angular quadrature sets: A4P2, A4P4, and A8P4. The SN solutions are simulated with a variety of angular quadrature sets: S4, S8, S12, S16, and S20. The dashed line is the Monte Carlo reference.

On the fine grid, the MB method has the best accuracy, and is slightly more accurate than the MOC method. SSC and STEP method has the worst accuracies.

In conclusion, depending on the problems, the MB methods are comparable to or slightly better than MOC method. It is clear that MB method is significantly more accurate than the SSC and STEP method. In the next chapter, two-dimensional problems on curved spatial grid are studied.

CHAPTER V

Two-Dimensional Problems with Curved Spatial Grids

In the past, multidimensional discrete ordinates methods treated only Cartesian and triangular mesh geometries, except for the simple cases in which the problem could be transformed to cylindrical or spherical coordinates. This chapter presents several working discrete ordinates methods for problems with spatial grids having curved boundaries. The focus of this chapter is two-dimensional ($x - y$ geometry) problems, in which the solution is independent of the axial variable z .

5.1 The Scope of Geometry

We consider spatial grids that consist of any planar shapes bounded by lines and circles or any other curve that can be parametrized. Although our method is not restricted to lines and circular arcs, we discuss only lines and circular arcs as examples. The reader may underestimate the complexity of geometries formed by lines and circular arcs. So in Figure 5.1, a geometry containing a triangle (three lines) and three circles is provided. In this figure, there are 13 spacial cells, each of which is bounded by lines and circular arcs. Since most of the readers of this thesis will have a nuclear engineering background, most of the examples provided in this thesis

assume a special case shown in Figure 5.2. This is a simplified fuel assembly from a pressurized water reactor (PWR), which is composed of a coarse grid of squares. Inside each square, concentric circles centered at the center of the square could be present. Such a square with potential concentric circles inside is called a “**pin-cell**”. Inside each pin-cell, there are fine spatial cells bounded by lines and circles. One example of the pin-cell is the green square in Figure 5.2. Next, some terminologies are introduced to facilitate later discussions.

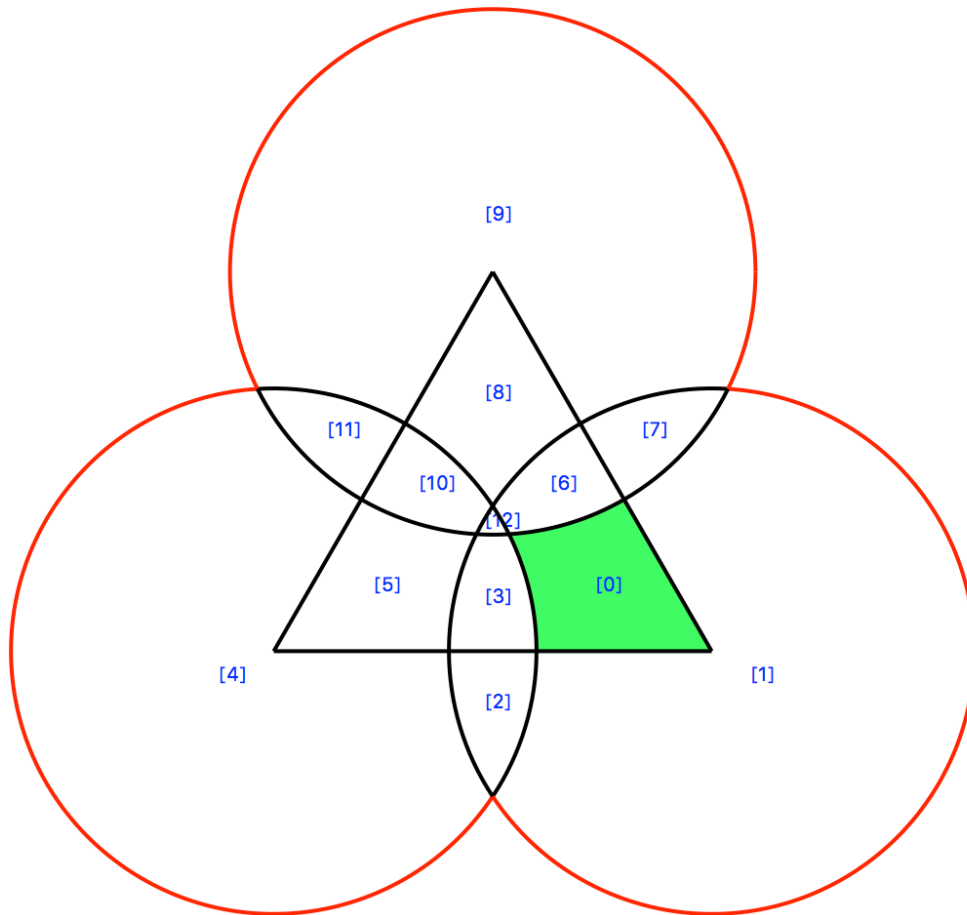


Figure 5.1: Example of planar geometry formed by lines and circular arcs. There are 13 spatial cells, and the spatial cell numbered “0” is green. The black lines are the boundaries inside, and the red lines are the boundaries of the outline.

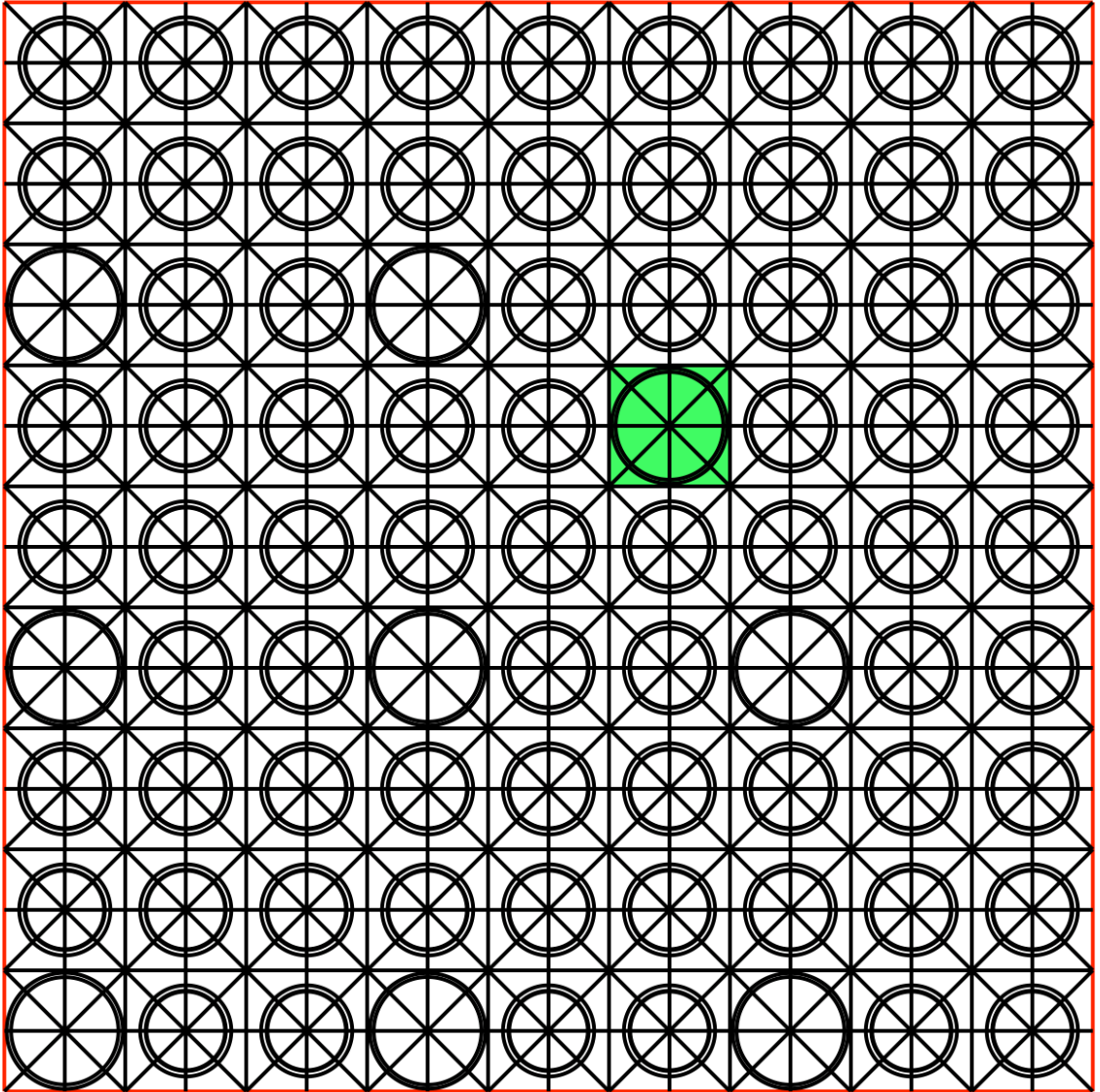


Figure 5.2: A simplified PWR assembly, which is composed of a grid of squares. Each square may contain concentric circles, which is called a “**pin-cell**”. One example is marked in green, which is a guide tube. Most problems considered in this thesis are of this type. There is a “coarse” grid of square pin-cells, and each coarse cell has “fine” spatial cells bounded by lines and circular arcs.

5.1.1 Topology

The curves in Figure 5.1 divide the plane into 13 different finite areas. Each area is called a “cell”, and the curves bounding it in the counter-clockwise direction are called “**boundaries**”. Figure 5.3 describes two cells and their boundaries. All boundaries are oriented in the counter-clockwise direction. The direction of a boundary is relative to a cell. For cell f , all boundaries are denoted as $C(f)$:

$$C(f) = \{c | c \text{ is a boundary of cell } f\}. \quad (5.1)$$

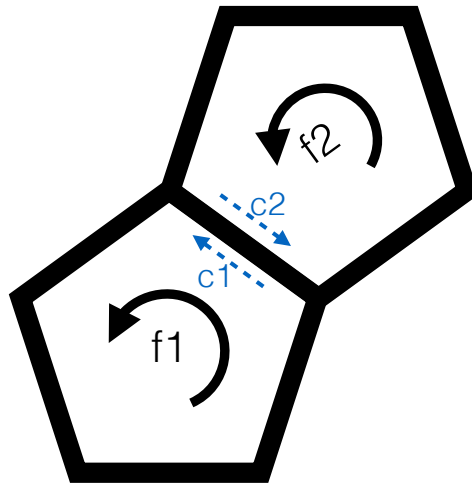


Figure 5.3: Two cells and their boundaries. Two boundaries c_1 and c_2 have opposite directions when belonging to two neighboring cells f_1 and f_2

Figure 5.3 shows that though boundaries c_1 and c_2 are coincident, they have different directions and belong to two neighboring cells f_1 and f_2 . Table 5.1 summarizes important terms.

It is important to keep in mind that boundaries of a cell have directions as if one walks on the boundaries in the counter-clockwise direction. The outer normal vector of a boundary is a unit vector perpendicular to the tangential direction of the boundary, and pointing to the “right” as one walks on the boundary counter-

Table 5.1: List of topology terms

TERM	EXPLANATION
Cell	A two-dimension bounded area
Boundary	The curves bound a cell, in counter-clockwise direction

clockwise. See Figure 5.4 for clarification.

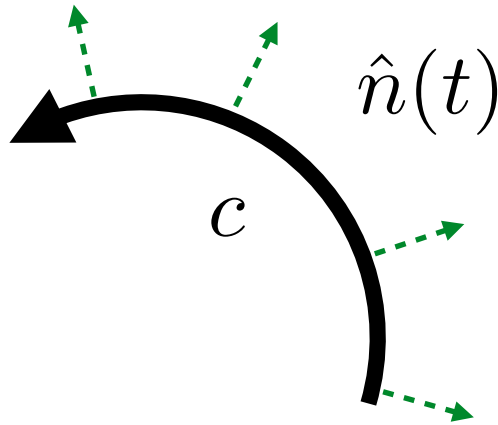


Figure 5.4: Normal vector $\hat{n}(t)$ of boundary c pointing to the “right”.

5.1.2 Parametrization

A boundary is parametrized by associating all points on it with real numbers. Here is an example:

$$\vec{x} = \vec{p}(t), \quad a \leq t \leq b, \quad (5.2)$$

where the parameter t increases in the direction of the boundary. A linear boundary can be parametrized by:

$$\vec{x} = \vec{o} + t \hat{d}, \quad a \leq t \leq b, \quad (5.3)$$

$$|\hat{d}| = 1, \quad (5.4)$$

where \vec{o} is one point that the line passes through, and \hat{d} is a unit vector pointing along the line. A visualization of the parametrization of a linear boundary is shown in Figure 5.5.

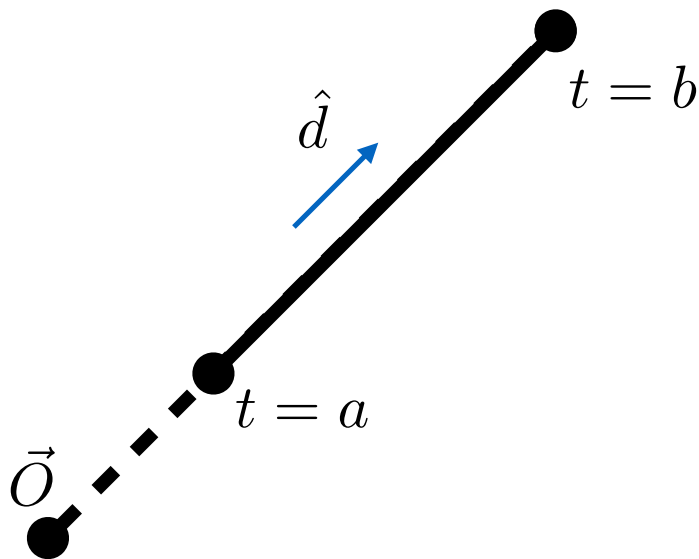


Figure 5.5: The parametrization of a linear boundary. The location \vec{O} is a point on the line and \hat{d} is a unit vector in the direction of the line. The points with parameter of $t = a$ and $t = b$ are the end points of the linear boundary.

A portion of a circular arc boundary can be parametrized by:

$$\vec{x} = \vec{c} + r \begin{pmatrix} \cos t \\ \sin t \end{pmatrix}, \quad a \leq t \leq b, \quad (5.5)$$

where \vec{c} is the center and r is the radius. A visualization of the parametrization of a circular arc boundary is shown in Figure 5.6.

The linear and circular arc boundaries are very powerful in the construction of complex geometries. For example, the outline of any cell in Figure 5.1 can be formed by the shapes described in Figure 5.5 and 5.6.

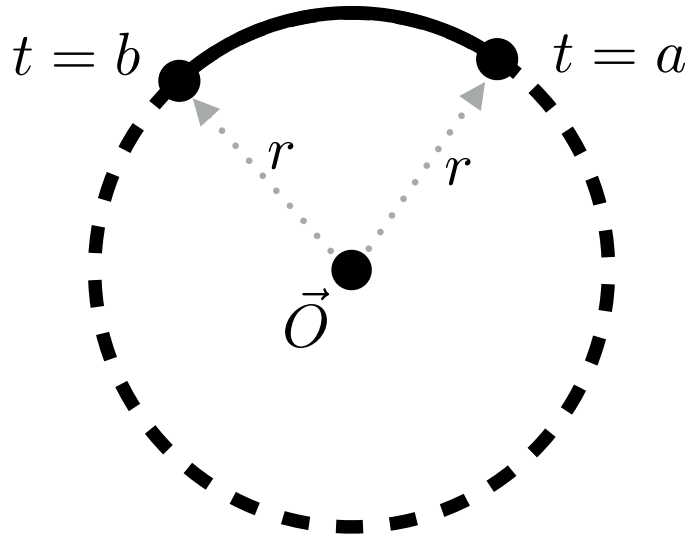


Figure 5.6: The parametrization of a circular arc boundary. The location \vec{O} is the center of the circle, and r is the radius of the circle. The points with parameter of $t = a$ and $t = b$ are the end points of the circular arc boundary.

5.1.3 Cell and Boundary Integrals

We consider a boundary c with parametrization:

$$\vec{x} = \vec{p}(t), \quad a \leq t \leq b, \quad (5.6)$$

with normal vector $\hat{n}(t)$ as defined in Figure 5.4. We consider the x and y components of the position and normal vectors:

$$\vec{x}(t) = \begin{pmatrix} x(t) \\ y(t) \end{pmatrix}, \quad (5.7)$$

$$\hat{n}(t) = \begin{pmatrix} n_x(t) \\ n_y(t) \end{pmatrix}, \quad (5.8)$$

where $x(t)$, $y(t)$, $\hat{n}_x(t)$, and $\hat{n}_y(t)$ are scalar functions of t . Several one-dimensional integrals are defined as:

$$A_0(c) = \oint_c ds = \int_a^b dt, \quad (5.9)$$

$$A_{1x}(c) = \oint_c n_x(s) ds = \int_a^b n_x(t) dt, \quad (5.10)$$

$$A_{1y}(c) = \oint_c n_y(s) ds = \int_a^b n_y(t) dt, \quad (5.11)$$

$$A_{2xx}(c) = \oint_c n_x(s) x(s) ds = \int_a^b n_x(t) x(t) dt, \quad (5.12)$$

$$A_{2xy}(c) = \oint_c n_x(s) y(s) ds = \int_a^b n_x(t) y(t) dt, \quad (5.13)$$

$$A_{2yx}(c) = \oint_c n_y(s) x(s) ds = \int_a^b n_y(t) x(t) dt, \quad (5.14)$$

$$A_{2yy}(c) = \oint_c n_y(s) y(s) ds = \int_a^b n_y(t) y(t) dt, \quad (5.15)$$

and

$$\vec{A}_1(c) = \oint_c \hat{n}(s) ds = \int_a^b \begin{pmatrix} n_x(t) \\ n_y(t) \end{pmatrix} dt = \begin{pmatrix} A_{1x}(c) \\ A_{1y}(c) \end{pmatrix}. \quad (5.16)$$

Next for a cell f , we define some two-dimensional integrals:

$$M_0(f) = \int_f d\vec{x}, \quad (5.17)$$

$$M_{1x}(f) = \int_f x d\vec{x}, \quad (5.18)$$

$$M_{1y}(f) = \int_f y d\vec{x}, \quad (5.19)$$

where $d\vec{x} = dx dy$. Specifically, $M_0(f)$ is the area of the cell f , and the point

$\left(\frac{M_{1x}(f)}{M_0(f)}, \frac{M_{1y}(f)}{M_0(f)}\right)$ is the center of mass of cell f .

5.2 The Multigroup Discrete Ordinates Neutron Transport Equation

We again consider the multigroup neutron transport equations with isotropic scattering. These equations are the topic of this thesis; our goal is to discretize them for problems defined on the spatial grids defined in the earlier section.

$$\begin{aligned} \hat{\Omega} \cdot \vec{\nabla} \psi_g(\vec{x}, \hat{\Omega}) + \Sigma_{t,g}(\vec{x}) \psi_g(\vec{x}, \hat{\Omega}) &= \frac{1}{4\pi} \sum_{g'=1}^G \Sigma_{s,g' \rightarrow g}(\vec{x}) \phi_{g'}(\vec{x}) \\ &+ \frac{\chi_g(\vec{x})}{4\pi k} \sum_{g'=1}^G \nu \Sigma_{f,g'} \phi_{g'}(\vec{x}), \end{aligned} \quad (5.20)$$

$$\phi_g(\vec{x}) = \int_{4\pi} \psi_g(\vec{x}, \hat{\Omega}') d\hat{\Omega}'. \quad (5.21)$$

Definitions of each quantity in this equation can be found in Table 5.2. For simplicity, we have again assumed isotropic scattering in equation (5.20). Equation (5.21) is the relationship between scalar flux and angular flux.

The discrete ordinates method approximates the neutron transport equation by replacing the continuous angular variable $\hat{\Omega}$ by a finite set of discrete angles $\hat{\Omega}_n$. These approximations reduce the neutron transport equation to the discrete ordinates equation given next. Definitions of additional terms can be found in Table 5.3. Equation (5.23) gives the relationship between the angular flux and the scalar flux.

Table 5.2: List of definitions of terms in neutron transport equation

TERM	TYPE	EXPLANATION
\vec{x}	vector	location
$\hat{\Omega}$	unit vector	direction
g	integer	the index of an energy group
G	positive integer	the number of energy groups
$\psi_g(\vec{x}, \hat{\Omega})$	scalar	the angular flux at location \vec{x} , traveling at angle $\hat{\Omega}$, in group g
$\vec{\nabla}$	operator	the vector gradient operator for a scalar function
$\Sigma_{t,g}(\vec{x})$	scalar	the macroscopic total cross section at \vec{x} , for group g
$\Sigma_{s,g' \rightarrow g}(\vec{x})$	scalar	the isotropic macroscopic scattering cross section at \vec{x} , scattering from energy group g' to group g
$\phi_g(\vec{x})$	scalar	the scalar flux at \vec{x} , for group g
$\chi_g(\vec{x})$	scalar	the neutron fission probability into group g , at \vec{x} (the “ fission spectrum ”)
$\nu\Sigma_{f,g}(\vec{x})$	scalar	the macroscopic neutron yield cross section at location \vec{x} , for group g
k	scalar	the effective reactivity coefficient, the eigenvalue of the problem

$$\hat{\Omega}_n \cdot \vec{\nabla} \psi_{n,g}(\vec{x}) + \Sigma_{t,g}(\vec{x}) \psi_{n,g}(\vec{x}) = \frac{1}{4\pi} \sum_{g'=1}^G \Sigma_{s,g' \rightarrow g}(\vec{x}) \phi_{g'}(\vec{x}) + \frac{\chi_g(\vec{x})}{4\pi k} \sum_{g'=1}^G \nu\Sigma_{f,g'}(\vec{x}) \phi_{g'}(\vec{x}), \quad (5.22)$$

$$\phi_g(\vec{x}) = \sum_{n=1}^M \omega_n \psi_{n,g}(\vec{x}), \quad (5.23)$$

$$\sum_{n=1}^M \omega_n = 4\pi. \quad (5.24)$$

The discrete ordinates equations describe the angular discretized neutron physics at the point \vec{x} . Integration over a cell is necessary to obtain cell-averaged neutron physics. We integrate the discrete ordinates equation over a cell f , with the assumption that the material inside f is homogeneous. The newly-appearing quantities in the cell-integrated discrete ordinates equation are defined in Table 5.4. An example

Table 5.3: List of definitions of additional terms in discrete ordinate equation

TERM	TYPE	EXPLANATION
n	integer	the index of discrete angle
M	integer	the total number of discrete angles
$\hat{\Omega}_n$	unit vector	the direction of flight
ω_n	scalar	the weight of the discrete angle at index n , i.e. the weight of $\hat{\Omega}_n$
$\psi_{n,g}(\vec{x})$	scalar	the neutron angular flux at \vec{x} , traveling in direction $\hat{\Omega}_n$, in group g

of a cell f and its boundaries $C(f)$ is illustrated in Figure 5.7.

$$\begin{aligned} & \hat{\Omega}_n \cdot \int_f \vec{\nabla} \psi_{n,g}(\vec{x}) d\vec{x} + \Sigma_{t,g,f} \int_f \psi_{n,g}(\vec{x}) d\vec{x} \\ &= \frac{1}{4\pi} \sum_{g'=1}^G \Sigma_{s,g' \rightarrow g,f} \int_f \phi_{g'}(\vec{x}) d\vec{x} + \frac{1}{4\pi k} \chi_{g,f} \sum_{g'=1}^G \nu \Sigma_{f,g',f} \int_f \phi_{g'}(\vec{x}) d\vec{x}. \end{aligned}$$

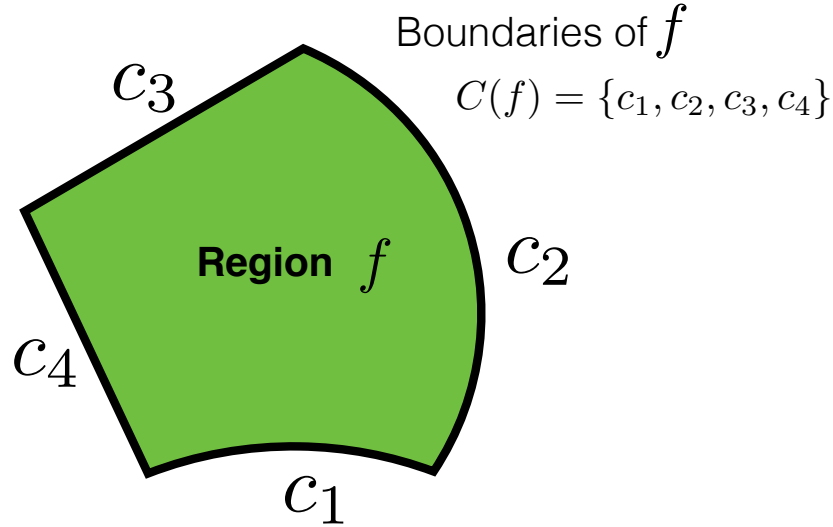


Figure 5.7: An example of a cell f and its boundaries $C(f)$. This example has four boundaries c_1 , c_2 , c_3 and c_4 .

The integration of the first term with the gradient operator can be expressed as

Table 5.4: List of definitions of additional terms in cell-integrated discrete ordinate equation

TERM	TYPE	EXPLANATION
$\Sigma_{t,g,f}$	scalar	the macroscopic total cross section in cell f , for group g
$\Sigma_{s,g' \rightarrow g,f}$	scalar	the macroscopic scattering cross section in cell f , scattering from group g' to group g
$\chi_{g,f}$	scalar	the neutron fission probability into group g , in cell f
$\nu\Sigma_{f,g,f}$	scalar	the macroscopic neutron yield cross section in cell f , for group g
$\psi_{n,g,c}$	scalar	the averaged angular flux on boundary c for group g , in direction $\hat{\Omega}_n$
$\bar{\psi}_{n,g,f}$	scalar	the averaged angular flux in cell f , for group g , in direction $\hat{\Omega}_n$
$\bar{\phi}_{g,f}$	scalar	the averaged scalar flux in cell f , for group g
$\phi_{g,c}$	scalar	the averaged scalar flux on the boundary c , for group g
$M_0(f)$	scalar	the volume of cell f
$\vec{A}_1(c)$	vector	an integration quantity for boundary c in the direction of boundary normal, see equation (5.16)
$C(f)$	set	the set of all boundaries of cell f , see equation (5.1)
$\hat{n}(\vec{x})$	unit vector	the normal vector at location \vec{x} on a boundary, see Figure 5.4 for definition

a sum of boundary integrals by the Divergence Theorem:

$$\int_f \vec{\nabla} \psi_{n,g}(\vec{x}) d\vec{x} = \sum_{c \in C(f)} \oint_c \hat{n}(s) \psi_{n,g}(\vec{x}(s)) ds. \quad (5.25)$$

We further define some cell-averaged fluxes and some boundary-averaged fluxes:

$$\psi_{n,g,c} = \frac{\hat{\Omega}_n \cdot \oint_c \hat{n}(s) \psi_{n,g}(\vec{x}(s)) ds}{\hat{\Omega}_n \cdot \oint_c \hat{n}(s) ds} = \frac{\hat{\Omega}_n \cdot \oint_c \hat{n}(s) \psi_{n,g}(\vec{x}(s)) ds}{\hat{\Omega}_n \cdot \vec{A}_1(c)}, \quad (5.26)$$

$$\phi_{g,c} = \frac{\hat{\Omega}_n \cdot \oint_c \hat{n}(s) \phi_g(\vec{x}(s)) ds}{\hat{\Omega}_n \cdot \oint_c \hat{n}(s) ds} = \frac{\hat{\Omega}_n \cdot \oint_c \hat{n}(s) \phi_g(\vec{x}(s)) ds}{\hat{\Omega}_n \cdot \vec{A}_1(c)}, \quad (5.27)$$

$$\bar{\psi}_{n,g,f} = \frac{\int_f \psi_{n,g}(\vec{x}) d\vec{x}}{\int_f d\vec{x}} = \frac{\int_f \psi_{n,g}(\vec{x}) d\vec{x}}{M_0(f)}, \quad (5.28)$$

$$\bar{\phi}_{g,f} = \frac{\int_f \phi_g(\vec{x}) d\vec{x}}{\int_f d\vec{x}} = \frac{\int_f \phi_g(\vec{x}) d\vec{x}}{M_0(f)}. \quad (5.29)$$

The cell-averaged angular flux and boundary-averaged angular fluxes are illustrated in Figure 5.8.

Then the cell-averaged discrete-ordinates multigroup transport equation is concisely expressed as equation (5.30). This equation describes the conservation of neutrons inside the cell f with energy group g and traveling at direction index n . It is also called the “**neutron balance equation**”.

$$\begin{aligned} & \sum_{c \in C(f)} \hat{\Omega}_n \cdot \vec{A}_1(c) \psi_{n,g,c} + \Sigma_{t,g,f} M_0(f) \bar{\psi}_{n,g,f} \\ &= \frac{1}{4\pi} \sum_{g'=1}^G \Sigma_{s,g' \rightarrow g,f} M_0(f) \bar{\phi}_{g',f} + \frac{1}{4\pi k} \chi_{g,f} \sum_{g'=1}^G \nu \Sigma_{f,g',f} M_0(f) \bar{\phi}_{g',f}. \end{aligned} \quad (5.30)$$

The terms on the right hand side of equation (5.30) are the source terms. Addi-

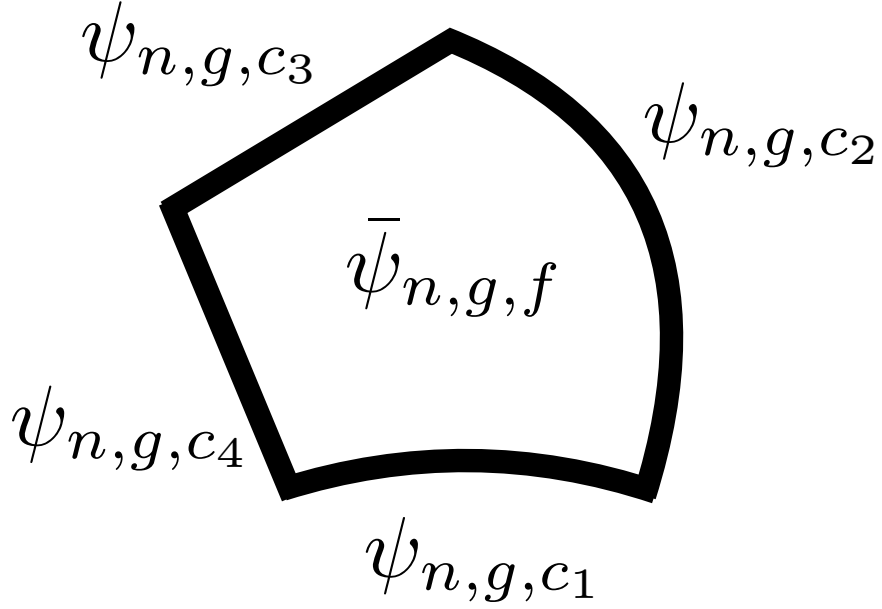


Figure 5.8: An illustration of the averaged angular fluxes in direction $\hat{\Omega}_n$ and group g of cell f and its four boundaries c_1 , c_2 , c_3 and c_4 .

tional quantities are defined in Table 5.5 to simplify the notation.

$$\bar{Q}_{s,g,f} = \frac{1}{4\pi} \sum_{g'=1}^G \Sigma_{s,g' \rightarrow g,f} \bar{\phi}_{g',f}, \quad (5.31)$$

$$\bar{Q}_{f,g,f} = \frac{1}{4\pi} \chi_{g,f} \sum_{g'=1}^G \nu \Sigma_{f,g',f} \bar{\phi}_{g',f}, \quad (5.32)$$

$$Q_{s,g,f,c} = \frac{1}{4\pi} \sum_{g'=1}^G \Sigma_{s,g' \rightarrow g,f} \phi_{g',c}, \quad (5.33)$$

$$Q_{f,g,f,c} = \frac{1}{4\pi} \chi_{g,f} \sum_{g'=1}^G \nu \Sigma_{f,g',f} \phi_{g',c}. \quad (5.34)$$

With these definitions, the neutron balance equation (5.30) can be rewritten more concisely as:

$$\sum_{c \in C(f)} \hat{\Omega}_n \cdot \vec{A}_1(c) \psi_{n,g,c} + \Sigma_{t,g,f} M_0(f) \bar{\psi}_{n,g,f} = M_0(f) \left[\bar{Q}_{s,g,f} + \frac{1}{k} \bar{Q}_{f,g,f} \right]. \quad (5.35)$$

Table 5.5: List of definitions of source terms in neutron balance equation

TERM	TYPE	EXPLANATION
$\bar{Q}_{s,g,f}$	scalar	the averaged scattering source of energy group g in the cell f , see equation (5.31)
$\bar{Q}_{f,g,f}$	scalar	the averaged fission source of energy group g in the cell f , see equation (5.32)
$Q_{s,g,f,c}$	scalar	the averaged scattering source of energy group g on the boundary c of cell f , see equation (5.33)
$Q_{f,g,f,c}$	scalar	the averaged fission source of energy group g on the boundary c of cell f , see equation (5.34)

5.3 Re-entrant Boundaries

Consider a cell f . If its set of boundaries $C(f)$ contains a part of circular arc c , a neutron traveling at an arbitrary direction $\hat{\Omega}_n$ and entering the boundary c , may also exit the boundary c . If this happens, the boundary c is called a “**re-entrant boundary**”. Figure 5.9 shows an example of a re-entrant boundary.

Re-entrant boundaries occur for spatial grids with curved boundaries; they do not occur for spatial grids with planar boundaries. Special measures are necessary to deal with the re-entrant boundaries, so as to make the sweep process stable. The sweep process may be unstable when sweeping “against” the direction of neutron flight.

Let us consider a boundary c with parametrization: $\vec{x} = \vec{p}(t)$, $a \leq t \leq b$. The boundary c is defined as:

$$\text{“Incoming”} : \hat{\Omega}_n \cdot \hat{n}(t) < 0, \quad \text{for all } a \leq t \leq b, \quad (5.36)$$

$$\text{“Outgoing”} : \hat{\Omega}_n \cdot \hat{n}(t) > 0, \quad \text{for all } a \leq t \leq b. \quad (5.37)$$

A re-entrant boundary is neither “**incoming**” or “**outgoing**”, because not all points on the boundary have the same sign of $\hat{\Omega}_n \cdot \hat{n}(t)$. To remove this ambiguity, we split the cell f according to the following rule:

“Splitting Rule”

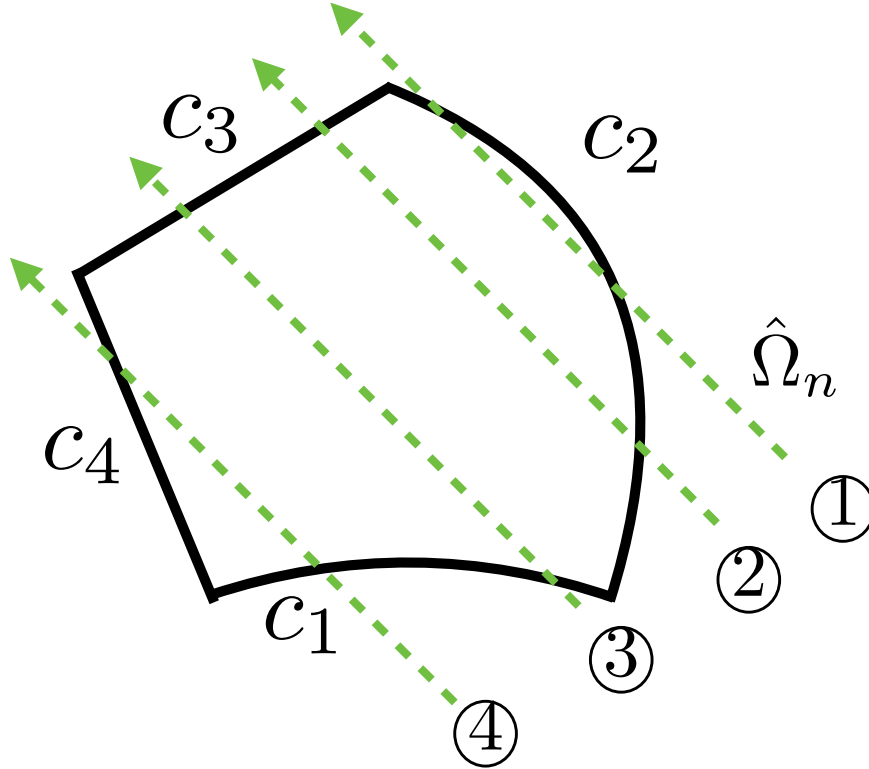


Figure 5.9: An illustration of four rays ①,②,③,④ in the direction $\hat{\Omega}_n$. Ray ① enters boundary c_2 and exits c_2 ; ray ② enters boundary c_2 and exits c_3 ; ray ③ enters boundary c_1 and exits c_3 ; ray ④ enters boundary c_1 and exits c_4 . c_2 is a “**re-entrant boundary**” of the direction $\hat{\Omega}_n$.

Consider direction $\hat{\Omega}$. For each re-entrant circular arc boundary c of cell f , split f with a line which is perpendicular to $\hat{\Omega}$, and which passes through the center of the circle of which the re-entrant boundary is a part. This divides the cell into several cells, all the boundaries of which are now unambiguously “**incoming**” or “**outgoing**”.

For the example in Figure 5.9, there is one re-entrant boundary. So this cell is split into two cells following the rule above. After it is split, there are no re-entrant boundaries. See Figure 5.10 for a visualization of applying the splitting rule.

Another example is a pin-cell geometry, which is shown in Figure 5.11. (See Figure 5.2 for the definition of a pin-cell.) The square pin-cell in this figure has one circle

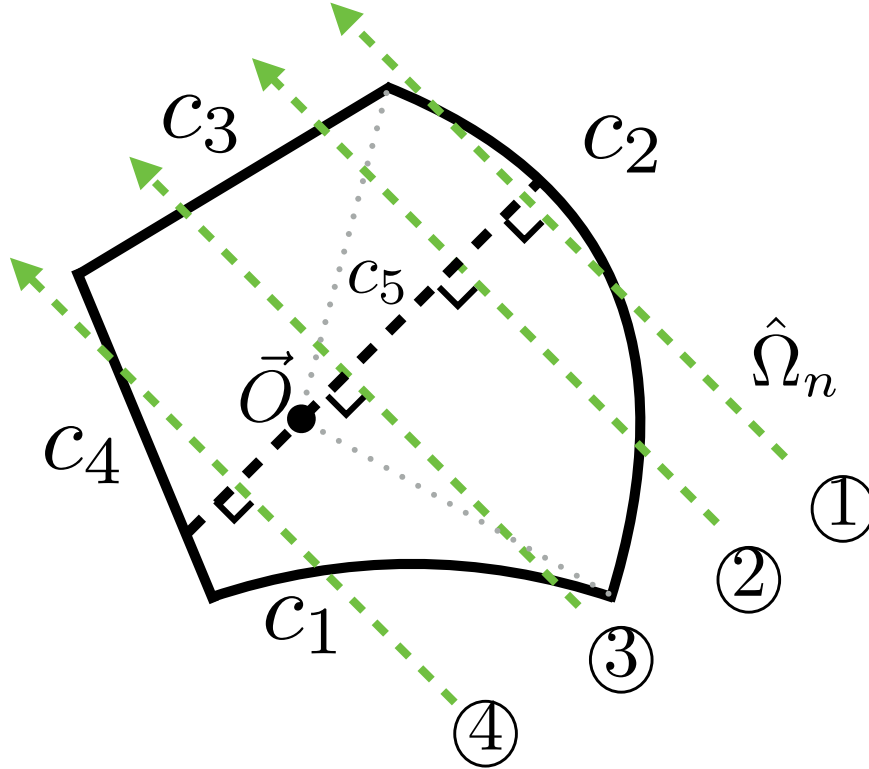


Figure 5.10: Example of the applying of the “**rule of a fixed**”. The re-entrant boundary is c_2 . There are four rays ①,②,③,④ in the direction $\hat{\Omega}_n$. The cell is then split with a line which is perpendicular to $\hat{\Omega}_n$, and which passes \vec{O} , which is the center of the boundary c_2 . After, ray ① enters boundary c_2 and exits c_5 ; ray ② enters boundary c_2 and exits c_5 ; ray ③ enters boundary c_1 and exits c_5 ; Ray ④ enters boundary c_1 and exits c_5 . A re-entrant boundary no longer exists. The line added is marked as dashed to indicate the “split” is temporary only for the angle $\hat{\Omega}_n$.

centered at the center of the square, which is divided into 8 angular sectors. The cells numbered “[0]”, “[4]”, “[9]” and “[10]” in the left figure have re-entrant boundaries for the direction of $\hat{\Omega}$. These cells are split with the line passing through the circle’s center and perpendicular to direction of $\hat{\Omega}$. The result is shown in the figure on the right, which has no re-entrant boundaries.

So the spatial grids depend somewhat on the direction of flight. With different direction of flight, the splitting creates different spatial grids. This somewhat increases the complexity for implementation of the method. However as indicated by the dashed

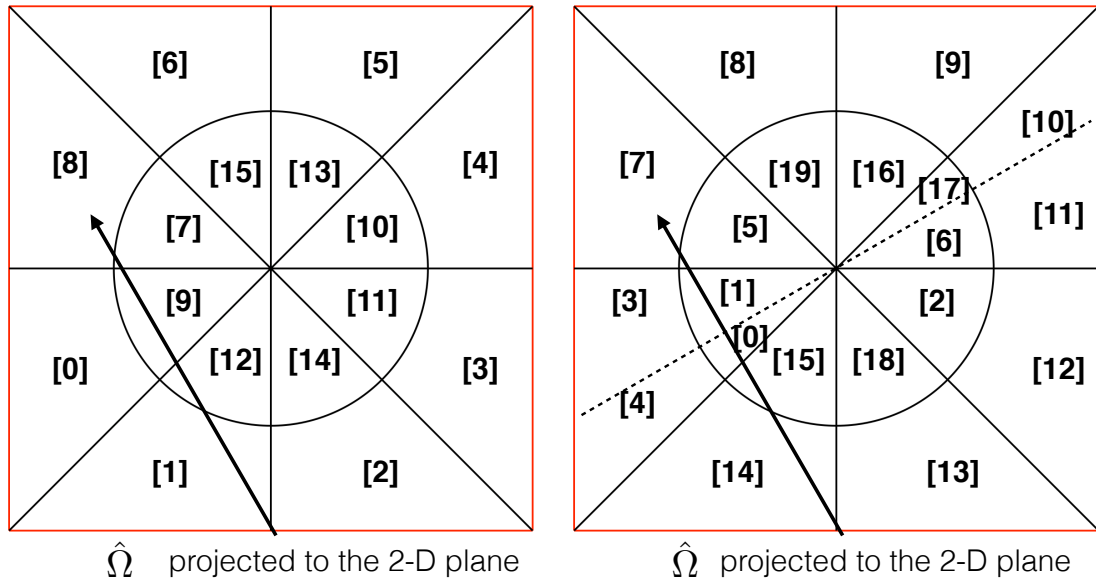


Figure 5.11: The cells numbered “[0]”, “[4]”, “[9]” and “[10]” of the left figure has re-entrant boundaries for the direction of $\hat{\Omega}$. The cells after split with a line passing through the center of the circle, which is perpendicular to $\hat{\Omega}$. It results cells numbered “[0]”, “[1]”, “[3]”, “[4]”, “[6]”, “[17]”, “[10]” and “[11]” in the right figure. There are no re-entrant boundaries after. The line added is marked as dashed to indicate the “split” is temporary only for the angle $\hat{\Omega}$.

line in Figure 5.11, the “split” of cells is temporary. It is done only during a sweep in the specified direction, and it is not done for other directions of flight. In principle, each direction of flight in the quadrature set could have fine spatial cells within a pin-cell that are temporary “split” during the sweeping process.

5.4 Categorization of Boundaries

A discussion of the categorization of boundaries of a cell deserves a single section because its understanding is required for later sections about the auxiliary equations. Consider a cell f . For a specified direction $\hat{\Omega}$, all its boundaries $C(f)$ should be categorized as “incoming”, “outgoing” and “parallel”.

Intuitively, for a specific direction of flight, a boundary is “**incoming**” if the neutrons enter the cell through the boundary. It is “**outgoing**” if the neutrons exit the cell through the boundary. It is parallel if the neutron flight is parallel to the boundary. Figure 5.12 shows the categorization of the boundaries of the cells in the first example of the previous section 5.3. See Figure 5.10. In that example, there was a re-entrant boundary, which was split by the procedure discussed in the previous section 5.3. (See the “splitting rule”.)

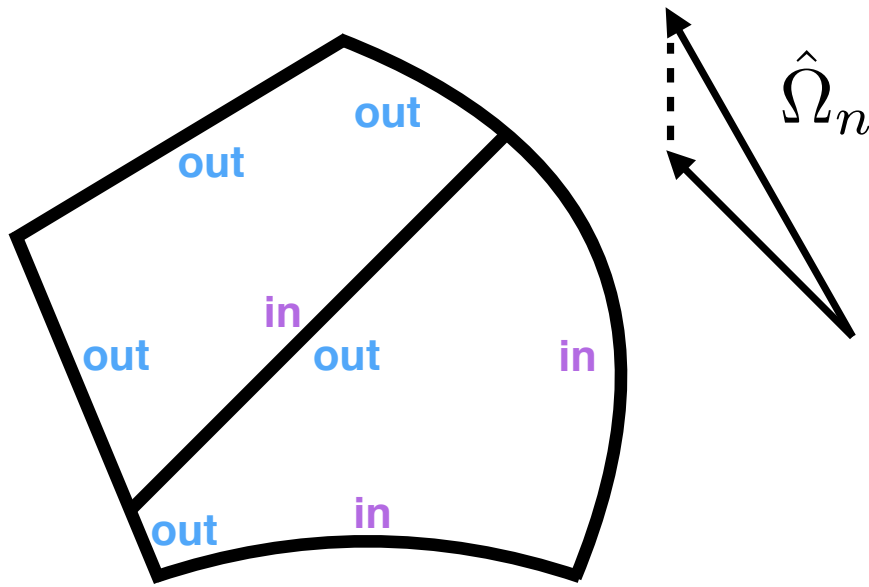


Figure 5.12: The categorization of boundaries as “**incoming**”, “**outgoing**” and “**parallel**”. A parallel boundary does not appear in this example.

Instead of the intuitive categorization of whether a boundary is incoming, outgoing or parallel, there is an analytic criteria that enables a computer code to be implemented for an automatic categorization. Recall the definition of the $\vec{A}_1(c)$ vector of a boundary c , which is parametrized with $\vec{p}(t)$, $a \leq t \leq b$ (see equation (5.6)), and which has a normal vector $\hat{n}(t) = (n_x(t), n_y(t))$ (see equation (5.8)). We repeat

the definition of equation (5.16):

$$\vec{A}_1(c) = \int_a^b \begin{pmatrix} n_x(t) \\ n_y(t) \end{pmatrix} dt. \quad (5.38)$$

Then a criteria for categorization of the boundaries $C(f)$ of a cell f at direction $\hat{\Omega}$ is:

$$C_{in}(f, \hat{\Omega}) = \{c \in C(f) \mid \vec{A}_1(c) \cdot \hat{\Omega} < 0\}, \quad (5.39)$$

$$C_{out}(f, \hat{\Omega}) = \{c \in C(f) \mid \vec{A}_1(c) \cdot \hat{\Omega} > 0\}, \quad (5.40)$$

$$C_{para}(f, \hat{\Omega}) = \{c \in C(f) \mid \vec{A}_1(c) \cdot \hat{\Omega} = 0\}. \quad (5.41)$$

See Figure 5.13 for an example of how the \vec{A}_1 vector can be used to categorize the boundaries. Table 5.6 summarizes the criteria of categorization.

Because every re-entrant boundary is “split” with the process described in the section 5.3, there are no re-entrant boundaries. Therefore, $\hat{\Omega} \cdot \hat{n}(t)$ has the same sign for all points on each boundary of the cell. So, the inner product $\hat{\Omega} \cdot \vec{A}_1$ for a boundary has the same sign with $\hat{\Omega} \cdot \hat{n}(t)$ for all points on the boundary. As a result, $\hat{\Omega} \cdot \vec{A}_1$ can be used to determine correctly whether the boundary is “**incoming**”, “**outgoing**” or “**parallel**”.

Table 5.6: The criteria for categorization of the boundaries of a cell at a specific direction

c is an “ incoming ” boundary of f in direction $\hat{\Omega}$: if $\vec{A}_1(c) \cdot \hat{\Omega} < 0$
c is an “ outgoing ” boundary of f in direction $\hat{\Omega}$: if $\vec{A}_1(c) \cdot \hat{\Omega} > 0$
c is an “ parallel ” boundary of f in direction $\hat{\Omega}$: if $\vec{A}_1(c) \cdot \hat{\Omega} = 0$

Now for any angle $\hat{\Omega}$, all boundaries $C(f)$ can be categorized into three mutually

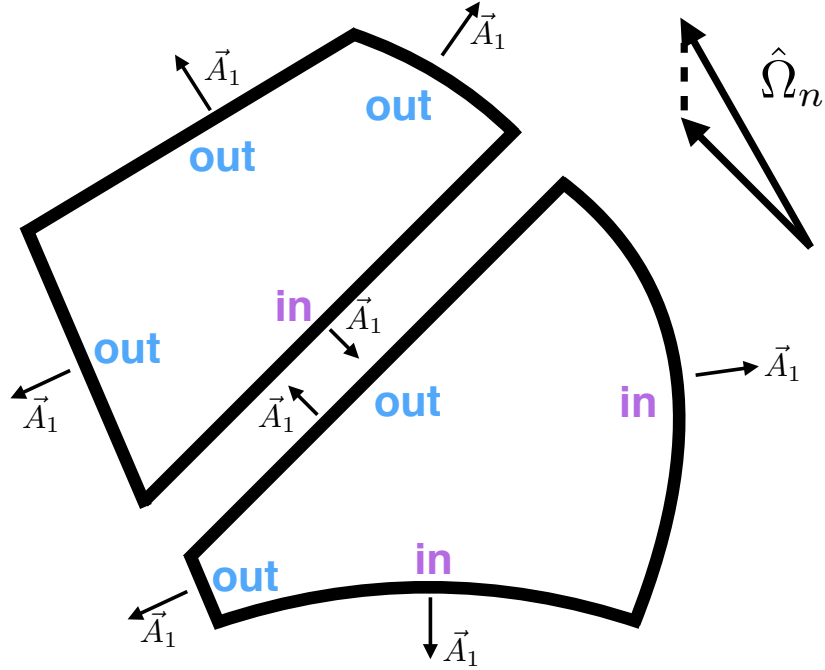


Figure 5.13: An analytic criteria, which is based on the sign of the dot product between the A_1 vector and the direction of traveling $\hat{\Omega}_n$, for categorization of a boundary as “**incoming**”, “**outgoing**” and “**parallel**”.

exclusive sets $C_{in}(f, \hat{\Omega})$, $C_{out}(f, \hat{\Omega})$ and $C_{para}(f, \hat{\Omega})$:

$$\forall \hat{\Omega}, \quad |\hat{\Omega}| = 1 :$$

$$C(f) = C_{in}(f, \hat{\Omega}) \cup C_{out}(f, \hat{\Omega}) \cup C_{para}(f, \hat{\Omega}), \quad (5.42)$$

$$C_{in}(f, \hat{\Omega}) \cap C_{out}(f, \hat{\Omega}) = \emptyset, \quad (5.43)$$

$$C_{in}(f, \hat{\Omega}) \cap C_{para}(f, \hat{\Omega}) = \emptyset, \quad (5.44)$$

$$C_{out}(f, \hat{\Omega}) \cap C_{para}(f, \hat{\Omega}) = \emptyset. \quad (5.45)$$

5.5 Auxiliary Equations

For any cell f , the unknowns in the neutron balance equation (5.35) for the direction $\hat{\Omega}_n$ and group g are:

$$\bar{\psi}_{n,g,f} \quad \text{for all cells } f, \quad (5.46)$$

$$\psi_{n,g,c} \quad \text{for any boundary } c \in C_{out}(f, \hat{\Omega}_n), \quad \text{for any } f. \quad (5.47)$$

We illustrate, in Figure 5.14, the averaged cell and boundary fluxes for common curved spatial cells that one encounters in a pin-cell. (See Figure 5.2 for the definition of a pin-cell) Figure 5.14 denotes the results of whether a boundary is incoming or outgoing. See section 5.4 for a discussion of the categorization of the boundaries. If a re-entrant boundary is encountered, the approach discussed in the section 5.3 will be applied.

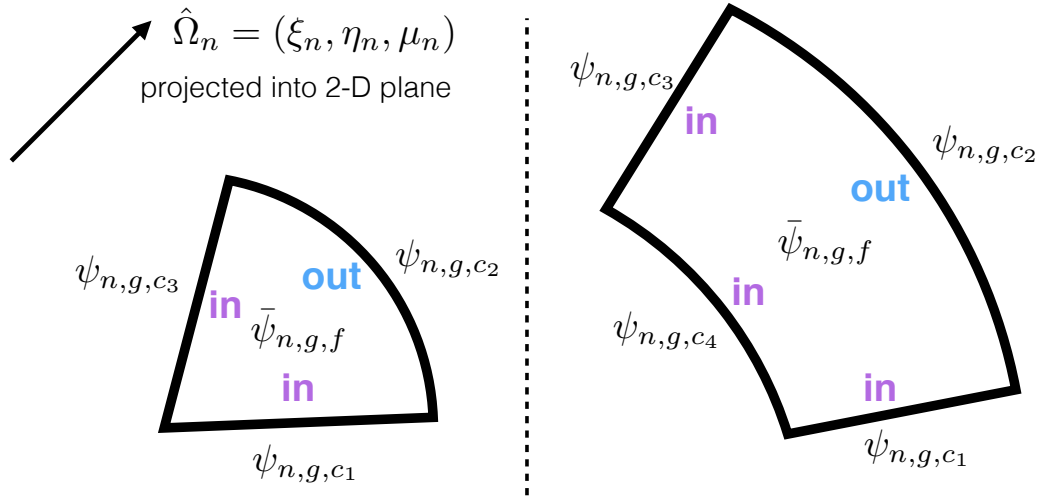


Figure 5.14: Examples of curved spatial cells that one usually encounter in a pin-cell geometry. The cell-averaged and boundary averaged fluxes are labeled. For the direction of flight $\hat{\Omega}$, all boundaries are categorized as “incoming”, which is marked as “in”, or is categorized as “outgoing”, which is marked as “out”.

For every specific direction, the number of unknowns equals the number of outgoing boundaries plus one. The neutron balance equation (5.35) gives us one equation already. So more equations, the number of which equals the number of outgoing boundaries, are necessary to solve for all unknowns in equation (5.46) and (5.47). These equations are called “**auxiliary equations**”. In the following subsections, three methods of providing auxiliary equations are given. The first two methods are the “**step method**” and the “**simplified step characteristic method**”. They are not very accurate, but they are provided here first for their simplicity, second for the reader to become accustomed to the notation, and third for their desired property that the solutions are always positive. The third method provided is a new “**multiple balance method**”, which is more accurate than the others.

5.5.1 The Step Method (STEP)

The step method is one of the traditional methods (*Lathrop, 1969*), which is here generalized to spatial grids with curved boundaries. The assumption made is that the outgoing boundary-averaged fluxes equal the cell-averaged flux. So the auxiliary equations are:

$$\psi_{n,g,c} = \bar{\psi}_{n,g,f}, \quad c \in C_{out}(f, \hat{\Omega}_n). \quad (5.48)$$

The definition of the outgoing boundaries can be found in equation (5.40). The STEP auxiliary equations for two example spatial cells that one usually encounters in a pin-cell geometry are illustrated in Figure 5.15.

5.5.2 The Simplified Step Characteristic Method (SSC)

Even though neutron transport is in two dimensions, it can be approximated as transporting on 1-D characteristic lines along the direction of flight. The length of

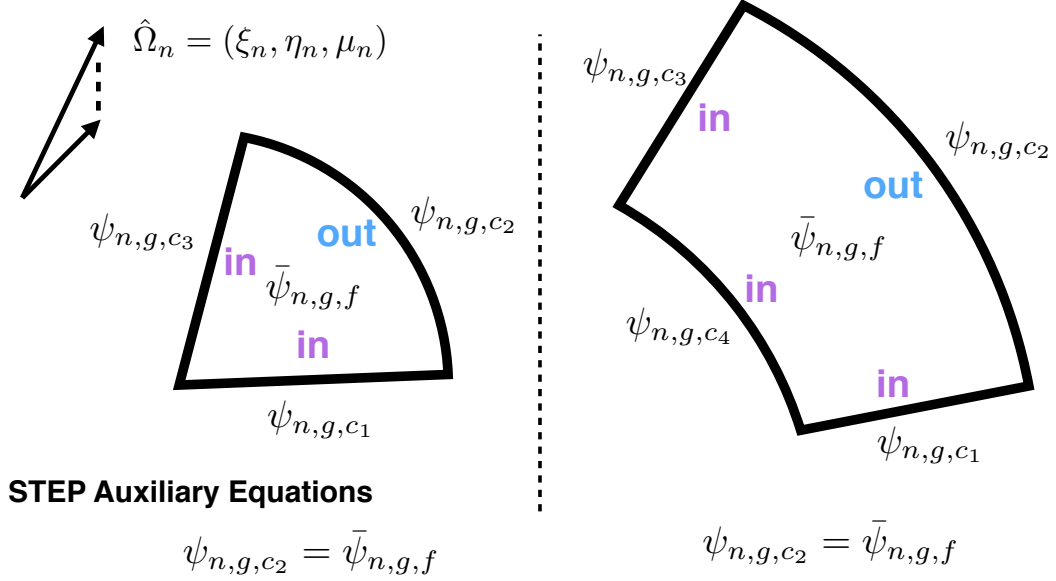


Figure 5.15: The STEP auxiliary equations for two example spatial cells that one usually encounters in a pin-cell geometry.

the characteristic line can be approximated as l , which is defined as:

$$d = - \sum_{c \in C_{in}(f, \hat{\Omega}_n)} \hat{\Omega}_n \cdot \vec{A}_1(c), \quad (5.49)$$

$$s = \frac{M_0(f)}{d}, \quad (5.50)$$

where we recall from equation 5.17:

$$M_0(f) = \text{the volume (area in 2D) of the cell } f, \quad (5.51)$$

and where the definition $\vec{A}_1(c)$ can be found in equation (5.16), which is repeated here:

$$\vec{A}_1(c) = \int_a^b (\hat{n}(t)) dt,$$

and we recall that the parametrization of a boundary c is:

$$\vec{x} = \vec{p}(t), \quad a \leq t \leq b.$$

The terms d and l in these formula are the side lengths of a box, with one side parallel to the direction of flight. Two example spatial cells that one usually encounters in a pin-cell geometry are given in Figure 5.16. These boxes with side lengths d and l are marked in green.

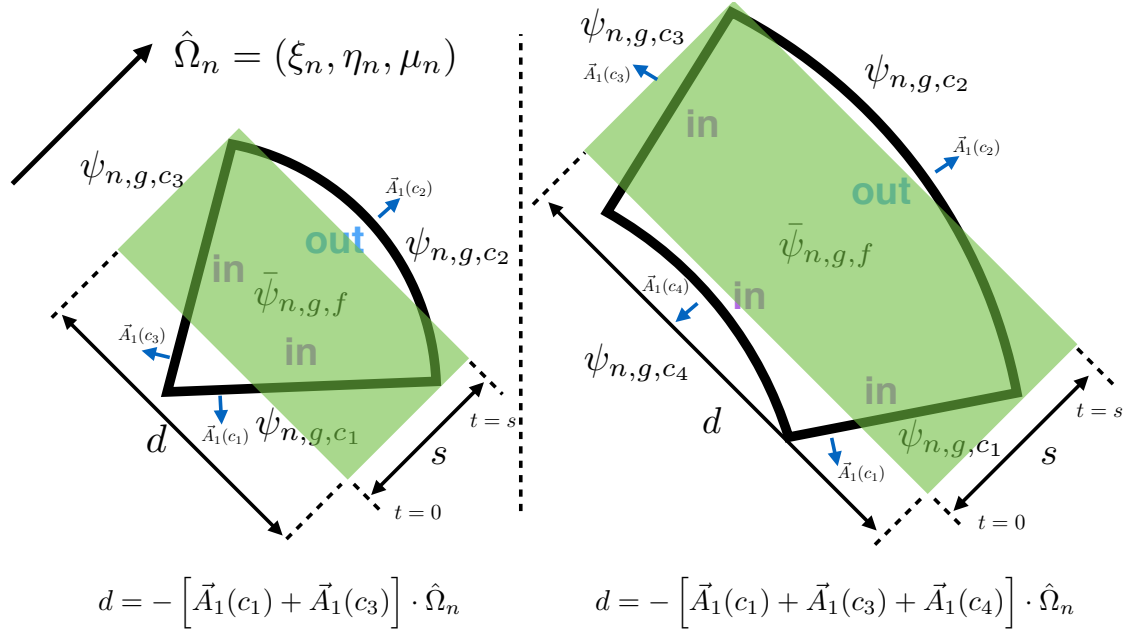


Figure 5.16: In the simplified step characteristic method, the two-dimensional transport is approximated by a one-dimensional transport process along the t axis from $t = 0$ to $t = s$. s and d are the length and the width of the box marked in green. One side of the box is parallel to the direction of flight. The width d is the shallow of the cell projected to a line perpendicular to the direction of flight. The green box has the same area as the that of the cell. These requirements determine the width and length of the green box. Two example spatial cells that one usually encounters in a pin-cell geometry are depicted in the figure.

The height d as defined in equation (5.49) is the shadow of the cell onto a line

that is perpendicular to the direction of flight. The length s is chosen so that the area of the cell, i.e. $M_0(f)$, equals the area of the box, i.e. $s d$:

$$s d = M_0(f). \quad (5.52)$$

The approximate one-dimensional transport equation is:

$$\mu_n \frac{d\psi_{1d}(t)}{dt} + \Sigma_t \psi_{1d}(t) = \bar{Q}, \quad 0 \leq t \leq s, \quad (5.53)$$

where the transport cross section and the source terms are defined as:

$$\Sigma_t = \Sigma_{t,g,f}, \quad (5.54)$$

$$\bar{Q} = \bar{Q}_{s,g,f} + \frac{1}{k} \bar{Q}_{f,g,f}. \quad (5.55)$$

See Table 5.5 for definitions of $\bar{Q}_{s,g,f}$ and $\bar{Q}_{f,g,f}$ above. The solution to this one-dimensional transport equation (5.53) is:

$$\psi_{1d}(t) = \frac{\bar{Q}}{\Sigma_t} (1 - e^{-\Sigma_t t / \mu_n}) + \psi_{1d}(0), \quad 0 \leq t \leq s, \quad (5.56)$$

and the evaluation of the flux at the end $t = s$ is:

$$\psi_{1d}(s) = \frac{\bar{Q}}{\Sigma_t} (1 - e^{-\Sigma_t s / \mu_n}) + \psi_{1d}(0), \quad (5.57)$$

where $\psi_{1d}(0)$ is chosen to be an averaged of the incoming flux:

$$\psi_{1d}(0) = \frac{\sum_{c \in C_{in}(f, \hat{\Omega}_n)} \hat{\Omega}_n \cdot \vec{A}_1(c) \bar{\psi}_{n,g,c}}{\sum_{c \in C_{in}(f, \hat{\Omega}_n)} \hat{\Omega}_n \cdot \vec{A}_1(c)}, \quad (5.58)$$

which is defined despite that it is not used in the derivation of an auxiliary equation.

The averaged flux on this one-dimensional line is:

$$\bar{\psi}_{1d} = \frac{1}{s} \int_0^s \psi_{1d}(t) dt \quad (5.59)$$

$$= \frac{\bar{Q}}{\Sigma_t} \left(1 - \frac{1 - e^{-\Sigma_t s / \mu_n}}{\Sigma_t s / \mu_n} \right) + \psi_{1d}(0) \frac{1 - e^{-\Sigma_t s / \mu_n}}{\Sigma_t s / \mu_n}. \quad (5.60)$$

Eliminating $\psi_{1d}(0)$ in equations (5.57) and (5.60), we get:

$$\psi_{1d}(s) = \frac{\bar{Q}}{\Sigma_t} \left(1 - \frac{(\Sigma_t s / \mu_n) e^{-\Sigma_t s / \mu_n}}{1 - e^{-\Sigma_t s / \mu_n}} \right) + \bar{\psi}_{1d} \frac{(\Sigma_t s / \mu_n) e^{-\Sigma_t s / \mu_n}}{1 - e^{-\Sigma_t s / \mu_n}}. \quad (5.61)$$

The auxiliary equations are obtained by first setting the fluxes on the outgoing boundaries equal to $\phi(s)$, and second setting the average cell flux to $\bar{\psi}$:

$$\bar{\psi}_{n,g,c} = \psi_{1d}(s), \quad c \in C_{out}(f, \hat{\Omega}_n), \quad (5.62)$$

$$\bar{\psi}_{n,g,f} = \bar{\psi}_{1d}. \quad (5.63)$$

Next, we define l to simplify equations:

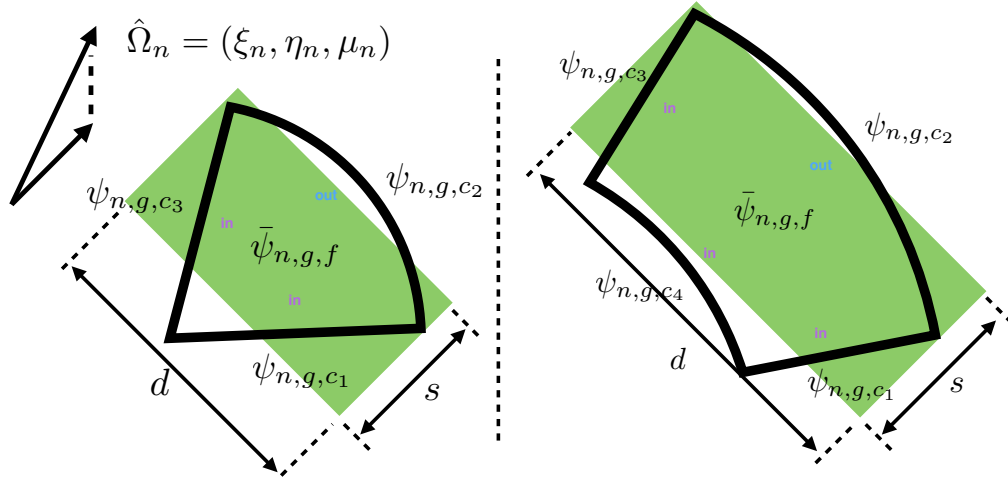
$$l = s / \mu_n. \quad (5.64)$$

Introducing equations (5.62), (5.63) into equation (5.61), we get:

$$\psi_{n,g,c} = \frac{\bar{Q}}{\Sigma_t} \left(1 - \frac{(\Sigma_t l) e^{-\Sigma_t l}}{1 - e^{-\Sigma_t l}} \right) + \bar{\psi}_{n,g,f} \frac{(\Sigma_t l) e^{-\Sigma_t l}}{1 - e^{-\Sigma_t l}}, \quad c \in C_{out}(f, \hat{\Omega}_n). \quad (5.65)$$

See equations above for definitions of the quantities in the auxiliary equation (5.65).

The SSC auxiliary equations for two example spatial cells that one usually encounters in a pin-cell geometry are illustrated in Figure 5.17.



SSC Auxiliary Equations

$$\psi_{n,g,c_2} = \psi_{1d}(s) \quad \psi_{1d}(s) = \frac{\bar{Q}}{\Sigma_t} \left(1 - \frac{(\Sigma_t l) e^{-\Sigma_t l}}{1 - e^{-\Sigma_t l}} \right) + \bar{\psi}_{n,g,f} \frac{(\Sigma_t l) e^{-\Sigma_t l}}{1 - e^{-\Sigma_t l}} \quad l = s/\mu_n$$

Figure 5.17: The SSC auxiliary equations for two example spatial cells that one usually encounters in a pin-cell geometry.

5.5.3 The Multiple Balance Method (MB)

The auxiliary equations in the step method and the simplified characteristic method contain no neutron physics. So it is more favorable if the auxiliary equations have forms similar to the neutron balance equation. Here we generalize the method to two-dimensional curved spatial grid problems.

Consider a cell f , a weight function $w_c(\vec{x})$ is defined for each boundary c in $C(f)$. This weight function is linear and non-negative inside cell f , which has the maximum value of 1 on a point on the outgoing boundary, and has a minimum value of 0. There

are many possibilities, one example is:

$$w_c(\vec{x}) = a_c \vec{A}_1(c) \cdot \vec{x} + b_c, \quad (5.66)$$

$$\forall \vec{x} \in \text{cell } f : 0 \leq w_c(\vec{x}) \leq 1, \quad (5.67)$$

$$\exists \vec{x}_0 \in \text{cell } f : w_c(\vec{x}_0) = 0, \quad (5.68)$$

$$\exists \vec{x}_0 \in \text{boundary } c : w_c(\vec{x}_0) = 1 \quad (5.69)$$

These conditions will determine the unknowns a_c and b_c , which depends on the boundary c . See equation (5.16) for the definition of the vector $\vec{A}_1(c)$.

We recall that the neutron balance equation can be thought as if the leakage term plus the collision term equals the scattering source plus the fission source:

$$\begin{aligned} \text{Leakage} &+ \text{Collision} = \text{Scattering} + \text{Fission} \\ \hat{\Omega} \cdot \int_f \vec{\nabla} \psi_g(\vec{x}) d\vec{x} + \int_f \Sigma_t \psi_g(\vec{x}) d\vec{x} &= \frac{1}{4\pi} \sum_{g'} \int_f \Sigma_s \phi_{g'}(\vec{x}) d\vec{x} + \frac{\chi_g}{4\pi k} \sum_{g'} \int_f \nu \Sigma_f \phi_{g'}(\vec{x}) d\vec{x}. \end{aligned}$$

For the auxiliary equation of the multiple balance method, the discrete ordinates equation is multiplied by the weight function $f_d(\vec{x})$ for outgoing boundary d , and is integrated over the cell:

$$\begin{aligned} \text{Leakage} &+ \text{Collision} = \text{Scattering} + \text{Fission} \\ \hat{\Omega} \cdot \int_f w_d(\vec{x}) \vec{\nabla} \psi_g(\vec{x}) d\vec{x} + \int_f w_d(\vec{x}) \Sigma_t \psi_g(\vec{x}) d\vec{x} &= \frac{1}{4\pi} \sum_{g'} \int_f w_d(\vec{x}) \Sigma_s \phi_{g'}(\vec{x}) d\vec{x} + \frac{\chi_g}{4\pi k} \sum_{g'} \int_f w_d(\vec{x}) \nu \Sigma_f \phi_{g'}(\vec{x}) d\vec{x}. \end{aligned}$$

By the divergence theorem, we have exactly:

$$\int_f w_d(\vec{x}) \vec{\nabla} \psi_g(\vec{x}) d\vec{x} = \sum_{c \in C(f)} \oint_c w_d(\vec{x}) \psi_g(\vec{x}) \hat{n}(\vec{x}) ds - \int_f [\vec{\nabla} w_d(\vec{x})] \psi(\vec{x}) d\vec{x} \quad (5.70)$$

where the flux in boundary integral terms are approximated by the boundary-averaged value, and the flux in the volume integral terms is approximated by the cell-averaged

value:

$$\oint_c w_d(\vec{x})\psi(\vec{x})\hat{n}(\vec{x})ds \approx \oint_c w_d(\vec{x})\psi_c\hat{n}(\vec{x})ds, \quad (5.71)$$

$$\int_f [\vec{\nabla}w_d(\vec{x})]\psi(\vec{x})d\vec{x} \approx \int_f [\vec{\nabla}w_d(\vec{x})]\bar{\psi}d\vec{x}. \quad (5.72)$$

The multiple balance approximation sets the fluxes in the ‘‘collision’’, ‘‘scattering’’ and ‘‘fission’’ terms to be the outgoing flux. The leakage term, by the divergence theorem, is expressed as sum of boundary-averaged fluxes and a cell-averaged flux term:

Approximations for Auxiliary Equation for the Boundary d :

Leakage	Collision	Scattering	Fission
$\int_f w_d \vec{\nabla} \psi(\vec{x}) d\vec{x} \approx \sum_{c \in \mathcal{C}(f)} \oint_c w_d \psi_c \hat{n} ds - \int_f (\vec{\nabla} w_d) \bar{\psi} d\vec{x}$	$\psi(\vec{x}) \approx \psi_d$	$\phi(\vec{x}) \approx \phi_d$	$\phi(\vec{x}) \approx \phi_d$

Without loss of generosity, we derive the auxiliary equations for the outgoing boundary labeled c as an example. The weight function corresponding is $w_c(\vec{x})$. The auxiliary equation is obtained by integrating the discrete ordinates equation (5.22) with the weight function $w_c(\vec{x})$. This integration resembles the finite element method. But in the multiple balance method, the flux in each cell is not assumed to have any predefined shape.

$$\begin{aligned} & \hat{\Omega}_n \cdot \int_f w_c(\vec{x}) \vec{\nabla} \psi_{n,g}(\vec{x}) d\vec{x} + \Sigma_{t,g,f} \int_f w_c(\vec{x}) \psi_{n,g}(\vec{x}) d\vec{x} \\ &= \frac{1}{4\pi} \sum_{g'=1}^G \Sigma_{s,g' \rightarrow g,f} \int_f w_c(\vec{x}) \phi_{g'}(\vec{x}) d\vec{x} + \frac{1}{4\pi k} \chi_{g,f} \sum_{g'=1}^G \nu \Sigma_{f,g',f} \int_f w_c(\vec{x}) \phi_{g'}(\vec{x}) d\vec{x}, \end{aligned}$$

where $d\vec{x} = dx dy$. By integration by parts:

$$\begin{aligned} \int_f w_c(\vec{x}) \vec{\nabla} \psi_{n,g}(\vec{x}) d\vec{x} &= \hat{\Omega}_n \cdot \sum_{d \in C(f)} \oint_d w_c(\vec{x}) \psi_{n,g}(\vec{x}) \hat{n}(s) ds \\ &\quad - \hat{\Omega}_n \cdot \int_f \vec{\nabla} w_c(\vec{x}) \psi_{n,g}(\vec{x}) d\vec{x}. \end{aligned} \quad (5.73)$$

To obtain an equation depending only on $\bar{\psi}_{n,g,f}$, $\psi_{n,g,c}$ for each outgoing boundary $c \in C_{out}(f, \hat{\Omega}_n)$ (see equations (5.46) and (5.47) for the form of the auxiliary equations), careful approximations are applied to equation (5.73) according to the discussions above. The first approximation is applied to the boundary integral in the leakage term, where the flux on the cell boundaries are assumed to be constant:

Leakage boundary term:

$$\hat{\Omega}_n \cdot \sum_{d \in C(f)} \oint_d w_c(\vec{x}) \psi_{n,g}(\vec{x}) \hat{n}(s) ds \approx \hat{\Omega}_n \cdot \sum_{d \in C(f)} \left(\oint_d w_c(\vec{x}) \hat{n}(s) ds \right) \psi_{n,g,d}. \quad (5.74)$$

The second approximation is applied to the cell integral in the leakage term, where the flux in the cell is assumed to be the cell-averaged value:

Leakage cell term:

$$\begin{aligned} &\hat{\Omega}_n \cdot \int_f \vec{\nabla} w_c(\vec{x}) \psi_{n,g}(\vec{x}) d\vec{x}, \\ &\approx \hat{\Omega}_n \cdot \left(\int_f \vec{\nabla} w_c(\vec{x}) d\vec{x} \right) \bar{\psi}_{n,g,f}, \\ &= \hat{\Omega}_n \cdot \left(\sum_{d \in C(f)} \oint_d w_c(\vec{x}) \hat{n}(s) ds \right) \bar{\psi}_{n,g,f}. \end{aligned} \quad (5.75)$$

The third approximation is applied to the collision term, where the flux inside the

cell is assumed to be a constant and equal to the outgoing flux:

$$\mathbf{Collision:} \quad \Sigma_{t,g,f} \int_f w_c(\vec{x}) \psi_{n,g}(\vec{x}) d\vec{x} \approx \Sigma_{t,g,f} \left(\int_f w_c(\vec{x}) d\vec{x} \right) \psi_{n,g,c}. \quad (5.76)$$

As we already noted in chapter III, this approximation in the above equation (5.76) might seem strange, since when integrating over a cell, it is more natural to assume the flux to be a constant and equal to the cell-averaged flux. However in the multiple balance equation, each term in the auxiliary equation is meant to resemble the balance equation, “centered” on the boundary of a cell. So the approximation in the above equation (5.76) assumes that the flux inside the cell is taken to be equal to the outgoing flux. This approximation is applied to the scattering and fission term as well, so the fourth approximation is:

Scattering:

$$\frac{1}{4\pi} \sum_{g'=1}^G \Sigma_{s,g' \rightarrow g,f} \int_f w_c(\vec{x}) \phi_{g'}(\vec{x}) d\vec{x} \approx \frac{1}{4\pi} \sum_{g'=1}^G \Sigma_{s,g' \rightarrow g,f} \left(\int_f w_c(\vec{x}) d\vec{x} \right) \phi_{g',c}. \quad (5.77)$$

The fifth approximation is applied to the fission term, where the flux is again assumed to be equal to the outgoing boundary-averaged flux:

$$\begin{aligned} \mathbf{Fission:} \quad & \frac{1}{4\pi k} \chi_{g,f} \sum_{g'=1}^G \nu \Sigma_{f,g',f} \int_f w_c(\vec{x}) \phi_{g'}(\vec{x}) d\vec{x} \\ & \approx \frac{1}{4\pi k} \chi_{g,f} \sum_{g'=1}^G \nu \Sigma_{f,g',f} \left(\int_f w_c(\vec{x}) d\vec{x} \right) \phi_{g',c}. \end{aligned} \quad (5.78)$$

We recall the definitions of source terms from Table 5.5, the fourth and fifth approx-

imations (5.77) and (5.78) are rewritten as:

$$\frac{1}{4\pi} \sum_{g'=1}^G \Sigma_{s,g' \rightarrow g,f} \int_f w_c(\vec{x}) \phi_{g'}(\vec{x}) d\vec{x} \approx \left(\int_f w_c(\vec{x}) d\vec{x} \right) Q_{s,g,f,c}, \quad (5.79)$$

$$\frac{1}{4\pi k} \chi_{g,f} \sum_{g'=1}^G \nu \Sigma_{f,g',f} \int_f w_c(\vec{x}) \phi_{g'}(\vec{x}) d\vec{x} \approx \left(\int_f w_c(\vec{x}) d\vec{x} \right) \frac{1}{k} Q_{f,g,f,c}. \quad (5.80)$$

We introduce the approximate equations (5.74), (5.75), (5.76), (5.79) and (5.80) into equation (5.73), and choose it at each outgoing boundary to be an auxiliary equation:

$$\begin{aligned} & \hat{\Omega}_n \cdot \sum_{d \in C(f)} \left(\oint_d w_c(\vec{x}) \hat{n}(s) ds \right) (\psi_{n,g,d} - \bar{\psi}_{n,g,f}) + \left(\int_f w_c(\vec{x}) d\vec{x} \right) \Sigma_{t,g,f} \psi_{n,g,c} \\ &= \left(\int_f w_c(\vec{x}) d\vec{x} \right) \left[Q_{s,g,f,c} + \frac{1}{k} Q_{f,g,f,c} \right], \quad c \in C_{out}(f, \hat{\Omega}_n). \end{aligned} \quad (5.81)$$

Equation (5.81) is the auxiliary equation. If we compare equation (5.81) with the neutron balance equation (5.35), we see that the two have a very similar form. So we call this method as the “**multiple balance method**”. From the definition of the weight function $w_c(\vec{x})$ from conditions in equation (5.66) and the notation from equation (5.10), (5.11), (5.12), (5.13), (5.14), (5.15), (5.17), (5.18) and (5.19):

$$\oint_d w_c(\vec{x}) \hat{n}(s) ds = \begin{pmatrix} a_c(A_{1x}(c)A_{2xx}(d) + A_{1y}(c)A_{2xy}(d)) + b_c A_{1x}(d) \\ a_c(A_{1x}(c)A_{2yx}(d) + A_{1y}(c)A_{2yy}(d)) + b_c A_{1y}(d) \end{pmatrix}, \quad (5.82)$$

$$\int_f w_c(\vec{x}) d\vec{x} = a_c(A_{1x}(c)M_{1x}(f) + A_{1y}(c)M_{1y}(f)) + b_c M_0(f). \quad (5.83)$$

The multiple balance equation reduces to:

$$\begin{aligned}
& \hat{\Omega}_n \cdot \sum_{d \in C(f)} \begin{pmatrix} a_c(A_{1x}(c)A_{2xx}(d) + A_{1y}(c)A_{2xy}(d)) + b_c A_{1x}(d) \\ a_c(A_{1x}(c)A_{2yx}(d) + A_{1y}(c)A_{2yy}(d)) + b_c A_{1y}(d) \end{pmatrix} (\psi_{n,g,d} - \bar{\psi}_{n,g,f}) \\
& + [a_c(A_{1x}(c)M_{1x}(f) + A_{1y}(c)M_{1y}(f)) + b_c M_0(f)] \Sigma_{t,g,f} \psi_{n,g,c} \\
& = [a_c(A_{1x}(c)M_{1x}(f) + A_{1y}(c)M_{1y}(f)) + b_c M_0(f)] \left[Q_{s,g,f,c} + \frac{1}{k} Q_{f,g,f,c} \right], \\
& c \in C_{out}(f, \hat{\Omega}_n). \tag{5.84}
\end{aligned}$$

Though equation (5.84) is a little tedious, every term is now defined. Moreover, both the neutron balance equation (5.35) and auxiliary equations (5.84) are equations for the cell-averaged flux and boundary-averaged fluxes, as defined in equations (5.46) and (5.47). The MB auxiliary equations for two example spatial cells that one usually encounters in a pin-cell geometry are illustrated in Figure 5.18.

5.6 Sweep

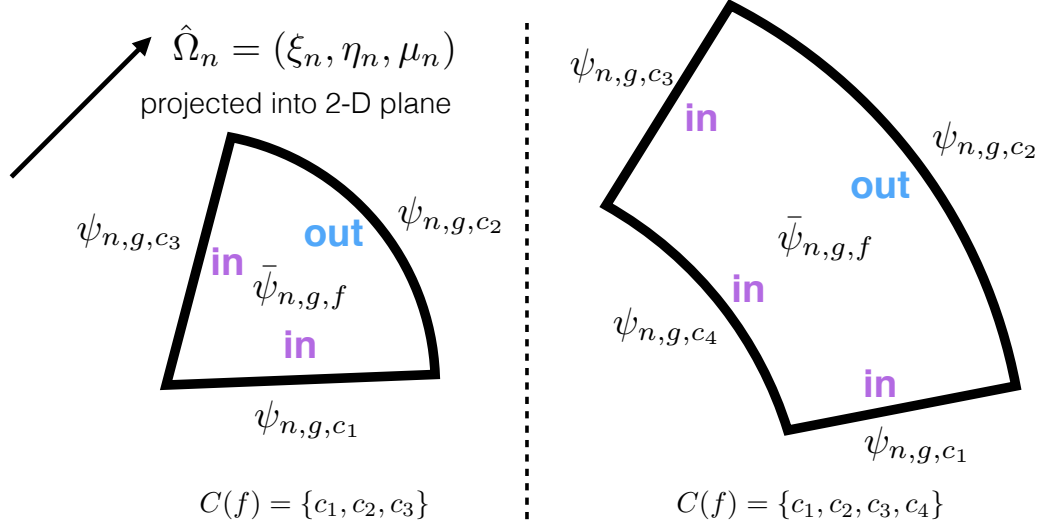
The previous sections introduce the unknowns in a single spatial cell:

$$\forall n = 1..M, g = 1..G :$$

$$\bar{\psi}_{n,g,f} \quad \text{for all cells } f, \tag{5.85}$$

$$\psi_{n,g,c} \quad \text{for any boundary } c \in C(f), \text{ all cells } f. \tag{5.86}$$

The neutron balance equation and the auxiliary equation discussed in the section 5.5 provide enough equations to solve for these unknowns. A 2D curve spatial grid contains many spatial cells with curved boundary. Each cell is visited once. The sweep order must satisfy the condition that the incoming fluxes are calculated before a cell is visited. Figure 5.19 shows one example of the sweeping a geometry formed



Balance Equation

$$\sum_{c \in C(f)} \hat{\Omega}_n \cdot \vec{A}_1(c) \psi_{n,g,c} + \Sigma_{t,g,f} M_0(f) \bar{\psi}_{n,g,f} = M_0(f) \left[\bar{Q}_{s,g,f} + \frac{1}{k} \bar{Q}_{f,g,f} \right].$$

MB Auxiliary Equation

$$\sum_{d \in C(f)} \hat{\Omega}_n \cdot \vec{\alpha}_{c_2,d} (\psi_{n,g,d} - \bar{\psi}_{n,g,f}) + \beta_{c_2} \Sigma_{t,g,f} \psi_{n,g,c_2} = \beta_{c_2} \left[Q_{s,g,f,c_2} + \frac{1}{k} Q_{f,g,f,c_2} \right].$$

Figure 5.18: The MB auxiliary equations for two example spatial cells that one usually encounters in a pin-cell geometry. The definitions of the terms $\vec{\alpha}_{c,d}$ and β_c are defined in equation (5.84). In these examples, only the boundary c_2 is outgoing, so only one auxiliary equation is needed.

with four triangles with neutrons traveling at the direction of the black arrows. Such an order of solving plays an important role in a sweep process.

Next, we determine a procedure to generate the the sweeping order. We consider two neighboring cells f_1 and f_2 with a common boundary c , where for the direction $\hat{\Omega}$, c is the outgoing boundary of f_1 , and c is the incoming boundary of f_2 . Then, we draw two nodes f_1 and f_2 and a directed edge from f_1 to f_2 . Figure 5.20 illustrates this procedure. For the geometry as shown in Figure 5.19, a graph is created in Figure 5.21, which is helpful to get the sweep order. In a sweep, the cell at the starting node of a directed edge needs to be visited before the cell at the end node of a directed edge.

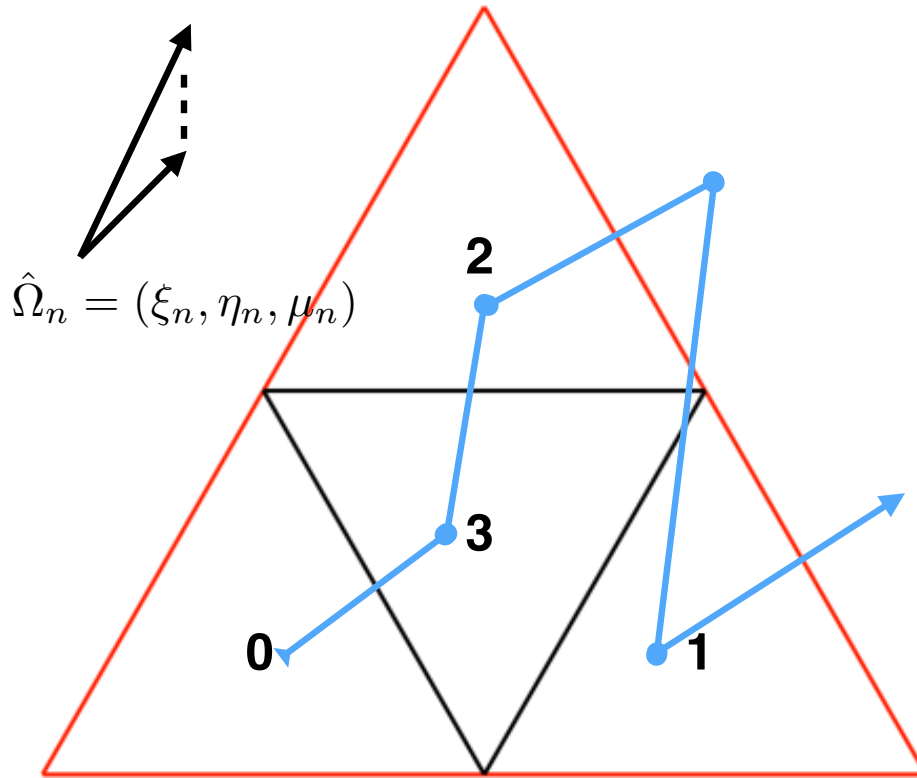


Figure 5.19: The sweep process of four triangles for the direction of the $\hat{\Omega}$. The order is cell 0, 3, 2 and 1. The solving of each cell uses the fluxes of incoming boundaries obtained either from boundary conditions or from the fluxes of outgoing boundaries of cells solved earlier.

After the creation of the graph as shown in Figure 5.21, finding the sweeping order is equivalent to a well studied problem in computer science: “finding the topological order of a directed acyclic graph,” whose algorithm is called the “**topological sorting algorithm**”. A description of the algorithm can be found in *Kahn* (1962), which is written in the early ways of describing computer algorithm. In modern way, the algorithm is described as:

```

function DFS (node)
  visited [node] = yes
  for neighbor of node

```



```

if (not visited[neighbor]) then
DFS (neighbor)
end if
end for
push node into list front
end function

function sort ()
for all nodes
if not visited[node] then
DFS(node)
end if
end for
end function

```

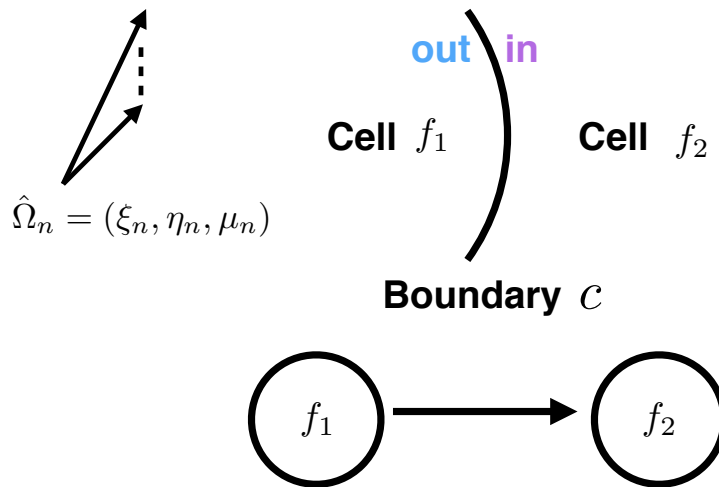


Figure 5.20: Boundary c is the an outgoing boundary of cell f_1 , and is an incoming boundary of cell f_2 . Then two nodes f_1 and f_2 and a directed edge from f_1 to f_2 are drawn in a graph.

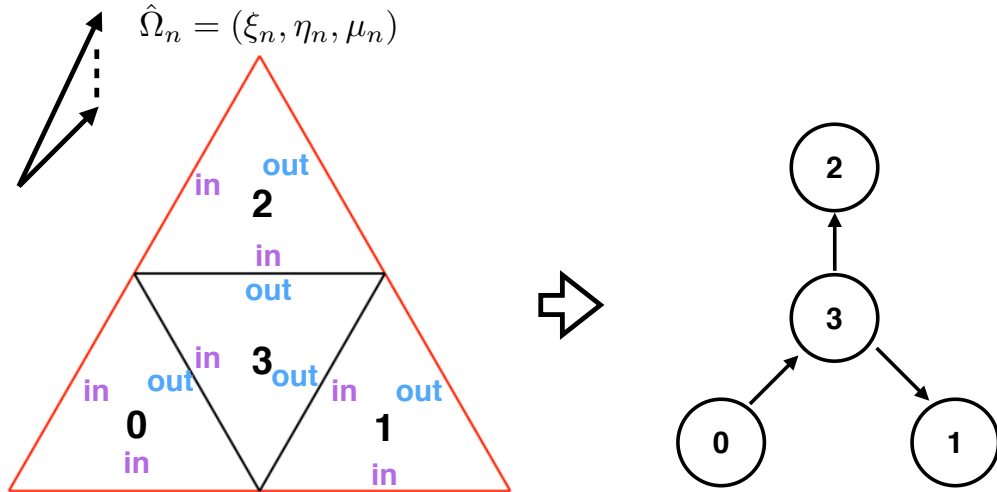


Figure 5.21: A graph showing the sweep orders between two neighboring cells for the four-triangle geometry. In a sweeping, the cell at the starting node of a directed edge needs to be visited before the cell at the end node of a directed edge.

Another example is shown in Figure 5.22, which is a frequently encountered pin-cell geometry. In this example, the re-entrant cells have been split according to the procedure discussed in section 5.3. A graph showing the relative order of sweeping between two neighboring cells is also shown in Figure 5.22. By the “topological sorting algorithm”, a valid sweep order is shown in Figure 5.23.

Next we consider a problem, which contains a coarse Cartesian grid of pin-cells, and each coarse cell is a pin-cell, which contains a fine spatial grid of cells with curved boundaries, as the one shown in Figure 5.24. Then a valid sweeping order determines two stages: first, we sweep over the coarse grid with a procedure discussed in section 3.5, and second, we sweep each pin-cell fine grid based on the procedure discussed in this section.

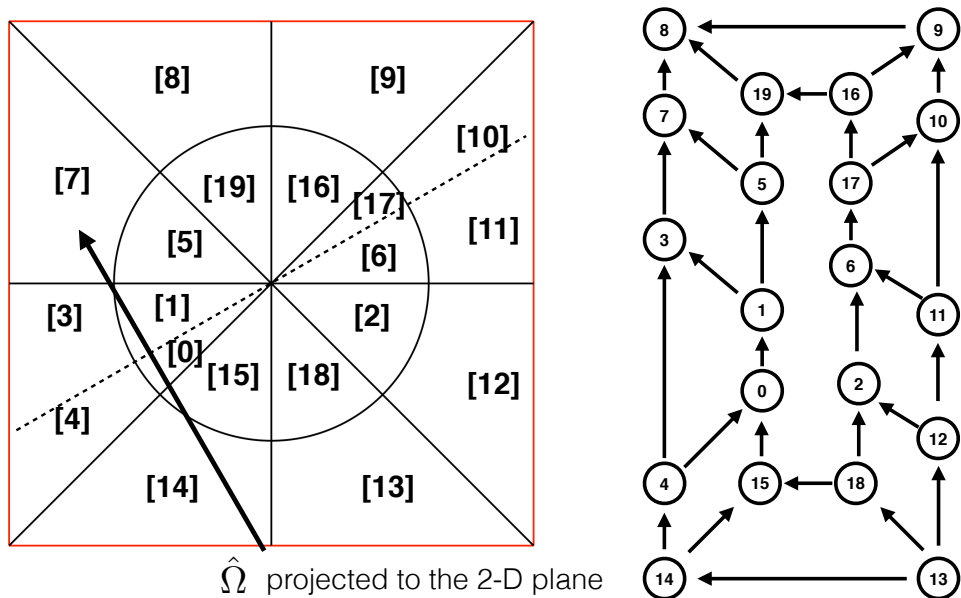


Figure 5.22: A graph showing the sweep orders between two neighboring cells for the pin-cell geometry. In a sweeping, the cell at the starting node of a directed edge needs to be visited before the cell at the end node of a directed edge.

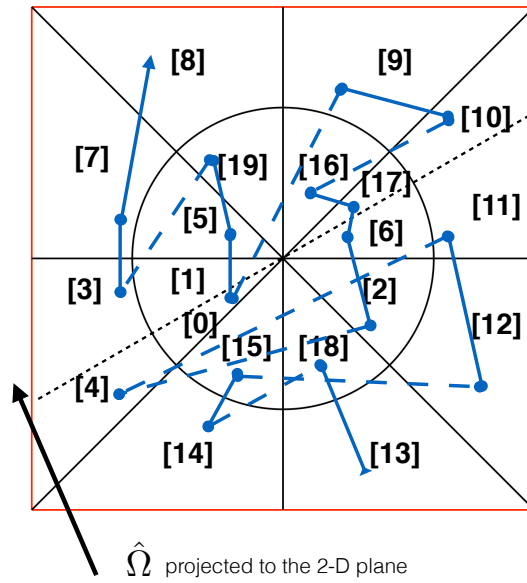


Figure 5.23: A valid sweeping order of a pin-cell at direction $\hat{\Omega}$ is 13, 18, 14, 15, 12, 11, 4, 2, 6, 17, 16, 10, 9, 0, 1, 5, 3, 7, 8. The order is visualized in the graph.

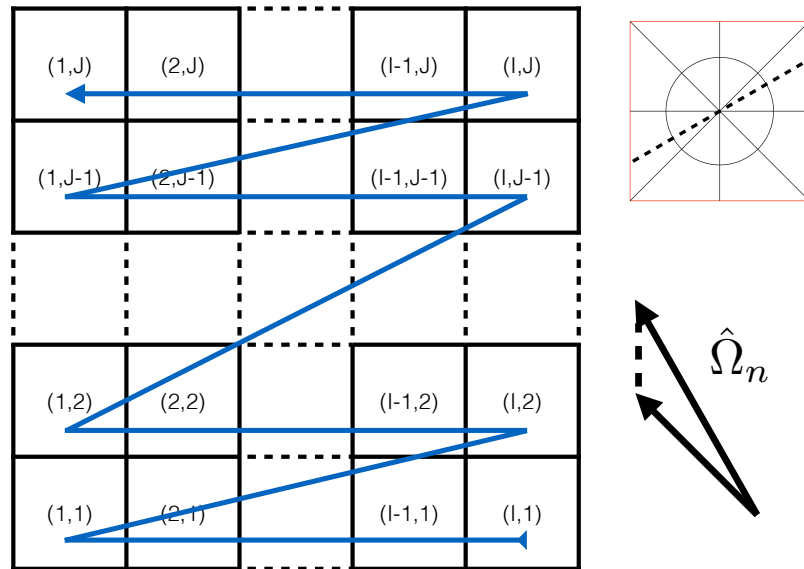


Figure 5.24: A valid sweeping order of a coarse Cartesian grid of pin-cells at direction $\hat{\Omega}$ is determined in two stages. First, we sweep over the coarse grid with a procedure discussed in section 3.5, and second, we sweep each pin-cell fine grid based on the procedure discussed in this section.

CHAPTER VI

Numerical Results for Two-Dimensional One-group Problems with Curved Spatial Grids

The performance of the discrete ordinates (SN) methods on curved spatial grids is studied in this chapter and the next chapter. The problems considered in this chapter have only one energy group. The one-group approximation is crude, but the purpose is to provide reasonably simple problems to understand how the new methods behave compared to existing methods. The discussion begins with a list of one-group cross sections that are used. This is followed by two single pin-cell problems, and then a mini-assembly with an array of pin-cells. More realistic multigroup problems will be considered in the next chapter.

A main goal of the thesis is to compare the new methods to MOC. This section is provided to simplify the comparisons between the SN and the MOC methods. We study the accuracies as a function of time cost for different methods. Each method will have a separate curve, whose data points are calculated for a variety of angular quadrature sets, which are defined in Table 6.1.

Table 6.1: List of number of angles in selected quadrature sets

QUADRATURE SET	NUMBER OF ANGLES
MOC Quadrature Set	
A4P2	64
A4P4	128
A8P4	256
SN Quadrature Set	
S4	24
S8	80
S12	168
S16	288
S20	440

See Table 4.1 for definitions of the quadrature sets abbreviations

6.1 One-group Cross Sections

In a pressurized water reactor, a unit of construction is called a pin-cell, see Figure 6.1. A pin-cell contains the fuel region, the gap, the clad and the moderator. In this section, simple problems with one-group cross sections are described. A reasonably approximate set of one-group cross sections is listed in Table 6.2. For the Westinghouse AP1000 reactor, a special material called the integral fuel burnable absorber (IFBA) exists in some types of pin-cells. The IFBA material is ZrB_2 , which has a very large absorption cross section. A reasonable one-group cross section for IFBA is also provided in Table 6.2.

Table 6.2: List of one-group cross section

MATERIAL	ABSORPTION Σ_a (cm ⁻¹)	NUFISSION $\nu\Sigma_f$ (cm ⁻¹)	FISSION Σ_f (cm ⁻¹)	SCATTERING Σ_s (cm ⁻¹)
Fuel	0.121437	0.19427	0.0788062	0.377744
Gap	0	0	0	3.08906E-05
Clad	0.00313575	0	0	0.280904
Moderator	0.0116829	0	0	1.06112
IFBA	16.5538	0	0	0.26015

These cross sections are generated from the CASL VERA benchmark problem 1. The fuel is 3.1wt% enriched UO_2 . The gap is Helium gas. The Clad is the Zircaloy-4

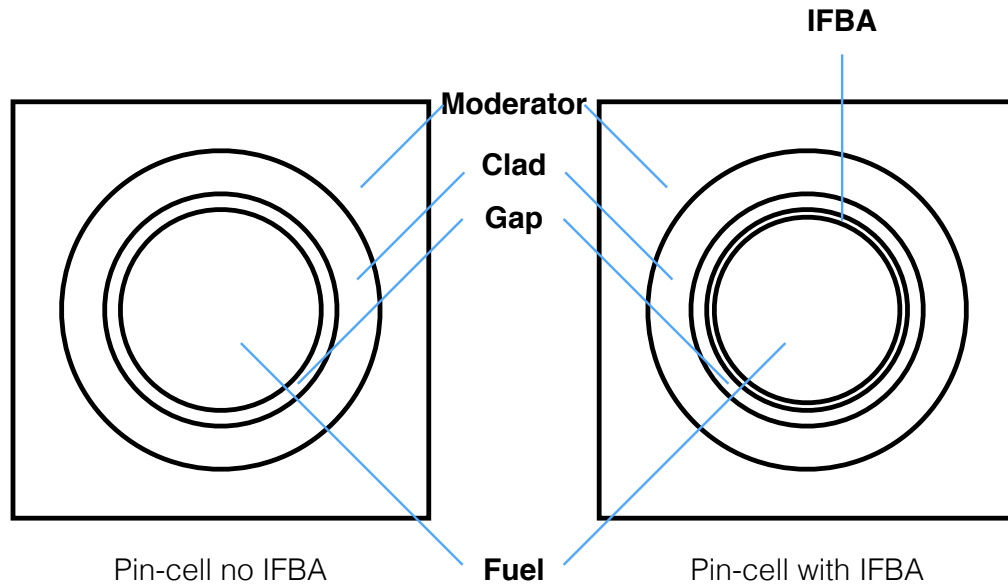


Figure 6.1: Material types in a fuel pin-cell of a pressurized water reactor. Dimensions are exaggerated to show the clad, gap and IFBA, which are much thinner than depicted here.

zirconium alloy. The moderator is water, and as stated earlier, the IFBA is ZrB_2 .

6.2 Single Pin-cell Problems

The discussion of numerical results begins with two single pin-cell problems. One has no IFBA region, and the other has IFBA. See Figure 6.1 for a distinction between the two. The dimensions shown in Table 6.3 are adapted from the CASL VERA Core Physics Benchmark Problem 1 (*Godfrey, 2014*).

6.2.1 Non-IFBA Pin-cell Problem

The pin-cell is divided into a coarse grid of 32 spatial cells and a fine grid of 304 spatial cells. See Figure 6.2.

The problem was solved with different numerical methods. The Monte Carlo

Table 6.3: Pin-cell Dimension Information

DIMENSION	VALUE FOR IFBA PIN-CELL (cm)	NON-IFBA PIN-CELL (cm)	VALUE FOR IFBA PIN-CELL (cm)
Pitch (Size of the Square)			1.26
Outer radius of fuel			0.4096
Outer radius of IFBA	0.4106		N/A
Outer radius of gap			0.418
Outer radius of clad			0.475

solution is used as the benchmark. The benchmark solution is the result of 25 million Monte Carlo particles, with a small uncertainty of 0.03% in flux, and 20 pcm in k -eigenvalue. Table 6.4 summarizes the k -eigenvalue comparison, and time-storage costs for each simulation. Table 6.5 summarizes the solution and error analysis. For convenience, the names of the numerical methods are abbreviated as defined in Table 4.1. The fluxes are normalized such that the area-averaged flux in the fuel region is 1.0.

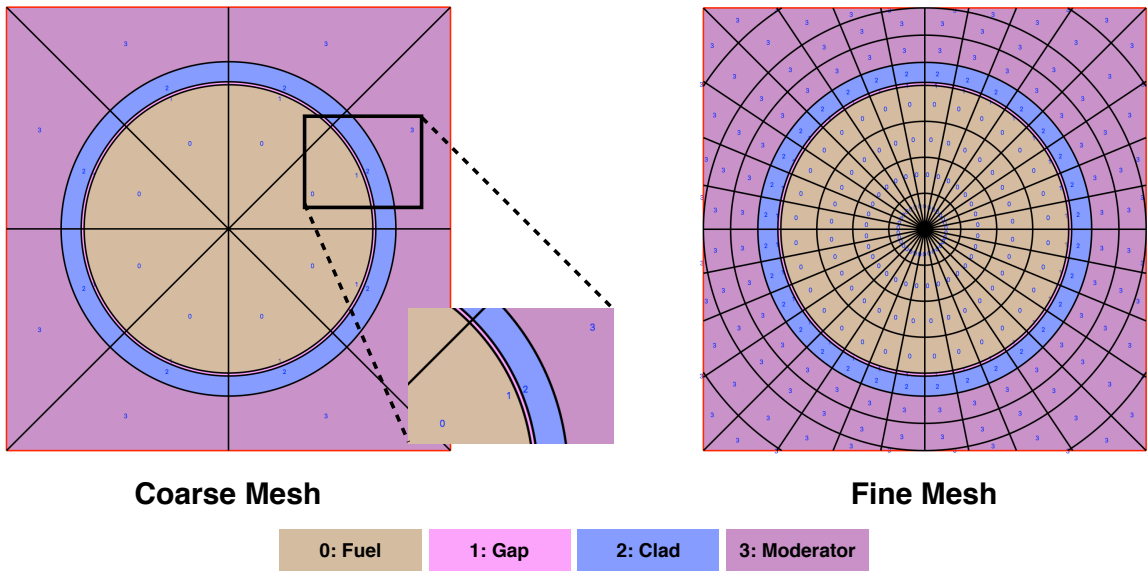


Figure 6.2: The coarse grid and fine grid of the pin-cell without the IFBA coating outside the fuel cylinder. There are 32 spatial cells in the coarse grid and 304 spatial cells in the fine grid.

Table 6.4: List of k -effective, time & storage cost of non-IFBA pin-cell problem

METHOD	KEFF	KEFF ERROR. (pcm)	TIME PER IT- ERATION (ms)	STORAGE (MB)
Coarse Grid				
MOC A8P4 D0.05	1.37113	3	0.7	0.128
MOC A8P4 D0.005	1.37105	-5	6.8	1.261
MOC A8P4 D0.0005	1.37106	-3	70.6	12.538
STEP S4	1.37133	24	0.2	0.032
STEP S8	1.37149	40	0.4	0.033
STEP S16	1.37155	45	1.0	0.034
SSC S4	1.37062	-47	0.2	0.032
SSC S8	1.37078	-31	0.4	0.033
SSC S16	1.37085	-25	1.2	0.034
MB S4	1.37084	-25	0.5	0.032
MB S8	1.37103	-6	1.3	0.033
MB S16	1.37111	2	5.5	0.034
Fine Grid				
MOC A8P4 D0.05	1.31480	-5629	1.6	0.288
MOC A8P4 D0.005	1.37108	-1	15.3	2.712
MOC A8P4 D0.0005	1.37106	-3	146.6	26.853
STEP S4	1.37081	-28	0.9	0.259
STEP S8	1.37108	-1	3.3	0.255
STEP S16	1.37122	13	16.8	0.255
SSC S4	1.37058	-51	1.1	0.259
SSC S8	1.37085	-24	3.9	0.255
SSC S16	1.37099	-10	15.9	0.255
MB S4	1.37049	-60	3.7	0.259
MB S8	1.37079	-30	12.7	0.255
MB S16	1.37103	-6	69.1	0.255

In this problem, solutions obtained on the coarse grid and the fine grid are compared. From the results in Table 6.5, the fine grid solutions are, not surprisingly, more accurate than the coarse grid solution. The deterministic methods all have spatial truncation errors. So the finer the spatial cells are, the more accurate the solution is.

The two figures 6.3 and 6.4 describe the error comparisons of the pin-cell problem without the IFBA layer: one for the coarse grid, and the other for the fine grid. (See subsection 6.2.1.) Equation (2.68) for the definition of the relative errors. The MOC method achieves smaller errors in the flux than the STEP, SSC and MB methods for

Table 6.5: List of solution of non-IFBA pin-cell problem

METHOD	FUEL FLUX	GAP FLUX	CLAD FLUX	MOD- ERATOR FLUX	FLUX ERROR (%)
MC	1.00000	0.99605	0.99486	0.99115	N/A
Coarse Grid					
MOC A8P4 D0.05	1.00000	0.99613	0.99458	0.99105	0.015
MOC A8P4 D0.005	1.00000	0.99616	0.99493	0.99146	0.017
MOC A8P4 D0.0005	1.00000	0.99614	0.99487	0.99136	0.012
STEP S4	1.00000	0.99579	0.99417	0.98995	0.071
STEP S8	1.00000	0.99547	0.99374	0.98912	0.120
STEP S16	1.00000	0.99534	0.99358	0.98881	0.139
SSC S4	1.00000	0.99803	0.99655	0.99358	0.179
SSC S8	1.00000	0.99772	0.99613	0.99275	0.133
SSC S16	1.00000	0.99757	0.99594	0.99242	0.113
MB S4	1.00000	0.99773	0.99625	0.99245	0.128
MB S8	1.00000	0.99719	0.99567	0.99144	0.072
MB S16	1.00000	0.99696	0.99541	0.99103	0.054
Fine Grid					
MOC A8P4 D0.05	1.00000	0.85017	1.00480	0.99981	7.353
MOC A8P4 D0.005	1.00000	0.99612	0.99490	0.99128	0.008
MOC A8P4 D0.0005	1.00000	0.99608	0.99483	0.99118	0.002
STEP S4	1.00000	0.99678	0.99505	0.99263	0.084
STEP S8	1.00000	0.99627	0.99440	0.99125	0.026
STEP S16	1.00000	0.99534	0.99405	0.99051	0.063
SSC S4	1.00000	0.99750	0.99589	0.99385	0.163
SSC S8	1.00000	0.99699	0.99523	0.99245	0.083
SSC S16	1.00000	0.99671	0.99488	0.99172	0.044
MB S4	1.00000	0.99702	0.99597	0.99432	0.176
MB S8	1.00000	0.99656	0.99547	0.99275	0.090
MB S16	1.00000	0.99636	0.99505	0.99149	0.025

the same time costs. The MOC solution is accurate because the flux is spatially very flat, as shown from Table 6.5, and a fundamental assumption of MOC is that in each spatial cell, the scalar flux is flat. Among all the SN methods, the multiple balance method is more accurate than the simplified step characteristic method, which is more accurate than the step method.

For the coarse grid, the multiple balance method has an error in flux about 4 times that of MOC, no matter whether the MOC ray spacing is 0.05 cm, 0.005 cm or 0.0005 cm. The time cost of the multiple balance method is 30 times, 3 times, and

No IFBA Pin-cell Coarse Grid

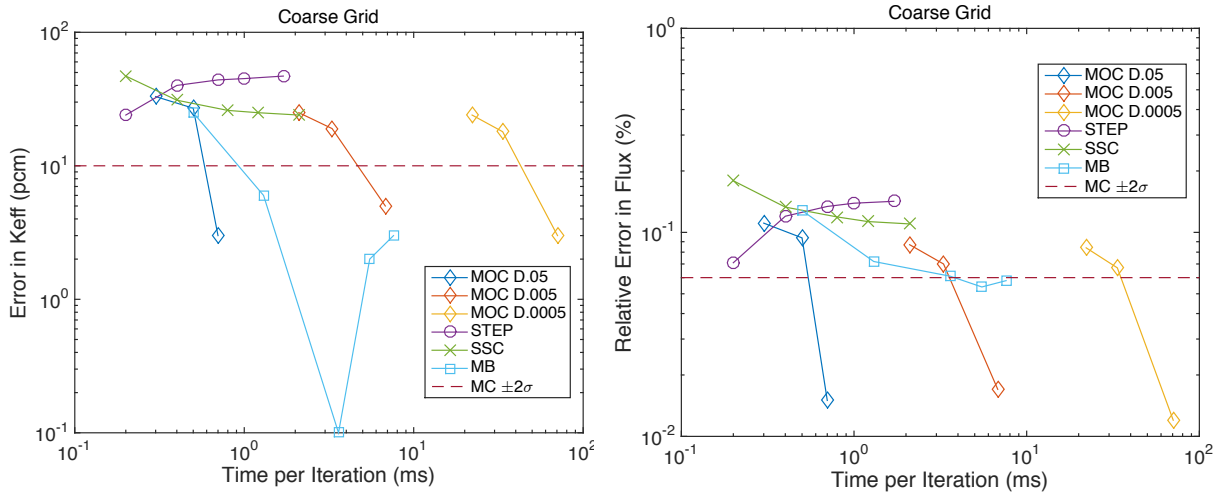


Figure 6.3: The error comparisons for the pin-cell problem without the IFBA layer on the coarse grid. The MOC solutions data points are simulated with a variety of angular quadrature sets: A4P2, A4P4, A8P4. The SN solutions data points are simulated with a variety of angular quadrature sets: S4, S8, S12, S16, S20. The dashed line is the Monte Carlo uncertainties within two standard deviations.

1/3 that of MOC with ray spacing 0.05 cm, 0.005 cm and 0.0005 cm respectively. The storage cost of the multiple balance method is 1/4, 1/40 and 1/400 that of MOC with ray spacing 0.05 cm, 0.005 cm and 0.0005 cm respectively.

For the fine grid, the multiple balance method has a flux error about 3 times that of MOC with ray spacing 0.005 cm. The time cost of the multiple balance method is 4 times that of MOC with ray spacing 0.005 cm. The storage cost of the multiple balance method is 1/10 that of MOC with ray spacing 0.005 cm.

It worth noting that for the fine grid, the MOC solution with a ray spacing of 0.05 cm has a larger error. The average size of spatial cells in the fine grid is on the order of 0.05 cm. With a 0.05 cm ray spacing, the MOC rays do not pass through all the spatial cells. This points out a fundamental character of MOC: **the ray spacing**

No IFBA Pin-cell Fine Grid

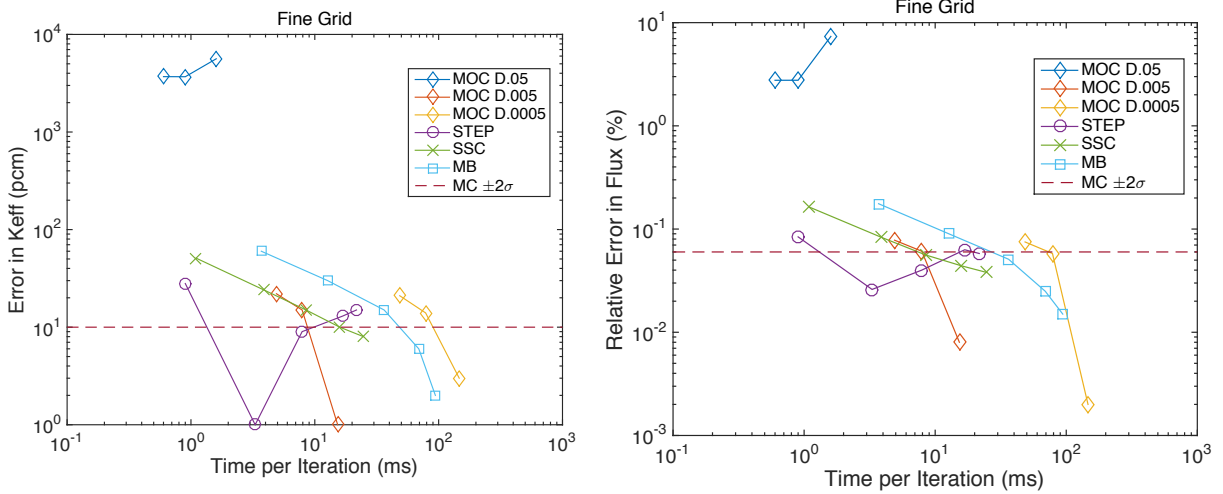


Figure 6.4: The error comparisons for the pin-cell problem without the IFBA layer on the fine grid. The MOC solutions data points are simulated with a variety of angular quadrature sets: A4P2, A4P4, A8P4. The SN solutions data points are simulated with a variety of angular quadrature sets: S4, S8, S12, S16, S20. The dashed line is the Monte Carlo uncertainties within two standard deviations.

needs to be much smaller than the average spatial cell size.

In summary, for the first pin-cell problem, the error of the multiple balance SN solution is about one order of magnitude larger than that of MOC with a time cost about one order of magnitude larger. However, when the spatial cell size becomes smaller, the multiple balance SN method becomes less disadvantageous.

We also note that this is a fairly simple problem, in which the scalar flux solutions is quite “flat”. We will see that for more realistic problems in which the scalar flux has significant spatial gradient, the methods compare quite differently. The next test problem with IFBA layer is more difficult.

6.2.2 IFBA Pin-cell Problem

In the Westinghouse AP1000 reactor, some pin-cells have a thin layer of IFBA material painted outside the fuel cylinders, see Figure 6.1 for an illustration. The IFBA material has a very large absorption cross section, see Table 6.2. The thickness of this layer is very small, on the order of 0.001 cm, about 1/1000 the size of a pin-cell. However IFBA can greatly influence the k -eigenvalue of the problem. Because of its large effect, a study of the IFBA pin-cell is important. As seen from later numerical results, IFBA requires very small ray spacings for MOC.

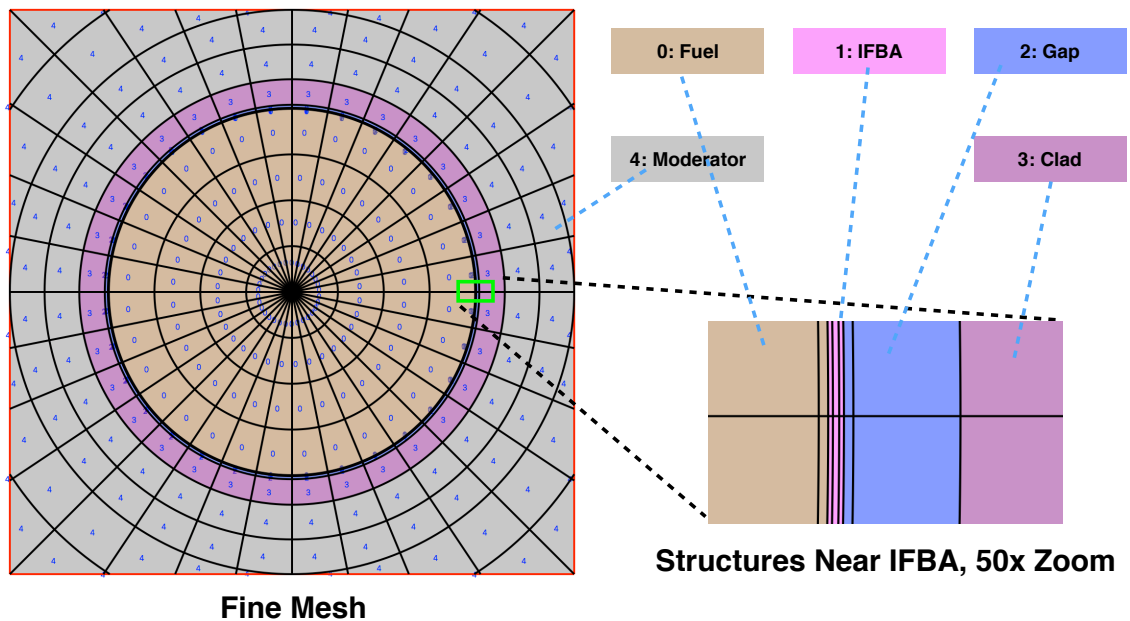


Figure 6.5: The fine grid of spatial cells of a pin-cell with IFBA coating outside the fuel cylinder. There are 464 spatial cells. A zoom-in subplot is shown for the very fine spatial cells inside and near the IFBA layer.

The solutions with different methods are compared in Table 6.6 and Table 6.7. See Table 4.1 for definitions of the methods' name abbreviations. The methods compared include a variety of ray spacings for MOC, which has 8 azimuthal angles per quadrant and 4 polar angles per octant. The comparison also includes the multiple balance SN

method with a variety of angular quadrature sets. There are 12, 40, 144 angles projected into $x - y$ plane for the S4, S8 and S16 angle set respectively.

Table 6.6: List of k -effective, time & storage cost of IFBA pin-cell problem

METHOD	KEFF	KEFF ERROR. (pcm)	TIME PER IT- ERATION (ms)	STORAGE (MB)
MC	0.89024	20	N/A	N/A
MOC A8P4 D0.005	0.90167	1142	21.3	3.352
MOC A8P4 D0.004	0.88847	-177	24.2	4.175
MOC A8P4 D0.002	0.88887	-138	52.6	8.324
MOC A8P4 D0.001	0.88944	-80	101.7	16.597
MOC A8P4 D0.0005	0.89024	-1	206.6	33.163
STEP S4	0.88678	-347	1.4	0.400
STEP S8	0.88821	-203	4.8	0.393
STEP S16	0.88884	-140	26.2	0.393
SSC S4	0.88255	-769	1.7	0.400
SSC S8	0.88388	-637	6.2	0.393
SSC S16	0.88448	-576	24.4	0.393
MB S4	0.88689	-335	5.7	0.400
MB S8	0.88804	-220	19.8	0.393
MB S16	0.88841	-184	100.6	0.393

See Table 4.1 for definitions of the methods' name abbreviations

Figure 6.6 describes the error comparisons for the pin-cell problem with the IFBA layer on the fine grid. (See subsection 6.2.2.) Again, the MOC solution is accurate because the flux is still quite flat, as shown from Table 6.7, and a fundamental assumption of MOC is that in each spatial cell, the scalar flux is flat.

The MOC solutions with the ray spacing of 0.05 cm becomes worse when simulated with more angles. This is explained by the fact that the ray spacing is not fine enough, so that a cell could have no tracks for some directions. This is explained by Figure 6.8.

The next comparison is the flux in the IFBA region. Figure 6.7 compares the scalar flux of the Monte Carlo and MOC methods with 0.0005 cm and 0.005 cm ray spacing, and also the S16 multiple balance method. There is a slight dip of the scalar flux in the IFBA region because of the strong absorption. MOC with 0.0005 cm ray

Table 6.7: List of solution of IFBA pin-cell problem

METHOD	FUEL FLUX	IFBA FLUX	GAP FLUX	CLAD FLUX	MOD- ERATOR FLUX	FLUX ERROR (%)
MC	1.00000	0.94923	0.96498	0.97472	0.97736	N/A
MOC A8P4 D0.005	1.00000	0.91281	0.97083	0.97799	0.97943	1.75
MOC A8P4 D0.004	1.00000	0.95419	0.96586	0.97502	0.97757	0.24
MOC A8P4 D0.002	1.00000	0.95338	0.96535	0.97498	0.97748	0.20
MOC A8P4 D0.001	1.00000	0.95165	0.96530	0.97503	0.97747	0.12
MOC A8P4 D0.0005	1.00000	0.94921	0.96611	0.97521	0.97757	0.06
STEP S4	1.00000	0.95867	0.97293	0.97911	0.98172	0.64
STEP S8	1.00000	0.95510	0.97140	0.97736	0.97846	0.43
STEP S16	1.00000	0.95360	0.97038	0.97634	0.97676	0.33
SSC S4	1.00000	0.97067	0.97590	0.98242	0.98553	1.24
SSC S8	1.00000	0.96742	0.97430	0.98062	0.98219	1.02
SSC S16	1.00000	0.96600	0.97323	0.97955	0.98046	0.92
MB S4	1.00000	0.95771	0.97094	0.97868	0.98425	0.61
MB S8	1.00000	0.95502	0.96956	0.97786	0.98090	0.41
MB S16	1.00000	0.95449	0.96909	0.97661	0.97857	0.33

See Table 4.1 for definitions of the methods' name abbreviations

spacing and the S16 multiple balance method have solutions close to the Monte Carlo reference.

But the MOC solution with 0.005 cm ray spacing has a significantly lower IFBA flux than Monte Carlo reference. This may be explained by the illustration in Figure 6.8. This figure illustrates that when the ray spacing is wide enough, there are directions in which the rays might not pass through the cell. So the angular flux for that cell in that direction may be zero. Since the scalar flux in the cell is obtained by summing the angular fluxes from all directions, the scalar flux will be artificially low when the angular flux in some direction is zero. This may be an important reason why the MOC solution with a ray spacing of 0.005 cm in Figure 6.7 is incorrectly low. The new multiple balance method is advantageous because such an unphysical low scalar flux in the IFBA region does not occur.

We emphasize that for all the SN methods, **only one spatial grid** is needed. The second spatial grid of fine rays is not required. So the new multiple balance method

IFBA Pin-cell Fine Grid

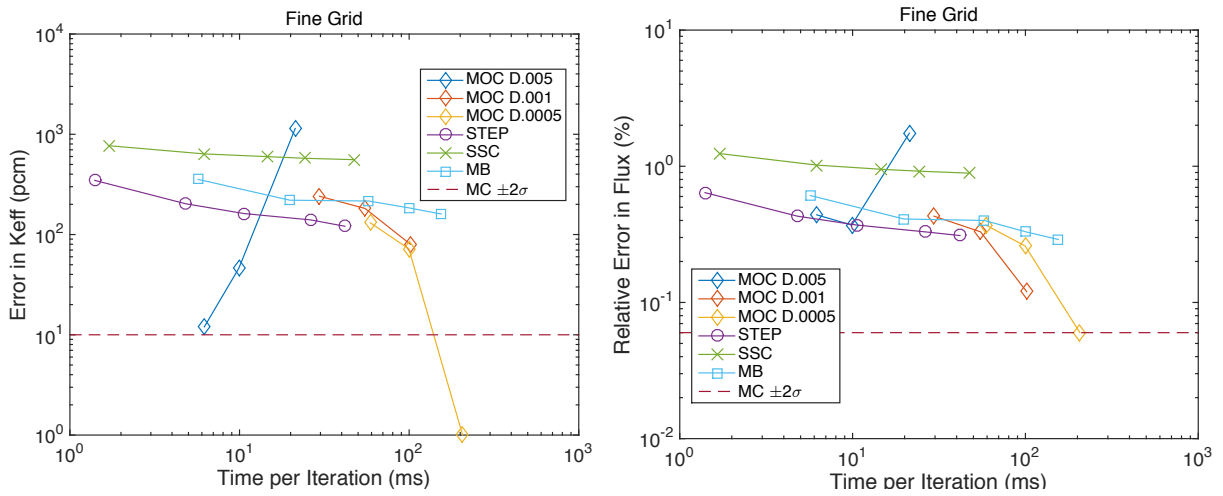


Figure 6.6: The error comparisons for the pin-cell problem with a thin IFBA layer on the fine grid. The MOC solutions data points are simulated with a variety of angular quadrature sets: A4P2, A4P4, A8P4. The SN solutions data points are simulated with a variety of angular quadrature sets: S4, S8, S12, S16, S20. The dashed line is the Monte Carlo uncertainties within two standard deviations.

has the advantage of easier implementation.

In the first two problems, the STEP method has surprisingly small errors. This can perhaps be explained by the fundamental STEP assumption: the outgoing fluxes equal the cell averaged flux. The fluxes in the first two problems are quite flat. So not surprisingly, the STEP method is also accurate.

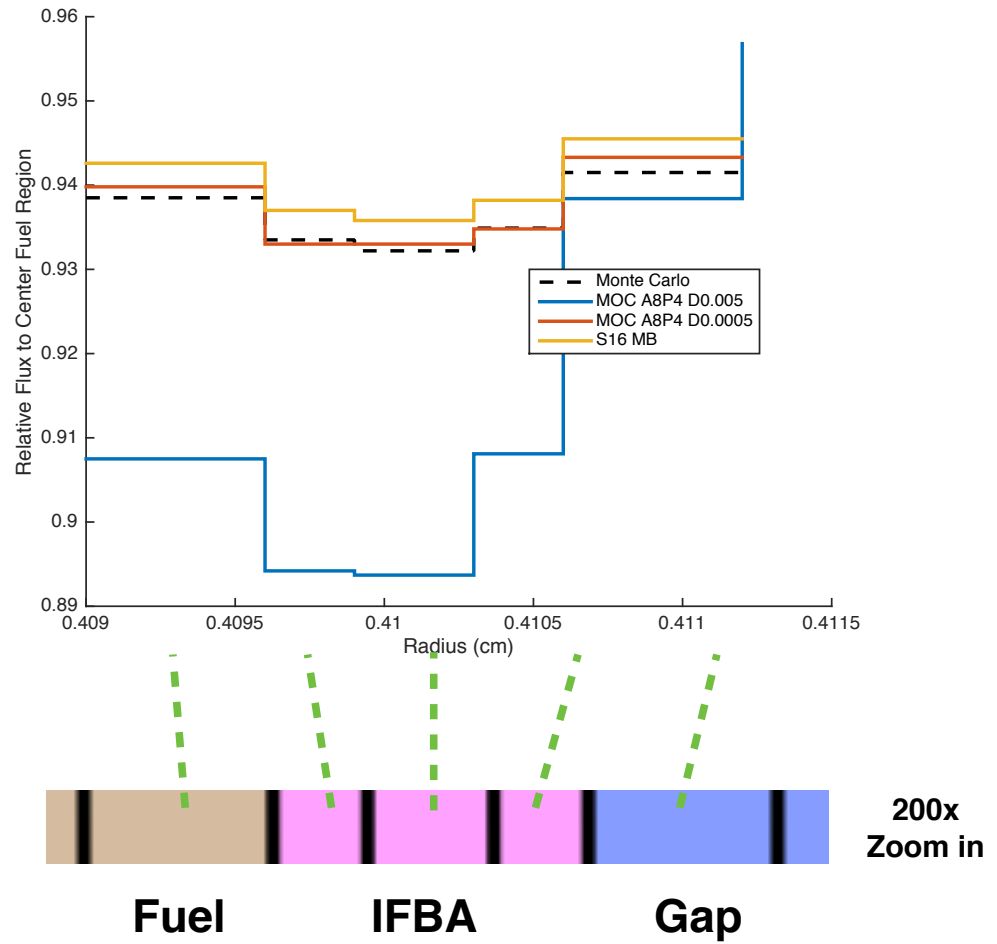


Figure 6.7: Detailed scalar flux inside and near the IFBA region. A dip in flux is observed because of large absorption cross section. MOC with wide ray spacing may result an unphysical low flux. See Figure 6.8 for an explanation.

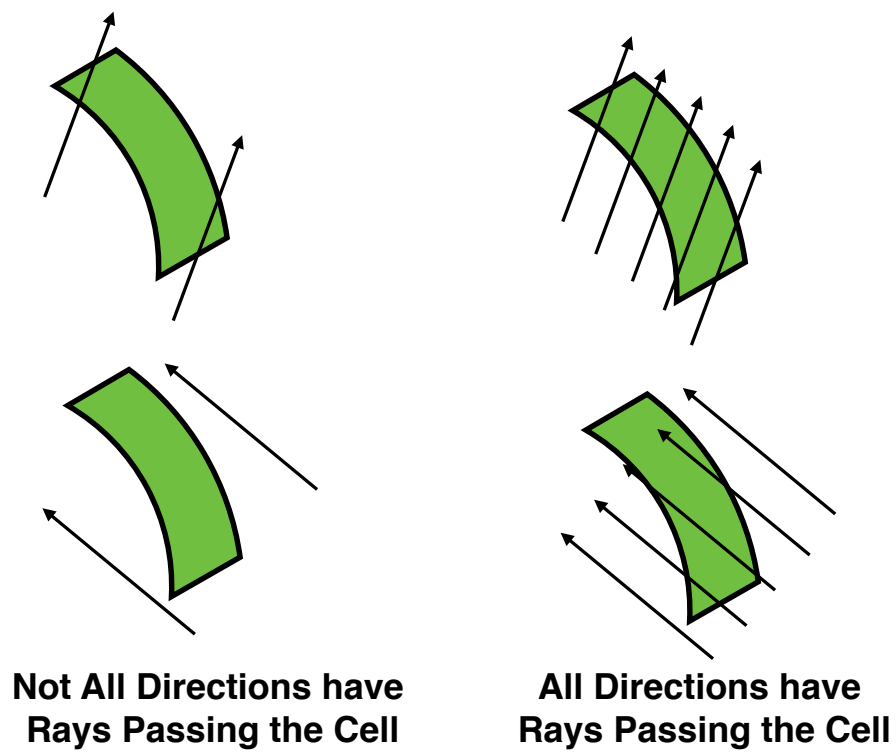


Figure 6.8: A simplified depiction of MOC rays passing through a cell. When ray spacing is wide, there may be no tracks in the cell.

6.3 Mini-assembly Problem

The third problem is a mini-assembly containing a 3x3 grid of pin-cells. There is a 2x2 grid of UO₂ pin-cells in the center, with reflecting boundary conditions. The moderator is water surrounding the UO₂ pin-cells, with vacuum boundary conditions. See Figure 6.9 for an illustration. These pin-cells are identified by the coordinates (i, j) , $0 \leq i \leq 2$, $0 \leq j \leq 2$.

The fuel pin-cells are discretized into 48 spatial cells for the coarse grid, and 96 spatial cells for the fine grid. The moderator pin-cells are discretized into 16 spatial cells. The spatial cells and the materials are illustrated in Figure 6.10.

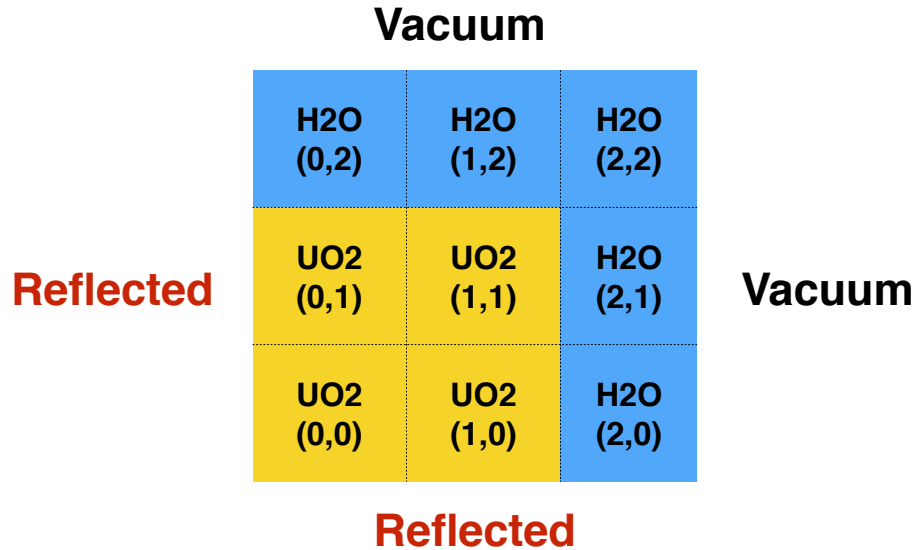


Figure 6.9: An illustration of the mini-assembly pin-cell layout. Four fuel pin-cells are in the center with reflected boundaries, which is surrounded by five moderator pin-cells with vacuum boundaries.

The k_{eff} , time and storage costs are compared in Table 6.8, and the pin-cell power of the fuel pin-cells are shown in Table 6.9. The pin-cell averaged fluxes for selected methods are compared in Figure 6.11. The pin-cell power and pin-cell averaged fluxes are normalized to be 1.0 for the pin-cell at coordinate $(0, 0)$.

The two figures 6.12 and 6.13 describe the comparisons of k and max-min pin

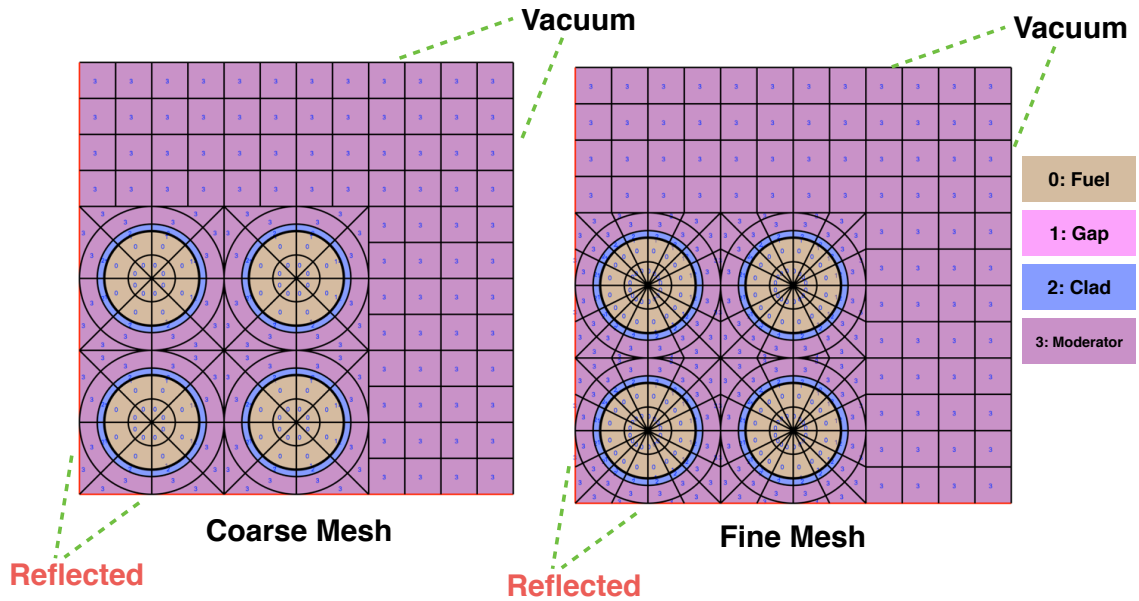


Figure 6.10: The coarse grid and fine grid. For each fuel pin-cell, there are 48 spatial cells in the coarse grid, and 96 spatial cells in the fine grid. For both cases, the moderator pin-cells have 16 spatial cells.

power for the mini-assembly problem: one for the coarse grid, and the other for the fine grid. (See section 6.3.)

For the same time costs, the MB solution has smaller errors than the MOC, STEP and SSC solutions. MOC is also more accurate than SSC, which is more accurate than STEP. In this problem, the fluxes drop about 80% from the highest pin-cell to the lowest pin-cell, which can be seen from Figure 6.11. Therefore, the neutron flux for this problem has a significant tilt - it is much less “flat” than in the first two problems. A possible reason why the MB method is the most accurate is because the derivation of the MB method does not assume that the flux is flat in a cell, while the other methods, i.e. STEP, SSC and MOC methods all assume the flux in a cell to be flat.

This indicates a character of the multiple balance method: the finer grid is necessary to allow the multiple balance method to show its advantages. The reader may argue that a fine grid may not be practical in reactor lattice calculation. However

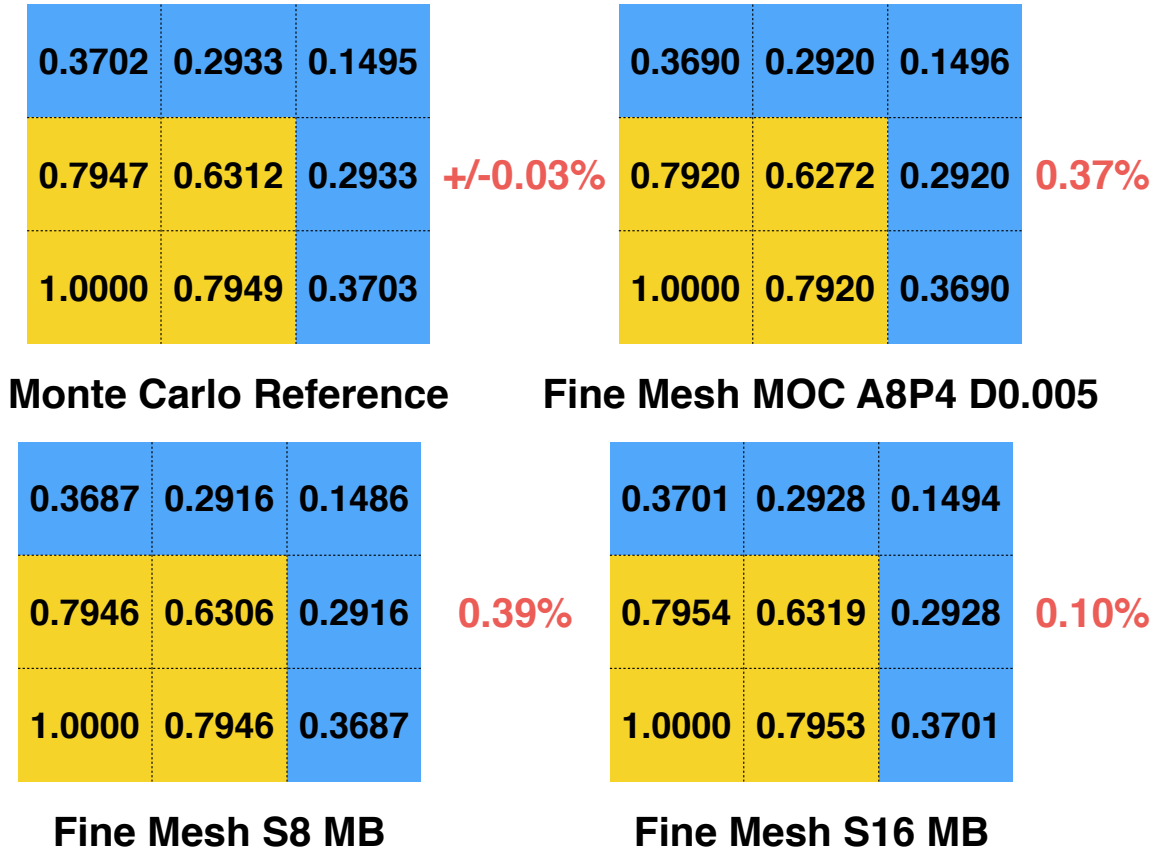


Figure 6.11: The pin-cell averaged fluxes, which are normalized to 1.0 for the pin-cell at coordinate (0, 0). The percentage in red marks the relative error from the Monte Carlo reference, calculated with the formula defined in equation (2.68).

the “fine” grid as shown in the section 6.3 only costs twice of that the “coarse grid”. Also, the ray spacing required for accurate MOC solution constitutes a much finer grid than the one used by the SN methods in these figures. See Figure 6.14 for an illustration.

Since the mini-assembly problem more closely resembles realistic problems, we expect the MB method to be more favorable than MOC for whole core simulations. This hypothesis will be tested further in our multigroup simulations with cross sections of higher fidelity.

In summary, the one-group problems treated here suggest that the MB method is

Table 6.8: List of k-effective, time & storage cost of the mini-assembly problem

METHOD	KEFF	KEFF ERROR. (pcm)	TIME PER IT- ERATION (ms)	STORAGE (MB)
MC	0.45717	3	N/A	N/A
Coarse Grid				
MOC A8P4 D0.05	0.45148	-569	4.9	0.823
MOC A8P4 D0.01	0.45143	-574	25.4	4.051
MOC A8P4 D0.005	0.45147	-571	51.0	8.093
STEP S4	0.42326	-3391	1.2	0.325
STEP S8	0.42683	-3034	4.0	0.346
STEP S16	0.42827	-2890	17.5	0.357
SSC S4	0.43253	-2464	1.4	0.325
SSC S8	0.43684	-2033	5.1	0.346
SSC S16	0.43853	-1864	21.0	0.357
MB S4	0.45017	-700	4.9	0.325
MB S8	0.45423	-294	17.0	0.346
MB S16	0.45534	-183	86.4	0.357
Fine Grid				
MOC A8P4 D0.05	0.45212	-505	5.5	0.944
MOC A8P4 D0.01	0.45200	-517	27.3	4.612
MOC A8P4 D0.005	0.45203	-514	55.2	9.205
STEP S4	0.42279	-3438	1.8	0.482
STEP S8	0.42662	-3055	6.8	0.501
STEP S16	0.42854	-2863	32.4	0.511
SSC S4	0.43404	-2313	2.2	0.482
SSC S8	0.43864	-1853	8.8	0.501
SSC S16	0.44059	-1658	43.1	0.511
MB S4	0.45108	-609	7.2	0.482
MB S8	0.45528	-190	36.1	0.501
MB S16	0.45717	-1	132.9	0.511

See Table 4.1 for definitions of the methods' name abbreviations

competitive with the MOC method, and that for problems with substantial spatial variations in the neutron flux, the MB method may be significant more accurate than MOC. This conjecture will be tested further in more realistic multigroup simulations considered in the next chapter.

Table 6.9: List of pin-cell power of the mini-assembly problem

METHOD	PIN POWER (0,0)	PIN POWER (0,1)	PIN POWER (1,0)	PIN POWER (1,1)	PIN POWER ERROR (%)	Max- min Pin Power Ratio
MC	1.0000	0.7953	0.7955	0.6323	0.03	1.5816 \pm 0.0005
Coarse Grid						
MOC A8P4 D0.05	1.0000	0.7934	0.7934	0.6300	0.25	1.5874
MOC A8P4 D0.01	1.0000	0.7938	0.7938	0.6300	0.23	1.5873
MOC A8P4 D0.005	1.0000	0.7939	0.7939	0.6301	0.22	1.5871
STEP S4	1.0000	0.7840	0.7840	0.6118	1.91	1.6344
STEP S8	1.0000	0.7867	0.7867	0.6176	1.40	1.6192
STEP S16	1.0000	0.7873	0.7873	0.6183	1.32	1.6173
SSC S4	1.0000	0.7874	0.7874	0.6166	1.43	1.6217
SSC S8	1.0000	0.7902	0.7902	0.6226	0.89	1.6061
SSC S16	1.0000	0.7909	0.7909	0.6236	0.80	1.6037
MB S4	1.0000	0.7983	0.7984	0.6359	0.39	1.5695
MB S8	1.0000	0.7995	0.7994	0.6377	0.56	1.5683
MB S16	1.0000	0.7992	0.7992	0.6376	0.54	1.5679
Fine Grid						
MOC A8P4 D0.05	1.0000	0.7923	0.7923	0.6282	0.43	1.5918
MOC A8P4 D0.01	1.0000	0.7927	0.7927	0.6284	0.39	1.5913
MOC A8P4 D0.005	1.0000	0.7928	0.7928	0.6285	0.38	1.5912
STEP S4	1.0000	0.7779	0.7779	0.6036	2.75	1.6566
STEP S8	1.0000	0.7812	0.7812	0.6096	2.20	1.6405
STEP S16	1.0000	0.7822	0.7822	0.6112	2.04	1.6361
SSC S4	1.0000	0.7824	0.7824	0.6100	2.11	1.6394
SSC S8	1.0000	0.7859	0.7859	0.6164	1.52	1.6224
SSC S16	1.0000	0.7870	0.7870	0.6181	1.35	1.6178
MB S4	1.0000	0.7936	0.7936	0.6275	0.41	1.5928
MB S8	1.0000	0.7949	0.7949	0.6311	0.10	1.5837
MB S16	1.0000	0.7959	0.7959	0.6326	0.05	1.5799

See Table 4.1 for definitions of the methods' name abbreviations

Mini-assembly Coarse Grid

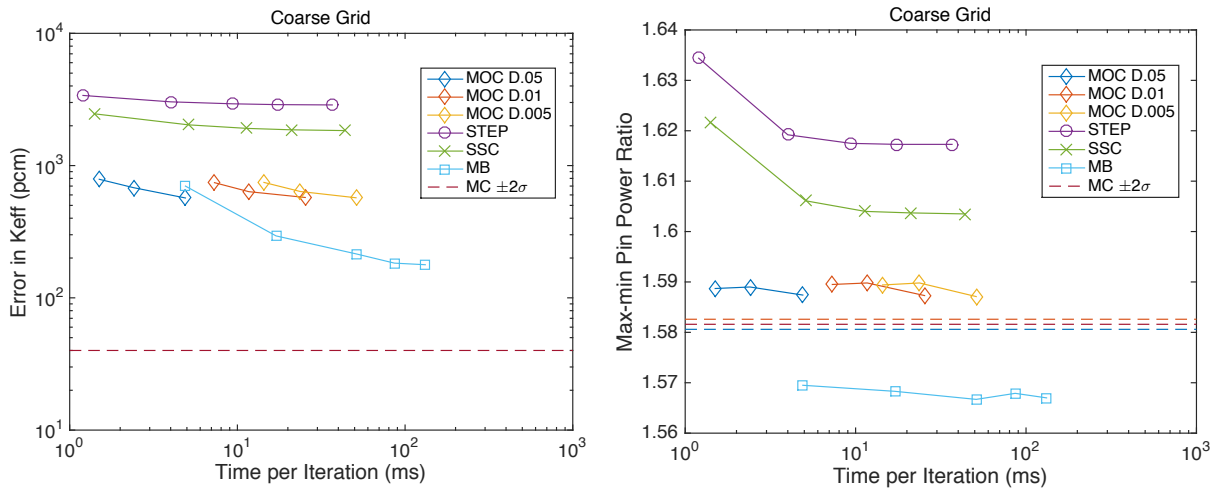


Figure 6.12: The comparisons of k and max-min pin power ratio for the mini-assembly problem on the coarse grid. The MOC solutions data points are simulated with a variety of angular quadrature sets: A4P2, A4P4, A8P4. The SN solutions data points are simulated with a variety of angular quadrature sets: S4, S8, S12, S16, S20. The dashed line is the Monte Carlo reference.

Mini-assembly Fine Grid

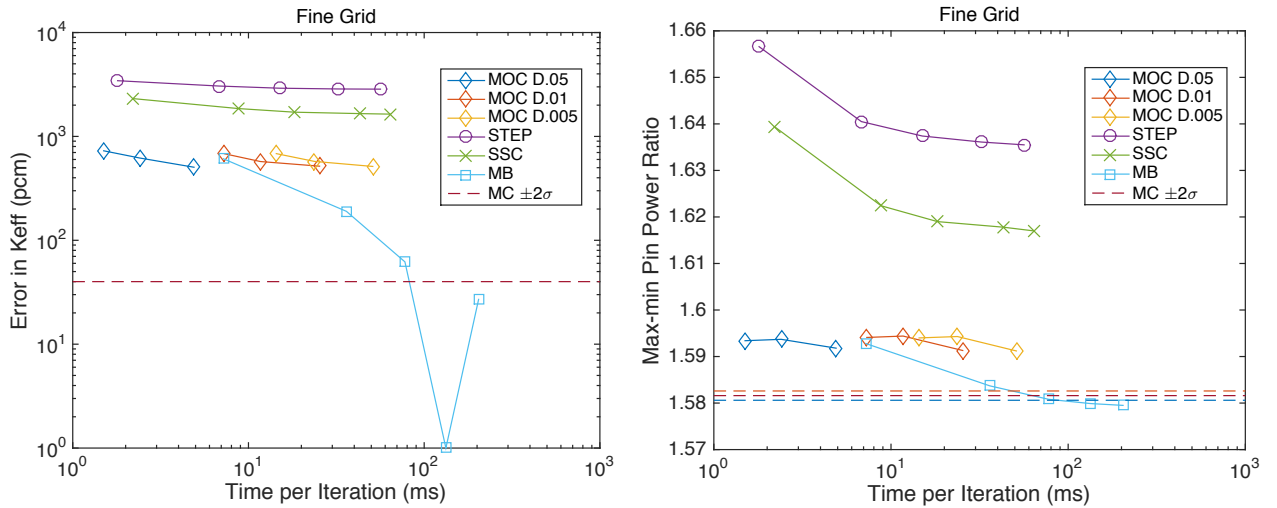


Figure 6.13: The comparisons of k and max-min pin power ratio for the mini-assembly problem on the fine grid. The MOC solutions data points are simulated with a variety of angular quadrature sets: A4P2, A4P4, A8P4. The SN solutions data points are simulated with a variety of angular quadrature sets: S4, S8, S12, S16, S20. The dashed line is the Monte Carlo reference.

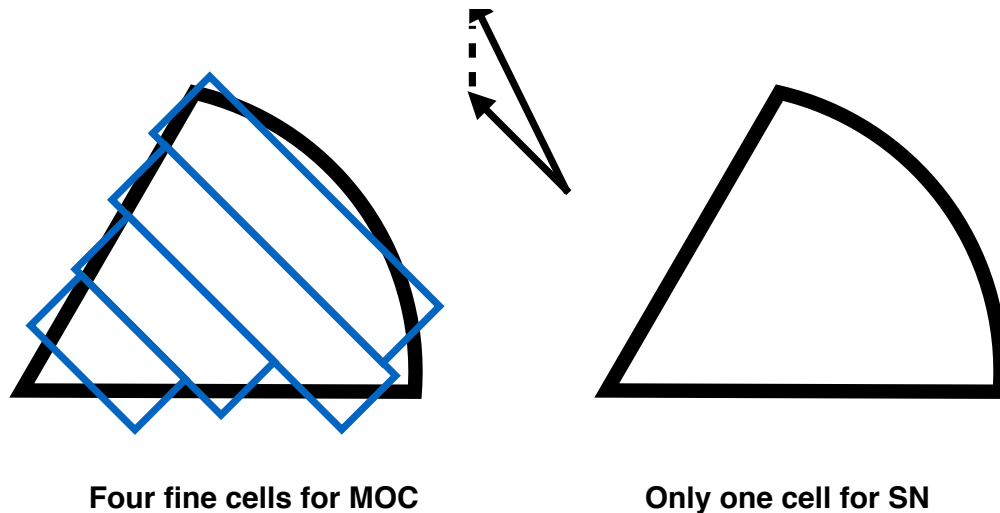


Figure 6.14: MOC rays passing through a cell will divide it into one or more fine cells.

CHAPTER VII

Numerical Results for Two-Dimensional Multigroup Problems with Curved Spatial Grids

In this chapter, we study the performance of discrete ordinates (SN) methods for 2-D multigroup problems with curved spatial grids. To make the problems more realistic, we use the Winfrith Improved Multigroup Scheme-D (WIMS-D) library to generate cross sections. WIMS-D is one of the most widely-used reactor lattice codes that is available in the public domain. (*Askew et al.*, 1966) The data library of this code is called the WIMS-D library. (*Halsall*, 1991) The problems in this chapter are some of the CASL VERA benchmark problems (*Godfrey*, 2014) plus a mini-assembly problem. These contain realistic model problems for simulations ranging from a single pin-cell to a full assembly.

7.1 WIMS-D Cross Section

The WIMS-D library contains microscopic cross sections for many nuclides that are important for reactor simulations. The data library used in this thesis was published by IAEA in 2014 (*Aldama*, 2014), and was generated from the ENDF/B-VII.1 evaluated nuclear data library (*Chadwick and et al.*, 2011).

The data library contains 185 materials in either 69 or 172 groups. We used the

172 group cross sections, in which groups 1-92 are “fast” groups, 46-92 are “resonance” groups, and 93-172 are “thermal” groups. The fission spectrum is shown in Figure 7.1.

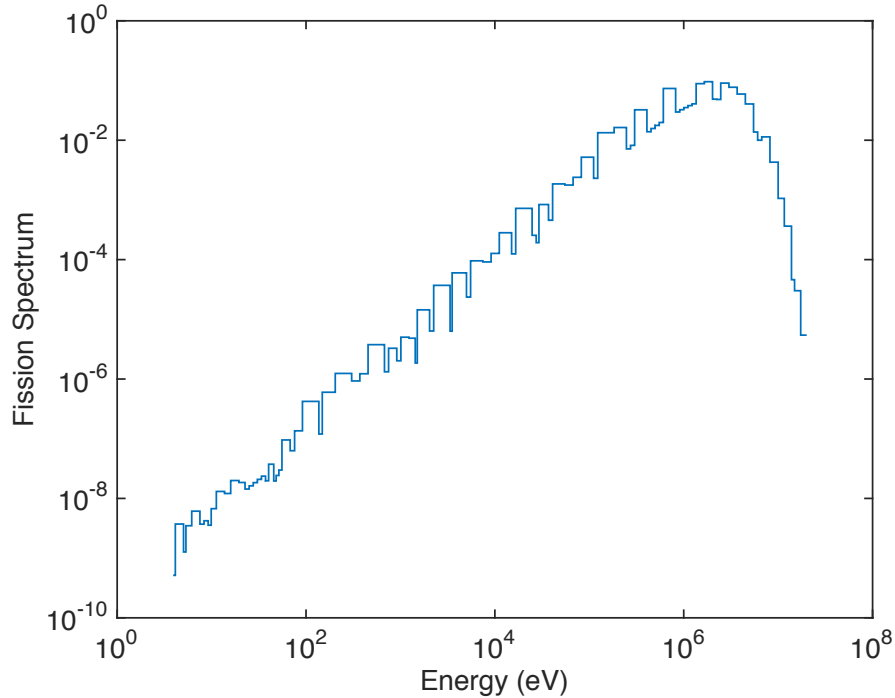


Figure 7.1: The fission spectrum in WIMS-D cross section library.

The microscopic cross sections included are: transport-corrected total, absorption, fission, nu-fission, and the scattering matrix. Each cross section is temperature-dependent within the resonance range, i.e. groups 46-92. Resonance phenomena are important for neutron slowing down, the accurate treatment of which is necessary to make the multigroup cross sections valid. (*Williams, 1966*) The WIMS-D library contains the following information for each resonant nuclide:

- σ_p : potential scattering cross section,
- $I_a(\sigma_b, T)$: absorption resonance integral,
- $I_f(\sigma_b, T)$: fission resonance integral,
- λ : the Golstein-Cohen parameter,

where T is the temperature, and σ_b is the “background” cross section as defined below. Consider a material containing M nuclides. We designate the integer $1 \leq i \leq M$ as an index of the nuclide. For light water composed of 1H and ^{16}O as an example, we have $M = 2$, and we can designate the index $i = 1$ for 1H , and $i = 2$ for ^{16}O . Then the background cross section seen by nuclide r is defined in the WIMS-D library document (*Leszczynski et al.*, 2007) as:

$$\sigma_{b,r} = \sigma_{p,r} + \sum_{i=1}^M \frac{N_i}{N_r} \lambda_i \sigma_{p,i}, \quad (7.1)$$

where $\sigma_{b,r}$ is the background cross section for nuclide r , $\sigma_{p,i}$ is the microscopic potential scattering of the nuclide at index i , N_i is the atomic density of the nuclide at index i , and λ_i is the Goldstein-Cohen parameter of the nuclide at index i .

The Goldstein-Cohen parameter is a value between 0 and 1, and is used in the “intermediate resonance” (IR) approximation. This parameter was first invented by Goldstein and Cohen (*Goldstein and Cohen*, 1962). Later, their work became a classical method for resonance treatment (*Williams*, 1966; *Stammler and Abbate*, 1983). Careful work was done to generate the parameters in their method (*Leszczynski*, 1997, 1999).

The resonance self-shielded cross section, given by the WIMS-D library document (*Leszczynski et al.*, 2007), is:

$$\sigma_a(\sigma_b, T) = \frac{I_a(\sigma_b, T)}{1 - I_a(\sigma_b, T)/\sigma_b}, \quad (7.2)$$

$$\nu\sigma_f(\sigma_b, T) = \frac{I_f(\sigma_b, T)}{1 - I_a(\sigma_b, T)/\sigma_b}, \quad (7.3)$$

where σ_a is absorption cross section, and $\nu\sigma_f$ is the fission yield cross section.

Our treatment of resonance is a simplified approach in the sense that the self-shielding effects due to material heterogeneity are ignored. Modern approaches to

resonance treatments are reviewed in *Liu* (2015). Because the purpose in this chapter is to demonstrate the application of SN methods for realistic multigroup problems, high precision in the multigroup cross sections is not the goal here.

7.2 Material Compositions

For the problems considered in this thesis, we only need five materials, whose nuclide compositions are provided in Table 7.1. The “WIMS ID” is the identifier of the material in the WIMS-D data library. The atomic density is in units of “# per barn-cm”, where we define:

$$1 \text{ barn-cm} = 10^{-24} \text{ cm}^3. \quad (7.4)$$

Table 7.1: List of material compositions (*Godfrey, 2014*)

Material	WIMS ID	Atomic Density #/ barn-cm	Material	WIMS ID	Atomic Density #/barn-cm
Fuel (3.1wt% UO2)			Gap		
U-234	234	6.11864E-06	He	4	2.68714E-05
U-235	2235	7.18132E-04	Clad (Zircaloy-4)		
U-236	236	3.29861E-06	Zr	91	6.4439E+00
U-238	8238	2.21546E-02	Sn	118	9.5120E-02
O-16	6016	4.57642E-02	Fe	2056	1.3776E-02
IFBA			Cr	52	6.5600E-03
B-10	10	2.16410E-02	Hf-176	2176	3.4014E-05
B-11	11	1.96824E-02	Hf-177	2177	1.2096E-04
Zr	91	2.06616E-02	Hf-178	2178	1.7841E-04
Moderator			Hf-179	2179	8.9580E-05
O-16	6016	2.48112E-02	Hf-180	2180	2.3201E-04
H-1	3001	4.96224E-02			
B-10	10	1.07070E-05			
B-11	11	4.30971E-05			

7.3 Geometry of Pin-cells

We define three types of pin-cells. The first type is the “fuel” pin-cell, which contains an inner ring of fuel, coated by a thin layer of the IFBA material; outside the IFBA layer is the gap; outside the gap is the clad, surrounded by moderator. (The IFBA layer may not be present for a pin-cell.) The second type is the “guide tube” pin-cell, which contains a ring of clad. The third type is the “instruction tube” pin-cell, which is a type of “guide tube” inserted in the middle of an LWR fuel assembly. Figure 7.2 describes the geometry of pin-cells.

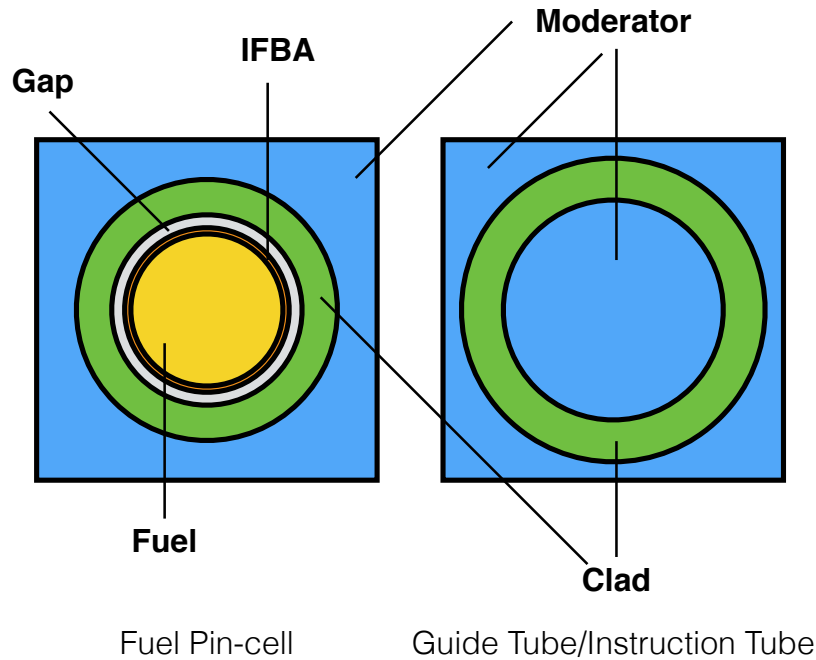


Figure 7.2: The geometry of pin-cells. Different materials are marked in different colors. The IFBA layer may not be present in a fuel pin-cell. The “instruction tubes” are “guide tube” pin-cells inserted in the middle of an LWR assembly. (*Godfrey, 2014*)

The dimensions of the fuel pin-cell (F), the guide tube pin-cell (GT), and the instruction tube pin-cell (IT) are given in Table 7.2. These pin-cells are the building blocks of the problems discussed in this chapter. We note that both the guide tube

and the instruction tube have similar geometries, but the inner and outer radii of the clad are slightly different. An instruction tube typically appears in the center of an assembly. This is clarified in the final problem that we study. (See Figure 7.7.)

Table 7.2: Pin-cell Dimension Information (*Godfrey, 2014*)

DIMENSION	VALUE (cm)
Pitch (Size of the Square)	1.26
Fuel Pin-cell (F)	
Outer radius of fuel	0.4096
Outer radius of IFBA	0.4106
Outer radius of gap	0.418
Outer radius of clad	0.475
Guide Tube Pin-cell (GT)	
Inner radius of clad	0.559
Outer radius of clad	0.605
Instruction Tube Pin-cell (IT)	
Inner radius of clad	0.561
Outer radius of clad	0.602

7.4 VERA Benchmark Problems

In this section we study three problems from the VERA benchmark problems (*Godfrey, 2014*), i.e. problems 1A, 1E, and 2A.

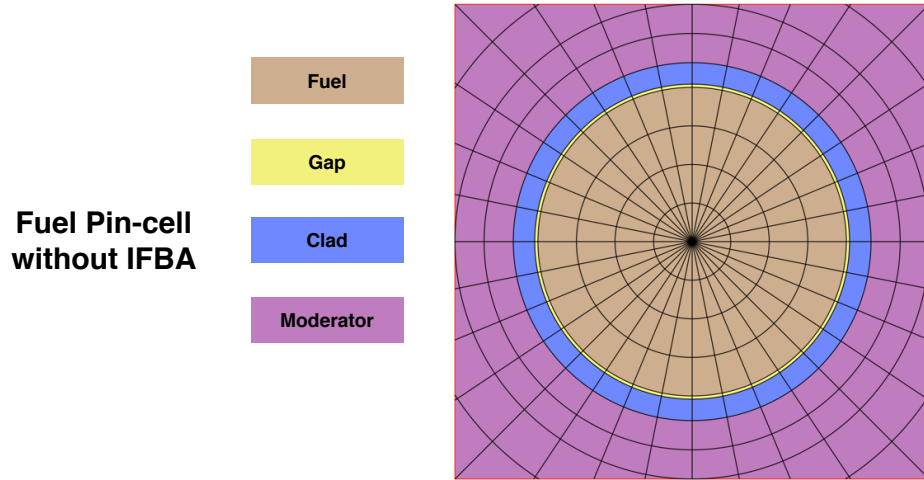
7.4.1 Problem 1A: Fuel Pin-cell without IFBA

7.4.1.1 Problem Description

The first problem considered here is the VERA benchmark problem 1A (*Godfrey, 2014*), which is a single fuel pin-cell without an IFBA layer. The pin-cell is divided into 32 angular sectors; the spatial grid is depicted in Figure 7.3.

7.4.1.2 Verification

The scalar fluxes are averaged over the fuel, gap, clad, and the moderator regions, and are normalized such that the “collision rate” in the fuel region is 1.0. The collision



Radial Meshes at Radii: 0.1024 cm, 0.2048 cm, 0.3096 cm, 0.4096 cm,
0.4180 cm, 0.4750 cm, 0.5535 cm, 0.6300 cm, 0.7200 cm

Figure 7.3: The spatial grid for Problem 1A: the fuel pin-cell without IFBA. All outer boundaries are reflecting.

rate is defined as the sum of the products between groupwise scalar flux and total cross section:

$$\text{CR} = \sum_{g=1}^G \Sigma_{t,g} \bar{\phi}_g, \quad (7.5)$$

where $G = 172$ for the 172-group cross sections.

Figure 7.4 compares the methods' accuracy in k -eigenvalues and collision rates versus time costs, where the numerical values are listed in Table 7.3 and Table 7.4.

The STEP and SSC methods are seen to be more accurate than MOC for the same computational cost. Among all SN methods, the step and SSC methods are more accurate than the MB method. This confirms our conjecture from Chapter VI that the MB method is less advantageous when the scalar flux is “flat”. For the MOC method with 0.05 cm and 0.02 cm ray spacings, the solutions become significantly less accurate when the ray spacing is not significantly smaller than the fine spatial

Table 7.3: List of k -effective versus time cost for Problem 1A

METHOD	KEFF	KEFF ERROR. (pcm)	TIME PER IT- ERATION (ms)	STORAGE (MB)
MC	1.257067	10.0	N/A	N/A
MOC D0.05 A8P4	1.172837	-8423.0	512	0.288
MOC D0.02 A8P4	1.254141	-292.6	1,250	0.693
MOC D0.01 A8P4	1.256535	-53.2	2,505	1.369
STEP S4	1.256893	-17.4	559	0.241
STEP S8	1.256154	-91.3	1,374	0.233
STEP S16	1.256151	-91.6	4,886	0.230
SSC S4	1.257674	60.7	590	0.241
SSC S8	1.257088	2.1	1,488	0.233
SSC S16	1.257172	10.5	5,290	0.230
MB S4	1.257711	64.4	1,530	0.241
MB S8	1.256200	-86.7	4,548	0.233
MB S16	1.256041	-102.6	16,774	0.230

See Table 4.1 for definitions of the methods' name abbreviations

Table 7.4: List of collision rates (CR) for Problem 1A

METHOD	FUEL CR PER AREA	GAP CR PER AREA	CLAD CR PER AREA	MODERA- TOR CR PER AREA	CR ER- ROR (%)
MC	1.00000	0.00012	0.67728	1.80659	0.030
MOC D0.05 A8P4	1.00000	0.00011	0.68740	1.81682	6.470
MOC D0.02 A8P4	1.00000	0.00012	0.67880	1.80986	2.230
MOC D0.01 A8P4	1.00000	0.00012	0.67863	1.81048	0.147
STEP S4	1.00000	0.00012	0.67723	1.80453	0.233
STEP S8	1.00000	0.00012	0.67820	1.81259	0.195
STEP S16	1.00000	0.00012	0.67838	1.81399	0.222
SSC S4	1.00000	0.00012	0.67656	1.79807	0.379
SSC S8	1.00000	0.00012	0.67756	1.80619	0.143
SSC S16	1.00000	0.00012	0.67773	1.80739	0.056
MB S4	1.00000	0.00012	0.67188	1.79439	1.263
MB S8	1.00000	0.00012	0.67556	1.80930	0.770
MB S16	1.00000	0.00012	0.67755	1.81449	0.389

See Table 4.1 for definitions of the methods' name abbreviations

grid size.

Problem 1A

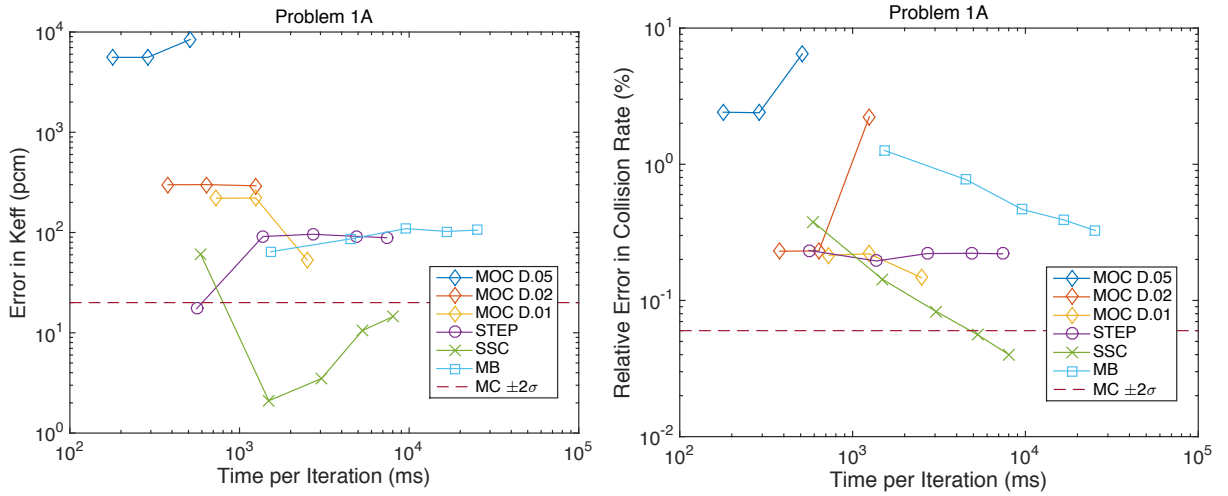


Figure 7.4: Error comparisons for problem 1A. The MOC solution data points are simulated with a variety of angular quadrature sets: A4P2, A4P4, A8P4. The SN solution data points are also simulated with a variety of angular quadrature sets: S4, S8, S12, S16, S20. The dashed lines are the Monte Carlo uncertainties within two standard deviations. The uncertainties in the Monte Carlo results are so small that the dashed lines cannot be distinguished from each other.

7.4.1.3 Validation

Another question is the quality of the multigroup cross sections. The reference k -eigenvalue is 1.183262 ± 0.000106 (Godfrey, 2014), while with the WIMS-D multigroup cross sections, we obtain 1.257067 ± 0.000100 . There is a clear difference between the two. We conclude that a more accurate resonance treatment is necessary to improve the solutions.

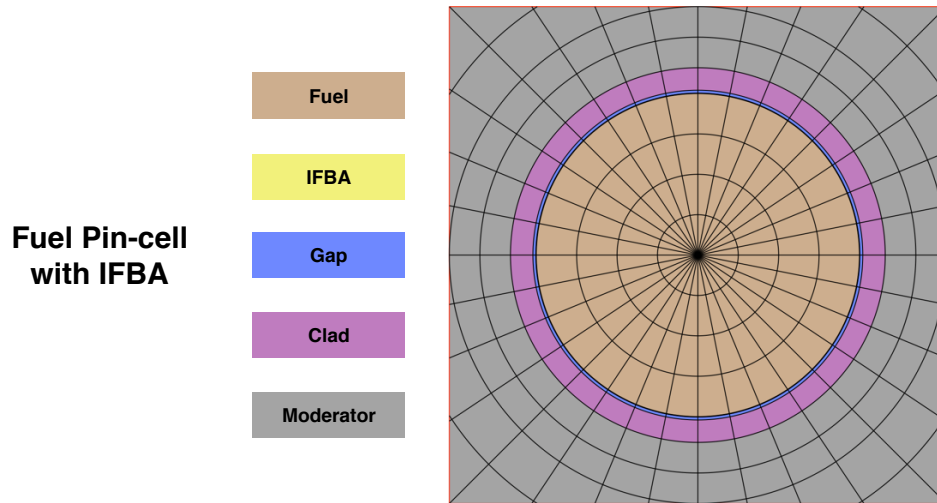
Table 7.5: Validation of WIMS-D cross section for problem 1A

DATA	KEFF	KEFF UNCERTAINTY.
WIMS Cross Section	1.257067	0.000100
CE KENO-VI.	1.183262	0.000106

7.4.2 VERA Benchmark Problem 1E: Fuel Pin-cell with IFBA

7.4.2.1 Problem Description

The second problem considered here is the VERA benchmark problem 1E (*Godfrey, 2014*), which is a single fuel pin-cell with an IFBA layer. The pin-cell is divided into 32 angular sectors; the spatial grid is depicted in Figure 7.5.



Radial Meshes at Radii: 0.1024 cm, 0.2048 cm, 0.3096 cm, 0.4096 cm, 0.4101 cm, 0.4106 cm, 0.4180 cm, 0.4750 cm, 0.5535 cm, 0.6300 cm, 0.7200 cm

Figure 7.5: The spatial grid for Problem 1E: the fuel pin-cell with an IFBA layer. All outer boundaries are reflecting.

7.4.2.2 Verification

Table 7.6 compares the methods' accuracy in k -eigenvalues versus time costs, while Table 7.7 compares the methods' accuracy in collision rates versus time costs.

Table 7.6 shows that the step method has the most accurate eigenvalue. For the collision rate, the discrete ordinates methods are more accurate than the MOC method, and the step method is slightly more accurate than the SSC and MB methods. We note that for wide ray spacings of 0.05 cm and 0.005 cm, the MOC method

Table 7.6: List of k -effective versus time cost for Problem 1E

METHOD	KEFF	KEFF ERROR. (pcm)	TIME PER IT- ERATION (ms)	STORAGE (MB)
MC	0.808911	7.8	N/A	N/A
MOC D0.05 A8P4	0.806746	-216.5	329	0.316
MOC D0.005 A8P4	0.815416	650.5	2,975	3.352
MOC D0.0005 A8P4	0.808156	-75.5	29,367	33.163
STEP S4	0.810348	143.7	425	0.400
STEP S8	0.809427	51.6	1,011	0.393
STEP S16	0.809387	47.6	3,888	0.393
SSC S4	0.804893	-401.8	446	0.400
SSC S8	0.803891	-502.0	1,228	0.393
SSC S16	0.803858	-505.3	4,556	0.393
MB S4	0.809932	102.1	1,050	0.400
MB S8	0.807264	-164.7	4,073	0.393
MB S16	0.8065944	-231.7	15,630	0.393

See Table 4.1 for definitions of the methods' name abbreviations

Table 7.7: List of collision rates (CR) for Problem 1E

METHOD	FUEL CR PER AREA	IFBA CR PER AREA	GAP CR PER AREA	CLAD CR PER AREA	MODERA- TOR CR PER AREA	CR ER- ROR (%)
MC	1.00000	11.80899	0.00013	0.69990	1.73811	0.030
MOC D0.05 A8P4	1.00000	9.98188	0.00011	0.70870	1.76455	9.268
MOC D0.005 A8P4	1.00000	11.56318	0.00013	0.70148	1.74578	0.959
MOC D0.0005 A8P4	1.00000	11.83350	0.00013	0.70154	1.74324	0.193
STEP S4	1.00000	11.77599	0.00013	0.70046	1.73790	0.218
STEP S8	1.00000	11.77628	0.00013	0.70147	1.74586	0.259
STEP S16	1.00000	11.77020	0.00013	0.70160	1.74698	0.297
SSC S4	1.00000	11.93305	0.00013	0.70056	1.73232	0.526
SSC S8	1.00000	11.94121	0.00013	0.70162	1.74036	0.517
SSC S16	1.00000	11.93673	0.00013	0.70174	1.74130	0.507
MB S4	1.00000	11.78824	0.00013	0.69409	1.72691	1.177
MB S8	1.00000	11.83790	0.00013	0.69833	1.74212	0.711
MB S16	1.00000	11.85466	0.00013	0.70051	1.74752	0.403

See Table 4.1 for definitions of the methods' name abbreviations

is highly inaccurate. This is probably because of the thin IFBA layer. (See section 6.2.2 for a detailed discussion.)

Our conjecture from Chapter VI is again confirmed that the MB method is less

Problem 1E

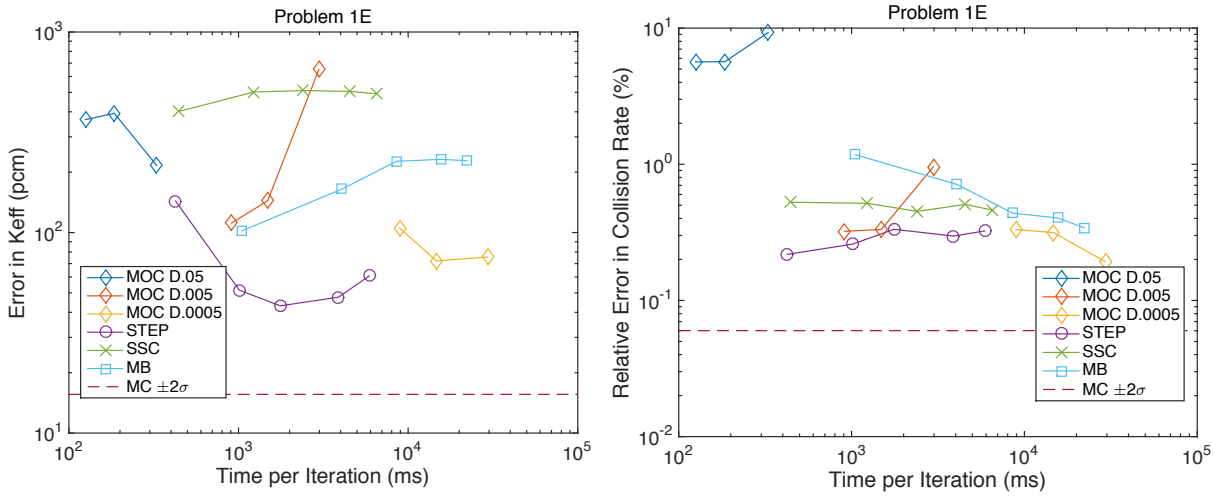


Figure 7.6: Error comparisons for problem 1E. The MOC solution data points are simulated with a variety of angular quadrature sets: A4P2, A4P4, A8P4. The SN solution data points are also simulated with a variety of angular quadrature sets: S4, S8, S12, S16, S20. The dashed lines are the Monte Carlo uncertainties within two standard deviations. The uncertainties in the Monte Carlo results are so small that the dashed lines cannot be distinguished from each other.

advantageous over MOC when the scalar flux is “flat”.

Also, because the storage requirements of SN methods have only a weak dependence on the angular quadrature sets, the storage costs are significantly lower than that of MOC.

7.4.2.3 Validation

The reference k -eigenvalue is 0.772366 ± 0.000078 (Godfrey, 2014), while with the WIMS-D multigroup cross sections, we obtain 0.808911 ± 0.000078 . There is a clear difference between the two. We again conclude that a more accurate resonance treatment is necessary to improve the solutions.

Table 7.8: Validation of WIMS-D cross section for problem 1E

DATA	KEFF	KEFF UNCERTAINTY.
WIMS Cross Section	0.808911	0.000078
CE KENO-VI.	0.772366	0.000078

7.4.3 VERA Benchmark Problem 2A: Zero Power Fuel Assembly

7.4.3.1 Problem Description

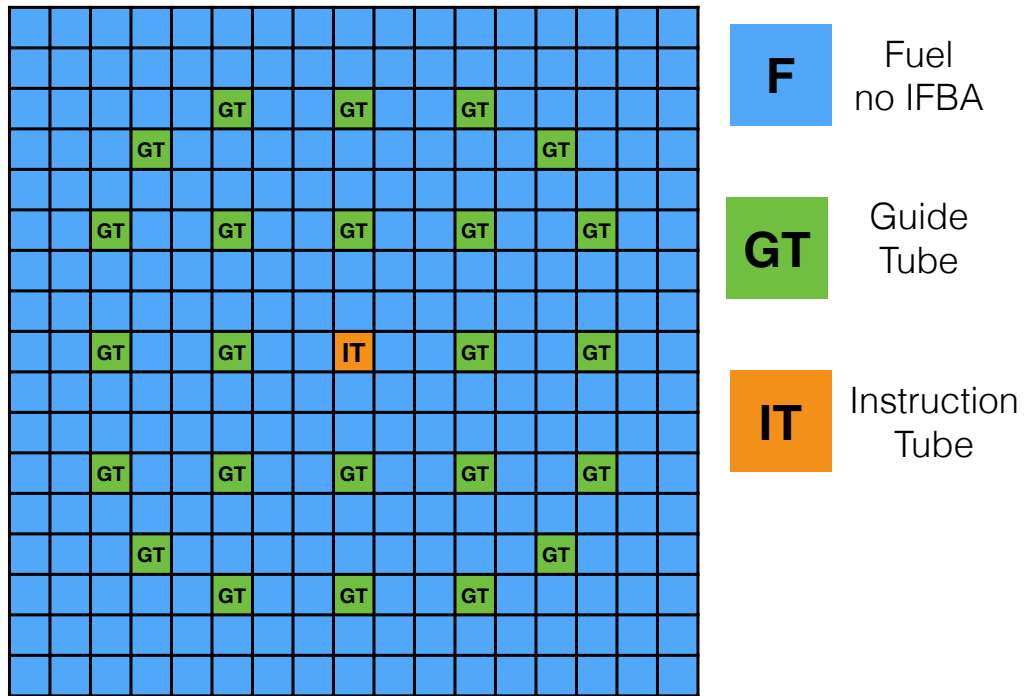


Figure 7.7: The geometry of VERA benchmark problem 2A, which is a fuel assembly. There are 25 empty guide tubes and one centered instruction tube. All outer boundaries are reflecting.

The third problem considered here is a fuel assembly, which contains 25 guide tubes, and one instruction tube in the center (*Godfrey, 2014*). All outer boundaries are reflecting. Figure 7.7 illustrates the assembly geometry. Each pin-cell is divided into 16 angular sectors. The spatial grid is shown in Figure 7.8. Because of symmetry, it is sufficient to consider only a quarter of the assembly with all reflecting outer boundaries.

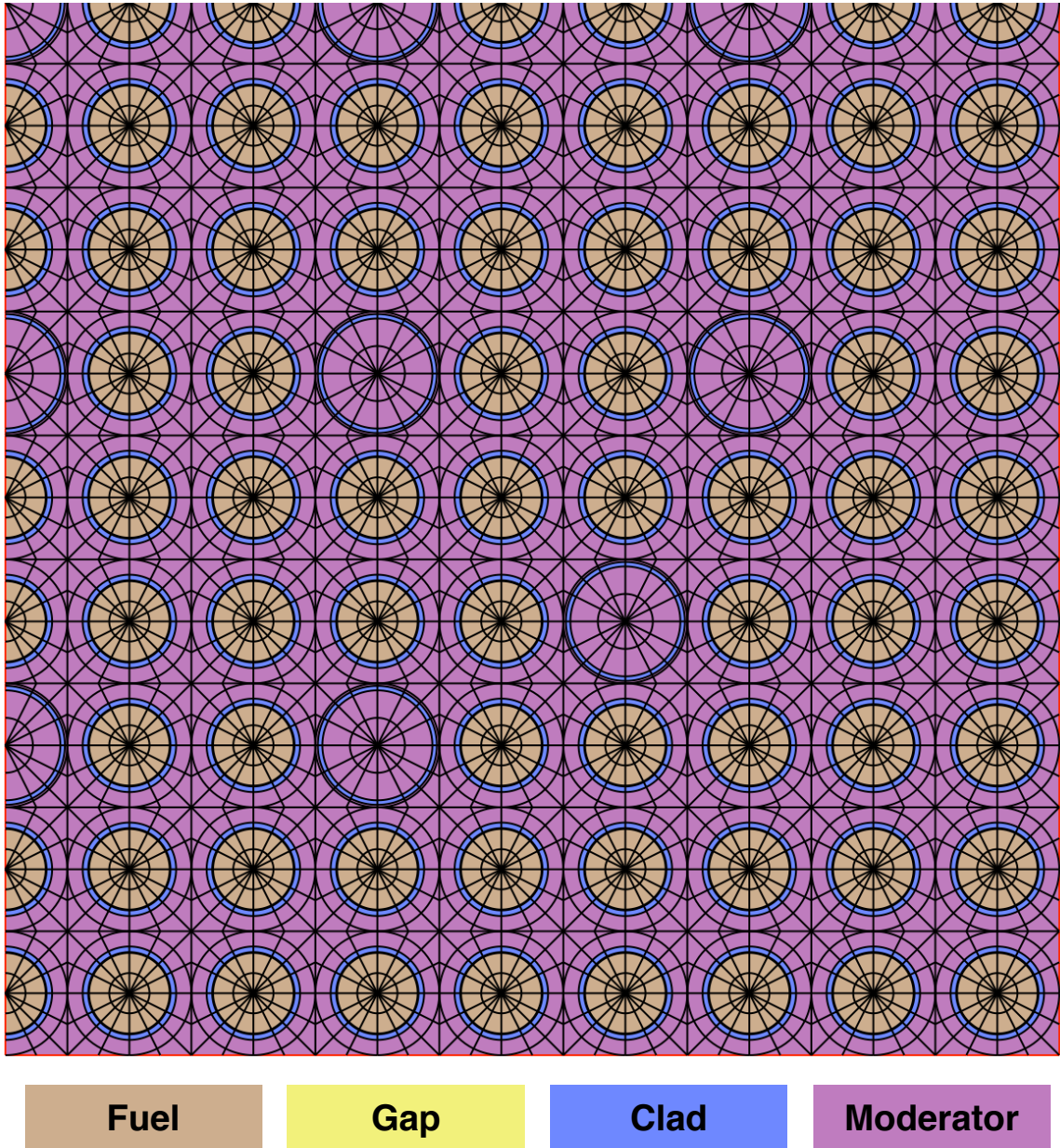


Figure 7.8: The spatial grid for Problem 2A. All outer boundaries are reflecting.

7.4.3.2 Verification

Table 7.9 compares the accuracies of k -eigenvalue and the maximum and minimum pin-cell powers. The pin-cell powers are normalized so that the average is 1.0, and the power distributions are compared in Figure 7.10, whereas the error in power

Table 7.9: List of k -effective versus time & pin-cell power for Problem 2A

METHOD	KEFF	KEFF ER- ROR. (pcm)	TIME PER ITER- ATION (ms)	MAX PIN POWER	MIN PIN POWER	MAX- MIN PIN POWER RATIO	ERROR IN PIN POWER RATIO (%)	STORAGE (MB)
MC (100 Million)	1.24552	4	N/A	1.0594	0.9160	1.1566	0.16	N/A
MOC A4P2 D0.05	1.24144	-407	3,913	1.0593	0.9201	1.1513	-0.46	5.467
MOC A4P4 D0.05	1.24138	-413	5,613	1.0594	0.9202	1.1513	-0.46	5.467
MOC A4P2 D0.02	1.24509	-43	8,478	1.0540	0.9185	1.1475	-0.79	13.097
MOC A4P4 D0.02	1.24503	-49	12,494	1.0599	0.9170	1.1558	-0.07	13.097
STEP S4	1.24507	-45	12,486	1.0564	0.9193	1.1490	-0.66	5.133
STEP S8	1.24403	-149	32,421	1.0556	0.9199	1.1474	-0.79	4.954
SSC S4	1.24746	194	12,837	1.0599	0.9167	1.1561	-0.04	5.133
SSC S8	1.24659	107	30,751	1.0589	0.9172	1.1545	-0.18	4.954
MB S4	1.24478	-74	23,421	1.0608	0.9161	1.1580	0.12	5.133
MB S8	1.24314	-238	58,598	1.0597	0.9168	1.1558	-0.07	4.954

See Table 4.1 for definitions of the methods' name abbreviations

distribution is compared in Figure 7.11. Figure 7.9 compares the k -eigenvalue and maximum to minimum pin-cell power ratios.

In this problem, the MB and SSC methods are more accurate than the MOC methods, while the STEP method is the least accurate. The quarter assembly problem is reasonably complex for practical reactor simulations, and we can see that the MB method is quite accurate. This again suggests that SSC and MB are alternative methods to MOC for reactor simulations.

With all reflecting outer boundaries, the problem simulates an assembly in the center of the reactor. So the flux is more flat than an assembly near the outer rim of the reactor. We see again that, when the solution is more flat, the advantage of MB over the MOC method is less significant.

From the pin-power distributions, the SSC and MB methods have comparable error with MOC for comparable execution cost (within 2 to 3 times).

Problem 2A

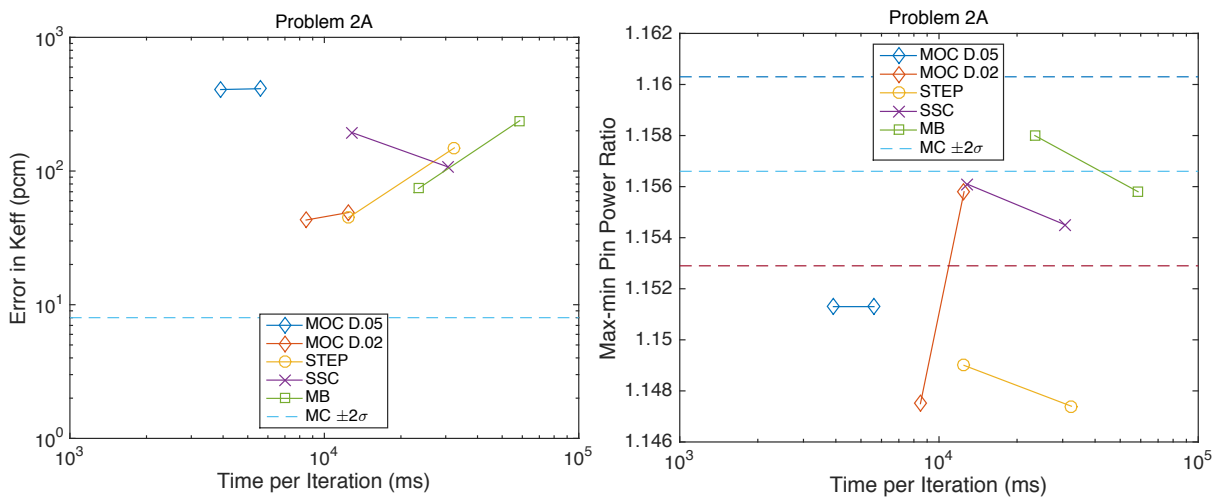


Figure 7.9: Error comparisons for the problem 2A. The MOC solution data points are simulated with two angular quadrature sets: A4P2, A4P4. The SN solution data points are also simulated with two angular quadrature sets: S4, S8. The dashed line shows the Monte Carlo uncertainties within two standard deviations. The uncertainties in the Monte Carlo k -eigenvalues are so small that the dashed lines cannot be distinguished from each other.

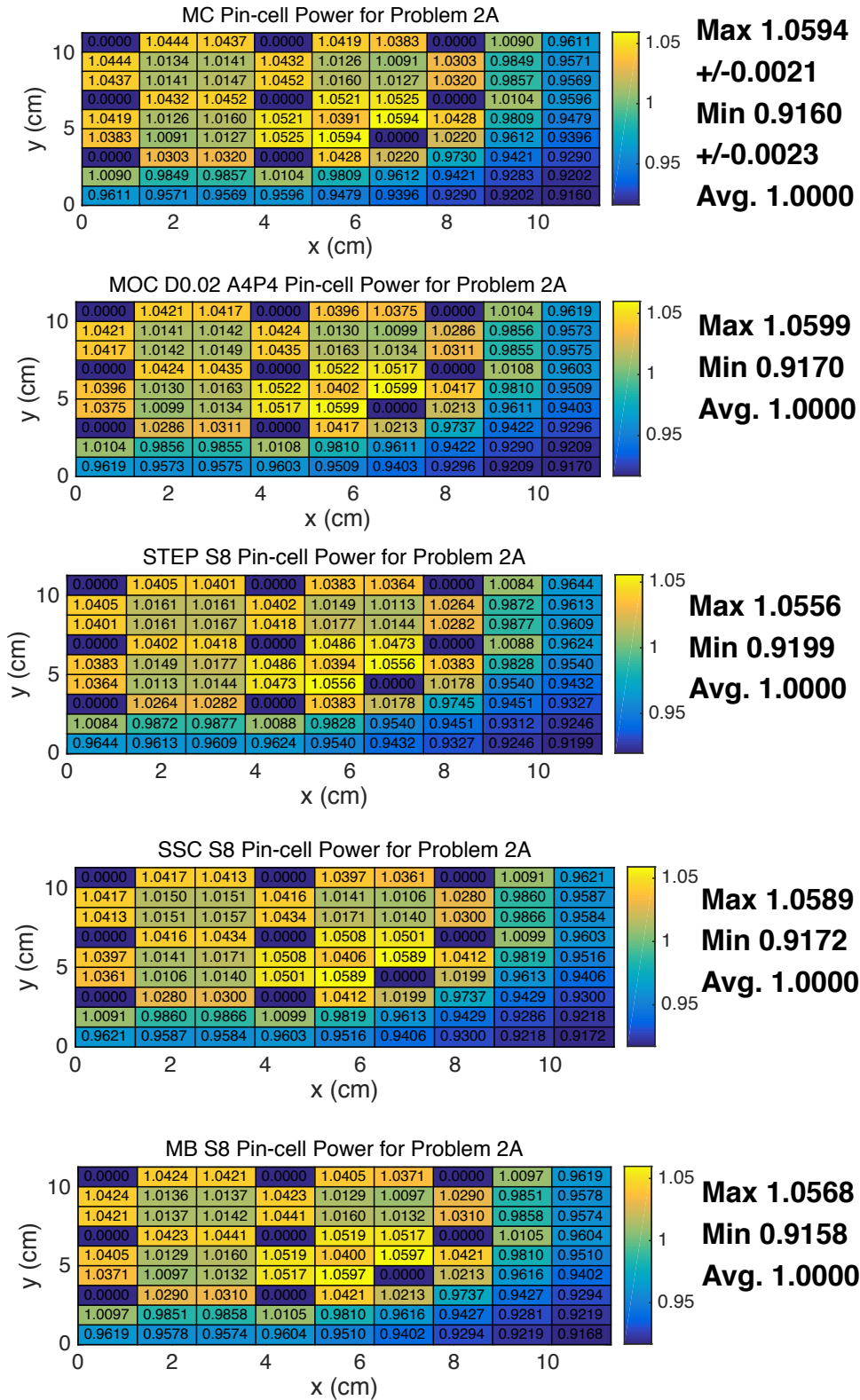


Figure 7.10: Comparison of pin-cell power distributions for Problem 2A.

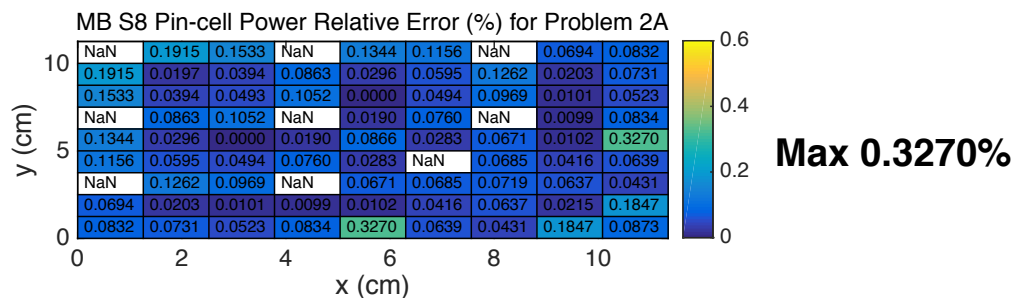
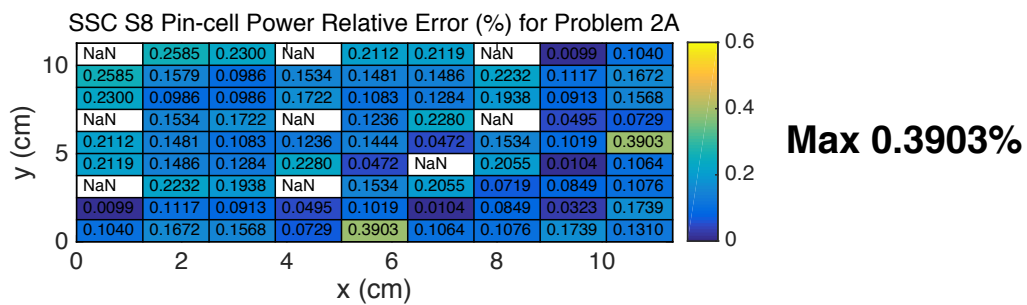
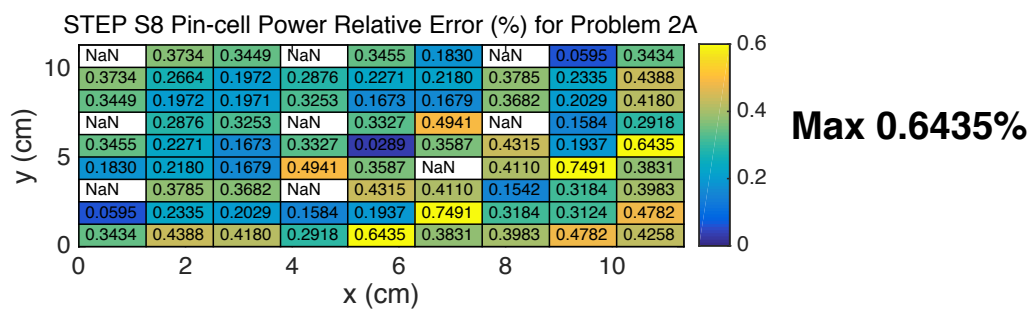
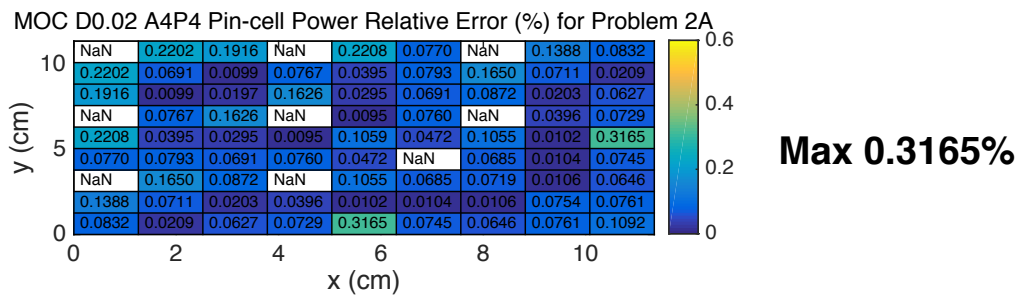


Figure 7.11: Comparison of pin-cell power error distributions for Problem 2A.

7.4.3.3 Validation

Table 7.10 and Figure 7.12 compare the k -eigenvalue and pin-cell power distributions with the reference KENO-VI results (Godfrey, 2014). With the WIMS-D multigroup cross section, we over-estimate the k -eigenvalue, and we under-estimate the pin-cell power for pin-cells away from the center of the assembly. Nonetheless, in general the WIMS-D library produces a quite faithful shape of the power distribution.

Table 7.10: Validation of WIMS-D cross section for problem 2A k -eigenvalue

DATA	KEFF	KEFF	ER-	MAX PIN	MIN PIN	MAX-MIN	PIN
		ROR.	(pcm)	POWER	POWER	POWER	RATIO
WIMS Cross Section	1.24552	4		1.0594	0.9160	1.1566	
CE KENO-VI.	1.18273	2		1.0513	0.9394	1.1191	

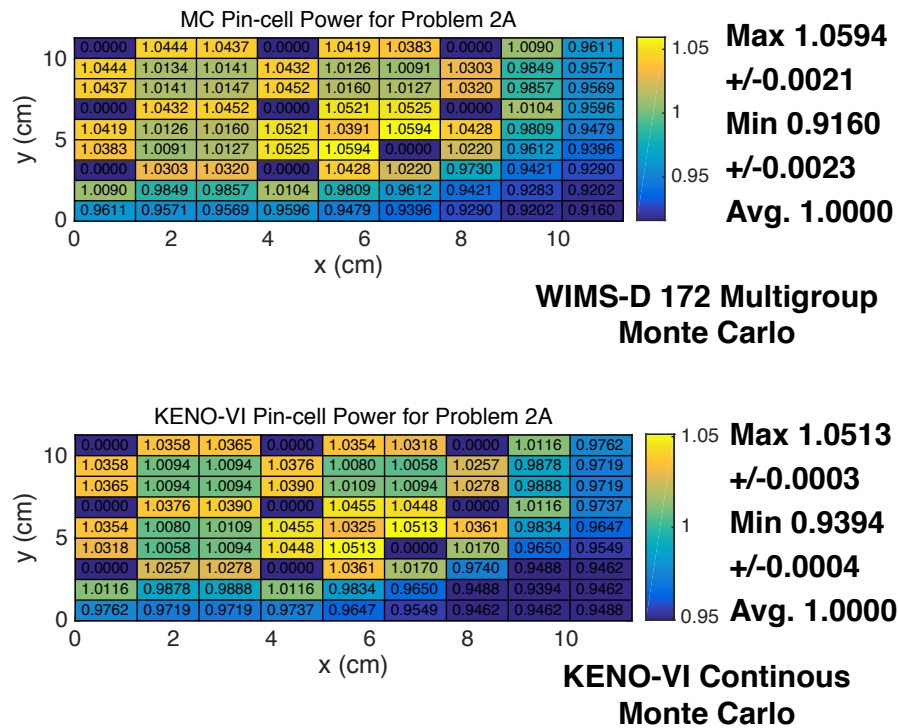


Figure 7.12: Validation of WIMS-D cross sections for problem 2A pin-cell power

7.5 Problems with a Large Flux Gradient

In the previous section 7.4, we studied the VERA benchmark problems, which have “flat” fluxes. In this section, we study two modified VERA benchmark problems to test the behavior of the SN methods under more “difficult” conditions, i.e. there are large gradients in the solutions.

7.5.1 Mini-assembly Problem

7.5.1.1 Problem Description

The first problem considered here is the mini-assembly problem, which we first saw earlier in section 6.3, when we studied the one-group problems. The geometry is shown in Figure 6.9. The fuel pin-cells in this problem have no IFBA layers. The materials use multigroup cross sections as described in Table 7.1.

Each fuel pin-cell is divided into 16 angular sectors, and each moderator pin-cell is divided into a 4x4 sub-grid of squares. The spatial grid is illustrated in Figure 7.13.

7.5.1.2 Verification

The solutions are normalized so that the maximum power in the fuel pin-cells is 1.0. Table 7.11 compares the errors in k -effective versus the the time cost. Table 7.12 compares the pin-cell powers. Figure 7.14 compares the k -eigenvalue and maximum to minimum pin-cell power ratios. Figure 7.15 compares pin-power distribution in different methods. In this problem, the pin-cell power drops 30% from the “hottest” pin-cell to the “coldest” pin-cell.

In this problem, the MB solution is significantly more accurate than the MOC solution, which is more accurate than the SSC and STEP solutions. This confirms our conjecture from Chapter VI that the MB method is more accurate than MOC when the scalar flux is less-flat.

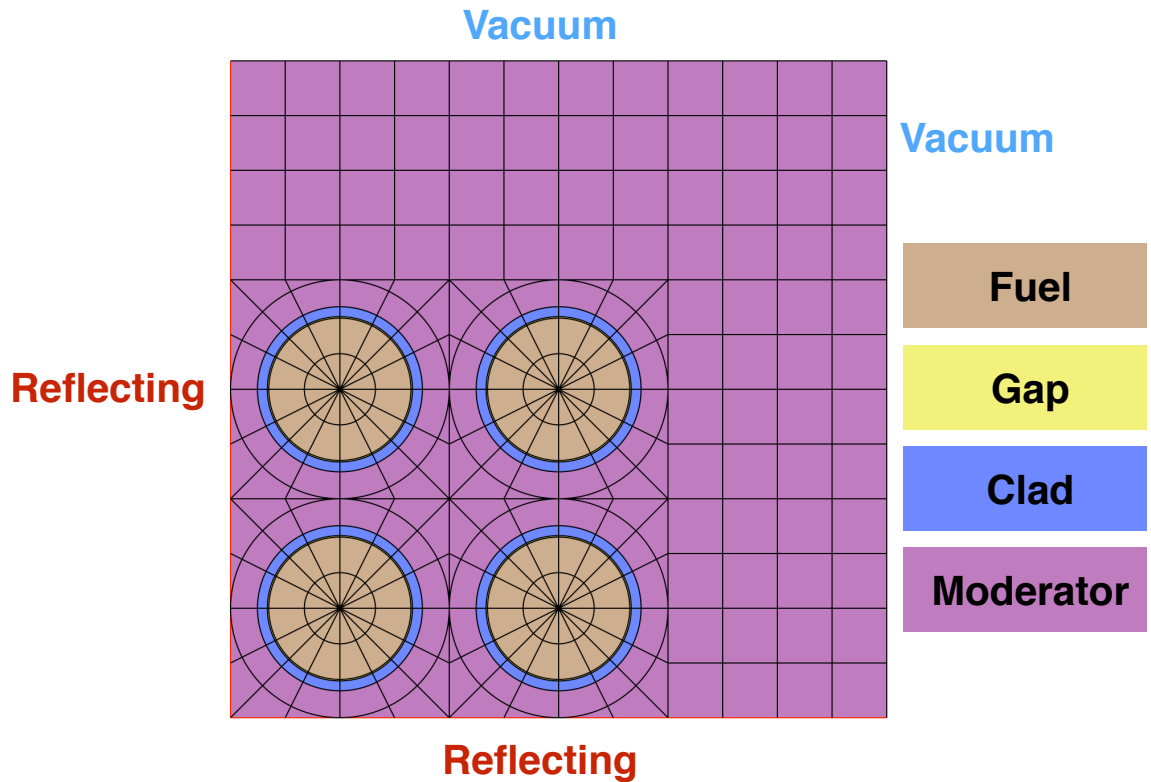


Figure 7.13: The spatial grid for the mini-assembly problem, which consists of a 3x3 grid of pin-cells. The top and right boundaries next to the moderator pin-cells are vacuum, and the bottom and left boundaries next to the fuel pin-cells are reflecting.

Again, we see that the storage requirements of discrete ordinates methods have only a weak dependence on the angular quadrature sets.

7.5.2 VERA Benchmark Problem 2A with Vacuum Boundaries

7.5.2.1 Problem Description

The second problem considered here is the same one as the VERA benchmark problem 2A discussed in section 7.4.3, except that the assembly has vacuum boundary conditions.

Table 7.11: List of k -effective versus time cost for mini-assembly problem

METHOD	KEFF	KEFF ERROR. (pcm)	TIME PER IT- ERATION (ms)	STORAGE (MB)
MC	0.064116	3.5	N/A	N/A
MOC D0.05 A8P4	0.062722	-139.4	1,042	0.944
MOC D0.02 A8P4	0.062660	-145.5	2,511	2.324
MOC D0.01 A8P4	0.062751	-136.5	4,966	4.611
STEP S4	0.054602	-951.3	559	0.357
STEP S8	0.056187	-792.9	1,233	0.344
STEP S16	0.056794	-732.2	4,740	0.340
SSC S4	0.056486	-762.9	568	0.357
SSC S8	0.058221	-589.5	1,414	0.344
SSC S16	0.058886	-522.9	5,333	0.340
MB S4	0.061722	-239.3	1,209	0.357
MB S8	0.062832	-128.4	3,693	0.344
MB S16	0.063734	-38.2	16,928	0.340

See Table 4.1 for definitions of the methods' name abbreviations

Table 7.12: List of pin-cell power of the mini-assembly problem

METHOD	PIN POWER (0,0)	PIN POWER (0,1)	PIN POWER (1,0)	PIN POWER (1,1)	PIN POWER ERROR (%)	Max- min Pin Power Ratio
MC	1.0000	0.8771	0.8770	0.7633	0.044	1.3102 \pm 0.0008
MOC A8P4 D0.05	1.0000	0.8721	0.8721	0.7539	0.731	1.3264
MOC A8P4 D0.02	1.0000	0.8724	0.8724	0.7544	0.691	1.3255
MOC A8P4 D0.01	1.0000	0.8727	0.8727	0.7547	0.662	1.3250
STEP S4	1.0000	0.8488	0.8488	0.7216	3.555	1.3858
STEP S8	1.0000	0.8555	0.8555	0.7303	2.769	1.3692
STEP S16	1.0000	0.8583	0.8583	0.7343	2.425	1.3618
SSC S4	1.0000	0.8551	0.8551	0.7306	2.780	1.3687
SSC S8	1.0000	0.8618	0.8618	0.7394	1.992	1.3524
SSC S16	1.0000	0.8646	0.8646	0.7436	1.635	1.3449
MB S4	1.0000	0.8731	0.8731	0.7581	0.468	1.3191
MB S8	1.0000	0.8741	0.8741	0.7586	0.389	1.3182
MB S16	1.0000	0.8737	0.8737	0.7587	0.407	1.3181

See Table 4.1 for definitions of the methods' name abbreviations

7.5.2.2 Verification

Table 7.13 compares the accuracies of the k -eigenvalue and the maximum and minimum pin-cell powers. The pin-cell powers are normalized so that the average is

Mini-assembly

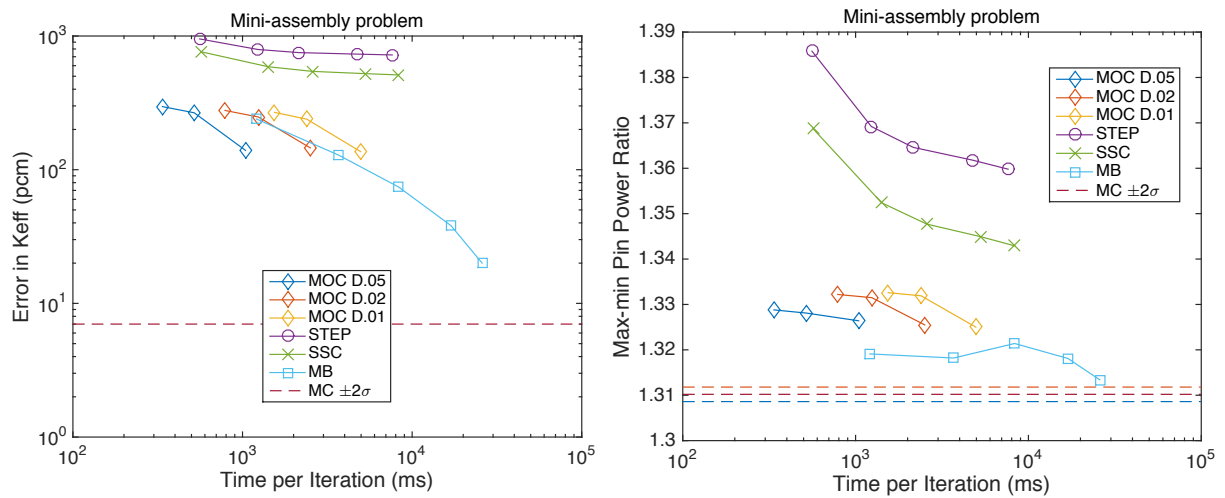


Figure 7.14: Error comparisons for the mini-assembly problem. The MOC solution data points are simulated with a variety of angular quadrature sets: A4P2, A4P4, A8P4. The SN solution data points are also simulated with a variety of angular quadrature sets: S4, S8, S12, S16, S20. The dashed lines are the Monte Carlo uncertainties within two standard deviations. The uncertainties in the Monte Carlo k -eigenvalues are so small that the dashed lines cannot be distinguished from each other.

1.0, and the power distributions are compared in Figure 7.17, while the error in power distribution is compared in Figure 7.18. Figure 7.16 compares the k -eigenvalue and maximum to minimum pin-cell power ratios.

In this problem, the MB method has the smallest error in k -eigenvalue, and the SSC method has the smallest error in the pin-power. We notice that the SSC and MB method are much more accurate than the STEP method, and are comparable to the MOC method. However, the MB method is slightly more inaccurate at the corner pin-cell with minimum pin power. This also suggests that SSC and MB are alternative methods to MOC for reactor simulations.

With all vacuum outer boundaries, the problem simulates a single assembly. So

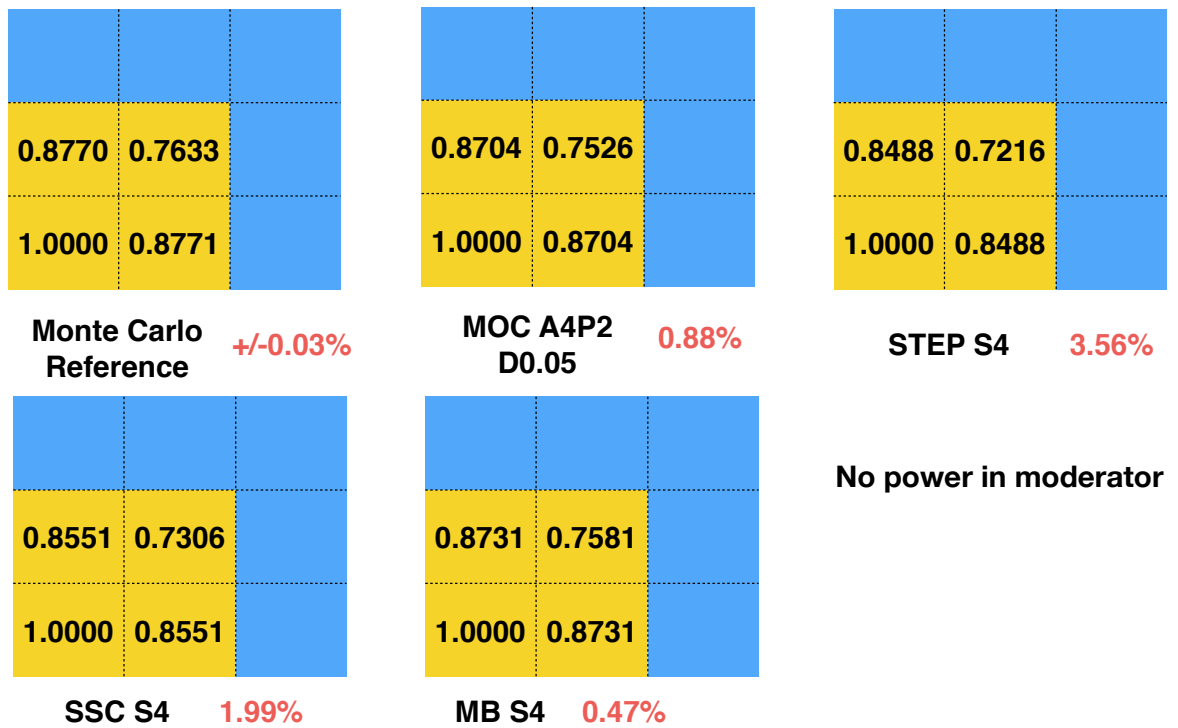


Figure 7.15: Pin-power distribution from the MC, MOC, STEP, SSC and MB method. The uncertainty in the pin-power and the error between other methods other than MC and the MC method is provided as well.

the flux has a descending gradient from the center to the outer rim of the reactor. We see again that, when the solution is less flat than the problem with all reflecting boundaries, we see that SSC method achieves smaller pin-power than MOC. The MB solution is as accurate as MOC in most of the pin-cells besides those near the vacuum boundaries. A possible reason is that the flux is very small near the vacuum boundaries, and 4 digits after the decimal numbers are kept in numerical values, so this could cause an error upto 1%. Another possible reason is the yet unknowns potential deficiency of MB method in dealing with vacuum boundary conditions. Despite the big errors of MB solutions near the vacuum boundaries, the numerical results confirm the conclusion from the previous problem: if the problem has a large

Table 7.13: List of k -effective versus time & pin-cell power for Problem 2A Vacuum

METHOD	KEFF	KEFF ER- ROR. (pcm)	TIME PER ITER- ATION (ms)	MAX PIN POWER	MIN PIN POWER	MAX- MIN PIN POWER RATIO	ERROR IN PIN POWER RATIO (%)	STORAGE (MB)
MC (100 Million)	0.48501	7	N/A	2.0387	0.0935	21.8119	0.03	N/A
MOC A4P2 D0.05	0.48085	-416	4,204	2.0248	0.0931	21.7487	-0.29	5.467
MOC A4P4 D0.05	0.48085	-416	6,849	2.0358	0.0938	21.7036	-0.50	5.467
MOC A4P2 D0.02	0.48306	-195	15,426	2.0382	0.0933	21.8457	0.15	13.097
MOC A4P4 D0.02	0.48306	-195	24,733	2.0489	0.0939	21.8200	0.04	13.097
STEP S4	0.46546	-1,955	12,808	2.0319	0.0961	21.1436	-3.06	2.567
STEP S8	0.46636	-1,865	33,160	2.0258	0.0977	20.7349	-4.94	2.477
SSC S4	0.47717	-784	12,341	2.0758	0.0934	22.2248	1.89	2.567
SSC S8	0.47813	-688	36,361	2.0308	0.0934	21.7430	-0.32	2.477
MB S4	0.48273	-228	41,555	2.0506	0.0885	23.1706	6.23	2.567
MB S8	0.48303	-198	99,074	2.0438	0.0910	22.4593	2.97	2.477

See Table 4.1 for definitions of the methods' name abbreviations

gradient in the pin-power, the SSC and MB methods become more advantageous.

Problem 2A with Vacuum Boundaries

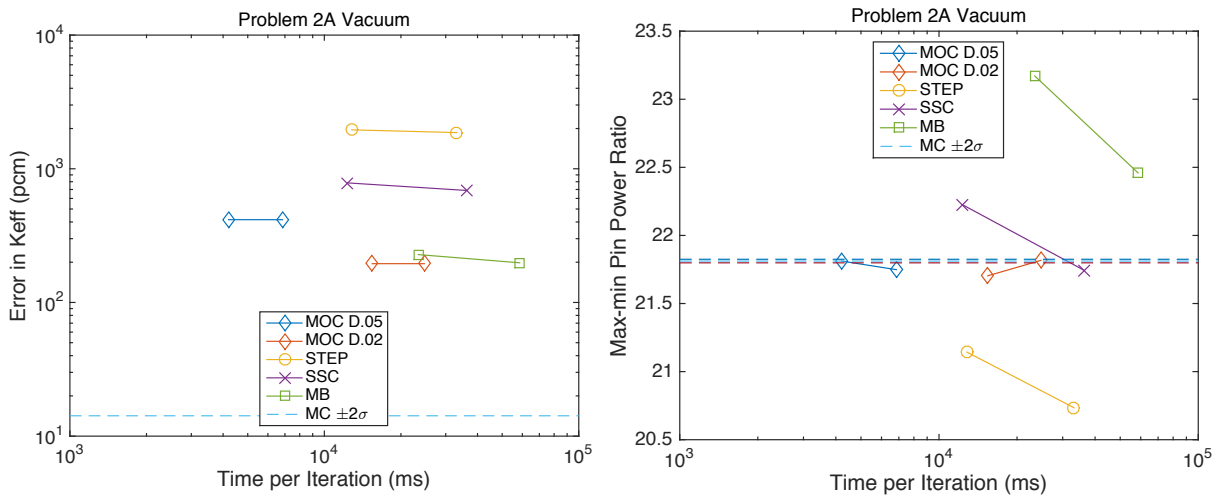


Figure 7.16: Error comparisons for the problem 2A with vacuum boundaries. The MOC solution data points are simulated with two angular quadrature sets: A4P2, A4P4. The SN solution data points are also simulated with two angular quadrature sets: S4, S8. The dashed line shows the Monte Carlo uncertainties within two standard deviations. The uncertainties in the Monte Carlo k -eigenvalues are so small that the dashed lines cannot be distinguished from each other.

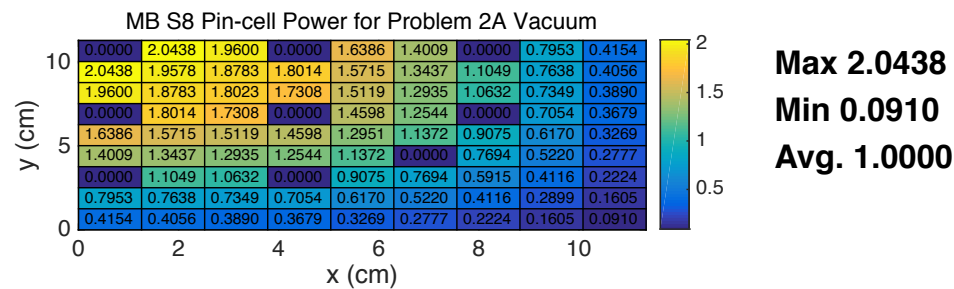
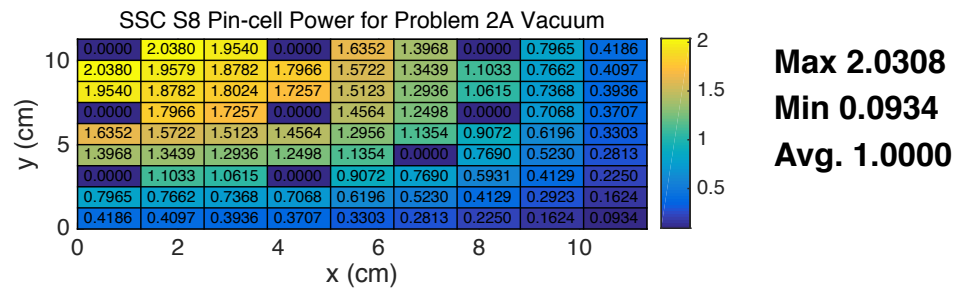
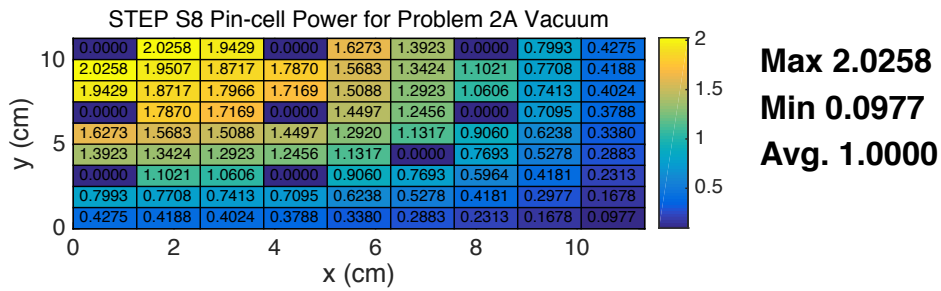
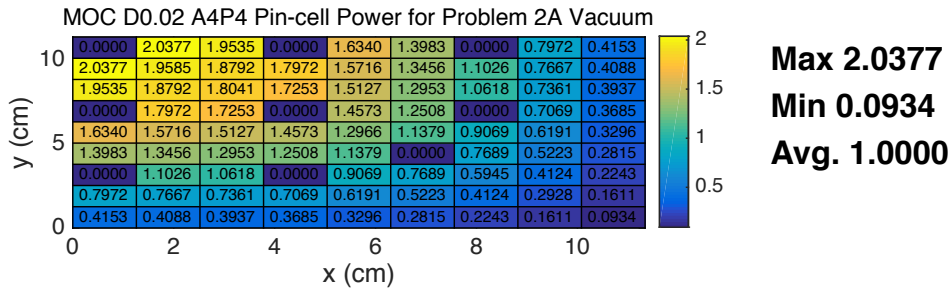
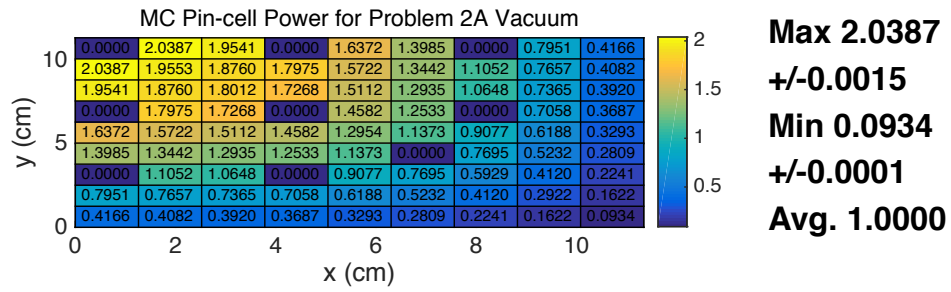
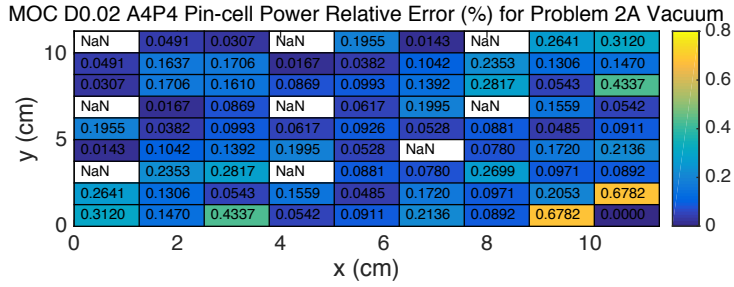
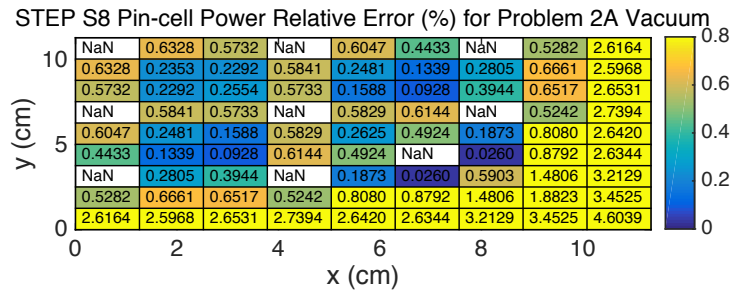


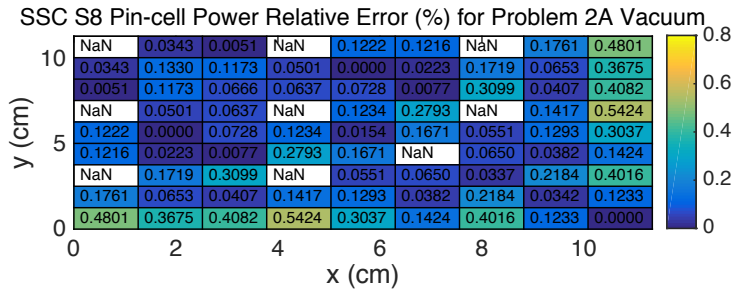
Figure 7.17: Comparison of pin-cell power distributions for Problem 2A with vacuum boundaries.



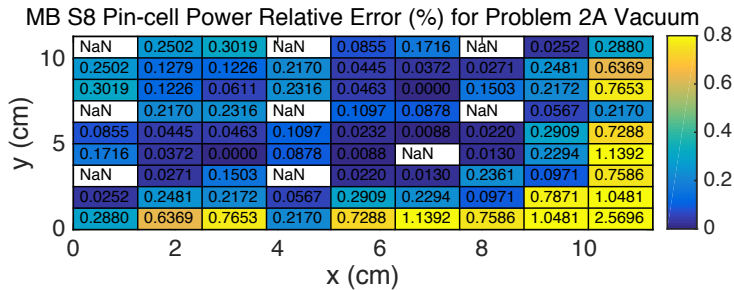
Max 0.6782%



Max 4.6039%



Max 0.5424%



Max 2.5696%

Figure 7.18: Comparison of pin-cell power error distributions for Problem 2A with vacuum boundaries.

7.6 Summary

In this chapter, we have studied realistic problems from a simple pin-cell to an assembly, using an industrial standard multigroup cross section library. We demonstrate that the discrete ordinates that the SSC and MB method can be alternative methods to MOC for reactor simulations.

Overall, we find that the SSC and MB method are comparable to MOC in both accuracy and computational cost.

CHAPTER VIII

Conclusions & Future Work

8.1 Conclusions

The accomplishments in the thesis can be summarized as follows:

1. The principal accomplishment encompasses the derivation, implementation, and testing of two new 2D “Simplified STEP Characteristics” (SSC) “Multiple Balance” (MB) discrete-ordinates methods, which are applicable for systems having curved interfaces between material regions, and which treats these curved surfaces analytically.
2. All previous discrete-ordinates methods, implemented in available 2D production computer codes, were formulated only for problems containing spatial cells with planar boundaries. This creates geometric approximations and inefficiencies for modeling any physical system with curved boundaries – the curved boundaries must be approximated using a great many very fine spatial cells, each fine cell having a planar boundary. (This is one reason why Monte Carlo is considered to have a fundamental advantage over deterministic methods: Monte Carlo does not require material interfaces to be planar.) In this thesis, we have considered spatial grids that, for certain types of LWR problems, have no geometrical approximation.

3. Historically, a fundamental reason for *not* trying to develop discrete ordinates methods for problems with spatial cells having curved boundaries has been the issue of re-entrant boundaries. If spatial cells have curved boundaries, then there will be directions of flight for which a curved boundary is neither incoming nor outgoing; it is *re-entrant*. (Re-entrant boundaries cannot occur when the boundaries of all spatial cells are planar.) Re-entrant boundaries create a major obstacle in sweeping, due to issues of stability that occur if one tries to sweep through a system in a direction that is not consistent with the direction of flight. In this thesis, we have dealt with the re-entrant boundary issue by (i) temporarily “splitting” a cell with a re-entrant boundary into two cells, each of which has no re-entrant boundaries, (ii) sweeping through the split cells, and (iii) combining the results of sweeping through the split cells to obtain estimates of the cell-averaged flux for the original spatial cell. For problems having pin-cell geometries, this “splitting” process is conceptually straightforward.
4. The MOC method, which is currently the method-of-choice for multidimensional reactor core transport calculations, uses:
 - (a) Unoptimized “modular” quadrature sets, with directions of flight that are efficient for applying MOC on systems with square coarse spatial cells, but have angular weights that are not optimized and do not preserve the integral-preserving properties of standard discrete-ordinates quadrature sets.
 - (b) *Two* fine spatial grids: the geometrical “flat source” regions on which the scattering and fission sources are represented as spatially constant, and the “ray-spacing” (the distance between different characteristic rays). To achieve high accuracy, the “fine grid” flat source regions must be small to minimize the error created by assuming the source in these regions to

be “flat”. In addition, the ray spacings should be small compared to the “fine grid” size, in order that there are several rays in each direction of flight crossing each fine cell. Therefore, to achieve high accuracy, an MOC calculation must be run with a very fine “fine” grid, and an even finer ray spacing.

In contrast, the SSC and MB methods developed in this thesis are conventional discrete ordinates methods in the sense that (i) they use standard, highly-optimized discrete ordinates quadrature sets, and (ii) they have a single user-specified spatial grid.

5. We have implemented and tested the SSC and MB methods for problems with realistic 2D pin cell geometries, and have compared the accuracy of the SSC, MB and MOC solutions against the computer run times. Our results are mixed. Generally, for “easy” problems in which the neutron flux is spatially flat, the MOC method is more efficient than SSC and MB. (We believe the reason for this to be that the MOC method is designed by assuming the scattering and fission sources within a fine cell to be flat. If in fact these sources *are* flat, then MOC *should* be optimal.) However, for more difficult problems in which the spatial gradients of the flux are not small, we generally find the SSC and MB methods to be more accurate.
6. In general, we find for difficult problems that for the SSC and MB methods to generate a highly accurate solution, a somewhat finer “fine” spatial grid must be used than the “flat-source” grids commonly employed for MOC today. However, this “somewhat finer” fine grid is much coarser than the “ultra-fine” ray spacing that is required for MOC to give accurate results. In other words: although SSC and MB do require a finer fine grid than MOC does today, it does not require this grid to be anywhere near as fine as the required MOC ray spacing.

7. We also generally find that the SSC and MB methods require *significantly* less storage than MOC.
8. Overall, we find the SSC and MB methods to be at least competitive to MOC for 2D problems. Although we have tried to seriously test the SSC and MB methods, it is clear that our experience is limited. Nonetheless, we believe that the method has basic advantages that are not shared by MOC.

8.2 Future Work

Possible future work includes the following:

1. The SSC and MB methods should be tested on a wider range of realistic 2D problems.
2. The SSC and MB methodology should be generalized to account for anisotropic scattering. This generalization should be straightforward. No actual change in the SSC and MB spatial discretization methods itself is required; the only modification is that the scattering source term will become direction-dependent.
3. This thesis has focused on 2D LWR problems, in which the basic geometrical unit of the system is a “pin cell” – a square region having annular subregions with boundaries consisting of concentric circles with centers at the center of the pin cell. Other types of reactors, in particular BWRs, have more complicated geometries. The SSC and MB methods should be considered for these problems also.
4. The SSC and MB methods were developed in this thesis for 2D problems. It should be straightforward to generalize the SSC and MB methods to 3D problems having geometries that are similar to the LWR 2D geometry considered here – in particular, having curved surfaces that are basically 2-D in nature.

Clearly, the more complicated the 3D geometry, the more complicated – and expensive to implement – will be the SSC and MB methods. Nonetheless, there is no apparent reason why the SSC and MB methods should not be adaptable to 3D. Moreover, given the widely-acknowledged inability of MOC to realistically treat 3D geometries, it seems highly likely that for 3D problems, methods such as SSC and MB will be considerably more efficient than MOC.

5. This thesis extends the SSC and MB discrete ordinates methods on Cartesian and triangular grids to neutron transport on curved spatial grids. It should also be straightforward to develop similar numerical methods for fluid mechanics and electro-magnetics on curved spatial grids. A benefit of this approach is that the triangularization is no longer required, and the curved boundaries will be treated exactly.

BIBLIOGRAPHY

BIBLIOGRAPHY

- Aldama, D. L. (2014), *Documentation for WIMSD-formatted libraries based on ENDF/B-VII.1 evaluated nuclear data files with extended actinide burn-up chains and cross section data up to 2000 K for fuel materials.*, 36 pp., International Atomic Energy Agency, Vienna, Austria.
- Anderson, D. E. J., and C. W. Hord (1977), Multidimensional Radiative Transfer: Application to Planetary Coronae, *Planet Space Science*, 25, 563–571.
- Askew, J. (1972), A Characteristics Formulation of the Neutron Transport Equation in Complicated Geometries, *AEW-R-1108*.
- Askew, J., F. Fayers, and P. Kemshell (1966), A general description of the code WIMS, *J. Br. Nucl. Energy Soc.*, 5, 564.
- Briesmeister, J. (1997), *MCNP- A General Monte Carlo N-Particle Transport Code*, Los Alamos National Laboratory.
- Carlson, B., and G. Bell (1958), Solution of the Transport Equation by the SN method, *Proc. U.N. Intl. Conf. Peaceful Uses of Atomic Energy*.
- Chadwick, M., and et al. (2011), ENDF/B-VII.1 Nuclear Data for Science and Technology: Cross Sections, Covariances, Fission Product Yields and Decay Data, *Nuclear Data Sheets*, 112, 2887–2996.
- Chandrasekhar, S. (1960), *Radiative Transfer*, Dover, New York.
- DeHart, M. (2003), *NEWT: A New Transport Algorithm for Two-Dimensional Discrete Ordinate Analysis in Non-Orthogonal Geometry*, Oak Ridge National Laboratory.
- Godfrey, A. (2014), Vera Core Physics Benchmark Progression Problem Specifications, Revision 4, *CASL*, *CASL-U-2012-0131-004*, 1–173.
- Goldstein, R., and E. Cohen (1962), Theory of Resonance Absorption of Neutrons, *Nuc. Sci. Eng.*, 13, 132.
- Halsall, M. (1991), A review of the WIMS nuclear data library, *Nucl. Energy*, 30, 285–290.

- Hebert, A. (2009), *Applied Reactor Physics*, Presses Internationales Polytechnique, Canada.
- Hyun, M. R., H. Cho, C. H. Lim, Y. S. Jung, and H. G. Joo (2014), Preliminary Assessment of nTRACER and McCARD Direct Whole Core Transport Solutions to VERA Core Physics Benchmark Problems, *Transactions of the American Nuclear Society, Anaheim, California, Nov. 09 – 13*.
- Kahn, A. B. (1962), Topological sorting of large networks, *Communications of the ACM*, 5, 558–562.
- Lathrop, K. (1969), Spatial Differencing of the Transport Equation: Positivity VS. Accuracy, *J. Comp. Phys.*, 4, 475.
- Leszczynski, F. (1997), *Goldstein Cohen Parameters for Preparation of Multi-group Libraries, Rep. CAB-CNEA for WLUP*, Bariloche Atomic Center, National Atomic Energy Commission, Argentina.
- Leszczynski, F. (1999), *Goldstein Cohen Parameters for Preparation of Multi-group Libraries, II. Sensitivity Analysis and Final Remarks, Rep. CAB-CNEA for WLUP*, Bariloche Atomic Center, National Atomic Energy Commission, Argentina.
- Leszczynski, F., D. L. Aldama, and A. Trkov (2007), *WIMS-D Library Update: final report of a coordinated research project*, 321 pp., International Atomic Energy Agency, Vienna, Austria.
- Lewis, E., and W. Miller Jr. (1984), *Computational Methods of Neutron Transport*, John Wiley and Sons.
- Li, S., B. Zhang, Z. Liu, Y. Yan, H. Yu, Y. Chen, and G. C. Zhang (2013), COSINE 软件包组件参数计算程序 LATC 中 S_N 运输模块的开发和初步验证 (Chinese), Development and Preliminary Validation of the S_N Transport Modular in Lattice Code LATC of COSINE Package, *Atomic Energy Science and Technology*, 47 Suppl.
- Liu, Y. (2015), *Ph.D. Thesis: A Full Core Resonance Self-shielding Method Accounting for Temperature-dependent Fuel Subregions and Resonance Interference*, University of Michigan.
- Lucas, D. (2005), Core Modeling of the Advanced Test Reactor with the Attila Code, *M&C 2005: International Topical Meeting on Mathematics and Computation, Supercomputing, Reactor Physics, and Nuclear and Biological Applications*, Avignon, France.
- Lux, I., and L. Koblinger (1991), *Monte Carlo Particle Transport Methods: Neutron and Photon Calculations*, CRC Press, Boca Raton, Florida.
- Marleau, G., A. Hebert, and R. Roy (2013), A User Guide for DRAGON Version 4, *Institut de genie nucleaire, Ecole Polytechnique de Montreal, IGE-294*.

- McLane, V. (2001), *Data Formats and Procedures for the Evaluated Nuclear Data File, ENDF-6*, Brookhaven National Laboratory.
- Metropolis, N., and S. Ulam (1949), The Monte Carlo Method, *American Statistical Association*, 44, 247.
- Morel, J., and E. Larsen (1990), A Multiple Balance Approach for Differencing the SN Equations, *Nuc. Sci. and Eng.*, 105, 1–15.
- MPACT Team (2013), MPACT User Manual, *University of Michigan, Ann Arbor*.
- Reed, W., and T. Hill (1973), *Triangular Mesh Methods for the Neutron Transport Equation (LA-UR-73-479)*, Los Alamos Scientist Laboratory Report.
- Seed, T., and W. Miller Jr. (1978), *TRIDENT: a new triangular mesh discrete ordinates code (LA-UR-77-2511)*, Los Alamos National Laboratory.
- Spanier, J., and E. Gelbard (1969), *Monte Carlo Principles and Neutron Transport Problems*, Addison-Wesley Publishing Company.
- Stammler, R., and M. Abbate (1983), *Methods of Steady-state Reactor Physics in Nuclear Design*, Academic Press, London.
- Williams, M. (1966), *The Slowing Down and Thermalization of Neutrons*, North-Holland, Amsterdam.
- Yee, B. C., and E. W. Larsen (2015), A New Multiple Balance Method for Spatially Discretizing the SN Equations, *Proc. ANS MC2015, Nashville, TN, April 19-23, 2015, American Nuclear Society*.